PRODUCTION OF BIOFUELS FROM VARIOUS LIGNOCELLULOSIC STREAMS BY LIQUEFACTION

REGINA HOI MAN SIU

Doctor of Philosophy

ASTON UNIVERSITY

September 2022

Aston University
Production of biofuels from various lignocellulosic streams by liquefaction
Regina Hoi Man Siu
Doctor of Philosophy
September 2022

Thesis Abstract

This PhD research project aimed to study the application of lignocellulosic biomass and waste lignin in a conventional hydrothermal liquefaction process aiming production of bio-liquids as a value-added by-product to achieve middle-range distillates used in the biorefinery streams delivering transportation fuels.

Pine wood, wheat straw and LignoBoost lignin were characterised and selected for hydrothermal liquefaction and liquefaction in molten salts. To fully understand the thermal degradation of the studied feedstock, biochemical components cellulose, xylan (hemicellulose) and Organosolv lignin were also introduced and characterised by analytical pyrolysis (Py-GC-MS). Analytical pyrolysis allowed the prediction of feedstocks' thermal degradation reaction network and assessing potential constituents of bio-liquids (bio-crudes). Metal analysis was conducted to give a better insight into the inorganic components of biomass and their potential interaction with molten salts during liquefaction.

Kinetic assessments, using Kissinger, Kissinger-Akahira-Sunose (KAS) and Flynn-Wall-Ozawa (FWO) models, on the studied biomass and biochemical components were calculated using the results acquired from TGA. The activation energies from the kinetic models (KAS and FWO) were used to obtain the thermodynamic parameters, including enthalpy, Gibbs free energy and entropy. Enthalpy and Gibbs free energy results have shown that additional heat is required during the thermal decomposition. The entropy results revealed that the reaction was moving from a disorderly state to get closer to a thermodynamic equilibrium.

Hydrothermal liquefaction (HTL) experiments were conducted in a 300 ml batch reactor. The impact of the temperature (275, 300 and 325 °C) during HTL processing was investigated using LignoBoost lignin and pine wood. LignoBoost lignin was found with the highest bio-crude yield of 9.31 wt. % at the highest processing temperature of 325 °C. Whilst pine wood favoured a lower processing HTL temperature (300 °C) and obtained a bio-crude yield of 8.21 wt. %. Bio-products obtained from HTL processing (gas, liquids and solids) were characterised using various analytical equipment. The aqueous phase was analysed with the specifically developed methodology using high-performance liquid chromatography (HPLC). The HPLC revealed methanol and carboxylic acids (formic, acetic and propanoic acid) were found in HTL-derived aqueous phases of LignoBoost lignin and pine wood.

The molten salt mixture of $ZnCl_2$:KCl:NaCl was used in biomass liquefaction at a molar ratio of 44.3:41.9:13.8 %, respectively. The pure molten salt was characterised using x-ray diffraction (XRD) and differential scanning calorimetry (DSC) to understand the crystallinity and the thermal behaviours when used in the liquefaction processing. The DSC was used as a benchmark analysis for the assessment of thermal behaviour and quality from the molten salts, recovered after liquefaction experiments, prior to their re-application. From the DSC analysis, the recycled molten salts maintained the desirable melting point at the temperature region of 200 °C, which was in line with the theoretical and actual melting point of the unprocessed 'pure' molten salt.

Keywords: lignocellulosic biomass; hydrothermal liquefaction; molten salt; kinetic; thermodynamic

Therefore do not worry about tomorrow,

for tomorrow will worry about itself.

Each day has enough trouble of its own.

Matthew 6:34

Acknowledgements

I would like to express my sincere gratitude to my supervisor Dr Daniel Nowakowski who provided his continuous guidance, support and feedback over the years.

I would also like to thank Professor Tony Bridgwater for his advice throughout my research. And special thanks to Dr Jinesh Cherukkattu Manayil, who helped and trained me in the laboratory.

I want to express my gratitude to the ABC-Salt Research Consortium, particularly to project partners from Ghent University (Belgium) and the Norwegian University of Life Sciences (Norway). Adriana Estrada Leon and Frederik Ronsse are acknowledged for the collaboration and data sharing from liquefaction experiments work (chars and spent/recycled molten salt samples). Sepideh Niazi and Heidi Nygård for the guidance and FactSage modelling results for the interaction of biomass inorganic matter with potential molten salts interaction.

To my former and present fellow colleagues, especially Iram, Cristiane, Huan, Chris, Mo, Filipe and Jorge, who encouraged me throughout the years in EBRI and Aston University. Thank you to the staff, Katie, Mirjam and Paula, at EBRI and Aston University who have offered their support and the opportunities given to me.

To my pals and friends, it wouldn't have been the same without you guys. Thank you for keeping me sane.

Finally, I would like to thank mum, dad and Alan for their unconditional love and patience, who never stopped believing in anything that I do.

Table of Contents

List of Figures

List of Tables

List of abbreviations and acronyms

a.r.	as received
ABC-Salt	Advanced Biomass Catalytic Conversion to Middle Distillates in Molten Salts
Al	aluminium
A_o	pre-exponential factor
ASTM	American Society for Testing and Materials
°C	Celsius
C	carbon
Ca	calcium
$CaCl_2$	calcium chloride
$CaCO_3$	calcium carbonate
Cl	chlorine
d.b.	dry basis
DSC	Differential Scanning Calorimetry
DTG	Derivative Thermogravimetry
E_a	activation energy
Fe	iron
FWO	Flynn-Wall-Ozawa
g	grams
GC-MS	Gas Chromatography-Mass Spectrometry
GHG	Greenhouse Gas
H	hydrogen
H	Planck's constant
HHV	Higher Heating Value
HPLC	High Performance Liquid Chromatography
HTL	Hydrothermal Liquefaction
ICP-OES	Inductively Coupled Plasma-Optical Emission Spectroscopy
K	Kelvin
K	potassium
K_2CO_3	potassium carbonate
KAS	Kissinger-Akahira-Sunose
K_B	Boltzmann constant
$KCaCl_3$	chlorocalcite
KCl	potassium chloride
kJ	kilojoules
LHV	Lower Heating Value
m/z	mass-to-charge ratio
Mg	magnesium
min	minutes
MJ	megajoules
ml	millilitres
Mm	millimetres
Mn	manganese
mol	mole
N	nitrogen
n/a	not available
n/d	not detected
NaCl	sodium chloride

O	oxygen
P	phosphorus
Py-GC-MS	Pyrolysis-Gas Chromatography-Mass Spectrometry
R	universal gas constant
rpm	revolutions per minute
S	sulphur
SEM-EDX	Scanning Electron Microscope-Energy Dispersive X-ray
T	temperature
TGA	Thermogravimetric Analysis
Ti	titanium
T_m	peak temperature
vol	volume
wt. %	weight percentage
XRD	X-Ray Diffraction
XRF	X-Ray Fluorescence
$ZnCl_2$	zinc chloride
ZnO	zinc oxide
α	conversion
β	heating rate
ΔG	Gibbs free energy change
ΔH	enthalpy change
ΔS	entropy change
μl	micronlitres
μm	micronmetres

Chapter 1

Introduction

1.1. Background

There is an urge to move from fossil fuel resources and fossil fuel-derived products as they are a finite resource. Currently the transportation fuel has been heavily reliant on fossil-based petroleum sources to meet our daily lifestyle. The continuous use of fossil fuels leads to a negative effect on our climate and environment and eventually leading to global warming. Global warming is defined by the Intergovernmental Panel on Climate Change (IPCC) as "*an increase in combined surface air and sea surface temperatures averaged over the globe and over a 30-year period*" [1]. Greenhouse gases (GHGs) is a contributing factor to the global warming. These GHG emissions consist mainly of carbon dioxide (CO_2), methane (CH_4) and nitrous oxide (N_2O) [2]. Accumulation of these GHGs will build a greenhouse effect, which increases the global temperature and consequently lead to global warming. The increase in the global temperature causes droughts, floods, and extreme weather (sea level rise and biodiversity loss) [3]. To address this global concern, the Paris Agreement was set in 2015 and with the aim to limit global warming by well below 2 °C by reducing emissions. By reducing the GHG emissions, the UK also set a strategy in 2019 to reach net-zero GHG emissions by 2050 [4].

Therefore, our heavy reliance on fossil fuels will need to be diverted towards renewable energies. Renewable energy derived from natural resources are able to produce clean and sustainable energies. The different types of renewable energy resources available are wind, solar, geothermal, hydro and biomass. As the name suggest, wind energy is from harnessing wind. Solar power is harvested from the sun, whilst geothermal energy uses thermal energy from the earth's subsurface. Hydropower is obtained from the movement of water. Finally, biomass energy is defined as energy derived from living organisms or matter. Wind and solar energy are intermittent and variable, which cannot be solely relied on for energy production purposes. Both geothermal and hydropower can be difficult, as they are limited by the location and availability. Biomass can be found anywhere and can be an alternative to non-renewable fossil fuels whilst also reducing our overreliance on fossil fuels. Biomass can be used to generate electricity, heat and transportation fuels – known as biofuels.

Numerous technologies are available for the conversion of biomass to biofuels, and these are broadly categorised into thermochemical and biochemical processes. Thermochemical processes use heat to

convert biomass into biofuels, which are combustion, gasification, pyrolysis and liquefaction. Whereas, biochemical conversion technologies uses enzymes and other microorganisms to breakdown biomass, and these include anaerobic digestion (AD) and fermentation. Thermochemical conversion technology can be an efficient and rapid way of producing sustainable transportation fuel from biomass.

Biofuels from biomass are divided into first- and second-generation biofuels. First-generation biofuels or also known as the 'conventional' biofuels (bioethanol and biodiesel) and are produced from edible energy crops such as sugar-based crops (sugarcane and sugar beet), starch-based crops (wheat, corn and barley) or oil-based crops (sunflower, rapeseed and canola) [5]. The use of first-generation biofuels is currently competing with the food market resulting in an increase in food prices. This often triggers the food vs fuel debate and is seen as an unsustainable route to produce biofuels from first-generation feedstock.

This opens an opportunity to move from first-generation to second-generation biofuels. The second-generation biofuels use inedible crops and therefore are not competing directly with the food market. Usually, second-generation biofuels are often from lignocellulosic waste and can be collected from agricultural waste, forestry residues, but this can also include municipal solid waste (MSW), animal manure and food wastes. One good example can be agricultural waste such as wheat straw, which does not serve any other purpose after its grain removal and therefore is considered as a waste. Another good example would be the use of lignin, which is considered a waste and often a by-product from pulp mills. Lignin is an inexpensive and sustainable feedstock, which is used in Kraft pulp mill liquor for the generation of heat and electricity.

Using second-generation biofuels in thermochemical processing can be a solution to producing alternative renewable energy to meet the specification for the conventional biorefinery stream. Both pyrolysis and hydrothermal liquefaction (HTL) technologies are biomass-to-liquid process targeting the middle-distillates for transportation fuel production. With the pyrolysis process, biomass drying will be required and a high temperature range to achieve the optimum liquid yield. On the other hand, HTL avoids the requirement of drying and utilises lower temperature range, which can save costs in the long-term.

Currently the conventional way of producing sustainable biofuels for the transportation sector imposes many challenges. Especially biofuel production from lignocellulosic biomass, which will need pre-treatment prior to thermochemical processing (such as drying). Thermochemical processing is often followed by (catalytic) hydrotreatment or fluid catalytic cracking processes which could be reducing the oxygen content of the bio-crudes. Further upgrading by refining would be the final stage in order to be miscible with the transportation fuels.

Firstly, lignocellulosic biomass is made up of cross-linking polysaccharides, which are cellulose, hemicellulose and lignin at variable levels depending on the type and origin of the biomass. These biochemical compositions are cross-linked with each other providing the biomass with a rigid and crystalline structure. The structure of the biomass also makes it resistant to break down and is considered as a recalcitrant in nature. Therefore, a pre-treatment is needed in order to alter the chemical structure of lignocellulosic biomass, making it easier to breakdown during thermochemical processing.

Without the use of a pre-treatment step, directly feeding the biomass in a thermochemical conversion technology can be problematic. Often the main problems of feeding biomass into the system at high pressure are related to plugging, clogging, leakages and uneven flow resulting in poor quality and low production rates of the bio-products. One way to solve this is by combining a pre-treatment step with a thermochemical process. A less-studied approach is the use of molten salts in liquefaction. The use of molten salts in liquefaction allows the biomass to liquefy at low temperatures (< 200 °C) and at atmospheric pressure, as opposed to using high temperatures and high pressures. The biomass is liquefied with the molten salt and consists in the form of a slurry, which has not excessively cracked or repolymerised. The use of molten salt is advantageous, since the molten salts is known to be thermally stable and can act as a heat carrier and catalyst. Furthermore, the molten salt-biomass slurry will have a low-viscosity, and can easily facilitate the pumping of the slurry resulting in better control of the feeding system [6].

The liquefied slurry is pumped into the second processing stage using hydro-pyrolysis, which is the use of hydrogen at an elevated pressure in pyrolysis. The presence of the hydrogen in the pyrolysis process is expected to achieve a higher carbon yield, less char and less non-condensable gas formation. The slurry will be turned into a vapour and followed by a hydrodeoxygenation step with the help of a suitable and inexpensive catalysts, which is refined into hydrocarbons for middle distillate biofuel.

1.2. Aim and objectives

The aim of this PhD research study was to produce bio-liquids from lignocellulosic biomass and waste lignin by applying hydrothermal liquefaction process, whilst comparing the bio-products obtained from liquefaction in molten salts. The research objectives for this PhD research study were:

- Conducting an in-depth literature review on the biochemical components of biomass and the different types of thermochemical processing, including hydrothermal liquefaction (HTL), hydro-pyrolysis, upgrading routes for the biofuel production and the use of molten salts.
- To select the most promising biomass by using a variety of analytical methods (elemental analysis, thermogravimetric analysis and analytical pyrolysis) in order to understand the thermal properties of feedstock for HTL processing.
- To select non-isothermal models and calculate thermal decomposition kinetics of feedstock and applying the results for thermodynamics assessment, in order to utilise the results for molten salt recycling.
- To investigate the impact of process parameters on HTL product yields obtained from selected feedstock.
- To characterise the bio-products, including gas, solid and liquid products, obtained from HTL using various analytical methods and how the process parameter will impact the processing of biomass.
- To assess the thermal stability of the selected and recycled molten salts using differential scanning calorimetry.
- To compare the results obtained from solid products using the hydrothermal liquefaction and solids from liquefaction with molten salts.

1.3. Thesis structure

The current chapter (Chapter 1) outlines the introduction and the motivation of this PhD research project. This PhD research project will present the biofuel production from lignocellulosic biomass using liquefaction, including the aim and objectives, thesis structure and Horizon2020 ABC-Salt project.

Chapter 2 reports on the comprehensive review of the literature that will be covered in this thesis. The literature review consists of the biochemical composition of lignocellulosic biomass, which are cellulose, hemicellulose, and lignin. Literature review of the cellulose, which involves the Broido-Shafizadeh model, is included to elaborate on the thermal decomposition along with its chemical

structure. Whilst the section on hemicellulose will describe the different types of sugars and its structures that are found in softwood and hardwood lignocellulosic biomass. The biopolymer lignin section goes through the chemical structure and the different types of linkages found. Different processes of delignification production of various types of commercial lignin will also be included. The next part of the literature review discusses the different types of thermochemical conversions, which will go into hydrothermal liquefaction (HTL) and pyrolysis (hydro-pyrolysis) along with the upgrading routes. The literature review of HTL reports on the state-of-the-art review of the process parameters, including the process temperature, pressure, solvents, co-solvents, catalysts and residence time. The pyrolysis section reviews the hydro-pyrolysis studies in non-catalytic conditions.

Chapter 3 details the characterisation and selection of lignocellulosic biomass and lignocellulosic waste. A methodology is included on the feedstock used and a range of analytical equipment that is used for the characterisation of the feedstock, including the elemental analyser, inductively coupled plasma with optical emission spectroscopy (ICP-OES), thermogravimetric analyser (TGA) and pyrolysis-gas chromatography-mass spectrometry (Py-GC-MS). In addition, biochemical components cellulose, hemicellulose and lignin are individually studied using analytical pyrolysis to understand the thermal degradation of lignocellulosic biomass. The selected feedstock are used for further studies including the kinetic and thermodynamic studies in Chapter 4, hydrothermal liquefaction in Chapter 5 and the product analysis in Chapter 6.

Chapter 4 studies the kinetic and thermodynamic assessment on the thermal degradation of the selected lignocellulosic biomass along with the biomass model components (cellulose, hemicellulose and lignin). Kinetic models, including Kissinger, Kissinger-Akahira-Sunose (KAS) and Flynn-Wall-Ozawa (FWO) methods, are all model-free and non-isothermal methods. The kinetic parameters (the activation energy and pre-exponential factor) are acquired from the derivative thermogravimetric (DTG) profiles from thermogravimetric analyses (TGA) at different heating rates. Thermodynamic parameters for lignocellulosic biomass and model components including the enthalpy, Gibbs free energy and entropy, are obtained from the KAS and FWO methods.

Chapter 5 concentrates on the hydrothermal liquefaction (HTL) using lignocellulosic biomass and waste. The HTL experiments investigate the impact of temperature and the use of different feedstock. The methodology elaborates on the use of a 300 ml batch reactor for HTL experiments, as well as the characterisation of the gaseous, liquid and solid products obtained from the HTL experiments. A mass balance is included to get the yield of the products. The gas products are characterised using a GC and the bio-crude is characterised using an elemental analyser and GC-MS, whilst the aqueous phase is characterised using GC-MS and high-performance liquid chromatography (HPLC) using a new

developed method. The solid products are characterised using an elemental analyser and scanning electron microscopy (SEM).

The last research chapter, Chapter 6, discusses the product analyses on the characterisation of the (molten) salts, recycled salts and recovered chars. A methodology is included on how the molten salts are generated (molten salts are obtained from Norwegian University of Life Sciences), along with the recycled salts and the recovered chars (experiments are carried out in Ghent University). X-ray diffraction (XRD) analyses are studied on the 'pure' molten salts to understand the diffraction pattern. Inorganic metal analysis results (from Chapter 3) are used to investigate the most abundant inorganic matter found in lignocellulosic biomass, which are added to the 'pure' molten salts. XRD studies are used on the molten salts with added inorganics and compared with the 'pure' molten salts. Differential scanning calorimetry (DSC) is used to check the thermal stability of the molten salts and recycled salts, which are compared with each other. Whilst the recovered chars (from this chapter) and the chars acquired from the HTL (Chapter 5) experiments are compared using an elemental analyser and SEM imaging. X-ray fluorescence (XRF) analyses are used to investigate the presence of salts found in the recovered char.

Finally, Chapter 7 reports on the research aim and objectives are met. Suggestions on future work as well as planned dissemination are outlined in this section.

1.4. Horizon 2020 ABC-Salt Project

This PhD is funded by the Horizon2020 Advanced Biomass Catalytic Conversion to Middle Distillates in Molten Salt (ABC-Salt) project (project number 765089), which aims to produce biofuels from lignocellulosic biomass into middle distillates on an innovative scale in order to lower GHG emissions. The project seeks to integrate all existing thermochemical conversion technologies (including liquefaction, fast pyrolysis, hydrodeoxygenation and molten salt systems), whilst achieving higher liquid and carbon yields as well as eliminating the existing issues faced such as low yield in liquefaction processing, feeding biomass in hydro-pyrolysis, or high costs involved. Therefore, the project (as outlined in Figure 1) will use molten salts and lignocellulosic biomass in liquefaction at low temperatures and low pressure to produce a homogeneous slurry, which will improve chemical stability and achieve a higher biomass to hydrocarbon yields. The molten salt slurry will then go through hydro-pyrolysis and to have a lower char and permanent gas production. Followed by hydrodeoxygenation process, which will reduce hydrogen consumption thus improving the liquid yield to produce middle distillates.
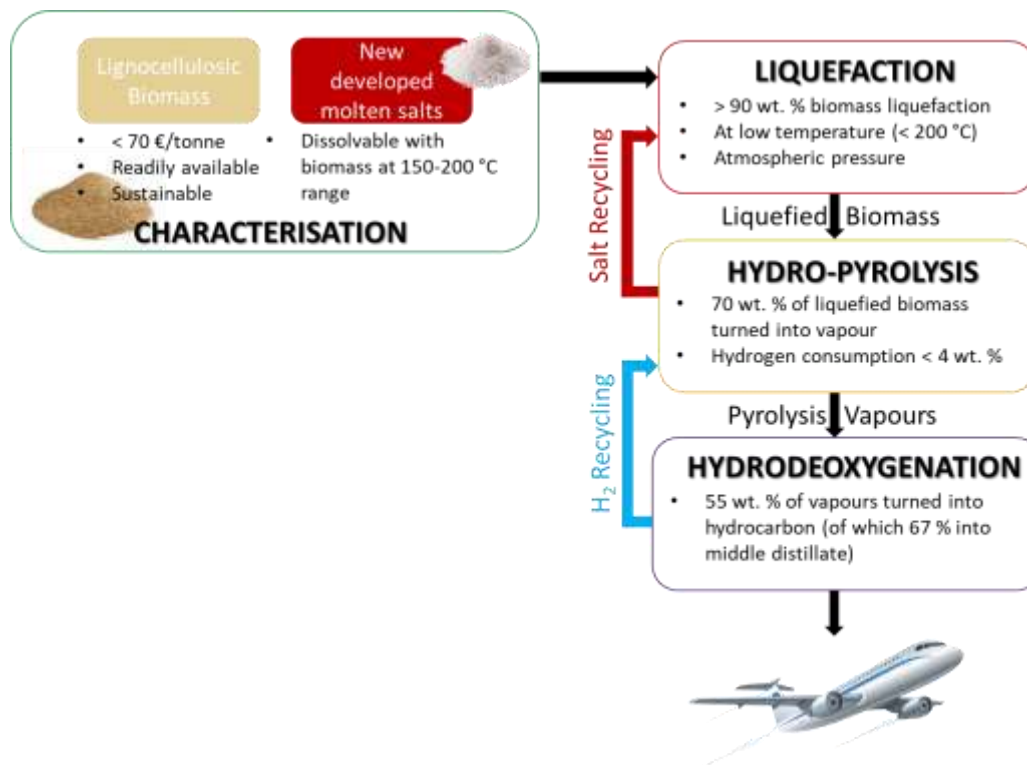
Figure 1. Proposed ABC-Salt research strategy to produce biofuels from biomass and molten salts.

The project is divided into seven work packages with the collaboration between nine European academia and industry partners. Research outputs presented in this PhD thesis are directly connected to the following work packages, tasks and deliverables as per ABC-Salt research consortium agreement:

- Work package 3 (WP3) – Primary liquefaction (feedstock selection, salt selection, handling and recycling)
    - Task 3.1 Feedstock selection and characterisation
    - Deliverable 3.2 Biomass and ash characteristics and analyses
- Work package 4 (WP4) – Hydro-pyrolysis in molten salts
    - Task 4.1 (High pressure) TGA studies
    - Task 4.4 Product analysis
    - Deliverable 4.1 Kinetic model of the thermal decomposition of biomass in molten salt hydro-pyrolysis
    - Deliverable 4.6 Thermodynamic models based recommendations for molten salt recycling system

A simplistic flow diagram of the ABC-Salt project is presented Figure 2 with red marked boxes highlighting the work packages that this PhD research study will be involved in.
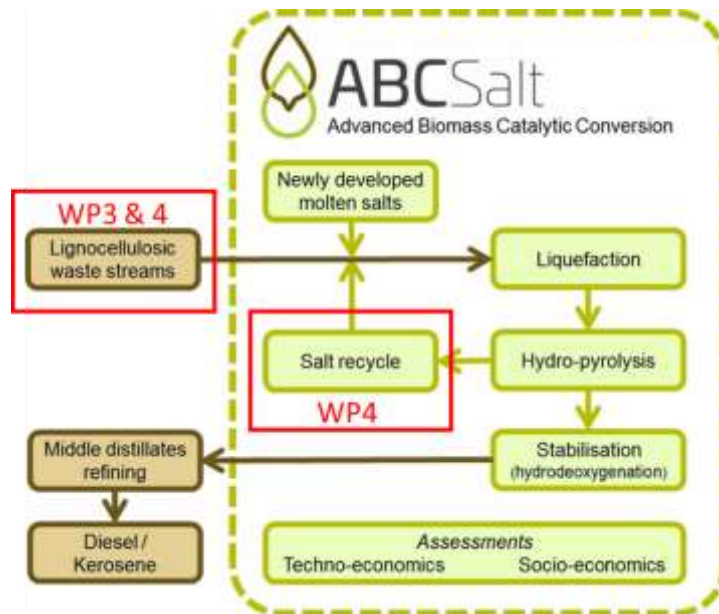
Figure 2. ABC-Salt project outlined with work packages where this PhD research project will be involved in.

Chapter 2

Literature review

2.1. Biomass and its biochemical composition

Biomass is a complex, organic material that is derived from living organisms and can be used as an alternative source of energy. It is a renewable source of energy, unlike fossil fuels. Lignocellulosic biomass is composed of cellulose, hemicellulose, lignin and small amounts of extractives and inorganic components. The three major components cellulose, hemicellulose and lignin are unequally distributed [7]. The cellulose, hemicellulose and lignin content will vary depending on the type of biomass, including woody, herbaceous and agricultural biomass, which are outlined in Table 1.

Table 1. Biochemical composition of various woody, herbaceous and agricultural biomass.

Biomass	Cellulose (%)	Hemicellulose (%)	Lignin (%)	References
Wheat straw	30-38	21-32	17-19	[8-11]
Barley straw	31-45	24-38	14-19	[9, 12, 13]
Pine	47-48	20-24	27-28	[14] [15] [16, 17]
Miscanthus	38-40	18-24	24-25	[18, 19]
Pine wood	39-40	24-29	20-28	[20]
Poplar wood	35	17	26	[21]
Switchgrass	31-32	22-25	18	[10]
Spruce	43-44	6-29.4	27.6-28	[22, 23]
Corn stover	378	25	19	[24]
Rice straw	28-36	23-28	12-18	[9, 25-27]
Oat straw	31-37	27-38	16-19	[13, 28]

2.1.1. Cellulose

Cellulose is the most abundant biopolymer available and considered as the main constituent in the cell wall of plant cells, which is responsible for its structural support [29]. A typical polymer structure of cellulose can be seen in Figure 3. The polysaccharide is often denoted by the chemical formula $(C_6H_{10}O_5)_n$ (where n is the degree of polymerisation) and exists out of repeating β-1,4 glucans arranged in a linear form. The degree of polymerisation (n) may vary from 6,000-8,000, but could get up to 15,000 depending on the type of biomass [17, 30]. The repeating D-glucopyranose units, which are 180° rotated to one another, are linked by β-1,4-glycosidic bonds [29, 31]. Each D-glucopyranose unit has a six-carbon ring where two are attached by the acetal bond (β-1,4-glycosidic bond) whilst the remaining four are attached to a hydroxyl group [32]. The β-1,4-glycosidic bonds are covalently bonded by hydrogen bonding (intermolecular and intramolecular bonding) forming a crystalline structure. The β-1,4-glycosidic bonds mainly cleave under acid or high-temperature conditions [7].
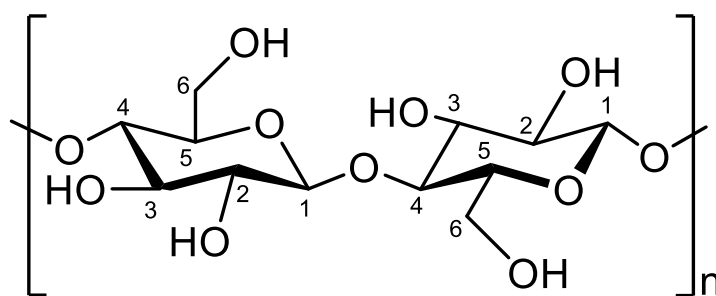
Figure 3. Structure of cellulose $(C_6H_{10}O_5)_n$ held by β-1,4-glycosidic bond.

The Broido-Shafizadeh model (see Figure 4) has been widely accepted where cellulose thermally depolymerised to generate 'activated cellulose', involving in the reduction the degree of polymerisation, and further decomposes into competitive reactions [33]. One reaction will generate tar or chars (anhydrosugars) and the other reaction will produce light gases [34]. During the formation of tar, mainly levoglucosan (1,6-anhydro-β-D-glucopyranose) is formed and secondary reactions/cracking are also occurring, which decomposes further down into monomeric anhydrosugars including hydroxyacetaladhyde (HAA), hydroxyactone, glyceraldehyde, 5-hydroxymethylfurfural (5-HMF) and furfural through ring-opening and reforming reactions [35]. However, several researchers have, including Shen and Gu [17] and Wang et al [36], proposed that there may be multiple reaction pathways occurring at the same time.
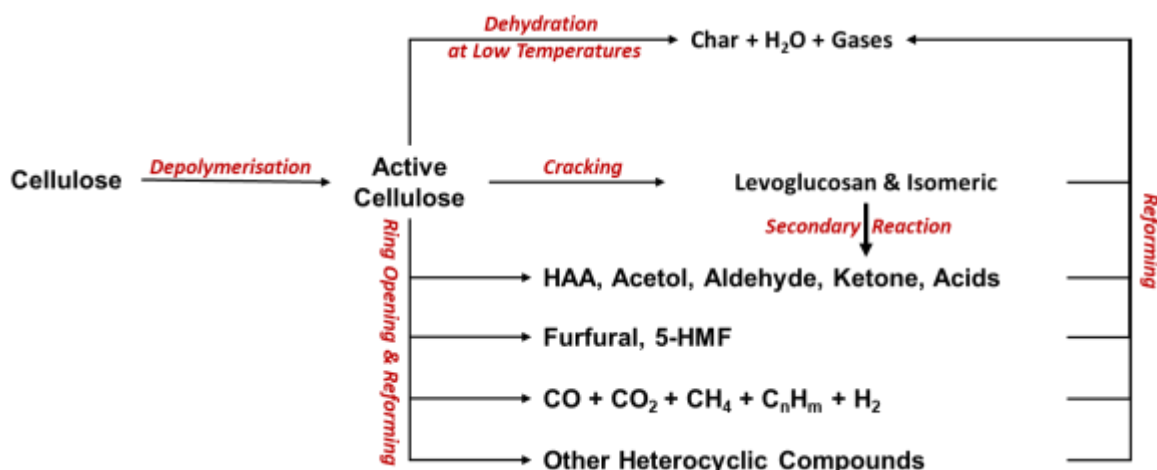
Figure 4. Pyrolytic degradation pathway of cellulose of Broido-Shafizadeh – adapted from [37].

2.1.2. Hemicellulose

Hemicellulose, a complex biopolymer and provides the linkage between cellulose and lignin, which are made up of short-chain heteropolysaccharides that alternate and have a branched and amorphous structure [7]. Unlike cellulose, hemicellulose has a degree of polymerisation of 80-200, lacking crystallinity and has less thermal stability [38]. Hemicellulose is composed of different building units, including pentose (D-xylose and L-arabinose) and hexose (D-glucose, D-mannose and D-galactose) sugars (see Figure 5 and Figure 6), uronic acids and acetyl group [7, 31]. Due to their unstable nature, it can be easily hydrolysed in acids to make up products such as sugars and organic acids, and soluble in alkali [39]. Hemicellulose has different types of sugar units, depending on the type of biomass (hardwood or softwood). Hardwood hemicellulose is mainly composed of glucuronoxylan (*O*-acetyl-4-*O*-methylglucurono-β-D-xylan), glucomannan and xyloglucan. Whereas, softwood hemicellulose include galactoglucomannans, arabinoglucoronoxylan and arabinogalactan.
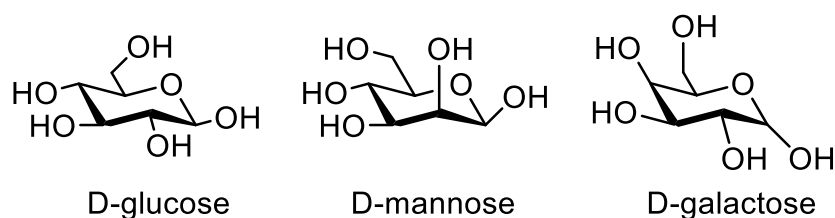
Figure 5. Hexoses (D-glucose, D-mannose and D-galactose).
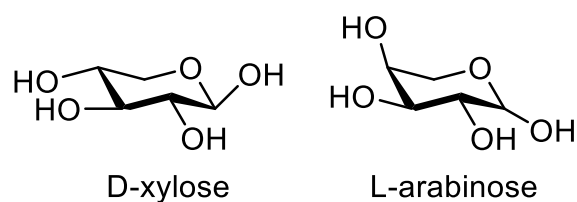
Figure 6. Pentoses (D-xylose and L-arabinose).

Glucuronoxylan or xylan (Figure 7), also known as *O*-acetyl-4-*O*-methyl-glucunorolxylan, is the most important hardwood hemicellulose polysaccharide and amounts approximately 80-90 % of hardwood hemicellulose [39]. The xylan is composed of D-xylose components and bonded with β-1,4-glycosidic bonds, but also bonded with one 4-*O*-methyl-α-D-glucuronic acid per ten xylose units [40].
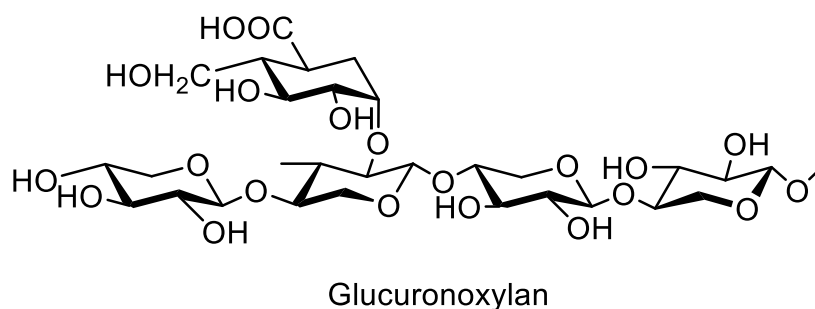
Figure 7. Structure of glucoronoxylan mainly found in hardwood hemicellulose.

Hardwood contains 2-5 % glucomannan (see Figure 8). Glucomannan is mainly composed of D-mannopyranosyl and D-glucopyranosyl residues whilst linked by 1→4 bonds. The ratio between the D-mannopyranosyl and D-glucopyranosyl will depend on the wood species [40].
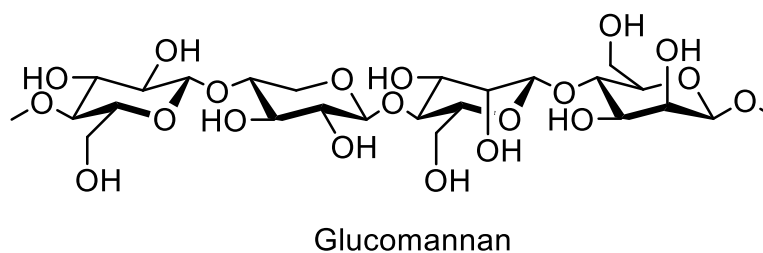
Figure 8. Structure of glucomannan found in hardwood hemicellulose.

Xyloglucan (Figure 9) is the most abundant polysaccharide in the hemcellulose unit, and amounts up to 20-30 % (except grasses) [41].
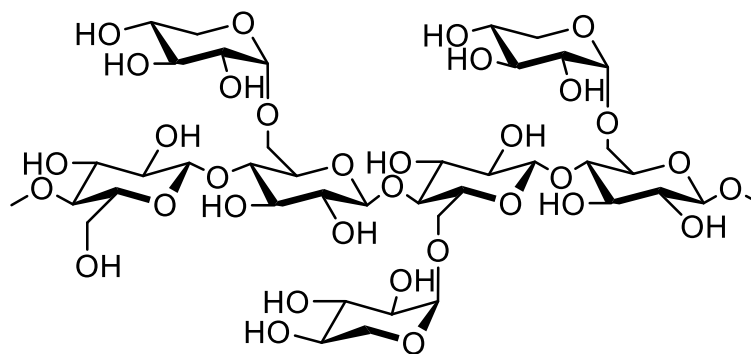
Xyloglucan

Figure 9. Structure of xyloglucan found in hardwood hemicellulose.

Galactoglucomannan, as presented in Figure 10, is a softwood hemicellulose and the most common polysaccharide found in softwoods.
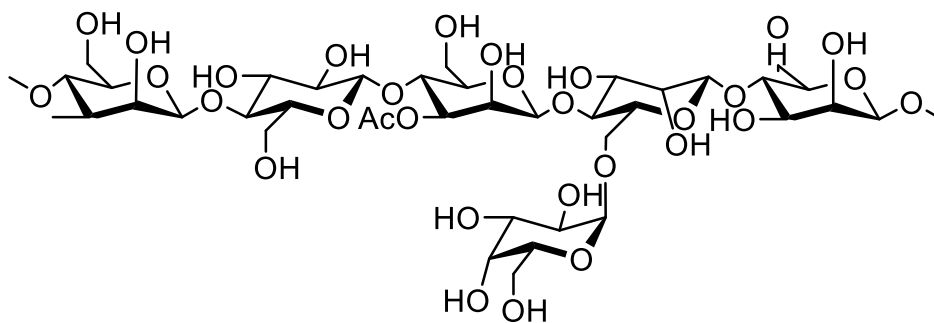
Galactoglucomannans

Figure 10. Structure of galactoglucomannans found in softwood hemicellulose.

Arabinoglucuronoxylan, presented in Figure 11, is mainly found in agricultural crops and bamboo and constitutes 5-10 % in softwood [42].
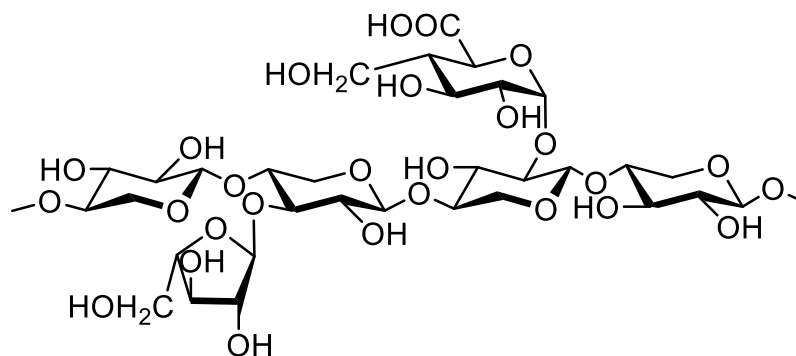
Arabinoglucuronoxylan

Figure 11. Structure of arabinoglucuronoxylan found in softwood hemicellulose.

Arabinogalactan (Figure 12) is found in the walls of wood fibres and occur in many plant gums [43]. However, less than 1 % by weight is found in the softwoods [44].
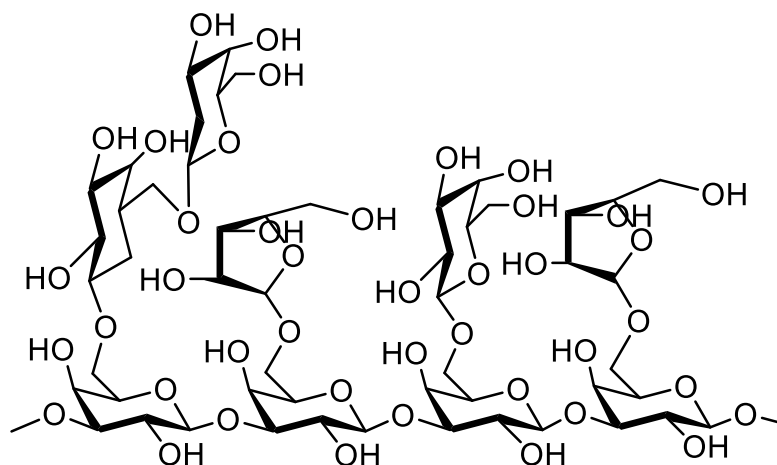
Arabinogalactan

Figure 12. Structure of arabinogalactan found in softwood hemicellulose.

2.1.3.   Lignin

Lignin is an aromatic biopolymer, a constituent found in vascular plants, which is mainly responsible for structural rigidity. Its structure is chemically diverse and heterogeneous (see Figure 13). The three-dimensional biopolymer can typically reach approximately 10-25 % depending on the type of biomass [7] and consists of various bonds, including hydroxyl and methoxy substituted phenylpropane derivatives [29].
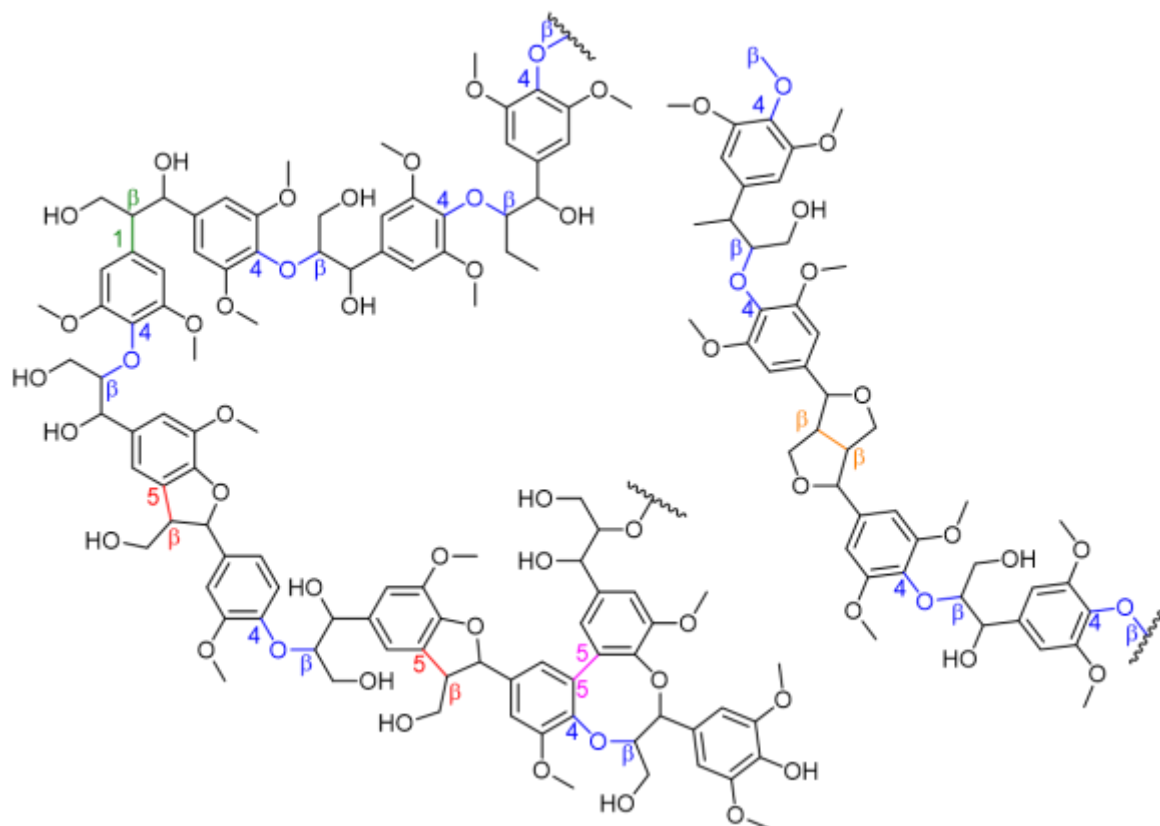
Figure 13. Lignin structure.

The phenylpropane is composed of three monolignols (monomers) (C9 units), which are coniferyl (3-methoxy-5-hydroxycinnamyl), sinapyl (3,5-dimethoxy 4-hydroxycinnamyl), and p-coumaryl (4-hydroxycinamyl) alcohols [7]. These aromatic monomers are also known as guaiacyl (G), syringyl (S), and p-hydroxyphenyl (H) units, respectively. Their difference lies in the number of methoxyl groups ($-OCH_3$) in the aromatics [45]. P-coumaryl has no methoxy group attached to the aromatic ring, whereas coniferyl has one methoxy group attached and sinapyl has two methoxy group attached to the aromatic ring (see Figure 14). Softwoods will have a larger proportion of guaiacyl units and small amounts of p-hydroxylphenyl units. Whereas, hardwoods is made up of both guaiacyl and syringyl units [46].
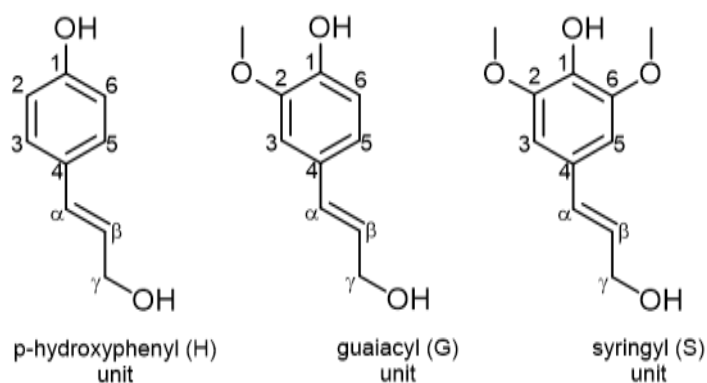
Figure 14. Monomeric structure of lignin.

The lignin structure is linked through different bonding, which are divided into three types including ether bonds (C-O), carbon-carbon (C-C) and ester bonds (O-C-O). Hence, lignin has a heterogeneous chemical structure. Furthermore, the lignin is cross-linked with different inter-unit linkages, including β-O-4, β-5, 5-5, 4-O-5, β-1 and β-β linkages (presented from Figure 15 to Figure 20). During a pyrolysis reaction, lignin initiates with cleaving of ether bonds (β-O-4 linkage) at low temperature yielding guaiacol-type and/or syringol-type components and can be seen below in Figure 21 [47].
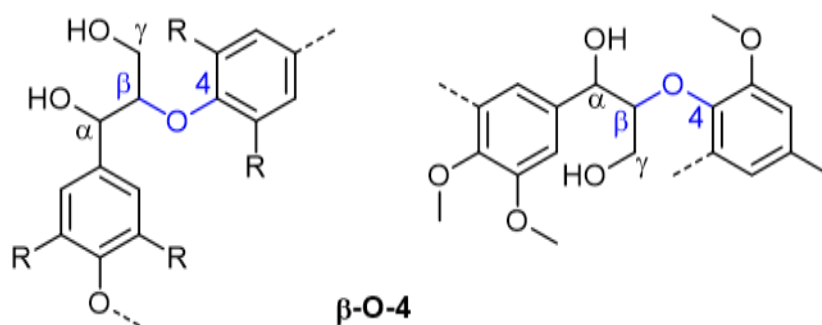
Figure 15. β-arylether (β-O-4).
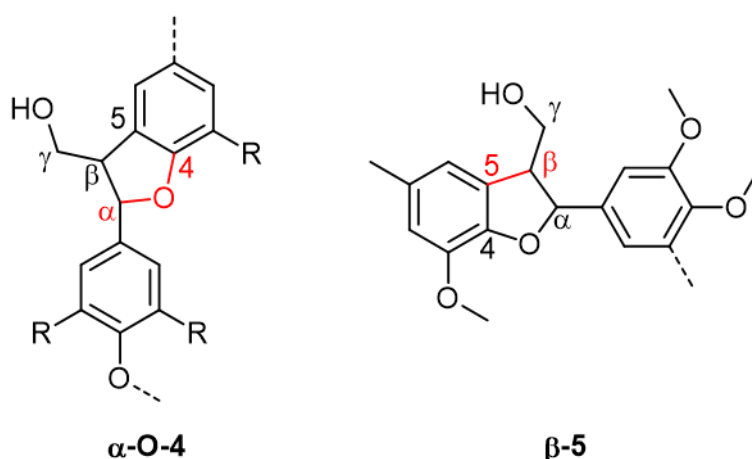
Figure 16. Phenyl coumaran (α-O-4 and β-5).

5-5
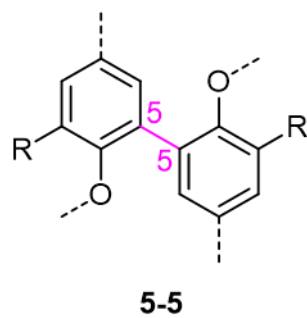
Figure 17. Biphenyl (5-5).

4-O-5
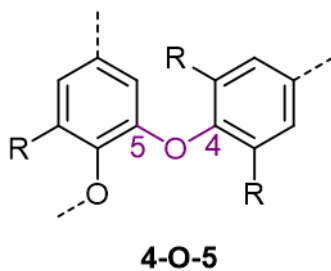
Figure 18. Diphenylether (4-O-5).

β-1
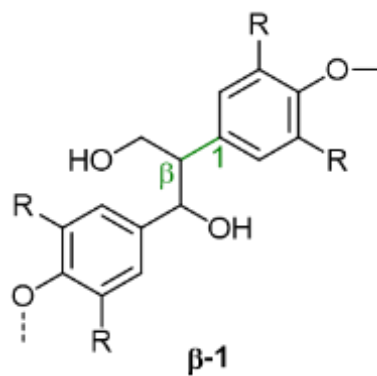
Figure 19. Diarylpropane (β-1).

β-β
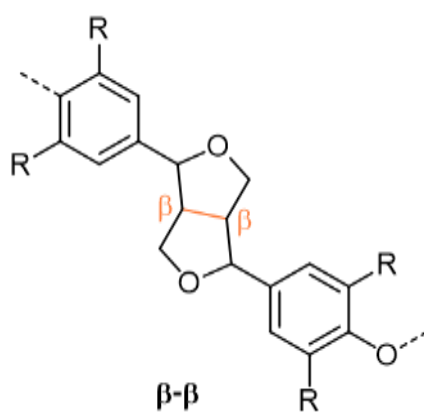
Figure 20. Resinol (β-β).
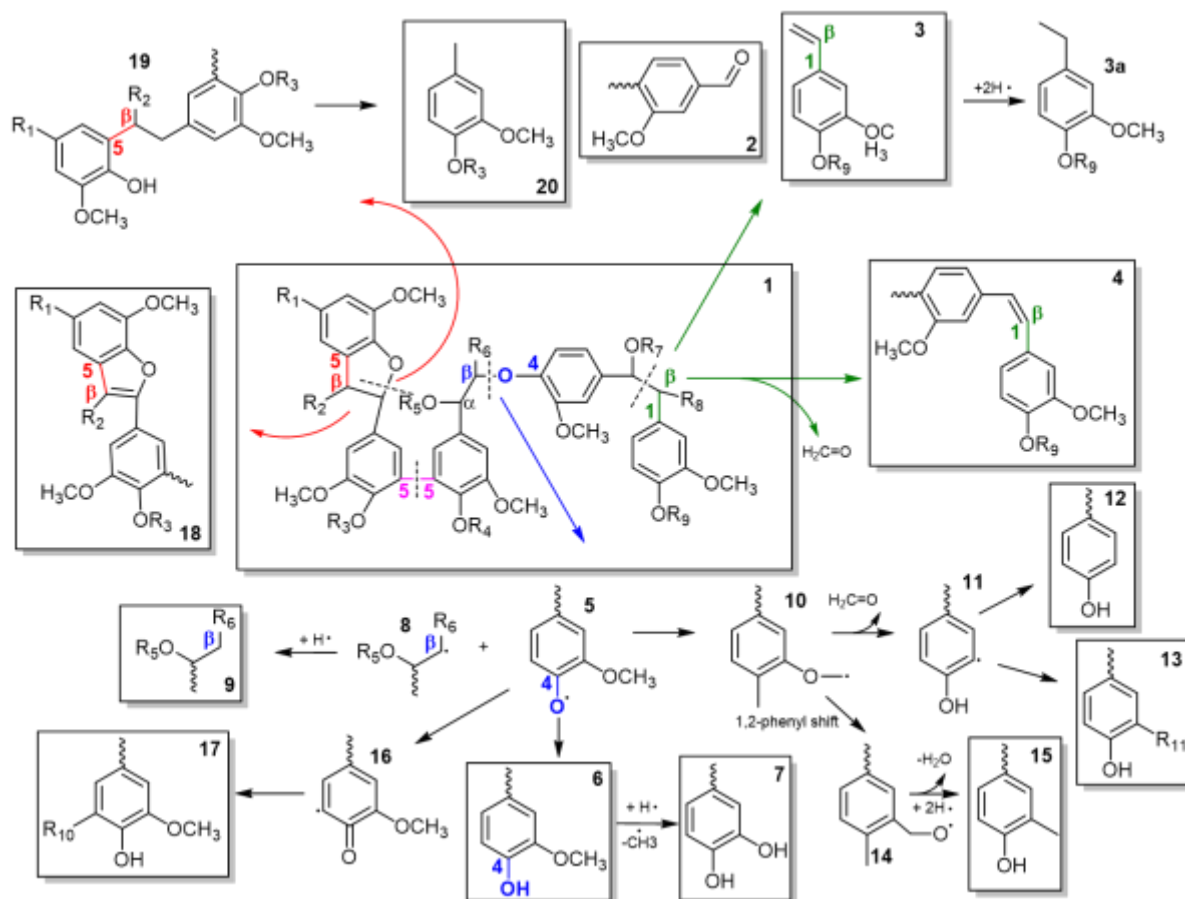
Figure 21. Lignin pyrolytic degradation reaction as proposed by literature.

Biphenyl (5-5); **β-arylether (β-O-4)**; **phenyl coumaran (β-5 and α-O-4)**; **diarylpropane (β-1)**
(1) Typical structure of lignin; (2) aldehydes; (3 and 3a) (reduced vinyl-) ethyl-phenols (4) stilbenes; (5) phenoxy radicals; (6) guaiacols; (7) catechols; (8, 10, 11, 14, 16) transient radicals; (9) aliphatics; (12) phenols; (13, 17) condensation products (i.e. *4-O-5 dimers*); (15) cresols; (18) β-5 product in primary decomposition step; (19) α-O cleavage product; (20) methyl guaiacols

Delignification processes

Lignin is often produced as waste or unused product from the pulp and paper industry, whereby the cellulose and part of hemicellulose fibres are separated from the lignin. Isolating lignin or the delignification process can be achieved by employing different methods, including physical pre-treatment, biological, chemical and solvent processes. This section will go into details of chemical and solvent processes since these processes are commercially well-known. The pulping/delignification processes will determine the final structure of the lignin. The main difference between the chemical and solvent processes is whether the lignin contains sulphites. The chemical process has three main pulping processes, which are sulphite, Kraft, and alkaline.

The sulphite process is also known as the lignosulphite process and is determined by the pH of the process used [48]. According to Lin and Lin [49], the sulphite process is operated at 140-170 °C and

uses sulphites or bisulphite salts of sodium, ammonium, magnesium or calcium in an aqueous solution for the digestion of wood. Two main reactions are occurring during the sulphonation process. For the lignin to dissolve, sulphonation and hydrolysis reactions are occurring during acidic conditions [50]. The loss of hydroxyl group or cleavage of the α-ether linkage occurs to form quinone methide intermediate with either phenolic or nonphenolic substrates via a benzylic cation (hydrolysis) during acidic conditions. The sulphite ions presence adds to quinone methide intermediates at the α-position to form benzyl sulphonic acid units (sulphonation). Furthermore, condensation reaction may also happen during the acidic condition between the benzylic carbon and carbon on the 6th position of another nuclei and could prevent the sulphonation reaction [51, 52].
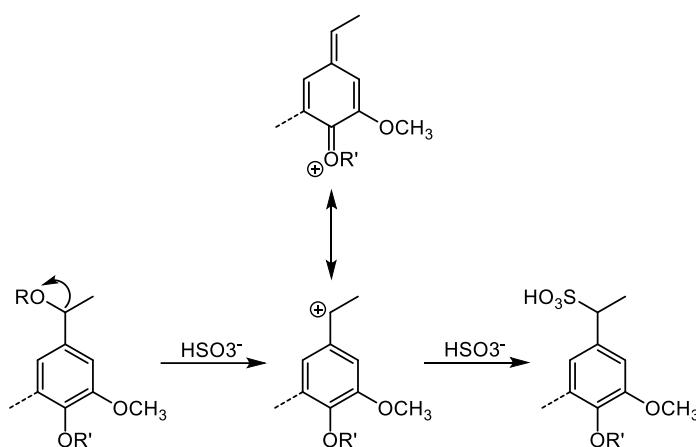
Figure 22. Sulphonation reaction [52].

The Kraft process utilises sodium sulphite or sodium hydroxide (white liquor) to treat their wood, thus removing 90-95 % of the lignin at a temperature of 155-175 °C. The cellulose is then separated from the lignin fluid fraction (black liquor) [53]. Whilst the Kraft lignin is isolated during this process from the black liquor by acid precipitation and neutralisation and dried into a solid form. Typical acids that are used during the Kraft processing are carbon dioxide, acetic acid, phosphoric acid, sulphuric acid and hydrochloric acid. The lignin yield during the precipitation step is mainly influenced by the pH, ion strength and processing temperature [54]. Degradation (forming products with a lower molecular mass, e.g. phenols) and condensation reaction are occurring during the delignification process of Kraft Lignin. During the degradation reaction, the cleavage of α- and β-aryl ether bonds are occurring. The α—aryl ether bond in the phenolic units are readily cleaved by conversion of phenolate unit into corresponding quinone methide intermediates [55]. Whereas the β-aryl ether linkage present in non-phenolic units involves attacking an ionised hydroxyl group. Condensation reaction proceeds with the Michael Addition reaction, where the quinone methide (or formaldehyde) acts as an acceptor and the phenolate ion acts as a nucleophile [55].

Kraft processing is well-established in the commercial world, such as the LignoBoost technology. The LignoBoost technology was demonstrated by a plant, which was developed and operated by Innventia and Chalmers University of Technology and currently owned by Metso Corporation [56]. It was aimed to reduce the operating costs and to improve plant efficiency, as the traditional process of lignin production caused several problems including partial plugging of the filter cake resulting in the need for a large filter area and impurities found in the lignin [57]. The traditional Kraft lignin has a relatively low dry solid content, high ash and sodium content and poor dewatering properties as opposed to the LignoBoost process. The LignoBoost process has a higher yield, high level of purity, low ash and sodium content, lower production cost as there is no need for a large filter area [57]. During the LignoBoost process, the black liquor is collected from the evaporation plant and precipitated by acidification using carbon dioxide and filtered. The main difference between the production of Kraft lignin and LignoBoost lignin is that after filtration the filter cake is redispersed and acidified in a low pH liquid rather than immediately washing the lignin after the filtration step [57]. In addition, sulphuric acid and sodium hydroxide are used in their washing process in order to minimise the sodium content found in their final LignoBoost lignin product [57].

Alkali lignin is also known as soda lignin was originally developed for non-woody raw materials, such as straw and bagasse, for the production of pulp. The feedstock is digested by using sodium hydroxide, lime, or calcium hydroxide in an aqueous solution at 160 °C [53].

Solvent based processing uses organic solvents (hence the name Organosolv process) in the delignification process, which includes ASAM (alkali-sulphite-anthraquinone-methanol), Organocell (sodium hydroxide, methanol and anthraquinone), Alcell (water and ethanol), Formacell (acetic acid and formic acid) and Milox (multistage peroxyacid treatment). The Organosolv processes generally use low-boiling point solvents, for example ethanol and methanol, and often mixed with water.

The ASAM process was developed in 1986 by Patt and Kordsachia using sodium sulphite (Na_2SO_3), sodium hydroxide (NaOH), anthraquinone ($C_{14}H_8O_2$) and methanol (CH_3OH). The wood is firstly steamed for approximately 15 minutes to remove moisture [53]. The sodium sulphite and sodium hydroxide are the main ingredients of the alkaline sulphite process, whilst anthraquinone and methanol act as a catalyst [58]. The process takes around 90-180 minutes at a temperature of 170-180 °C.

The Organocell process is split into two-stage processes whereby the first process uses methanol and water to digest the wood at 120 °C. The softened wood is transported to the digester where sodium hydroxide and a catalytic amount of anthraquinone are added and heated to 170 °C at a pressure of

13 bar. The duration of cooking and the amount of solvent needed will depend on the type of wood used [53, 59].

The Alcell process uses ethanol and water mixture (60:40) at a processing temperature of 175-195 °C for one hour. The produced lignin is mainly sulphur-free, and will also generate furfural as a by-product [60]. Ethanol will then be reduced to 12-21 % using flash distillation to separate the cellulose. Water and a strong acid are added to the black liquor to precipitate lignin and isolated by using centrifugal filtration, which leaves digested hemicellulose and small amounts of lignin fraction in the liquid. The ethanol is stripped from the liquid for reuse and leaving saccharides from digested hemicellulose. Xylose can be recovered and converted to furfural as a by-product [61].

The Formacell procedure utilises formic acid, acetic acid and water. Lower operating temperature and atmospheric pressure are employed in this process compared to using alcohols, as it provides easier cleavage of α-ether lignin resulting in a hydrolysis reaction and ultimately dissolving the lignin fragments in mild processing conditions [62]. High pulp and low lignin yield is produced from this process.

The Milox process uses formic acid and hydrogen peroxide to produce *in-situ* generated peroxyformic acid and highly selective and will not react to the holocellulose. The process has three stages and operates between 80 °C and 100 °C [53, 63].

2.1.4. Extractives and inorganic components

Extractives, can be referred to as natural products, are chemicals in biomass that can be extracted using polar (alcohol, methylene chloride, or water) and non-polar (hexane or toluene) solvents [30]. The extractives do not belong or constitute to the cell wall or cell layers, as they are functioning as intermediates in metabolism, energy reserves and plant defences against microbial and insect attack [64]. Extractives include alkaloids, proteins, resins, gums, saponins, pectins, simple sugars and starches, terpenes, and waxes [64, 65].

Furthermore, biomass will contain small amounts of inorganic minerals. These may include potassium, calcium, sodium, magnesium, silicon, phosphorus, sulphur, and chlorine. Small amounts of aluminium, titanium, vanadium, manganese, iron, cobalt, nickel, copper, molybdenum, and other heavy metals may also be found in the biomass [66]. Some of the inorganic content may contribute towards the growth of the biomass and may vary depending on the conditions of the environment.

2.2. Thermochemical conversion

Thermochemical conversion technologies utilise heat to decompose organic components of biomass into smaller molecular fragments to produce fuel products. There are various technologies that are able to thermally decompose biomass to yield different types of fuel products. This can be achieved by using hydrothermal processes, gasification, combustion and pyrolysis.

Hydrothermal processing or treatment is a thermochemical conversion to process biomass in a hot, pressurised and oxygen-free atmosphere to form bio-products (solids, liquids and gases). There are different types of hydrothermal processes depending on the process parameters (see Figure 23), including hydrothermal carbonisation (HTC), hydrothermal liquefaction (HTL) and hydrothermal gasification (HTG). The hydrothermal processing utilises pressure-temperature water phase diagram to highlight the hydrothermal regions with respect to water's liquid-vapour coexistence behaviour [39]. Solid, liquid and gaseous products are formed in all three hydrothermal processes depending on the process parameters including temperature and pressure. HTC utilises low temperatures (180-250 °C) and pressure (20-100 bar), which mainly yields solid products. As the name suggests, liquid is the main product obtained from HTL. The liquid product is split into the bio-crudes and aqueous phase. The HTL uses medium temperature (250-375 °C) and pressure (100-250 bar). Whereas HTG (also referred to as supercritical water gasification) uses high temperature (> 375 °C) and pressure (> 250 bar) [67], yielding mainly gaseous products.
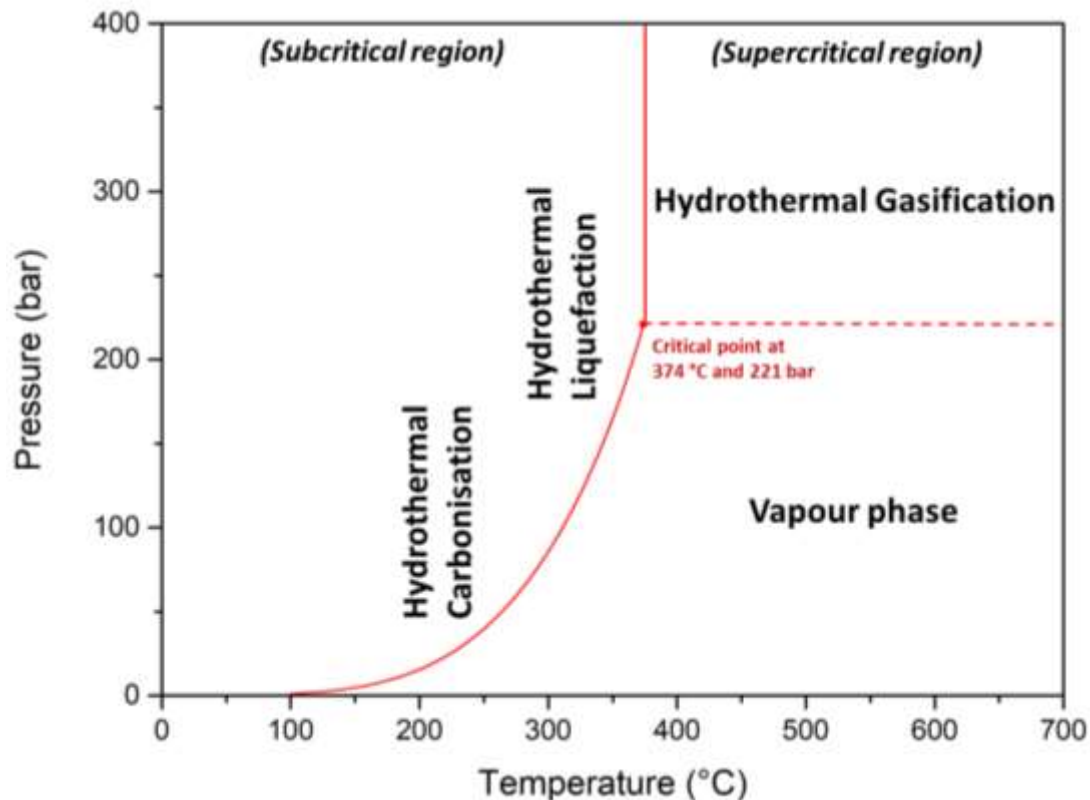
Figure 23. Different types of hydrothermal processing conditions.

The following sections will mainly focus on processing biomass from hydrothermal liquefaction and pyrolysis.

2.2.1.   Hydrothermal Liquefaction

Hydrothermal liquefaction (HTL) or sometimes known as direct liquefaction is a flexible thermochemical process, is a promising conversion technology which converts biomass to mainly liquid crudes as a main product. Gaseous, aqueous and solid phase products are also produced as by-products. The HTL process uses medium-pressure (100-250 bar) and low to moderate operating temperatures (250-375 °C) in the presence of a medium (often water). At these operating pressure and temperature, the water is in subcritical conditions and remains to be in a liquid phase, as the critical point occurs at 375 °C and 221 bar and anything above would be considered the supercritical conditions. Retention times are usually less than 90 min, depending on the feedstock. HTL is able to liquefy various types of feedstock, including agricultural waste, forestry residues, algae, industrial waste, sewage sludge, manure. HTL is seen as a promising alternative for the production of bio-crudes, as the process eliminates the pre-drying of feedstock. The bio-crude is the liquid biofuel produced

from HTL, which is black and is very viscous. The process uses water as a reactant and acts as a catalyst, which will reduce the extra costs of utilising catalysts. Furthermore, HTL uses low reaction temperature and therefore making it inexpensive when compared to other thermochemical processes, including pyrolysis and gasification [68]. However, the HTL uses high operating pressure which will raise the costs.

The HTL reaction network can be complex and little is understood, especially on the chemistry of lignocellulosic biomass during HTL reaction. The reaction mechanism of HTL is divided into depolymerisation, decomposition and recombination [69]. Temperature and pressure are the most dominant operating parameters, which will determine the structural changes of long chain polymers to short chain hydrocarbons. The lignocellulosic depolymerises to produce monomers, which will then decompose into small fragments through cleavage, dehydration (loss of water molecule), decarboxylation (loss of CO_2 molecule) and decarbonylation (CO elimination) [70, 71]. At the same time, oxygen removal occurs in the form of H_2O and CO_2 [69]. Recombination and repolymerisation reaction also may occur at the same time [72]. Therefore, the yield and composition will mainly depend on the operating temperature and pressure, but other factors like the selection of solvent or the usage of catalyst, and retention time are equally as important.

Table 2 on page 49 presents a summary table of the literature studies on HTL using different types of reactors, process parameters and the attained bio-crude yield. The process parameters include the process temperature, process pressure, and residence time, (co-)solvent and catalyst used.

2.2.1.1. Cellulose reaction network in hydrothermal liquefaction

The reaction network of cellulose can be seen in Figure 24. Cellulose will react at higher temperature by breaking down the hydrogen bond and resulting in weakening the crystallinity of cellulose. Cellulose in HTL reaction undergoes through a hydrolysis reaction to form water insoluble and soluble oligomers, and to form glucose [73]. Glucose is isomerised into the formation of fructose and decomposed to products such as 5-hydroxymethylfurfural (5-HMF) or organic acids, which occurs between 200 and 220 °C [74]. 5-HMF can also be produced from fructose pathway. At 300 °C, no sugars and only traces of 5-HMF were detected from a research conducted on hydrothermal degradation of cellulose [75]. Mainly levulinic acid, as well as formic acid, is formed from 5-HMF through hydration reaction in acidic conditions. Cyclopentanes is formed from levulinic acid [75]. Furfural is produced as a result from the loss of an acetol group in 5-HMF [76]. The intermediate 5-HMF will also go through decarbonylation and hydroxylation reaction at 200 °C, whereby the hydroxyl group is lost to form 4-hydroxy-4-methyl-2-pentanone [75].
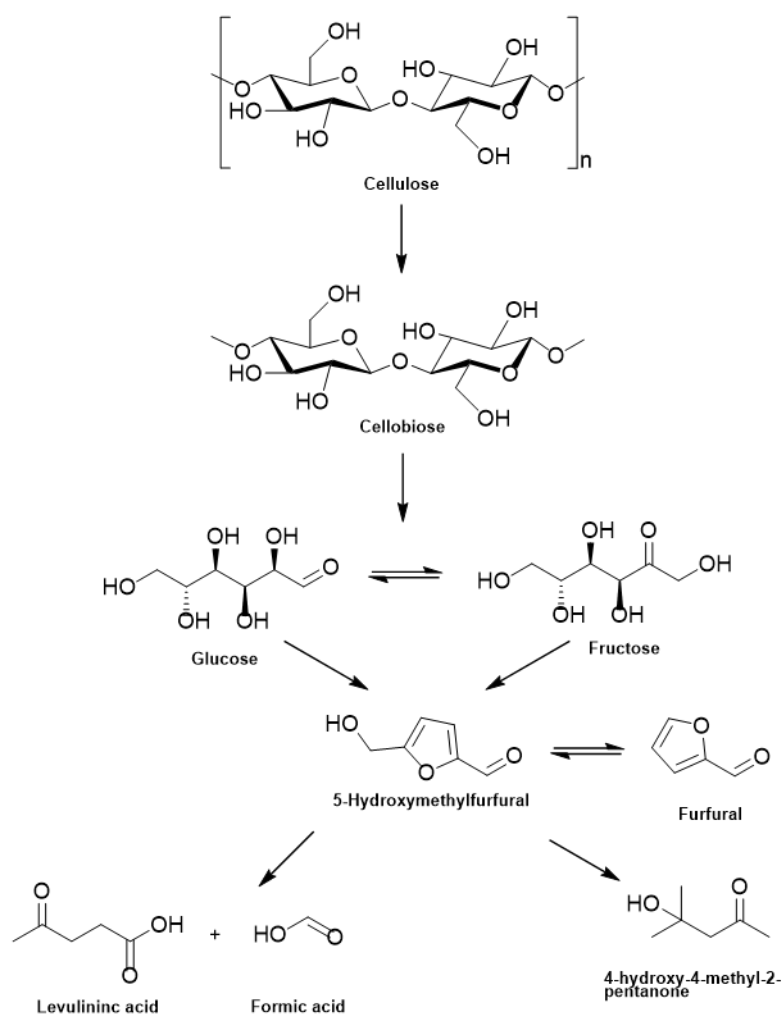
Figure 24. Proposed reaction pathway of cellulose during hydrothermal liquefaction processing.

2.2.1.2. Hemicellulose reaction network in hydrothermal liquefaction

Very few studies were found on HTL reaction network of hemicellulose. A reaction network of xylan (hemicellulose) can be found below in Figure 25. According to Xu and Li [70], hemicellulose is hydrolysed into two main monosaccharides – pentose and hexose. The two monosaccharides pentose and hexose undergo a dehydration reaction to form 5-HMF and furfural. Gao et al [77] studied the hydrothermal degradation of hemicellulose from triploid poplar. Hemicellulose was decomposed into mono- and oligosaccharides (at 180 °C), which were mainly xylose, 4-*O*-glucoronic acid, glucan, glucose and galactose. At 220 °C, furfural is primarily produced via dehydration reaction from xylose. Furfural further degrades into ethanol, acetic acid, formic acid, and lactic acid. At a higher temperature of 330 °C, an increase in the concentration of acetic acid was observed by Gao et al [77]. Similar pathway as cellulose was observed from glucose and galactose. Both sugars are dehydrated to 5-HMF and further degraded into levulinic acid and formic acid.
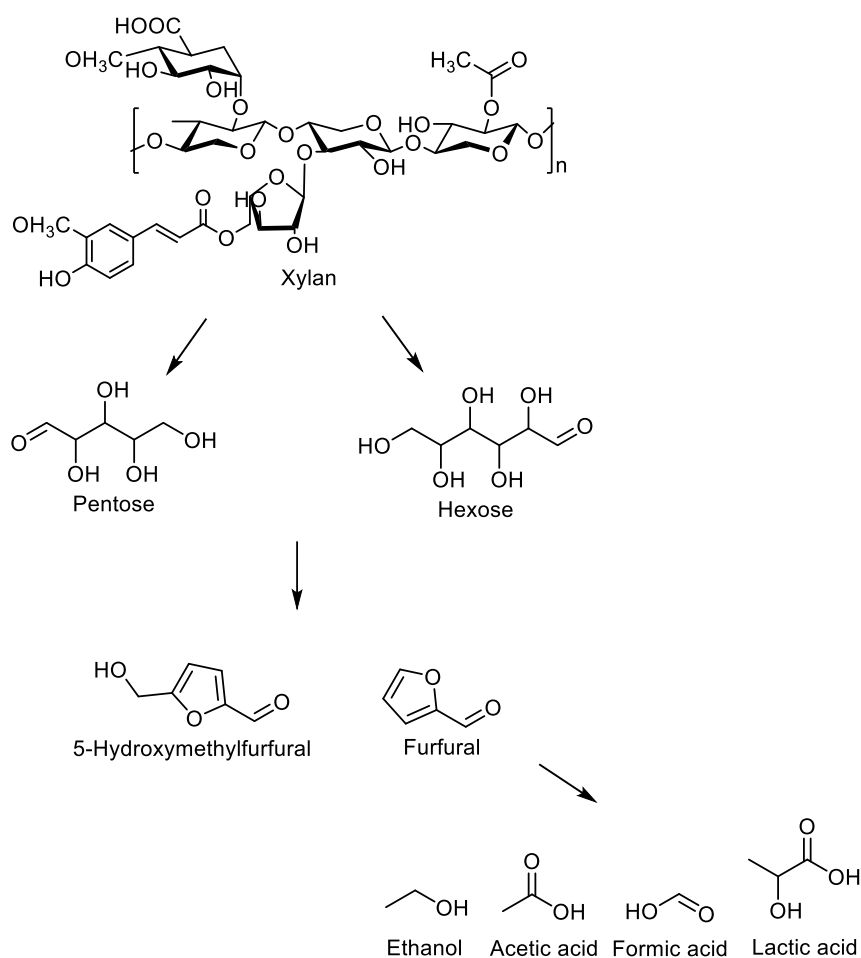
Figure 25. Proposed reaction pathway of xylan during hydrothermal liquefaction processing.

2.2.1.3. Lignin reaction network in hydrothermal liquefaction

A reaction pathway of lignin is presented in Figure 26. During liquefaction conditions, lignin in HTL reactions mainly yield phenolic products through hydrolysis reaction [78]. Hu et al [79] described that lignin will mainly produce chars at low temperature of 280 °C. Cleavage of the β-O-4 linkage also occurs at low temperatures, and through hydrolysis reaction produces predominantly 2-methoxyphenol (guaiacol) and guaiacol-derivative products, which include 4-ethyl-2-methoxyphenol, 2-methoxy-4-methylphenol (creosol) and 4-butyl-2-methoxyphenol. Once the reaction temperature increases of around 300-330 °C, the yield of guaiacol and guaiacol-derivative product will decrease and instead catechol and phenol are decomposed [80]. The reaction pathway of lignin in hydrothermal liquefaction conditions was also described through kinetic data by Yong and Matsumara [81], which is in agreement with the literature [78-80].
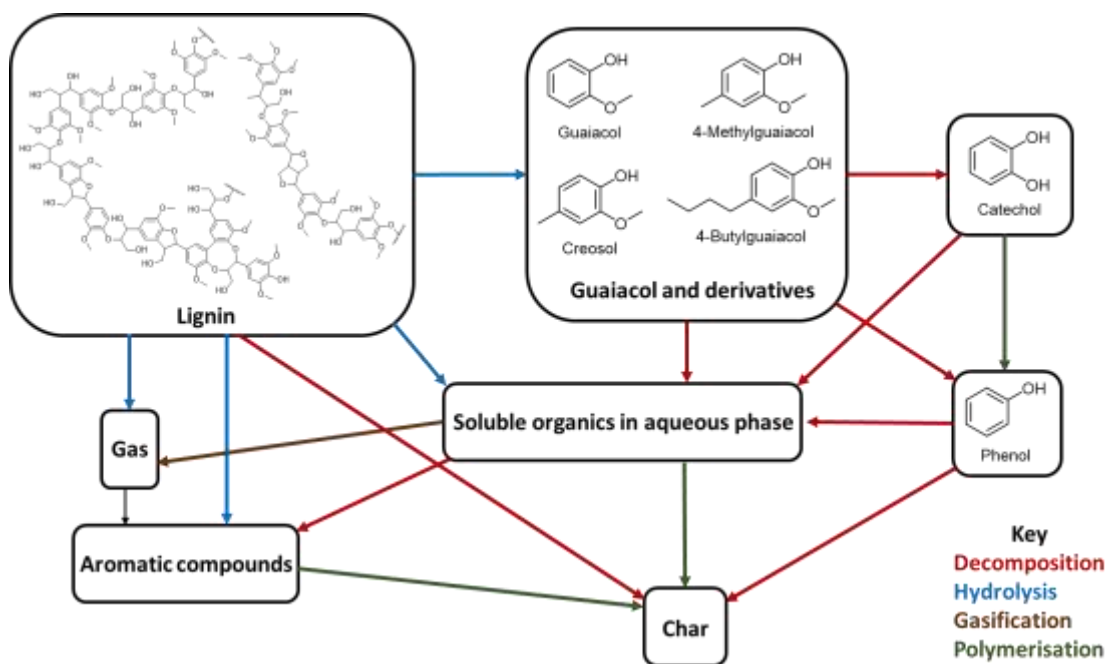
Figure 26. Reaction network of lignin in hydrothermal liquefaction condition adapted from [81].

From Figure 26, the aromatic compounds include naphthalene, benzene and toluene. Whilst the soluble organic compounds found in aqueous phase is from derived from hydrolysis reaction from lignin and the decomposition from guaiacol and its derivatives, catechol and phenol.

2.2.1.4. Effect of process temperature in hydrothermal liquefaction

Temperature is one of the most significant operating parameters which could affect the yield and properties of the bio-crudes. Furthermore, the temperature will influence directly on the rate of free radical reactions, and indirectly on the rate of ionic reactions by modifying the ionic product and dielectric constant of water [82]. Operating temperature ranges from 200 to 450 °C [83, 84]. De Caprariis et al [85] have studied the influence of temperature and performed their HTL experiments between 240 and 320 °C, which concluded that the maximum bio-crude yield obtained from walnut shell was at 320 °C with a holding time of 30 min. However, they also found that the bio-crude yield increased due to an increased amount of lignin content found in the biomass [85]. Whereas, Mathanker et al [86] studied temperatures at 250, 300, 350 and 375 °C using corn stover. The maximum bio-crude yield of 29.25 wt. % was found at 300 °C, but observed a constant decrease in both the bio-crude yield and aqueous phase above 300 to 375 °C [86]. Zhu et al [87] looked into the effect of the reaction temperature on the product distribution. They investigated temperature ranges between 300 to 400 °C and found that there is a temperature threshold. The maximum bio-crude yield was at 300 °C with 34.9 wt. %, whereas at 400 °C it decreased to 19.9 wt. %. Lower temperature (below 320 °C) favoured the production of bio-crude. They also concluded that whilst higher temperature

decreased the bio-crude yield, it did however improve the quality of the bio-crude as it reduced the oxygen content and improved the HHVs of bio-crude [87]. Furthermore, Sun et al [88], who explored the temperature range between 280 and 360 °C using paulownia. The yield of the crude oil improved with increasing the temperature up to 300 °C, and started decreasing when the temperature went above 300 °C. They established that there were two competing reactions occurring, which were hydrolysis and repolymerisation [88]. Ogi and Yokoyama [89] also established that a further increase in temperature will decompose the products into gaseous products and promote the repolymerisation or condensation of the intermediates into char. Akhtar and Amin [90] reviewed that the liquefaction of lignocellulosic biomass at 300 °C could be regarded as the optimum temperature to produce bio-crude, which seems to agree with most of the researches. Therefore, the yield of the bio-crude is dependent on the temperature. When the temperature is below 200 °C, solid products (bio-char) is the main product as hydrolysis and dehydration reactions are favoured. Whereas between 250 and 300 °C, the yield of the bio-crude increases as it leads to decomposition of gradual breakage from the lignocellulosic molecules into smaller components. Condensation reaction is followed which will increase the bio-crude yield [70].

2.2.1.5.   Effect of process pressure in hydrothermal liquefaction

Operating pressure is another important parameter in HTL processing. Water is often used as the solvent for HTL, which occurs at a temperature above the boiling point of water. At high temperature, solvents tend to split into two phases and requires a large heat supply to maintain the temperature. Therefore, pressure in HTL process is to maintain the solvent in a single-phase during subcritical and supercritical conditions by avoiding energy loss for the phase change of solvents and thereby reducing energy consumption or large enthalpy inputs [91, 92]. Pressure also increases the solvent density, which also promotes the efficiency to interact and penetrate molecules in lignocellulosic biomass [93]. However, multiple researchers have investigated and concluded that pressure at supercritical conditions is negligible or has little effect as it does not affect bio-crude yield. At supercritical conditions, the increase of solvent density causes a cage effect, which will prevents C-C bonds cleavage resulting in low fragmentation in lignocellulosic biomass [90]. Qian et al [94] investigated the effect pressure change from 250 bar to 440 bar and concluded that once water reached its critical point at 221 bar, the pressure had less effect on the bio-crude yield. Similar findings have been found by Mathanker et al [86] where bio-crude yield increased substantially at lower temperature, but once it reached higher temperatures (350-375 °C) the effect of pressure was negligible. However, Kruse et al [95] has described that high pressure at supercritical conditions, gas yield will depend highly on the

pressure. Whereas, Yang et al [96] introduced pressure from 5 bar to 20 bar prior starting their reactor, and found that there was very little impact on the bio-crude yield and the product distribution. But concluded that the reactor took a longer time to reach to its final temperature if there was less initial pressure introduced [96].

2.2.1.6. Effect of solvent, co-solvents and catalyst in hydrothermal liquefaction

Water is often used as a reaction medium in HTL experiments, as it is inexpensive and environmentally friendly. As mentioned above, water will act both as a catalyst and solvent, and remains to be in the liquid phase at subcritical conditions. At supercritical conditions (T = 374.2 °C and P = 220.5 bar), the viscosity of water is decreased and high solubility of organic substances, which makes it an ideal medium for homogeneous and efficient reaction [97]. Furthermore, water generates strong hydrogen bonding and high polarity, which makes it easier to recycle reaction medium [98]. At 25 °C and 1 bar, the dielectric constant is 78 Fm^{-1} and decreases to 14.07 Fm^{-1} at 350 °C and 200 bar, which indicates that the water molecule will change from very polar to non-polar. At ambient temperature and environment, water is benign and unlikely to react with organic molecules. Once the temperature increases, the shared electron by oxygen and hydrogen atoms will circulate evenly and the electronegativity of the oxygen molecule is reduced and resulting the water to be less polar [99]. However, water at high pressure can be at a major disadvantage since it will corrode the reactor, which will add significant costs to have high durable stainless steel metal alloys [100]. Therefore, (co)-solvents and/or catalysts are used in milder process conditions, since solvents with high polarity will give higher conversions [101]. Zhao et al [102] produced bio-crude from cornstalk using ethanol-water using Fe_2O_4 and achieved the highest yield of 50.46 wt. % bio-crude at 300 °C with a loading of 50/50 (v/v) ethanol-water. The research established that the Fe in liquefaction improved the yield and quality of the bio-crude [102]. Alper et al [103] investigated spruce wood with the use of 20 wt. % KF/Al_2O_3 catalyst, which promoted the bio-crude yield (13.9 wt. %) and decreased bio-char yield. Whereas, Cheng et al [104] used alcohol (methanol or ethanol) and water, which found that both of the co-solvents are the most effective solvents for eastern white pine sawdust in liquefaction. A maximum of 65 wt. % bio-crude yield was achieved at 300 °C and 15 min residence time. They also stated that the use of mono-solvent or water alone produced lower bio-crude yield of 40 wt. % [104]. It should also be noted that solvents and/or catalyst may increase the yield and improve the quality of the bio-char, but the utilisation of solvents and/or catalyst will have high costs involved as well as impacting the design of liquefaction processes.

2.2.1.7. Effect of residence time in hydrothermal liquefaction

The residence time, sometimes referred to as the reaction time or holding time, is the time at which the reactor is held at the desired temperature, which excludes heating and cooling time. Shorter residence time is preferred over longer residence time as it may cause repolymerisation of intermediate products and a decrease in the bio-crude yield. Short residence time also enhances the bio-crude yield [105]. However, Bayat et al [106] investigated on the HTL char yield, which concluded that the highest yield was obtained at 245 °C with no residence time (i.e. the reactor reached up to its desired temperature and cooled down straightaway) and lowest yield at 295 °C at 60 min residence time. Xu [70] claims that the residence time is a process parameter that can alter the conversion of lignocellulosic feedstock, bio-crude yield and the product composition. Furthermore, long residence time will increase the condensation reactions resulting in cracking of bio-oil, which causes intermediate products to form gas or depolymerise to produce coke thus decreasing the bio-crude yield [70]. Yang et al [96] reported the highest bio-crude yield of 31.63 % was achieved with a residence time of 10 min. At 30 min residence time, the bio-crude yield decreased to 22.68 %. Whereas Eboibi et al [107] found that longer residence time did increase the bio-crude yield at 310 °C, but at 350 °C the yield decreased with increase of residence time. Cao et al [108] deduced that with increasing temperature, lower residence time can reduce the chances of repolymerisation of the liquefaction products. Longer residence time should be applied at lower temperature, which will improve the conversion of raw feedstock and the yield of bio-crude [108].

Table 2. Summary of all literature studies of HTL, including reaction conditions, reactor type, catalyst/co-solvent and yield of bio-crudes.

Feedstock	Operating Parameters			Reactor	(co-)solvent	Catalyst	Bio-crude yield (wt. %)	References
	Temperature (°C)	Pressure (bar)	Retention Time (min)					
Xylo-oligosaccharides	180	-	0	Autoclave reactor	Water	-	16.5	[77]
Walnut shell	320	-	30	Tubular microreactor	Water	-	25	[85]
Corn stover	300	20	0	Autoclave reactor	Water	-	29.25	[86]
Barley straw	300	-	15	Autoclave reactor	Recycled aqueous phase	K_2CO_3	34.9	[87]
Sewage sludge	600	300	1	Mini batch reactor	Water	-	27.5	[94]
Spent coffee grounds	275	20	10	Autoclave reactor	Water	-	47.3	[96]
Corn stalk	300	20	30	Autoclave reactor	Ethanol-water	Fe_3O_4	50.46	[102]

Spruce wood	300	-	0	Batch reactor	Water	KF/Al$_2$O$_3$	13.9	[103]
Eastern white pine sawdust	300	20	15	Autoclave reactor	Methanol-water Ethanol-water	-	65	[104]
Food waste	240	1.4	30	Autoclave reactor	Water	-	27.5	[106]
Tetraselmis sp.	350	-	5	Batch reactor	Seawater	-	65	[107]
Corn straw	320	-	60	Batch reactor	Water	-	7.9	[109]
Peanut straw							14.6	
Soybean straw							15.8	
Rice straw							15.1	
Oak wood	320	-	15	Tubular microreactor	Water	Fe	38	[110]
Rice straw	280	-	15	Autoclave reactor	Ethanol	Ni-Al/SBA-15	56.2	[111]
Pine sawdust	300	-	60	Autoclave reactor	Ethanol-water	Co-Zn/HZSM-5	67.38	[112]

Sugarcane bagasse	320	-	15	Autoclave	Methanol-water	KOH	36.3	[113]
Sawdust	320	-	30	Autoclave	Cyclohexanol	-	79.1	[114]
					Tetralin		72.0	
					Ethanol		57.0	
					Isopropanol		47.7	
					Cyclohexane		44.5	

2.2.2.   Pyrolysis of lignocellulosic biomass

Pyrolysis is a thermochemical process, which decomposes organic material into gases, liquid and solids, taking place over a wide temperature range of 280-850 °C [115]. However, the proportions of the products can be varied over a wide range by adjusting the process parameters, including temperature, residence time, and heating rate. The liquid product of pyrolysis processed is known as bio-oil or pyrolysis oil. Bio-oil processed from lignocellulosic biomass consists of hundreds of oxygenated compounds and has approximately 30-40 wt. % of oxygen content, which makes it not ideal since it creates poor thermal stability, high acidity and immiscibility with conventional fuels [116]. Hydro-pyrolysis is an interesting technology to reduce the oxygen content found in the bio-oil. The reducing hydrogen atmosphere generate radicals, which will react with volatiles released by the biomass, usually in the presence of a catalyst, removing oxygen which can be released in the form of water, carbon monoxide and carbon dioxide, and producing hydrocarbons [117]. The hydro-pyrolysis process has advantages over hydrodeoxygenation or hydro-treating the bio-oil, as it requires lower pressures (about 30 bar). Moreover, the process itself generates heat (exothermic reaction), which helps and sustains the endothermal pyrolysis reactions that takes place in the reactor [118].

Hydro-pyrolysis

Few studies have investigated on non-catalytic conditions using hydrogen atmosphere in fast pyrolysis conditions. Venkatakrishnan et al [119] designed high-pressure, continuous flow fast-hydro-pyrolysis reactor at a laboratory scale. Using non-catalytic conditions, it was concluded that hydrogen (partial pressure of 50 bar) was not active at a temperature of 480 °C. At 580 °C, however, the molecules did start to react and formed light oxygenated species like glycolaldehyde and formic acid [119]. Furthermore, Meesuk et al [120] set-up a fluidised-bed reactor using silica sand (SiO_2) as fluidising particles to investigate the effect of the pyrolysis atmosphere. The experiment is conducted under hydrogen and nitrogen atmosphere at atmospheric pressure at a temperature of 650 °C without a catalyst. It was revealed that the addition of hydrogen decreased the bio-oil yield from 45.74 wt. % (nitrogen atmosphere) to 40.81 wt. % (hydrogen atmosphere). However, they established that under hydrogen atmosphere, it generated extra gases such as methane and carbon dioxide and concluded that lower molecular weight of bio-oils and some aromatic hydrocarbons were achieved under hydrogen atmosphere [120]. Dayton et al [121] used a fluidised bed system, and their process temperature conditions were 375-475 °C. It was summarised that the product distribution was influenced by the temperature conditions. Their nitrogen conditions generated to a larger yield of char

of 29-40 wt. %. This was reduced by half with using hydrogen at partial pressures between 0.5-3.0 bar. Furthermore, they claimed that an increase in hydrogen partial pressure will also increase the liquid and decreasing the gas yields [121]. Zhang et al [122] compared different gas atmospheres in fast pyrolysis process using nitrogen, carbon dioxide, carbon monoxide, methane and hydrogen atmosphere. The hydrogen atmosphere increased the contents of polymerisation precursors, and increased the HHV of the bio-oils [122]. A HHV of 17.8 MJ/kg was achieved in the nitrogen atmosphere, but this increased to 24.4 MJ/kg in the hydrogen atmosphere. Resende et al [117]conducted a state-of-the-art review of hydro-pyrolysis and summarised on non-catalytic fast hydro-pyrolysis that without the addition of catalysts in a fast hydro-pyrolysis system will not be sufficient for an extensive hydrogenation of oxygenated volatiles. It was stressed that the addition of catalyst will improve the conversion of biomass into aromatic hydrocarbons. Secondly, at conditions above 500 °C and 30 bar will cause hydrogen molecules to react with the pyrolysis volatiles and result in lower molecular species. The pressure also will increase the promotion of cracking reactions [117]. This statement is agreed by He et al [123] and conducted their hydro-pyrolysis experiments in a Py-GC-MS using Rh/ZrO_2 catalyst. The bio-oil produced were comparable with that of the upgraded bio-oil by hydrodeoxygenation process. It was also established that different biomass will have different effects on the pyrolysis process. For example, poplar sawdust will need a catalytic hydro-pyrolysis. Whereas, high-ash rice husk, which contained a high amount of mineral elements, can have high hydrocarbon selectivity without the aid of catalyst because of its self-catalysis [123].

2.2.3.   Bio-crudes upgrading routes

Bio-crudes/oil from biomass using thermochemical routes, including hydrothermal liquefaction (HTL) and pyrolysis, cannot be directly used as a transportation fuel. Often the bio-crudes processed from HTL and pyrolysis result in having a high oxygen content, low heating value, high viscosity, high acidity and chemical instability when compared to conventional fuels and requires further upgrading to avoid these issues. Hydrodeoxgenation is one way to upgrade the bio-crudes/oil processed from HTL and pyrolysis.

Hydrodeoxygenation

Hydrodeoxygenation (HDO) is also known as hydrotreating, which is a process that uses catalyst and high pressure hydrogen to remove oxygen in the form of water, carbon dioxide or carbon monoxide.

The HDO process is a promising route for bio-crude upgrading to produce transportation fuel as well as increase the hydrocarbon yield [124]. The process can take place at pressures up to 352 bar and using moderate temperature up to 500 °C [125]. However, some HDO processes require high hydrogen pressure, which will be an expensive process. Therefore, selection of catalyst is important for the HDO processing. Some of the catalysts utilised in the HDO processes are noble metals including ruthenium (Ru), platinum (Pt), and palladium (Pd) to increase the H/C and O/C atomic ratios [126]. Elkasabi et al [126] used HDO catalysts with 5 % metal loading (Ru, Pt, and Pd) on carbon supports in batch reactor. The bio-oils processed from switchgrass, eucalyptus and equine manure feedstock were upgraded in HDO conditions at 320 °C and 145 bar. It was concluded that bio-oil from switchgrass using Pt/C worked the best when it came to hydrogen consumption efficiency and deoxygenation efficiency when compared with eucalyptus and equine manure bio-oils [126]. Yue et al [127] used bio-crudes processed from dried sweet sorghum bagasse from HTL processing for HDO upgrading. The bio-crudes were upgraded using 1.5 g of Ru/C catalyst in a batch reactor at a temperature of 350 °C for 4 h with a starting pressure of approximately 35 bar. A bio-crude yield of 42 % and up to 96 % of hydrocarbon content was observed after HDO processing [127]. Noble metal catalysts are often seen as undesired catalysts in the industries due to severe catalyst deactivation from coking on the surface of the catalyst and poor reusability of the catalysts [128]. Therefore, Oh et al [129] used various metal catalysts including Ni/C, Ni/SBA-15, Ni/Al-SBA-15, NiMn/SBA-15 and Pt/C in a continuous-flow reactor. Before the HDO reaction, the catalyst were activated directly in the reactors under hydrogen atmosphere at a temperature of 550 °C for 3 hours. Bio-oil (processed from woody biomass) and ethanol (4:1 w/w) were introduced at a flow rate of 2 ml min^{-1} with a flow rate of 400 ml min^{-1} hydrogen and maintained at a pressure of 30 bar. The upgraded bio-oil were improved by 49.8 % as well as an improved higher heating value of 32.8-38 MJ kg^{-1} was observed. It was also concluded that the upgraded bio-oil was miscible with diesel from the support of an emulsifier. The emulsion of the upgraded bio-oil and diesel was stable for 6 months [129]. Bharath et al [130] used bimetallic Ni_3Fe catalyst on bio-oil, which improved a higher heating value of 36.78 MJ kg^{-1} and achieved the highest hydrocarbon content of 23.77 %.

2.3. Molten salts

Molten salt mixtures are a good media for various industrial applications (e.g. batteries, excellent heat transfer fluids, thermal energy storage, and biomass pyrolysis in biofuel production), as they have good thermodynamic properties. Molten salt mixture in pyrolysis is a less studied approach where decomposition occurs when biomass is fed into a pre-heated molten salt bath. The use of molten salts offers good advantages, as they are very stable at high temperatures and can be used over a wide range of temperatures (from 120 °C to above 1000 °C). Furthermore, the application of molten salts can be simultaneously used as a heat carrier, catalyst and solvent [131]. Nitrates are known to have good heat transfer performance when it comes to storing thermal solar energy [132]. However, nitrates are not stable molten salts and oxidise at temperatures above 350 °C, especially when in contact with carbon containing materials (i.e. biomass) [133]. Whereas, hydroxides are corrosives bases, which are used for the pre-treatment of wood. NaOH is a hydroxide and is able to solubilise hemicellulose and lignin by cleaving the ether and ester bonds [134]. Whilst, halides have a catalytic effect and able to decompose large molecules, which can be seen by a study conducted by Sada et al [135]. The study used molten salts, $ZnCl_2$ and KCl, in pyrolysis using Kraft and solvolysis lignin and found that the phenolic compounds are influenced by the composition of molten salts. It was also reported that a higher yield of cresols was found due to the use of molten salts [135]. Furthermore, Kudsy et al [136] used $ZnCl_2$ and KCl which found that different phenolic compounds depended on the molar ratio of the two salts used as well as the salt-to-lignin ratio. A patent issued by Datta et al [137] stated on the use of hydrates of inorganic salts, particularly $ZnCl_2$, which readily dissolved cellulose. Robelin and Chartrand [138] evaluated $ZnCl_2$, KCl and NaCl and modelled the phase diagrams (see Figure 27) for the three eutectic points. In addition, Xu et al [139] measured the melting points experimentally using differential scanning calorimetry (DSC) on $ZnCl_2$, KCl and NaCl. A summary table of the eutectic points of $ZnCl_2$, KCl and NaCl are given in Table 3.
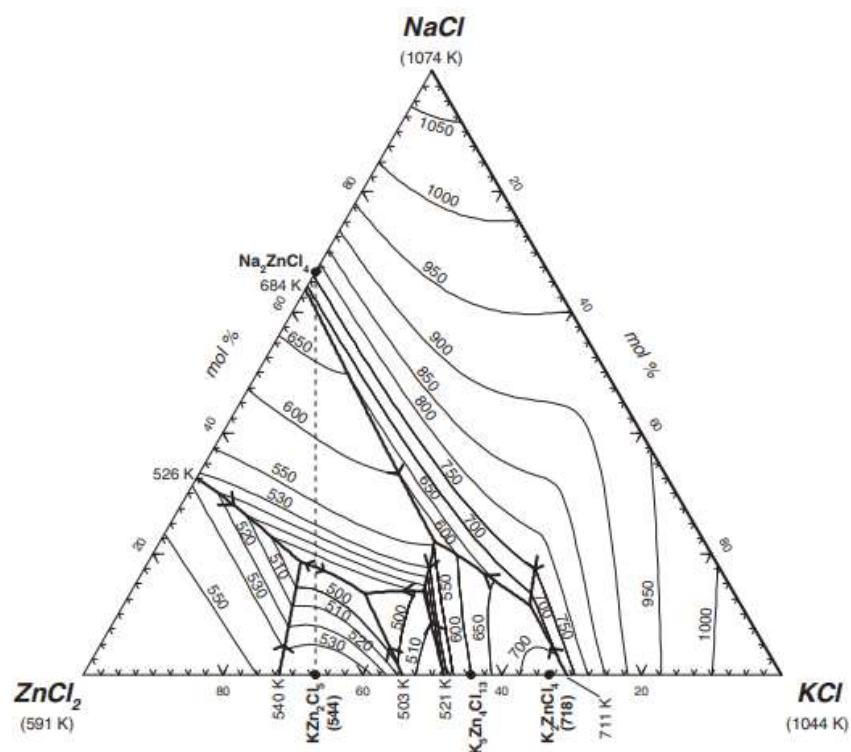
Figure 27. Phase diagram of ZnCl₂, KCl and NaCl.
Table 3. Theoretical and experimental eutectic points for ZnCl₂, KCl and NaCl

Molar composition (mol %)			Melting point (°C)	
ZnCl₂	KCl	NaCl	Theoretical	Experimental
44.3	41.9	13.8	229 [138]	199.4 [139]
59.5	21.9	18.6	213 [138]	198.7 [139]
52.9	33.7	13.4	204 [138]	210.3 [139]

Chapter 3   Feedstock characterisation and selection

3.1. Introduction

This chapter summarises the characterisation and selection of biomass feedstock used for kinetic studies (Chapter 4), hydrothermal liquefaction experiments and product analysis (Chapters 5 and 6, respectively). The key requirements for selecting the biomass was that the biomass was readily available and at a low-cost within Europe. One of the focuses was on feedstock resourcing for characterisation from forestry and agricultural sectors, as well as the pulp and paper industry (which produces lignin rich streams). The selected Lignocel® pine wood was used as a benchmark (reference) feedstock due to its immediate availability and its relatively low ash content. The characterisation of the inorganics in the biomass was crucial for further studies of its potential interaction of biomass inorganic elements with molten salts used in the liquefaction step. Wheat straw was selected as the second feedstock (agricultural residue) with a relatively high ash content compared to pine wood. This particular selection, considering biomass-ash content, was done to study potential interaction of biomass' inorganics with molten salt used in the liquefaction processing. The third feedstock was LignoBoost lignin (from Lignoboost process that involves production of Kraft sulphite pulping and ethanol). A wide range of analytical methods, including proximate, ultimate and thermogravimetric analysis, as well as analytical pyrolysis, gave a good understanding of the material for further thermal processing via hydrothermal liquefaction, liquefaction and hydro-pyrolysis in molten salts.

3.2. Methodology

3.2.1. Materials

3.2.1.1. Model components

The following model components were used in analytical pyrolysis (Chapter 3) and kinetic studies (Chapter 4) were all purchased from Sigma-Aldrich Ltd, cellulose $(C_6H_{10}O_5)_n$ (CAS: 9004-36-6); xylan from beechwood $(C_5H_{10}O_5)$ (CAS: 9014-63-5) – xylan was selected and accepted as a representative of hemicellulose, as hemicellulose is mainly composed of xylan [140, 141]; and Organosolv lignin $(C_{81}H_{92}O_{28})$ (CAS: 8068-03-9).

3.2.1.2. Biomass feedstock

The pine wood was purchased from Rettenmeier Holding AG in Germany. The wheat straw was provided by Rothamsted Research, UK. The wheat straw was harvested in Stamfordham in summer 2018, UK, and received as a whole residue after grain removal. The industrial LignoBoost lignin was provided by RISE Research Institute of Sweden AB, Sweden. LignoBoost lignin was produced from a softwood (using 50:50 spruce and pine wood) in Bäckhammer mill of Nordic Paper, which produces 159,000 tonnes of unbleached Kraft paper annually.

3.2.2. Feedstock preparation

The wheat straw was received as a batch sample in cuts of approximately 20 cm. The feedstock was ground before experiments using a Retsch Ltd., Germany, Heavy-Duty Cutting Mill, Type SM2000, to obtain a batch particle size below 1.00 mm. The pine wood sample did not require grinding, since the batch sample from the supplier was between 0.50 and 2.00 mm.

For analytical experiments (Chapter 3), kinetic studies (Chapter 4) and HTL processing (Chapter 5), a dedicated analytical fraction (below 0.25 mm – 60 mesh) was prepared from pine wood and wheat straw using an IKA A11 Basic Analytical Mill.

Supplied LignoBoost lignin was used in all experiments as received from the supplier.

3.2.3.   Proximate analysis and thermogravimetric analysis

Proximate and thermogravimetric analyses were conducted using a Mettler-Toledo TGA/DSC^3 STAR^E thermogravimetric analyser (TGA). The proximate analysis was to determine the biomass samples' moisture, volatile matter, and char content. Approximately 2.5 mg of biomass samples were weighed using Mettler-Toledo XP6 laboratory balance (accuracy of 0.001 mg) and inserted in an alumina crucible. All TGA experiments were conducted under inert atmosphere at a constant flow rate of 30 ml min^{-1}. The TGA programme was set at 40 °C and held for 5 minutes to ensure all air was removed. The biomass sample was then heated from 40 °C to 105 °C at a heating rate of 5 °C min^{-1} and held for 10 min to remove the biomass' moisture. The temperature was ramped up to 750 °C at a heating rate of 25 °C min^{-1} and held for 15 minutes. The biomass sample was cooled down from 750 °C to 40 °C at a cooling rate of 10 °C min^{-1}.

Feedstock ash content was calculated on a moisture free basis and carried out according to the E1755 ASTM standard method [142]. Prior to analysis the feedstock was dried at 105 °C for 24 hours. Approximately 2 g of biomass samples were weighed and ashed using a Carbolite AAF1100 furnace at 575 °C until constant weight was achieved.

The proximate analysis was determined using the following equations:

$$\text{Moisture (wt. \%)} = \frac{m_i - m_{105°C}}{m_i} \times 100 \qquad (3.2.1)$$

$$\text{Volatile Matter (wt. \%)} = 100 - \text{Char (wt. \%)} \qquad (3.2.2)$$

$$\text{Char (wt. \%)} = \frac{m_{105°C} - m_f}{m_{105°C}} \times 100 \qquad (3.2.3)$$

$$Ash\ (wt.\%) = \frac{m_f}{m_{105°C}} \times 100 \qquad (3.2.4)$$

$$Fixed\ Carbon\ (wt.\%) = Char\ (wt.\%) - Ash\ (wt.\%) \qquad (3.2.5)$$

Where:
- m_i = initial mass (wt. %) at initial temperature
- $m_{105°C}$ = mass recorded at 105 °C (wt. %)
- m_f = final mass (wt.%) after cooling to the initial temperature

3.2.4. Ultimate analysis

A ThermoFisher Scientific Flash 2000 Organic Elemental Analyser was used to determine carbon (C), hydrogen (H), nitrogen (N), and sulphur (S) content in the studied feedstock. Oxygen (O) content was calculated by difference. Sulphanilamide (containing 41.84 wt. % carbon, 4.68 wt. % hydrogen, 16.27 wt. % nitrogen and 18.62 wt. % sulphur) was used as a standard analysis prior to biomass analyses. Approximately 2.5 mg of biomass samples and 5.0 mg vanadium pentoxide (V_2O_5) – an oxidant to assist complete combustion – were weighed and inserted in tin capsules and combusted in excess oxygen in the elemental analyser. The analyser used a quartz reactor and heated up to 900 °C. The elemental analyser calculated the elemental composition by analysing carbon dioxide (CO_2), water (H_2O), nitrogen oxide and dioxide (NO_x), and sulphur dioxide (SO_2) concentrations in the gases. Gases were passed to a copper catalyst to remove any traces of oxygen and converted to the elemental gases separated by gas chromatograph (GC) and analysed using a thermal conductivity detector (TCD). C, H, N and S content (wt. % on a dry basis) were analysed in triplicates, and average values were taken at a 95 % confidence interval. Results from the ultimate analysis were used to calculate the heating values. The higher heating value (HHV) is defined as the amount of heat available in the biomass, which includes the latent heat of vaporisation of water in the fuel and reaction products. Whilst the lower heating value (LHV) does not include the latent heat of vaporisation [143]. The heating values, including HHV and LHV, were calculated using equations 3.2.6 and 3.2.7 [144]. These equations were chosen in consideration from the elemental analysis – carbon, hydrogen and ash content, for biomass.

$$HHV_{dry} \ (MJ \ kg^{-1}) = 0.3491C + 1.1783H + 0.1005S - 0.1034O - 0.0151N - 0.0211A \quad (3.2.6)$$

$$LHV_{dry} = HHV_{dry} - 2.442 \times \left(\frac{8.936H}{100}\right) \quad (3.2.7)$$

Where A is the ash.

3.2.5. Inorganic elemental analysis

Concentration of metals and other inorganic components of raw feedstock and feedstock-derived ash samples were carried out using acid digestion sample preparation (2 mg) for analysis using an Inductively-Coupled Plasma (ICP) technique with Optical Emission Spectroscopy using PerkinElmer Optima 7300DV ICP-OES spectrometer. According to Vassilev et al [3], the twelve ash-forming elements including aluminium (Al), calcium (Ca), chlorine (Cl), iron (Fe), potassium (K), magnesium (Mg), manganese (Mn), sodium (Na), phosphorus (P), sulphur (S), silica (Si) and titanium (Ti) are

commonly found in the biomass. Furthermore, these twelve ash-forming elements were taking into consideration for future assessment of biomass processing and potential interaction of biomass' inorganic elements with molten salts.

Prior analysis, the biomass were ashed at 575 °C until no weight difference was observed (according to ASTM E1755 method) using a Carbolite AAF1100 furnace [142]. The biomass and biomass-derived ash samples were dried at 80 °C for 4 hours and cooled in a desiccator. 0.25 g of dried samples were added to a digestion tube with 5 ml of nitric acid, which was mixed at a room temperature for 2 hours The sample was heated overnight and 5 ml of 25 % hydrochloric acid was added the following day and heated again at 80 °C. Upon cooling, all samples were analysed by ICP-OES.

3.2.6.   Pyrolysis-Gas Chromatography-Mass Spectrometry

All feedstock of 0.5 mg were inserted in a quartz tube, where quartz wool was packed at the end of the tube. The sample was pyrolysed in a platinum coil using a CDS Analytics 5200 Pyroprobe (Chemical Data Systems, Oxford, PA) to a pyrolysis temperature of 500 °C with dwell time for 15.0 s and at a ramp rate of 20 °C ms^{-1}. The volatilised products were trapped by Tenax-4™ adsorbent trap in order to avoid secondary reactions. The pyrolysis product was transferred to a close-coupled to a PerkinElmer Clarus 680 gas chromatograph (GC) and Clarus 600S mass spectrometer (MS). Helium was used as a carrier gas to separate the components using a PerkinElmer Elite-1701 column (cross-bond: 14% cyanopropylphenyl and 85% dimethyl polysiloxane; 30 m, 0.25 mm i.d., 0.25 mm df). The GC oven was held at 45 °C for 5 minutes, then heated at 2.5 °C min^{-1} to 250 °C and held at this temperature for 5 minutes. Separated components were individually identified in MS with ionisation source electron energy at 70 eV. Proposed assignments (m/z = 45-300) were made from mass spectra detection using the NIST 2011 MS library for final composition identification.

3.3. Results and Discussion

3.3.1. Ultimate analysis

The ultimate analysis and heating values results for pine wood, wheat straw and LignoBoost lignin, are presented in Table 4.

Table 4. Ultimate analysis and heating values of the selected lignocellulosic biomass.

Feedstock	Pine Wood	Wheat Straw	LignoBoost Lignin
Ultimate Analysis [d.b.]			
C (%)	47.82 ± 0.94	45.11 ± 0.21	62.55 ± 1.62
H (%)	6.56 ± 0.70	6.23 ± 0.22	5.82 ± 0.09
N (%)	0.17 ± 0.02	0.75 ± 0.01	0.25 ± 0.02
S (%)	0.00	0.11 ± 0.04	2.49 ± 0.09
O* (%)	45.45 ± 1.58	47.82 ± 0.18	28.89 ± 1.78
Heating Values			
HHV (MJ kg^{-1})	19.71	18.03	25.96
LHV (MJ kg^{-1})	18.28	16.67	24.69
molar ratio H/C	1.63	1.65	1.11
molar ratio O/C	0.71	0.80	0.35

d.b.= dry basis
*Oxygen was calculated by difference

The ultimate analysis showed the carbon (C), hydrogen (H), nitrogen (N) and sulphur (S) content of biomass, which determines the fuel efficacy and major components of biomass [145]. The oxygen (O) content was calculated from the difference. From the ultimate analysis, it is able to identify potential environmental impact when biomass is thermochemically processed [146]. The highest C content observed was Lignoboost lignin (62.55 wt. %), whilst wheat straw (45.11 wt. %) was seen with the least C content. With N content, wheat straw was found the highest with 0.75 wt. %. N is converted in N_2 (gaseous) and NO_x, which has an environmental impact. Whereas, S generates SO_2, which forms sulphates resulting in a build-up of condensates in boilers. LignoBoost lignin was found with 2.49 wt. % as the highest S content, which was expected, since the production used Kraft processing with a high amount of sulphur bonding [147]. Tomani [57] also claimed that the typical value of S would

be between 1 % and 3 %, where 2.5 % is a typical value in the LignoBoost lignin found from the demonstration plant, which the current result is in agreement with.

The higher heating values (HHV) and lower heating values (LHV) were calculated from Channiwala and Parikh equation [144]. The HHV represents gross calorific value and is referred to as the heat released of any fuel per unit of mass per unit volume of the fuel when burnt completely. Whereas, the LHV is also known as the net calorific value, which does not take into consideration of the latent heat of vaporisation of water. High volatile matter content and C and O will contribute to a higher HHV [146, 148]. Previous studies have also reported that a high lignin content will be correlated to a higher HHV content, and the results seemed to agree with the literature [149]. With LignoBoost lignin reported to have the highest HHV and LHV of 25.96 and 24.69 MJ kg^{-1} respectively, since it has the highest C content. Pine wood was found to have an HHV and LHV of 19.71 and 18.28 MJ kg^{-1} respectively, which seemed to agree with Gordobil et al [148]. Pine wood was found with the highest volatile matter and a higher HHV and LHV when compared with wheat straw (18.03 and 16.68 MJ kg^{-1}), and could also be assumed that pine wood has a higher lignin content than wheat straw.

3.3.2.   Metal analysis

Inorganic elements in all feedstock and prepared ash samples were determined by an Inductively-Coupled Plasma (ICP) technique with Optical Emission Spectroscopy (OES). The biomass ashes were prepared using a muffle oven and combusted at 575 °C for 8 hours. In this analysis, particular stress was on the 12 ash-forming elements found in biomass and biomass ashes including aluminium (Al), calcium (Ca), chlorine (Cl), iron (Fe), potassium (K), magnesium (Mg), manganese (Mn), phosphorous (P), sodium (Na), sulphur (S) and titanium (Ti) [66]. The 12 ash-forming elements takes into consideration of future assessment of biomass processing (liquefaction and hydro-pyrolysis), products (chars) and potential interaction of biomass' inorganic elements with molten salts used in the liquefaction step. The results of the 12-ash forming elements of three raw biomass samples and three ash-generated biomass samples are outlined in Table 5 and Table 6, respectively.

Table 5. Metal analysis for ash-forming elements (raw biomass feedstock).

Feedstock	Pine Wood (%)	Wheat Straw (%)	LignoBoost Lignin (%)
Al	0.0044	0.0238	0.0110
Ca	0.1100	0.0265	0.3550
Cl	0.1400	0.5100	n/d
Fe	0.0125	0.0299	0.0060
K	0.0320	0.9050	0.0170
Mg	0.0232	0.0526	0.0180
Mn	0.0133	0.0030	n/d
Na	0.0055	0.0085	0.0500
P	0.0034	0.0240	0.0060
S	n/d	n/d	2.4350
Si	0.0266	0.9500	0.0020
Ti	0.0010	0.0010	n/d

n/d = not detectable

Table 6. Metal analysis of ash-forming elements (for prepared ash reference samples).

Feedstock	Pine Wood Ash (%)	Wheat Straw Ash (%)	LignoBoost Lignin Ash (%)
Al	0.68	0.37	1.52
Ca	24.26	5.67	3.59
Cl	0.10	4.00	1.57
Fe	4.08	0.33	0.69
K	5.46	18.37	3.15
Mg	5.42	0.86	3.26
Mn	2.75	0.046	n/d
Na	0.96	0.45	9.58
P	0.83	0.42	0.17
S	2.06	1.37	17.73
Si	0.95	9.81	1.97
Ti	0.28	0.014	N/D

n/d = not detectable

Biomass consists out of a mixture of organic matter (cellulose, hemicellulose and lignin) and inorganic matter. From past research, it showed that the macronutrients of biomass are K, Ca, Mg, P and S, whereas the micronutrients are Fe, Mn, and Cl [66]. Non-essential nutrients for plant growth are Si, Al and Na, but considered essential depending on the biomass type [150]. Some of the nutrients, including P and K, are the main components of fertilisers that were introduced into the soil [151]. Once biomass have been thermally processed, the biomass residue or ash will be left with the inorganic matter. The inorganic matter or the ash-forming elements may pose challenges when

thermally processed including coking, slagging, abrasion, corrosion and fouling of the heat exchangers and furnaces in reactors when processed in large quantities. Furthermore, it is important when the biomass will be processed with the molten salts, which will contribute to further contamination when liquefied or hydro-pyrolysed in the reactors. Table 5 and Table 6 show the biomass samples' and biomass ashes' 12 ash-forming elements respectively.

Ca is the highest element found in both in pine wood and pine wood ash with 0.11 % and 24.26 % respectively, which is a typical characteristic of wood and wood barks [66]. Ca mainly exists in the form of oxides (CaO) after combustion and carbonates ($CaCO_3$) as an inorganic matter. High content of Ca is seen as unfavourable where Ca is able to react with Si to form an alkali silicates and lead to a lower melting point (below 700 °C) [152]. Other significant elements were K and Mn. These results (Ca, K and Mn) showed that in literature conducted by Vassilev et al [66] are commonly found in wood and woody biomass as an organic association. The Ca-K-Mn association are mainly presented in the form of carbonates, phosphates and sulphates in biomass and could be responsible for enhanced leaching behaviour, deposits formation, slagging and fouling during biomass combustion. However, it could also have a catalytic effect during thermochemical conversion of biomass [66]. Other typical elements found in wood and woody biomass are Mg, Fe and S, which were mainly served as a nutrient.

Wheat straw and its ashes had a substantial amount of K with 0.905 % and 18.37 % respectively, but this could be due to the nutrient intake during growth since K is considered a macronutrient. Furthermore, it could also be supplied as a fertiliser, for example K_2SO_4 [66]. After combustion, K is found as an oxide (K_2O). A significant amount of K is a major concern and together with Ca may contribute in the formation deposits on boiler surfaces [153]. K is related to a decreased ash melting temperature, which can cause slagging and fouling. Especially alkali metals (including K and Na) are contributors to slagging of the furnace in a gaseous state as well as fly ash particles [154]. Furthermore, K is known to be a highly mobile element, which is defined as the ability to come into physical contact with other materials [153]. The second highest element found in wheat straw ash was Si with 9.81 %, which is a common characteristic found in straw and herbaceous biomass and typically comes in the form of SiO_2. Si contributes to the plant's sturdiness or rigidness in tall grasses and straws [155]. Si also increases resistance to attack by fungal pathogens and insect pests [156]. The melting point of Si is around 1700 °C, which causes no problems during combustion. However, Si can easily react with alkali or alkaline earth metals, including K, Na and Ca, and form ashes with lower melting point and readily slag and foul at boiler furnace temperatures of around 800-900 °C [153, 157]. Cl was also found in wheat straw and its ash with 0.51 % and 4.00 % respectively, which is a pretty common element in straw [158]. Like K, Cl is also a highly mobile element, and especially

towards K. Cl functions as a charge compensation and osmoregulation, as well as the most problematic element when it comes to deposition, corrosion and fouling within the combustion units [66].

It is evident that LignoBoost lignin and its ashes to have a large amount of S with 2.435 % and 17.73 % respectively, since it has been washed using sulphuric acid and as discussed in the literature review. SO_2 can be formed when combusting in the reactor and will be challenging, which makes it an unsuitable for a sustainable feedstock since SO_2 is a pollutant. Na was found to be the second-highest inorganic with 0.05 % and 9.58 % in the biomass and biomass ash respectively. Na to most biomass is regarded as highly toxic at high concentrations and therefore Na is mainly found in small content in woods (which can be compared with pine wood and wheat straw) [159]. The substantial amount of Na found in LignoBoost originated from the use of sodium hydroxide in the washing process [57]. Other significant elements found in the biomass and its ashes were Ca, Mg and K, which are considered macronutrient and absorbed through the roots [160].

3.3.3. Proximate analysis

The thermogravimetric analysis (TGA) was applied to establish yields of moisture, volatile matter and char (proximate analysis) for biomass samples subjected to the pyrolytic decomposition. Those are presented in Table 7 along with the ash content from the application of the ASTM method E 1755 [142].

Table 7. Proximate analysis results of biomass.

Feedstock	Pine Wood	Wheat Straw	LignoBoost Lignin
Proximate Analysis			
Moisture (wt. %)	4.88	5.33	2.11
Volatile Matter (wt. %) d.b.	82.79	75.14	62.08
Char (wt. %)	17.21	24.86	37.92
Fixed Carbon (wt. %)	16.81	19.83	37.74
Ash (wt. %) d.b.	0.40	5.03	0.18

The moisture content represents the water content in the biomass. High moisture content indicates a potential issue when it comes to biomass storage resulting in increased chances of decomposing and thus loss of energy [161]. Furthermore, biomass with high moisture content need a pre-treatment

beforehand where biomass will have to be dried which can be time-consuming and not cost-effective. The ash content is the inorganic part left after burning the biomass in complete combustion. It is important to consider the ash content when selecting lignocellulosic biomass, as ash composition may cause technological and environmental problems. The char content is the solid residue after devolatilisation from biomass under inert (pyrolytic) conditions. The volatile matter is the condensable gases and vapours released during the thermal degradation and can be divided into light volatiles and tar [162]. A higher volatile matter is desirable as it will increase the amount of the production of bio-oil [163].

LignoBoost lignin had one of the lowest moisture content when compared with pine wood and wheat straw, as LignoBoost lignin was already dried during the production [57]. Pine wood is a clean wood and was anticipated to have a low ash content. The LignoBoost process is a known process to reduce the ash content of lignin, which explains why the ash content (d.b.) is 0.18 wt. %. Whereas, the ash content of wheat straw was found at 5.03 wt. %, which is relatively higher since it is agricultural biomass rather than woody biomass of 0.40 wt. %. It could also indicate the contamination from soil and how the wheat straw was handled during harvesting. The volatile matter of pine wood was observed the highest (82.79 wt. %) out of all three selected lignocellulosic biomass, which makes it an ideal feedstock to process for bio-liquid/crude production. LignoBoost lignin was found to have a minimum volatile matter of 62.08 wt. % and may be seen as the least desirable feedstock for thermochemical processing. Lignin itself is difficult to thermally decompose, and according to literature, it can decompose over a wider temperature range and will need a longer time to decompose due to its heterogeneous structure [141].

3.3.4. Thermogravimetric analysis

The mass loss curve and derivative thermogravimetric (DTG) profile from the TGA for pine wood, wheat straw and LignoBoost lignin are presented in Figure 28 showing the applied temperature from 40 to 750 °C at a heating rate of 25 °C min^{-1}.
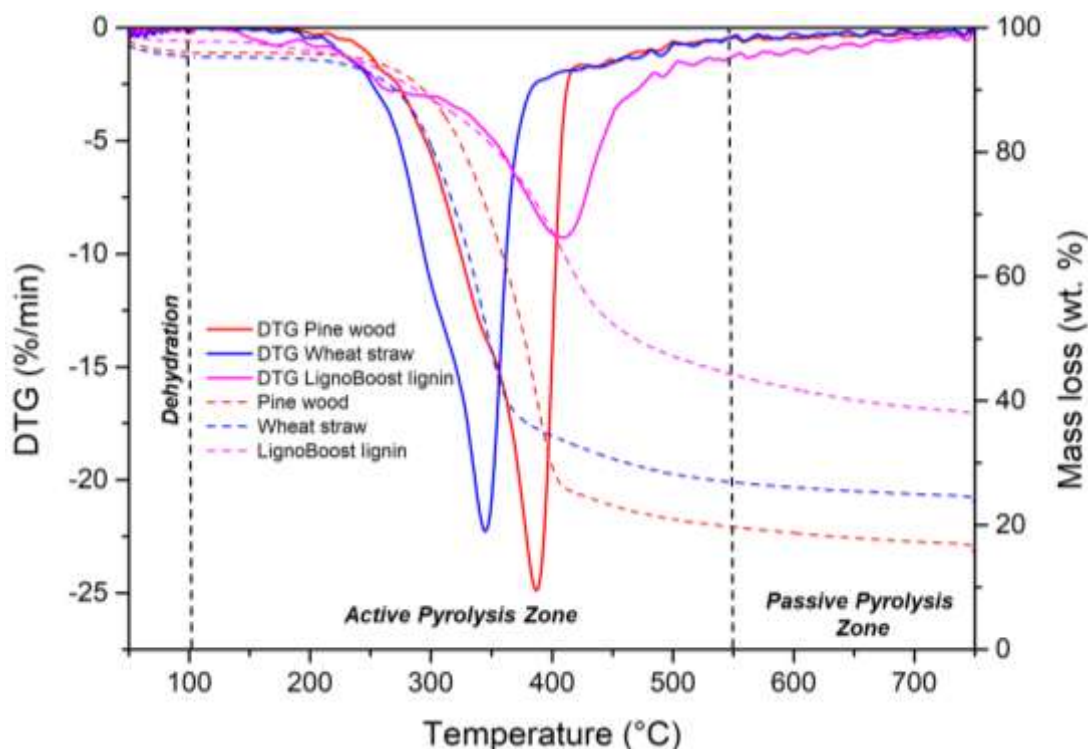
Figure 28. TGA (mass loss) and DTG of pine wood, wheat straw and LignoBoost lignin.

The TGA mass profile is reported in weight percentage as a function of temperature, whereas the DTG profile is reported in the percentage weight loss per minute as a function of temperature. The profile is split into three regions, which are dehydration, active pyrolysis and passive pyrolysis zones [164]. The dehydration zone occurred from ambient temperature to 105 °C, where also simple molecules are degraded.

The active pyrolysis zone occurs between 105-550 °C, where mainly loss of holocellulose (cellulose and hemicellulose) occurs. The decomposition of cellulose and hemicellulose generally takes place in the temperature of 270-380 °C and 250-380 °C respectively within the active pyrolysis range [165]. Anything above the temperature of 550 °C would be considered in the passive pyrolysis zone.

The shape of the DTG profile is often reflective to their lignocellulosic content of the biomass. From the TGA (mass loss) and DTG profile in Figure 28, it was revealed that initial pyrolytic decompositionof pine wood started at 195 °C and with the maximum weight loss occurring at 388 °C. Less-defined shoulder was observed around 350 °C in pine wood and was found to have the least char residueof 17.21 wt.%. Wheat straw started to decompose at 185 °C, whereas a slight shoulder

was observed at 295 °C. The shoulder decomposition highlights the initial region of thermal decomposition of hemicellulose. Furthermore, wheat straw decomposed at a lower temperature and was found to have a lower peak temperature of 345 °C due to a higher hemicellulose content found when compared to pine wood and LignoBoost lignin. This seems to agree with the literature, where hemicellulose degrades between 200-315 °C respectively [166-168]. Furthermore, Grønli et al [169] described the first slight shoulder is mainly attributed to the breakdown of hemicellulose. At the end of thermal degradation, wheat straw was found with 24.86 wt. % char residue. The initial decomposition temperature of LignoBoost lignin was at 140 °C with a DTG peak temperature of 410 °C. It was observed that LignoBoost lignin decomposed over a wider temperature range within both active and passive pyrolysis zones (from 140 °C to 650 °C). Like lignin, LignoBoost lignin has a complex chemical structure, as it is made up of various aromatic rings with different branches and covers a wide range of chemical bonds [170]. However, lignin contains lots of hydroxyl and methoxy side chains, which are easier to break since they require low bond energy and resulting in a low initial pyrolysis temperature and hence it started at 140 °C [171]. Cleavage of β-O-4 linkages occurs between 227-607 °C within the active pyrolysis zone, while secondary pyrolytic reactions are occurring where all types of bonds are broken down during passive pyrolysis region [172]. Furthermore, a significant amount of char was produced at the end of the pyrolysis reactions and was left with 37.92 wt. % residue at the end of the thermal degradation.

### 3.3.5.	Pyrolysis-Gas Chromatography-Mass Spectrometry (Py-GC-MS)

Pyrolysis-gas chromatography-mass spectrometry (Py-GC-MS) was introduced to study the formation of higher molecular-weight of hydrocarbons during the pyrolytic treatment of model components and studied biomass feedstock. Py-GC-MS chromatograms for studied model components – cellulose, xylan and Organosolv lignin along with biomass samples – LignoBoost lignin, pine wood and wheat straw and are all presented from Figure 29 to Figure 35 in sections 3.3.5.1 to 3.3.5.6. Peak assignments for the key pyrolytic decomposition products are given under each figure.

#### 3.3.5.1.	Cellulose

Figure 29 shows the pyrogram from the pyrolytic decomposition of cellulose at 500 °C with the NIST library peak assignments.
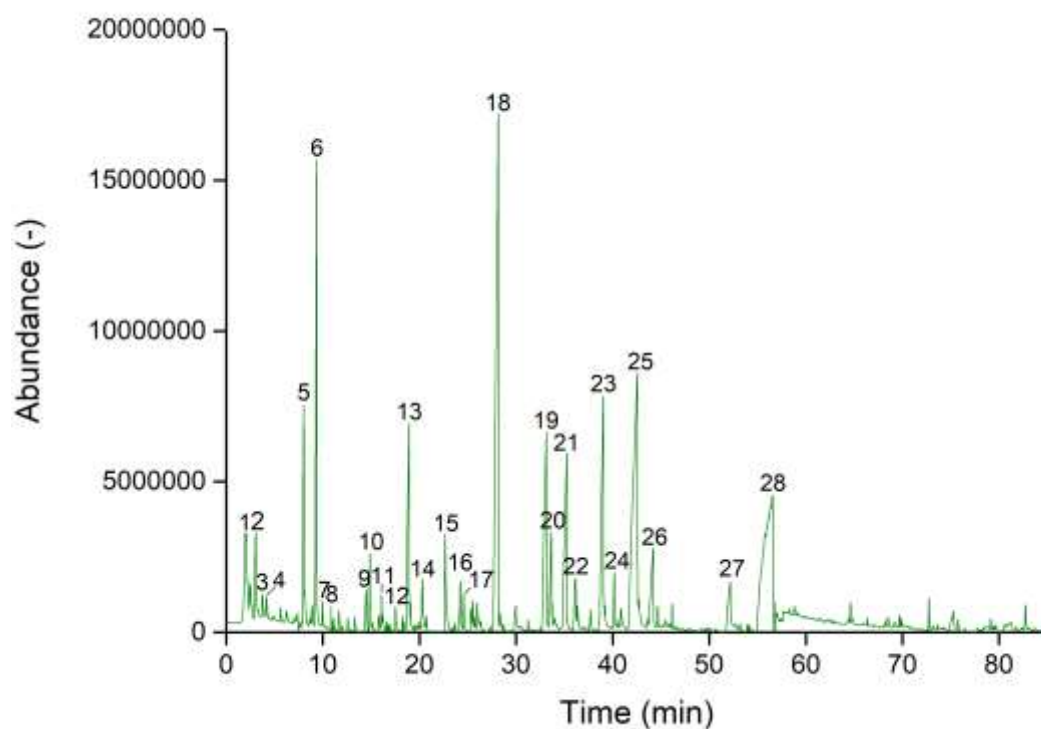
Figure 29. Py-GC/MS chromatogram for cellulose.
Peak assignment: (1) acetic anhydride; (2) methyl vinyl ketone; (3) acetic acid; (4) 2,3-butanedione; (5) 2(3H)-furanone; (6) furfural; (7) 2-propylfuran; (8) 5-methyl-2(3H)-furanone; (9) dihydro-4-hydroxy-2(3H)-furanone; (10) 1,2-cyclopentanedione; (11) 5-methyl-2-furancarboxaldehyde; (12) 2(5H)-furanone; (13) 3,4-dihydro-2-methoxy-2H-pyran; (14) 2-hydroxy-3-methyl-2-cyclopenten-1-one; (15) 2,5-dimethyl-4-hydroxy-3(2H)-furanone; (16) methyl 2-furoate; (17) 2,3-dimethylcyclohexane; (18) 1,6-anhydro-3,4-dideoxy-β-D-pyranosen-2-one (levoglucosenone); (19) heptanal; (20) 1,2-cyclohexanediol; (21) 1,4:3,6-dianhydro-α-D-glucopyranose; (22) 2-deoxy-D-galactose ; (23) 5-hydroxymethylfurfural; (24) *cis*-1,2-cyclohexanediol; (25) 3,4-anhydro-D-galactosan; (26) β-D-glucopyranose; (27) ; (28) 1,6-anhydro-β-D-glucopyranose (levoglucosan)

The Broido-Shafizadeh model confirmed the degradation route of cellulose from the intermediates (levoglucosan (peak 28) and levoglucosenone (peak 21)) and sugars (β-D-glucopyranose (peak 26) and 3,4-anhydro-D-galactosan (peak 25)) to lower molecular-weight products including furfural (peak 6), 5-hydroxymethylfurfural (peak 23) and acetic acid (peak 3). In this model, the pyrolytic degradation of cellulose starts with the decrease in degree of polymerisation (DP), which initiates the breakage of (1→4)-glycosidic bonds [33]. Cellulose undergoes through dehydration, condensation and depolymerisation reactions to form active cellulose [173]. The active cellulose undergoes thermal degradation and reforming reactions leading to defined end-products (including anhydrosugars, furans, light oxygenates and other low-weight molecular components), as shown in Figure 30.
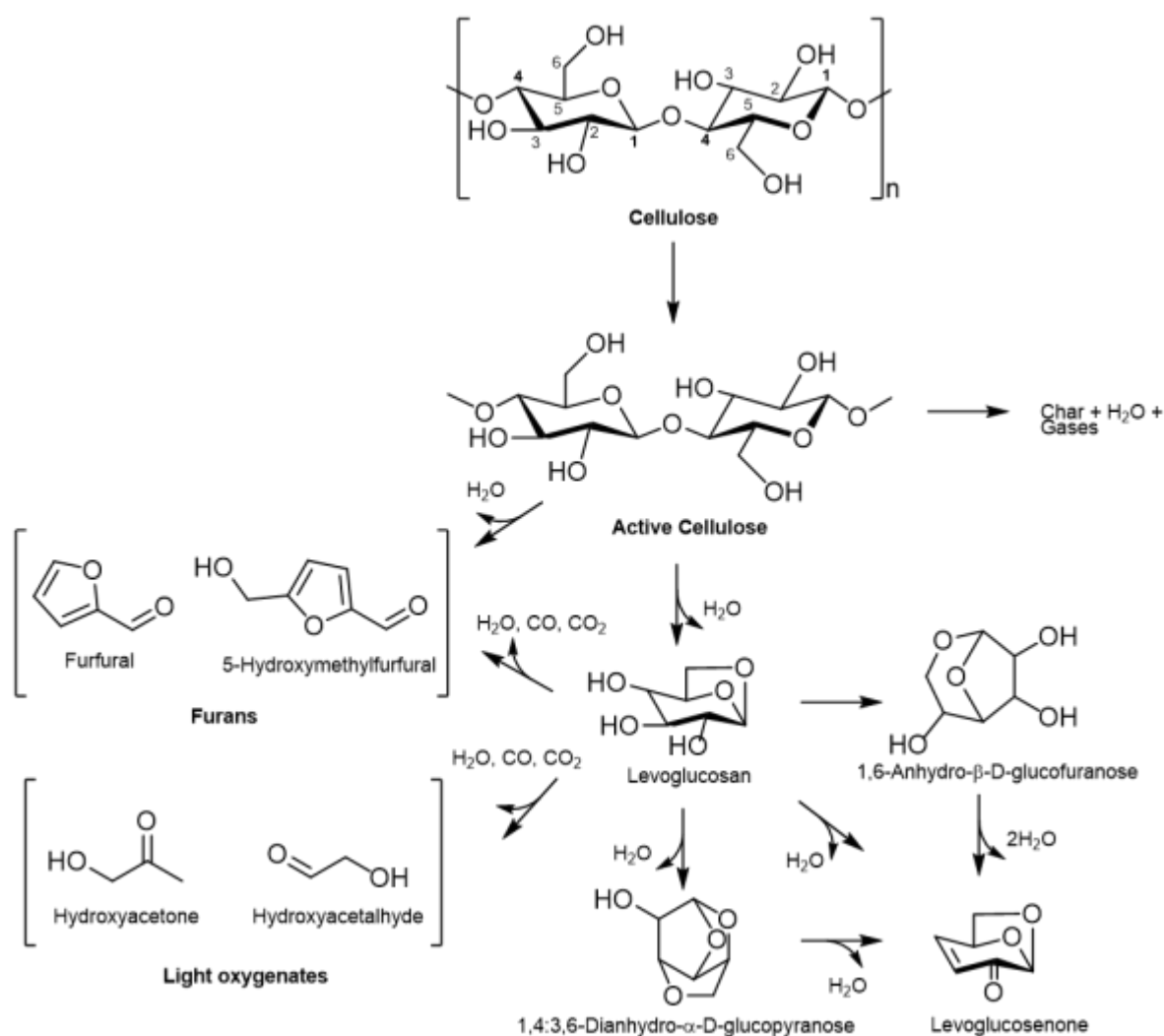
Figure 30. Proposed reaction pathway of cellulose pyrolysis.

The most prevalent anhydrosugar that was found from Py-GC-MS analysis of cellulose is 1,6-anhydro-β-D-glucopyranose (levoglucosan) in peak 28. Levoglucosan is formed from the cleavage of β-1,4-glucosodic linkage in the cellulose polymer and is followed by intramolecular rearrangement of monomer units [174]. The H atom of the C_6-OH group transfers the glycosidic bond in cellobiose (sub-unit of cellulose) [36]. Levoglucosan is considered as the primary pyrolysis product, as well as an intermediate for the formation of anhydro-monosaccharide products detected by Py-GC-MS analysis and including 5-hydroxymethylfurfural (peak 23), levoglucosenone (peak 18) and 1,4:3,6-anhydro-α-D-glucopyaranose (peak 21) through dehydration and isomerisation reactions [36, 175]. In this particular Py-GC/MS analysis, 1,6-anhydro-β-glucofuranose was expected from the theoretical degradation mechanism but was not found in this analysis. Anhydro-monosaccharide, 1,6-anhydro-3,4-dideoxy-β-D-pyranosen-2-one (levoglucosenone) was observed as the largest peak (peak 18) and was generated from intramolecular dehydration of C_3 hydroxyl and C_2 hydrogen atom of glucopyranose ring, which was derived from a secondary reaction of levoglucosan [176]. Another key cellulose pyrolysis marker is 5-hydroxymethylfurfural (5-HMF) (peak 23), which can be produced from direct ring-opening and rearrangement reactions on cellulose or during secondary reaction from levoglucosan. From cellulose, 5-HMF is formed during the dehydration process via the cleavage of the ring glucosidic bond on cellobiose unit to form an aldehyde unit on C_1. Followed by the formation of double bond between C_4 and C_5 through chain structure rearrangement. Another double bond between C_2 and C_3 is formed through the dehydration process of the hydroxyl group, whereby the acetal reaction of hydroxyl groups on C_2 and C_5 [177]. The secondary reactions of levoglucosan was described by Shafizadeh and Lai, whereby the pyran-ring of levoglucosan is broken to the hexose structure and followed by dehydration of the hydroxyl group and an acetal reaction on C_2 and C_5 [178]. Furfural is mainly a product of 5-HMF, which was confirmed by Shafizadeh and Lai, and Shen and Gu [17, 178]. Large amounts of low molecular weight products (C_2-C_4) were produced including acetic anhydride (peak 1), methyl vinyl ketone (peak 2), acetic acid (peak 3), 2,3-butanedione (peak 4), 2(3H)-furanone (peak 5), dihydro-4-hydroxy-2(3H)-furanone (peak 9) and 2(5H)-furanone (peak 12). Typical C_2-C_4 or light oxygenates products will include hydroxyacetaldehyde (HAA), glyceraldehyde and pyruvaldehyde but were not present, which are produced at elevated temperature [17, 35]. Most of the C_2-C_4 products (mainly furan products) are depolymerised reactions from anhydrosugars. Interestingly, 3,4-*anhydro*-D-galactosan was identified and is not considered a product from pyrolytic degradation of cellulose but mainly from hemicellulose [179]. Gaseous products (CO, CO_2 and H_2O) are largely associated with the production of char [180].

3.3.5.2. Xylan (hemicellulose)

The pyrolysis chromatogram for xylan is presented in Figure 31. Thermal degradation of this biomass constituents leads to generation of larger amounts of low molecular weight and volatile components. This is due to its lower thermal stability and lack of crystallinity compared to cellulose, including propanal (peak 1), 2-methylfuran (peak 2), 3-pentanone (peak 3), methyl formate (peak 4), 2,3-dihydro-1,4-dioxin (peak 5), 3-furaldehyde (peak 8), furfural (peak 9), 1,2-cyclopentanedione (peak 12) and 2(5H)-furanone (peak 14).
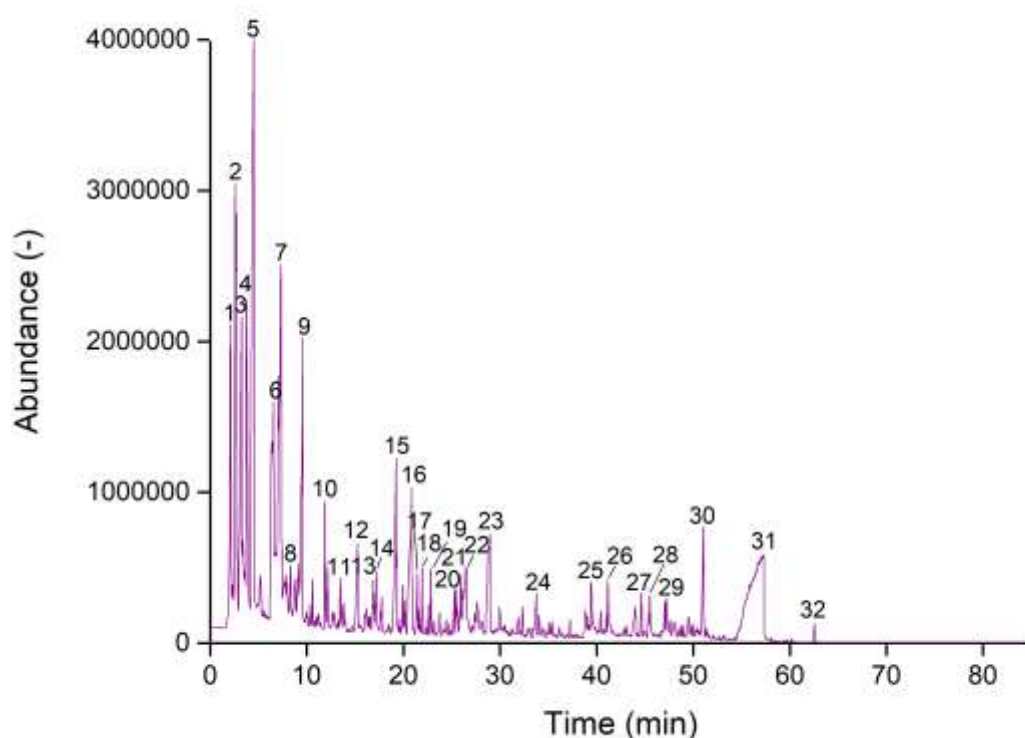
Figure 31. Chromatogram for xylan (hemicellulose).
Peak assignment: (1) propanal; (2) 2-methylfuran; (3) 3-pentanone; (4) methyl formate; (5) 2,3-dihydro-1,4-dioxin; (6) 1-penten-3-one; (7) 1-butoxy-2-butene; (8) 3-furaldehyde; (9) furfural; (10) 2-methyl-2-cyclopenten-1-one; (11) 4-cyclopentene-1,3-dione; (12) 1,2-cyclopentanedione; (13) 2,4-dimethylfuran; (14) 2(5H)-furanone; (15) 3,4-dihydro-2-methoxy-2H-pyran; (16) 2-hydroxy-3-methyl-2-cyclopenten-1-one; (17) 2,4-dimethyl-1,3-cyclopentanedione; (18) 3-methyl-1,2,4-cyclopentanetrione; (19) phenol; (20) 2-methylphenol (o-Cresol); (21) 4-ethyl-2-hydroxycyclopent-2-en-1-one; (22) 4-methylphenol (p-Cresol); (23) 2,5-dimethylphenol; (24) 3-Methylfuran-2,4-dione; (25) 1,2-dihydroxybenzene (catechol); (26) 3-methyl-1,2-benzenediol; (27) d-Mannose; (28) 3-hydroxybenzaldehyde; (29) 2-methyl-1,4-benzenediol; (30) 3,4-dihydro-6-hydroxy-2H-1-benzopyran-2-one; (31) 1,6-anhydro-β-D-glucopyranose (levoglucosan); (32) 1,6-anhydro-α-D-galactofuranose

Initial reaction of xylan starts cracking of side chain and acetic components will be produced in large quantities [181]. Acetic acid, as well as levulinic acid, are considered major components but were not observed in xylan. However, methyl formate (peak 4) was detected and is considered a formate ester of formic acid, which is also considered a major product of hemicellulose. Formic acid as well as acetic acid occurs from cracking of carboxyl group from 4-O-methylglucuornic xylan unit [182].

Furfural (peak 9) is considered a typical pyrolytic decomposition product of xylan. Its formation is taking place due to the cleavage of hemiacetal bond on depolymerised xylan followed by a dehydration reaction between the hydroxyl group on C_2 and C_5 position [177]. Furthermore, it can also be produced via a two-step dehydration of D-xylose at C_3 and C_4 position and followed by a rate-determining cyclisation step [183]. Other furan products, including 2-methyl furan (peak 2), 3-furaldehyde (paek 8), 2,4-dimethylfuran (peak 13) and 2(5H)-furanone (peak 14), are main produced from degradation 5-hydroxymethylfurfural (5-HMF) but not present in this analysis [182].

Levoglucosan (peak 31) was also observed in the pyrolytic decomposition of xylan. According to literature there would be no feasible mechanism for xylan to generate levoglucosan [184]. This could also have been 1,4-anhydro-D-xylopyranose which is the main condensable product at elevated temperatures, as these are backbone of xylan with a 4-O-methyl-α-D-glucuronic acid as a side chain [39, 177]. According to Ponder and Richards, cellulose is able to form freely 1,6-anhydride due to the free primary hydroxyl group at C_6. Whereas, xylosyl cation may be "stabilised" by intramolecular addition of hydroxyl group from another xylan molecule (transglycosylation). 1,4-anhydro-D-xylopyranose will act as an intermediate and consumed instantly to produce two-carbon and three-carbon, as well as gaseous products through cracking reactions [177]. However, Wang and his colleagues did find levoglucosan in pyrolytic degradation of xylan [182].

D-Mannose was also observed as a key component from xylan, which is a hexose and mainly derived from glucomannan. Glucomannan is a polysaccharide and is predominantly found in softwood, but it is also found in hardwoods. The glucomannan is composed of β-1,4-linked d-mannose backbone [185].

Taking into consideration possible xylan degradation network, a general degradation pathway is presented in Figure 32.
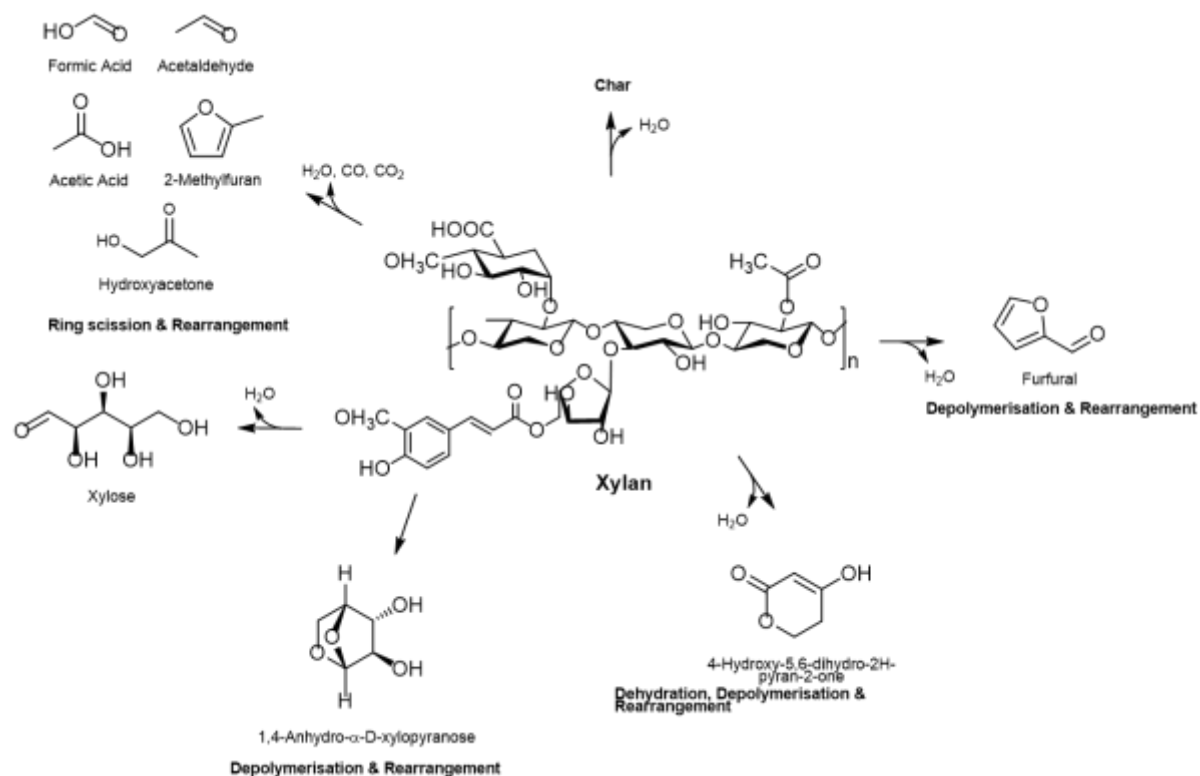
Figure 32. Proposed reaction pathway of xylan pyrolysis.

Peng and Wu [186] have described that the pyrolytic degradation of xylan is divided into four stages. Loss of water (stage 1) occurs at a temperature of around 190 °C. During second stage at (200-280 °C), also considered early pyrolysis stage, major weight loss of xylan occurs where high yields of CO_2 is generated at 200 °C [187]. Dehydration and fragmentation of side chains of xylan also occurs during the second stage, mainly acidic products (i.e. acetic acid and formic acid) and low molecular weight products (i.e. HA) are released [182]. The third stage, between 280 °C and 350 °C, is the main pyrolysis stage whereby dehydration, decarboxylation (CO_2) and decarbonylation (CO) takes place [186]. Release of CO is affected by decomposition of ring-opening intermediate, which could be explained by the formation of furfural (through ring-opening and rearrangement) [140]. The final stage takes place between 350-700 °C where char starts to form, and most volatiles are released from the char [186] .

3.3.5.3.   Organosolv Lignin

The Py-GC-MS pyrogram for Organosolv lignin is presented in Figure 33.
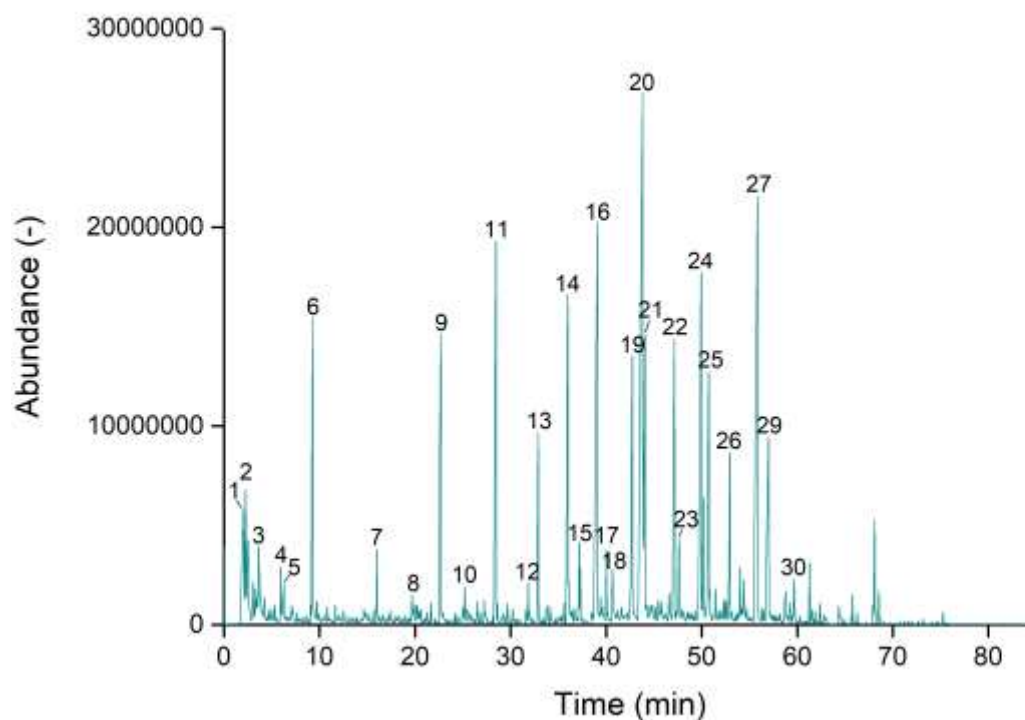
Figure 33. Chromatogram for lignin (Organosolv).
Peak assignment: (1) 1-methylcyclopropanemethane; (2) 3-methylfuran; (3) methyl formate; (4) 2-methylcyclopentanol; (5) propanoic acid; (6) furfural; (7) 5-methyl-2-furancarboxaldehyde; (8) ethyl furan-2-carboxylate; (9) 2-methoxyphenol (guaiacol); (10) 2-methylphenol (o-Cresol); (11) 2-methoxy-4-methylphenol (Creosol); (12) 3,4-dimethoxytoluene; (13) 4-ethyl-2-methoxyphenol; (14) 2-methoxy-4-vinylphenol; (15) 2-methoxy-4-(2-propenyl)phenol (eugenol); (16) 2,6-dimethoxyphenol (syringol); (17) 2-methoxy-4-propenylphenol (isoeugenol); (18) 3,4-dimethoxyphenol; (19) (E)-2-methoxy-4-(2-propenyl)phenol (*trans*-isoeugenol); (20) 1,2,4-trimethoxybenzene; (21) 4-hydroxy-3-methoxybenzaldehyde (vanillin); (22) 1,2,3-trimethoxy-4-methylbenzene; (23) 1-(4-hydroxy-3-methoxyphenyl)-ethanone (apocynin); (24) 3,4-dimethoxyacetophenone; (25) 3-(4-hydroxy-3-methoxyphenyl)-2-propenoic acid; (26) 1,2-dimethoxy-4-(1-methoxyethenyl)benzene; (27) 2,6-dimethoxy-4-(2-propenyl)-phenol; (28) 4-hydroxy-3,5-dimethoxy-benzaldehyde; (29) 1-(4-hydroxy-3,5-dimethoxyphenyl)-ethanone.

A mixture of high molecular-weight components, particularly phenolic compounds, have been found in pyrolytic degradation products of the complex matrix of lignin and its key building blocks such as syringol (S-lignin marker), guaiacol (G-lignin marker) and p-hydroxyphenyl units (H-lignin marker). S-lignin found in this analysis were syringol (peak 16), 2,6-dimethoxy-4-(2-propenyl)-phenol (peak 27), 4-hydroxy-3,5-dimethoxy-benzaldehyde (peak 28) and 1-(4-hydroxy-3,5-dimethoxyphenyl)-ethanone (peak 29). G-lignin include guaiacol (peak 9), creosol (peak 11), 4-ethyl-2-methoxyphenol (peak 13), 2-methoxy-4-vinylphenol (peak 14), eugenol (peak 15), isoeugenol (peak 17), 3,4-dimethoxyphenol

(peak 18), *trans*-isoeugenol (peak 19), vanillin (peak 21), apocynin (peak 23) and 3-(4-hydroxy-3-methoxyphenyl)-2-propenoic acid (peak 25). Lastly, H-lignin found in Organosolv was 2-methylphenol (peak 10).

According to Kawamoto, pyrolysis of lignin is dependent on the temperature where primary pyrolysis reaction occurs between 200 °C and 400 °C, and secondary pyrolysis reaction between 550 °C and 600 °C [46]. The primary pyrolysis reaction has more methoxyl group-related reactions, whereas the secondary reaction promotes the gasification of catechol reactions.

Primary pyrolysis reaction promotes the production of guaiacol (peak 9), 2-methoxy-4-vinylphenol (peak 14), syringol (peak 16), isoeugenol (peak 17), vanillin (peak 21) and apoycynin (peak 23). Secondary reactions promotes the generation of cresols and catechols, as well as the cracking of side chains of C-C bonds [46]. Mainly primary pyrolysis reactions products have been observed, but only o-cresol (peak 10) was the only secondary pyrolysis reaction product was identified in Figure 33 as the highest temperature was 500 °C.

Figure 21 in Chapter 2 (page 36) shows a general pyrolysis pathway of lignin based on literature adapted from a reference [188]. Key linkages are highlighted for the complex chemical structure of lignin -biphenyl (5-5), β-arylether (β-O-4), phenyl coumaran (β-5 and α-O-4), diarylpropane (β-1). Lignin dehydration starts at 200 °C and followed by the breakdown of β-O-4 linkage, which will generate guaiacol, dimethoxyphenol, dimethoxyacetophenone and trimethoxyacetophenone. The β-O-4 bond cleavage starts between 250 °C and 350 °C. At higher temperatures (370-400 °C), lignin will breakdown the C-C- bond between lignin and structural units [189].

3.3.5.4.   LignoBoost lignin

Lignin, a complex matrix made of different hydroxyl-methoxy-substituted phenol-propane units, showed substantial degradations during the thermal degradation process and produced wide-range of phenol and phenyl-derivatives. Figure 34 presents the Py-GC-MS pyrogram of LignoBoost lignin.
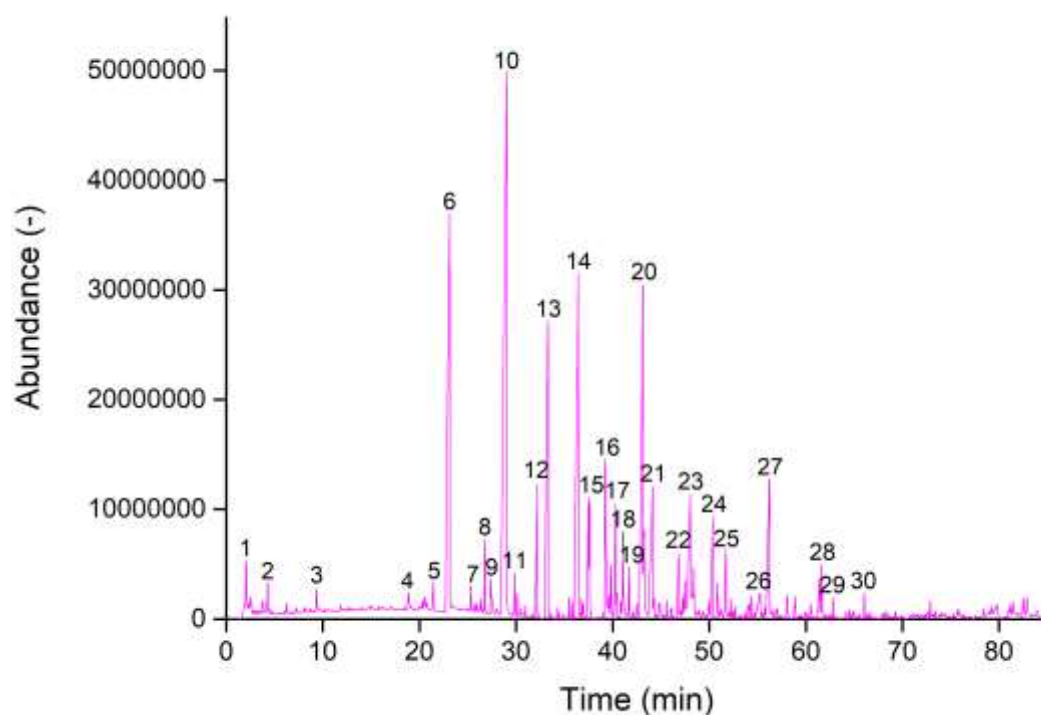
Figure 34. Chromatogram for LignoBoost lignin.
Peak assignment: (1) propyl mercaptan; (2) dimethyl sulphide; (3) furfural; (4) 2-methyl-1-phenylpropene; (5) 2,4-dimethyl-1,3-cyclopentanedione; (6) 2-methoxyphenol (guaiacol) (7) 2-methylpenol (o-Cresol); (8) 2-methoxy-6-methylphenol; (9) 4-methylphenol (p-Cresol); (10) 2-methoxy-4-methylphenol (creosol); (11) 2,5-dimethylphenol; (12) 2,3-dimethoxytoluene; (13) 3,4-dimethoxytoluene; (14) 2-methoxy-4-vinylphenol; (15) 2-methoxy-4-(2-propenyl)phenol (eugenol); (16) 1,2-dihydroxybenzene (catechol); (17) 2-methoxy-4-propenylphenol (isoeugenol); (18) 3-methyl-1,2-benzenediol; (19) 3-methoxy-5-methylphenol; (20) (E)-2-methoxy-4-(2-propenyl)phenol (*trans*-isoeugenol); (21) 4-hydroxy-3-methoxybenzaldehyde (vanillin); (22) 2-methoxy-4-propylphenol; (23) 1-(4-hydroxy-3-methoxyphenyl)-ethanone (apocynin); (24) 1-(4-hydroxy-3-methoxyphenyl)-2-propanone; (25) 4-ethoxy-3-anisaldehyde; (26) 1,6-anhydro-β-D-glucopyranose (levoglucosan); (27) 2-(4-hydroxy-3-methoxyphenyl)acetic acid (homovanillic acid); (28) 2,5-dimethoxybenzeneacetic acid; (29) 6,7-dimethoxy-2-tetralone; (30) ethyl homovanillate

Traces of sulphuric products were found between retention times 0-10 min, including propyl mercaptan (peak 1) and dimethyl sulphide (peak 2). The sulphuric products were derived from the LignoBoost process, which used sulphuric acid in order to increase the yield of the LignoBoost lignin [57]. G-lignin found in LignoBoost lignin include guaiacol (peak 6), 2-methoxy-6-methylphenol

(peak 8), creosol (peak 10), 2-methoxy-4-vinylphenol (peak 14), eugenol (peak 15), isoeugenol (peak 17), *trans*-isoeugenol (peak 20), vanillin (peak 21), apocynin (peak 23), 1-(4-hydroxy-3-methoxyphenyl)-2-propanone (peak 24), homovanillic acid (peak 27) and ethyl homovanillate (peak 30). H-lignin observed in LignoBoost lignin were *o*-cresol (peak 7), *p*-cresol (peak 9) and 2,5-dimethylphenol (peak 11). No S-lignin have been observed in LignoBoost lignin, since the lignin consists out of softwoods (50:50 spruce and pine) as described in section 3.2.1 on page 58. Traces of holocellulose markers have been detected including furfural (peak 3), 2,4-dimethyl-1,3-cyclopentandione (peak 4) and levoglucosan (peak 26).

Organosolv lignin and LignoBoost lignin are very similar, where both have lignin degradation products include guaiacol, creosol, eugenol, isoeugenol, *trans*-isoeugenol and apocynin. However, different delignification processes were utilised in Organosolv and LignoBoost lignin. The Organosolv process used organic solvents with low-boiling point solvents and therefore more holocellulose residues were observed in Organosolv lignin compared to LignoBoost lignin. The LignoBoost process removed most of the holocellulose and small amounts of sulphuric compounds can be found instead. Furthermore, syringol could be found in Organosolv, which was not detected in LignoBoost lignin. As Organosolv lignin was produced from a hardwood rather than a softwood.

3.3.5.5. Pine wood

The pine wood degradation revealed that there were mainly holocellulose and G-lignin products from the pyrogram shown in Figure 35.
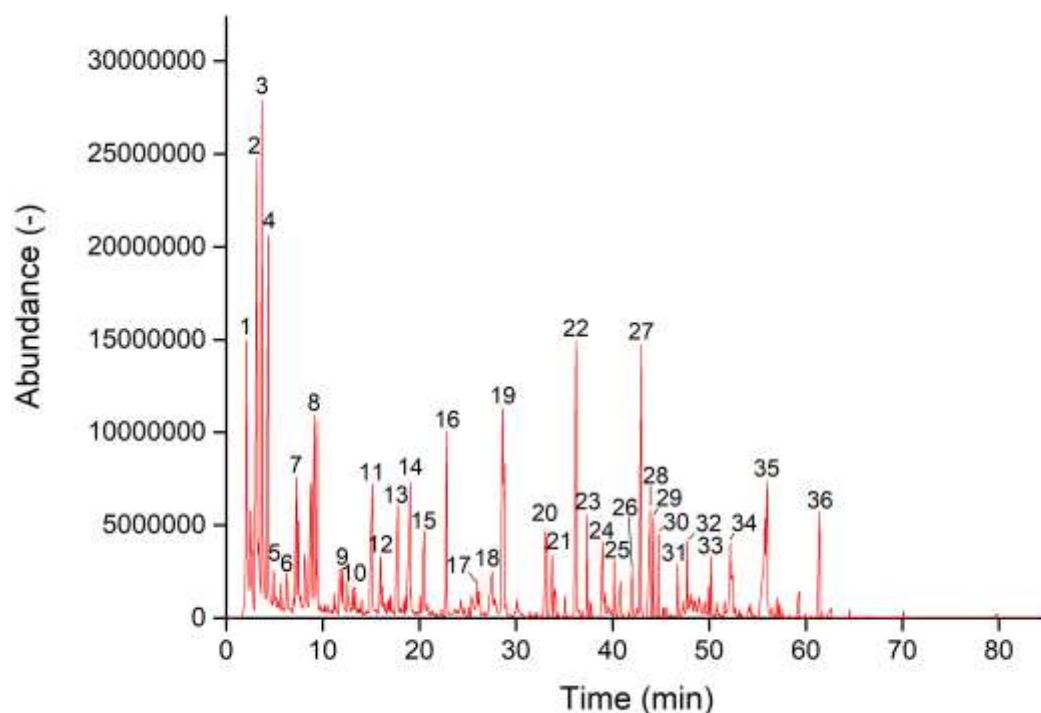
Figure 35. Chromatogram for pine wood.
Peak assignment: (1) 2,3-butanedione; (2) acetic acid; (3) 1-hydroxy-2-propanone (hydroxyacetone); (4) 3-methyl-2-pentanol; (5) methyl pyruvate; (6) 2-propenoic acid, 2-hydroxyethyl ester; (7) 2-methyl-2-butenal; (8) furfural; (9) 1-(acetyloxy)-2-propanone; (10) 4-cyclopenten-1,3-dione; (11) 2-hydroxy-2-cyclopenten-1-one; (12) 2-cyclohexen-1-ol; (13) 2(5H)-furanone; (14) 3,4-dihydro-2-methoxy-2H-pyran; (15) 2-hydroxy-3-methyl-2-cyclopenten-1-one; (16) 2-methoxyphenol (guaiacol); (17) tetrahydro-3-furanol; (18) 5-hydroxy-methyldihydrofuran-2-one; (19) 2-methoxy-4-methylphenol (Creosol); (20) 4-ethyl-2-methoxyphenol; (21) 3-methyl-2,4(3H,5H)-furandione; (22) 2-methoxy-4-vinylphenol; (23) 2-methoxy-4-(2-propenyl)phenol (eugenol); (24) 5-hydroxymethylfurfural; (25) 2-methoxy-4-propenylphenol (isoeugenol); (26) dihydro-5-hydroxy-2(3H)-furanone; (27) (E)-2-methoxy-4-(2-propenyl)phenol (*trans*-isoeugenol); (28) 4-hydroxy-3-methoxybenzaldehyde (vanillin); (29) 6-methoxy-3-methylbenzofuran; (30) Hexamethylbenzene; (31) 3-ethoxy-4-hydroxybenzaldehyde (ethyl vanillin); (32) 1-(4-hydroxy-3-methoxyphenyl)-ethanone (apocynin); (33) 1-(4-hydroxy-3-methoxyphenyl)-2-propanone; (34) 4-(3-hydroxy-1-propenyl)-2-methoxyphenol; (35) 2-(4-hydroxy-3-methoxyphenyl)acetic acid (homovanillic acid); (36) 3-(4-hydroxy-3-methoxyphenyl)-2-propenal

Acidic products were formed via degradation or decomposition derived from mainly hemicellulose, but can also be produced from cellulose, including acetic acid (peak 2), methyl pyruvate (peak 5), 2-propenoic acid, 2-hydroxyethyl ester (peak 6). Cellulose markers found in pine wood were 2,3-butanedione (peak 1) and hydroxyacetone (peak 3). Levoglucosan was observed in the pyrolytic decomposition of pine wood, but not labelled in Figure 35 and can be found in Appendix A on Table

A.5 on page 261. Holocellulose markers found in pine wood were 2-methyl-2-butenal (peak 7), furfural (peak 8), 1-(acetyloxy)-2-propanone (peak 9), 4-cyclopenten-1,3-dione (peak 10), 2-hydroxy-2-cyclopenten-1-one (peak 11), 2(5H)-furanone (peak 13), 3,4-dihydro-2-methoxy-2H-pyran (peak 14), 2-hydroxy-3-methyl-2-cyclopenten-1-one (peak 15), tetrahydro-3-furanol (peak 17), 5-hydroxy-methyldihydrofuran-2-one (peak 18) and 3-methyl-2,4(3H,5H)-furandione (peak 21). Abundant amounts of phenolic compounds from G-lignin markers is found in pine wood including guaiacol (peak 16), creosol (peak 19), 2-methoxy-4-vinylphenol (peak 22), eugenol (peak 23), isoeugenol (peak 25), *trans*-isoeugenol (peak 27), vanillin (peak28), ethyl vanillin (peak 31), apocynin (peak 32), 1-(4-hydroxy-3-methoxyphenyl)-2-propanone (peak 33), 4-(3-hydroxy-1-proppenyl)-2-methoxyphenol (peak 34), homovanillic acid (peak 35) and 3-(4-hydroxy-3-methoxyphenyl)-2-propenal (peak 36). No S-lignin can be found, as pine wood is a softwood. Similar lignin degradation products were found in the literature and confirming the presence of guaiacol, vanillin, isoeugenol, eugenol, apocynin and homovanillic acid as their main products [190, 191]. However, both literature also found coniferyl alcohol which was not observed in this study, as proposed by literature resources.

3.3.5.6.   Wheat straw

Large amounts of low-molecular weight products (C_2-C_4) were found in wheat straw (shown in Figure 36), which are all derived from holocellulose content including 2,3-dihydrofuran (peak 4), propionic acid (peak 7), propanal (peak 8), 2(5H)-furanone (peak 15).
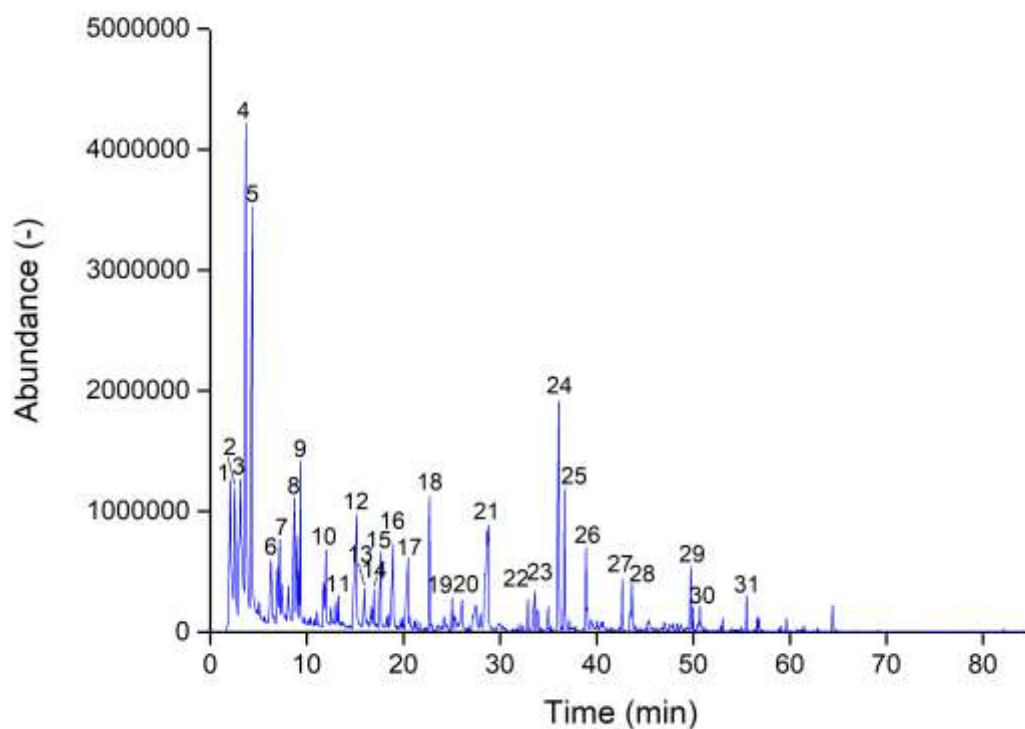
Figure 36. Chromatogram for wheat straw.
Peak assignment: (1) 1-methylcyclopropanemethanol; (2) 3-methylfuran; (3) 3-pentanone; (4) 2,3-dihydrofuran; (5) toluene; (6) 1-penten-3-one; (7) propionic acid; (8) propanal; (9) furfural; (10) 2-furanmethanol; (11) 4-cyclopenten-1,3-dione; (12) 1,2-cyclopentanedione; (13) 2-cyclohexen-1-ol; (14) 3-methyl-2-cyclopenten-1-one; (15) 2(5H)-furanone; (16) 3,4-dihydro-2-methoxy-2H-pyran; (17) 2-hydroxy-3-methyl-2-cyclopenten-1-one; (18) 2-methoxyphenol (guaiacol); (19) 3-ethyl-2-hydroxy-2-cyclopenten-1-one; (20) 3-methyl-1,2-cyclopentanediol; (21) propionic anhydride; (22) 4-ethyl-2-methoxyphenol; (23) dihydro-6-methyl-2H-pyran-3(4H)-one; (24) 4-hydroxy-2-methylacetophenone; (25) 2,3-dihydrobenzofuran; (26) 2,6-dimethoxyphenol (syringol); (27) (E)-2-methoxy-4-(1-propenyl)phenol (trans-isoeugenol); (28) 4-hydroxy-3-methoxybenzaldehyde (vanillin); (29) 3,5-dimethoxyacetophenone; (30) 3,4-dihydro-6-hydroxy-2H-1-benzopyran-2-one; (31) 2,6-dimethoxy-4-(2-propenyl)-phenol
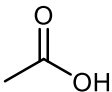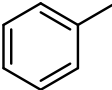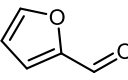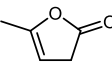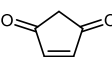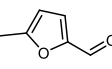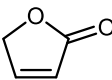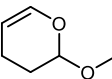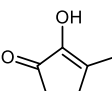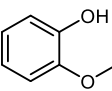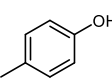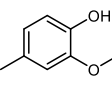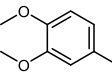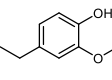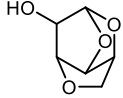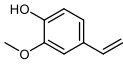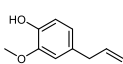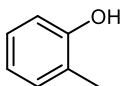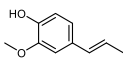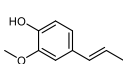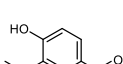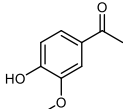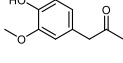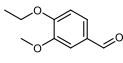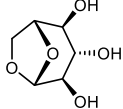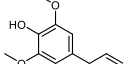
Additional low-molecular weight products can be found in the Appendix A in Table A.6 on page 270, which are not labelled in Figure 36. Furthermore, it can be observed that there are more products observed at earlier resident times (0-30 mins) with the highest peak generated by 2,3-dihydrofuran (peak 4) and toluene (peak 5). From section 3.2.5 on page 63, the most prominent inorganic matter found

in wheat straw was K. Alkali metals, especially K, are well-known catalysts which will initiate cracking reactions during fast pyrolysis and affect the product distribution in the composition of pyrolysis products [192]. This was also confirmed by Evans and Milne, whereby K promotes further decomposition of anhydrosugars (i.e. levoglucosan) into low-molecular products, including acetic and propionic acids (peak 7) [180]. From the pyrolytic decomposition of cellulose and xylan content in the previous sections, mainly holocellulose content are found at earlier resident times. Few lignin markers are found at a later resident time (> 30 mins), including guaiacol (peak 18), 4-ethyl-2-methoxyphenol (peak 22), syringol (peak 26), trans-isoeugenol (peak 27), vanillin (peak 28), 3,5-dimethoxyacetophenone (peak 29), 3,4-dihydro-6-hydroxy-2H-1-benzopyran-2-one (peak 30) and 2,6-dimethoxybenzaldehyde (peak 31). It is also evident that hemicellulose markers are dominant in wheat straw when comparing Figure 32 (xylan) and Figure 36 (wheat straw). Cyclopentanes were found to be the main products in wheat straw, which are derived from hemicellulose. 1,2-Cyclopentanedione (peak 12) is a typical hemicellulose pyrolysis product, which is formed through decomposition and recombination of ring-opened intermediates with C=O groups [186].

A detailed list of all detected components (retention time, name, formula, molecular weights, chemical structure, mass-to-charge ratio (m/z) and key precursor) can be found in Appendix A on page 2, which were all identified using the NIST Mass Spectral Library (2011). The individual products were assigned and categorised into cellulose, hemicellulose, holocellulose, lignin, guaiacol lignin, p-Hydroxyphenyl lignin or syringol lignin. The most abundant compounds found in all feedstock are outlined below in Table 8, where 26 individual components were identified for all studied feedstock.

Table 8. Most abundant components found in most of the feedstock.

Retention Time (min)	Name	Formula	MW	Structure	*m/z*	Key precursor
3.76	acetic acid	$C_2H_4O_2$	60		60.02 (100.0 %), 61.02 (2.2 %)	Holocellulose
4.26	toluene	C_7H_8	92		92.06 (100.0 %), 93.07 (7.6 %)	Lignin
9.39	furfural	$C_5H_4O_2$	96		96.02 (100.0 %), 97.02 (5.4 %)	Holocellulose
11.12	5-methyl-2(3H)-furanone	$C_5H_6O_2$	98		98.04 (100.0 %), 99.04 (5.4 %)	Holocellulose
13.33	4-cyclopenten-1,3-dione	$C_5H_4O_2$	96		96.02 (100.0 %), 97.02 (5.4 %)	Holocellulose
16.08	5-methyl-2-furancarboxaldehyde	$C_6H_6O_2$	110		110.04 (100.0 %), 111.04 (6.5 %)	Cellulose
17.69	2(5H)-furanone	$C_4H_4O_3$	84		84.02 (100.0 %), 85.02 (4.3 %)	Holocellulose
19.06	3,4-dihydro-2-methoxy-2H-pyran	$C_6H_{10}O_2$	114		114.07 (100.0 %), 115.07 (6.5 %)	Holocellulose
20.56	2-hydroxy-3-methyl-2-cyclopenten-1-one	$C_6H_8O_2$	112		112.05 (100.0 %), 113.06 (6.5 %)	Holocellulose
22.75	2-methoxyphenol (Guaiacol)	$C_7H_8O_2$	124		124.05 (100.0 %), 125.06 (7.6 %)	Guaiacol lignin
27.42	4-methylphenol (p-Cresol)	C_7H_8O	108		108.06 (100.0 %), 109.06 (7.6 %)	p-Hydroxyphenyl lignin
28.64	2-methoxy-4-methylphenol (Creosol)	$C_8H_{10}O_2$	138		138.07 (100.0 %), 139.07 (8.7 %)	Guaiacol lignin
31.31	3,4-dimethoxytoluene	$C_9H_{12}O_2$	152		152.08 (100.0 %), 153.09 (9.7 %)	Lignin
32.96	4-ethyl-2-methoxyphenol	$C_9H_{12}O_2$	152		152.08 (100.0 %), 153.09 (9.7 %)	Guaiacol lignin

35.11	1,4:3,6-dianhydro-α-D-glucopyranose	$C_6H_8O_4$	144		144.04 (100.0 %), 145.05 (6.5 %)	Cellulose
36.21	2-methoxy-4-vinylphenol	$C_9H_{10}O_2$	150		150.07 (100.0 %), 151.07 (9.7 %)	Guaiacol lignin
37.30	2-methoxy-4-(2-propenyl)phenol (Eugenol)	$C_{10}H_{12}O_2$	164		164.08 (100.0 %), 165.09 (10.8 %)	Guaiacol lignin
37.99	2-methylphenol (o-Cresol)	C_7H_8O	108		108.06 (100.0 %), 109.06 (7.6 %)	p-Hydroxyphenyl lignin
40.12	2-methoxy-4-propenylphenol (Isoeugenol)	$C_{10}H_{12}O_2$	164		164.08 (100.0 %), 165.09 (10.8 %)	Guaiacol lignin
42.91	(E)-2-methoxy-4-(2-propenyl)phenol (trans-Isoeugenol)	$C_{10}H_{12}O_2$	164		164.08 (100.0 %), 165.09 (10.8 %)	Guaiacol lignin
43.91	4-hydroxy-3-methoxybenzaldehyde (Vanillin)	$C_8H_8O_3$	152		152.05 (100.0 %), 153.05 (8.7 %)	Guaiacol lignin
47.72	1-(4-hydroxy-3-methoxyphenyl)-ethanone (Apocynin)	$C_9H_{10}O_3$	166		166.06 (100.0 %), 167.07 (9.7 %)	Guaiacol lignin
50.16	1-(4-hydroxy-3-methoxyphenyl)-2-propanone	$C_{10}H_{12}O_3$	180		180.08 (100.0 %), 181.08 (10.8 %)	Guaiacol lignin
51.56	4-ethoxy-3-anisaldehyde	$C_{10}H_{12}O_3$	180		180.08 (100.0 %), 181.08 (10.8 %)	Guaiacol lignin
54.74	1,6-anhydro-β-D-glucopyranose (Levoglucosan)	$C_6H_{10}O_5$	162		162.05 (100.0 %), 163.06 (6.5 %), 164.06 (1.0 %)	Cellulose
55.67	2,6-dimethoxy-4-(2-propenyl)phenol	$C_{11}H_{14}O_3$	194		194.09 (100.0 %), 195.10 (11.9 %)	Syringol lignin

Chapter 4
Kinetic and thermodynamic assessment on the thermal degradation of lignocellulosic biomass and biomass constituents

4.1. Introduction

Pyrolysis kinetics are vital to understanding design, selection, feasibility, scaling, and process optimisation, as the understanding in the pyrolytic behaviour can determine the optimum pyrolytic conditions [193]. The thermal decomposition of biomass gives a variety of products, and it is a complex process involving different competitive and concurrent reactions [194]. Determining kinetic parameters is important to target the end-product from thermal decomposition, considering process parameters and feedstock composition. The exact mechanism of biomass pyrolysis is still unclear since the process involves different heterogeneous reactions like breaking of bonds, bond formation, adsorption, desorption, surface/bulk diffusion, nucleation and others [193]. Generally, biomass thermal processing (including pyrolysis and liquefaction) results in chars, liquids, and gases as final products [195]. The activation energy associated with the formation of these products will always be different, and determination of activation energy of biomass thermal decomposition will be helpful to determine the pyrolysis process optimisation [33]. The formation of char and gas depends on heating rates and final temperature. The kinetics obtained at lower heating rates or lower final temperature cannot be directly applied to higher heating or higher temperature [196]. Therefore, the pyrolysis kinetics determined using thermogravimetric analyser (TGA), at relatively low heating rate cannot be directly correlated to the fast pyrolysis process which are carried out at high heating rates [197]. Often these results are extrapolated to fast pyrolysis heating rates, which is significantly higher and could potentially lead to inaccurate results [194]. However, the method can be used to understand the behaviour of various feedstock and its selection.

The pyrolytic decomposition of lignocellulosic biomass can be presumed as one single reaction, which was described by Shafizadeh et al [178]:

Biomass (solid) → Volatiles (gases + tar) + Char (solid residue)
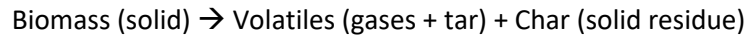
The chemical reaction rate in solid-state is given as:

$$\frac{d\alpha}{dt} = k\ (T)f(\alpha) \tag{4.1.1}$$

Where T is temperature (K) and α is conversion. Therefore, α is defined as:

$$\alpha = \frac{m_i - m}{m_i - m_f} \tag{4.1.2}$$

Where m_i is the initial mass of the sample, m is the mass at a certain time, and m_f is the final mass of the sample.

From equation 4.1.1, k(T) is expressed as Arrhenius equation:

$$k = A_o \exp\left(-\frac{E_a}{RT}\right) \tag{4.1.3}$$

Where k is the reaction rate constant, A_o is the pre-exponential factor (s^{-1}), E_a is the activation energy (kJ mol^{-1}), R is the universal gas constant (8.314 J mol^{-1} K^{-1}) and T is temperature (K).

There are various methods when analysing solid-state kinetic data, including model-fitting and model-free methods. Model fitting methods comprise fitting different models to the data. The model is chosen when it gives the best statistical fit as the model from which the kinetic parameters are calculated [198]. However, the disadvantage of model-fitting methods is their inability to determine the reaction model [199]. Model-free methods are commonly used due to their simplicity, less time-consuming, and the avoidance of errors connected with the choice of kinetic model [200]. The model-free method will require a series of measurements at different heating rates, which must be made for the same sample mass and the same volume flow of the atmospheric gas and their fluctuation could cause errors [198].

Under the model-free method, kinetic parameters can be calculated using two different TGA methods: isothermal and non-isothermal. In the isothermal conversion method, the decomposition measurements are performed at a constant temperature. In contrast, the non-isothermal method is preferred over the isothermal method, as it takes the full temperature range into consideration. The sensitivity and error can be improved if the measurements are performed using various linear heating rates, and the kinetic parameters can be calculated using the isoconversional method [197]. The kinetic parameters based on the TGA measurements were calculated using commonly used approximations developed by Kissinger, Kissinger-Akahira-Sunose and Flynn-Wall-Ozawa [201-203].

The kinetics assessment of biomass thermal decomposition assessment is conducted using TGA under inert atmosphere using different heating rates. The heating rates, final temperature, the flow of carrier gas, retention of volatiles, and presence of inorganics can all influence on the kinetic parameters as well as formation of char and gas [196, 204]. Thus, heating rates also have an impact on the kinetic parameters.

In isothermal methods, the biomass decomposition is performed at a constant temperature, whereas non-isothermal methods utilise various temperature ranges with different heating rates [205]. Using different heating rates, kinetic parameters can be calculated using isoconversional methods. The most common non-isothermal and isoconversional models for calculating kinetic parameters are Kissinger, Kissinger-Akahira-Sunose (KAS), Flynn-Wall-Ozawa (FWO), expressed by equations 4.1.4, 4.1.5 and 4.1.6 respectively [201, 206, 207].

Kissinger is a model-free and non-isothermal method where E_a value does not take conversion into consideration and assumes that there will be constant E_a. Instead, the E_a value can be calculated from the slope, which is equal to $-E_a/R$.

$$\ln\left(\frac{\beta}{T_m^2}\right) = \ln\left(\frac{A_o R}{E_a}\right) - \frac{E_a}{RT_m} \qquad (4.1.4)$$

Where T_m is the peak temperature (K) of the derivative thermogravimetric (DTG) curve, and β (K min^{-1}) is the heating rate.

KAS is also a non-isothermal method to calculate the kinetic energy, where $g(\alpha)$ is the mechanism function. The plot of $\ln(\beta_i/T_\alpha^2)$ versus $1/T$ is used to calculate the E_a, which gives a straight line.

$$\ln\left(\frac{\beta_i}{T_\alpha^2}\right) = \ln\left(\frac{AR}{E_a g(\alpha)}\right) - \frac{E_a}{RT_\alpha} \qquad (4.1.5)$$

The FWO is also a non-isothermal method to obtain E_a by using the linear relationship of $\ln(\beta)$ versus $1/T$.

$$\ln(\beta_i) = \ln\left(\frac{AE_a}{Rg(\alpha)}\right) - 5.331 - 1.052\frac{E_a}{RT_\alpha} \qquad (4.1.6)$$

The advantages and disadvantages of Kissinger, KAS and FWO are summarised in Table 9. A summary table on how the E_a and A_o is obtained is also shown in section 4.2.3 in Table 10 on page 94.

Table 9. Advantages and disadvantages of Kissinger, KAS and FWO kinetic analysis [208-211].

Method	Equation	Advantages	Disadvantages
Kissinger	$\ln\left(\frac{\beta}{T_m^2}\right) = \ln\left(\frac{A_o R}{E_a}\right) - \frac{E_a}{RT_m}$	The simplest method to estimate E_a.	E_a is assumed to be constant and does not take different conversion into account.
			Does not possess the sufficient sensitivity to differentiate between single and multi-step kinetics
Kissinger-Akahira-Sunose	$\ln\left(\frac{\beta_i}{T_\alpha^2}\right) = \ln\left(\frac{AR}{E_a g(\alpha)}\right) - \frac{E_a}{RT_\alpha}$	More accurate way of estimating E_a compared with Kissinger as it uses the function of conversion	The derivation of this method uses an oversimplified temperature integral approximation.
			Does not apply on processes when cooling occurs.
Flynn-Wall-Ozawa	$\ln(\beta_i) = \ln\left(\frac{A E_a}{R g(\alpha)}\right) - 5.331 - 1.052 \frac{E_a}{RT_\alpha}$	Allows estimating the E_a over an entire conversion range at different heating rates	May lead to significant errors of E_a, especially if conducting a series of runs at different heating rates
			Does not apply on processes when cooling occurs.

To understand the mechanism of pyrolytic decomposition and also the energy associated with thermal decomposition of biomass constituents the thermodynamic parameters such as enthalpy change (ΔH), Gibbs free energy change (ΔG), and entropy change (ΔS) were also calculated using equations 4.1.7, 4.1.8 and 4.1.9 respectively, which have been previously calculated as explained by [166, 212, 213]. Gibbs free energy (ΔG) is calculated using the peak temperature (T_m), Boltzmann constant (k_B) and Planck constant (h).

$$\Delta H = E_a - RT \tag{4.1.7}$$

$$\Delta G = E_a + RT_m \ln\left(\frac{k_B T_m}{hA}\right) \tag{4.1.8}$$

$$\Delta S = \frac{\Delta H - \Delta G}{T_m} \tag{4.1.9}$$

This chapter summarises studies on the thermal decomposition of the model constituents, including cellulose, xylan (hemicellulose) and Organosolv lignin. This is then compared to three feedstock, including pine wood, wheat straw and LignoBoost lignin, through its thermal behaviour using TGA. The thermal decomposition is then further determined by the kinetic and thermodynamic parameters. Reaction kinetics calculations presented in this chapter were introduced to explore thermal decomposition of selected biomass (Chapter 3) and reveal the best thermal degradation conditions for liquefaction and hydro-pyrolysis experiments carried out with the application of molten salts.

4.2. Methodology

4.2.1. Materials and feedstock preparation

Biomass feedstock and model components used for kinetic and thermodynamic assessment including, pine wood, wheat straw, LignoBoost lignin, cellulose, xylan and Organosolv lignin, were described and characterised in the previous chapter (Chapter 3 in 3.2.1.1 and 3.2.1.2 on page 58).

4.2.2. Thermogravimetric analysis

Biomass samples were carried out using thermogravimetric analyser (TGA) for the thermal decomposition reaction kinetics, which are also described in section 3.2.3 on page 59. All feedstock were pyrolysed under inert atmosphere with a flow rate of 30 ml min^{-1} and at the following heating rates of 2, 5, 10, 25, 50 and 75 °C min^{-1}. The samples were initially maintained at 40 °C for 5 min to purge unwanted air. The samples were heated at 5 °C min^{-1} from 40 °C to 105 °C, which was maintained for 10 min to remove moisture from biomass. Different heating rates (2, 5, 10, 25, 50 and 75 °C min^{-1}) were applied from 105 °C to 750 °C. The final temperature (750 °C) was held for 15 min, and cooled down to 40 °C at a cooling rate of 10 °C min^{-1}. From the TGA mass loss profiles, the first derivative were calculated and used to assess the kinetic parameters of thermal decomposition of the biomass feedstock.

4.2.3. Kinetic parameters

A set of equations are presented in Table 10, which shows how the activation energy values were obtained and were applied for the assessment of kinetics during thermal degradation of all feedstock under pyrolytic conditions. The Kissinger's activation energy values are obtained from the slope of the plot of $\ln\left(\frac{\beta}{T_m^2}\right)$ against $\frac{1}{T_m}$. The kinetic plot of Kissinger-Akahira-Sunose (KAS) between $\ln\left(\frac{\beta}{T_m^2}\right)$ against $\frac{1}{T}$ will give a slope used for the activation energy calculation. The activation energy of Flynn-Wall-Ozawa (FWO) is calculated from plotting a slope between $\ln(\beta)$ and $\frac{1}{T}$.

Table 10. Kissinger, KAS and FWO equation to obtain activation energy values.

Method	Expression	Obtaining E_a plot
Kissinger	$ln\left(\dfrac{\beta}{T_m^2}\right) = ln\left(\dfrac{A_o R}{E_a}\right) - \dfrac{E_a}{RT_m}$	$ln\left(\dfrac{\beta}{T_m^2}\right)$ vs $\dfrac{1}{T_m}$
Kissinger-Akahira-Sunose (KAS)	$ln\left(\dfrac{\beta}{T^2}\right) = ln\left(\dfrac{AR}{E_a g(\alpha)}\right) - \dfrac{E_a}{RT_\alpha}$	$ln\left(\dfrac{\beta}{T_m^2}\right)$ vs $\dfrac{1}{T}$
Flynn-Wall-Ozawa (FWO)	$ln(\beta_i) = ln\left(\dfrac{AE_a}{Rg(\alpha)}\right) - 5.331 - \dfrac{1.052 E_a}{RT_a}$	$ln(\beta_i)$ vs $\dfrac{1}{T}$

4.2.4. Thermodynamic parameters

The thermodynamic parameters were calculated from equations 4.1.7, 4.1.8 and 4.1.9 as described in section 4.1 on page 87.

$$\Delta H = E_a - RT \tag{4.1.7}$$

$$\Delta G = E_a + RT_m \ln\left(\frac{k_B T_m}{hA}\right) \tag{4.1.8}$$

$$\Delta S = \frac{\Delta H - \Delta G}{T_m} \tag{4.1.9}$$

In which the peak temperature (T_m) is of DTG curve is in Kelvins, Boltzmann's constant (k_B) is 1.381 x 10^{-23} J K^{-1} and Planck's constant (h) is 6.626 x 10^{-34} J s^{-1}.

4.3. Results and Discussion

4.3.1. Thermal analysis of biomass constituents

In order to fully understand the decomposition of biomass, the model components cellulose, xylan and Organosolv lignin has been subjected to thermogravimetric analysis (TGA) at a temperature of 750 °C at a heating rate of 25 °C min^{-1}. The other heating rates including 2, 5, 10, 50 and 75 °C min^{-1} for all biomass feedstock are shown in Appendix B on page 280. The derivative thermogravimetric (DTG) and mass loss curve profiles of the model components are shown in Figure 37.
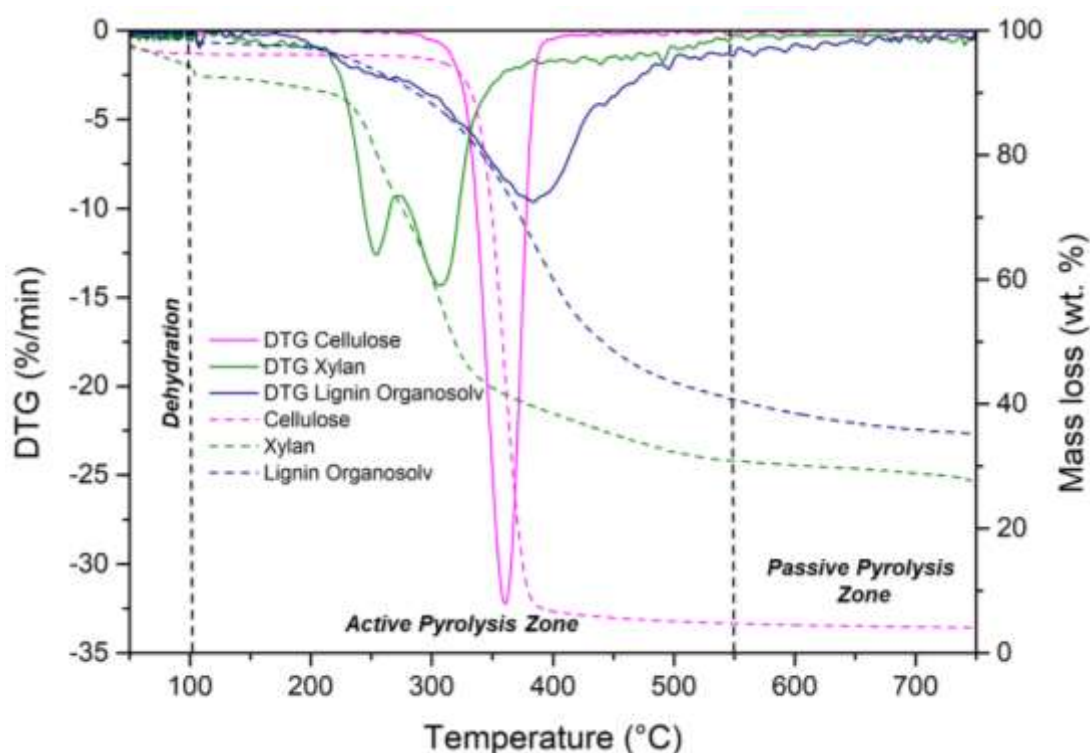
Figure 37. DTG curve and mass loss profile of model components cellulose, xylan and Organosolv lignin at a heating rate of 25 °C min^{-1}.

The profile is split into three regions, which are dehydration, active pyrolysis and passive pyrolysis zones [164]. The dehydration zone occurs from ambient temperature to 105 °C. The active pyrolysis zone occurs between 105-550 °C, and anything above 550 °C is the passive pyrolysis zone.

Cellulose degraded rapidly within the active pyrolysis zone compared to other feedstock, and decomposed between 287-416 °C. Cellulose consists of long biopolymers of D-glucose units with no branches and has a good thermal stability, and therefore decomposed at a narrow temperature range [170]. The narrow thermal decomposition is typical when it comes to linear polymers [214]. Cellulose's peak temperature was observed at 361 °C. Most of its feedstock was fully decomposed and had the lowest char content of 3.8 wt. %.

Xylan started its initial decomposition at 162 °C and decomposed into two stages. Hemicellulose is known to be thermally unstable, which explains why it started decomposing at a much lower temperature [204]. The first visible peak is observed at 254 °C. It was also observed by Shen et al [140] and Quan et al [170] were there were two peaks decomposed, and described that the first peak was occurring due to the cleavage of glycosidic bonds and the decomposition of the side-chain structure (such as 4-*O*-methylglucuronic unit) where acetic acid starts to form [215]. The second decomposition curve at 307 °C was described as the fragmentation of other depolymerised units to form furan (including furfural and 5-hydroxymethylfurfural) [215]. Xylan decomposed fully in the active pyrolysis zone and had a char content of 23.5 wt. %.

Organosolv lignin degraded over a wider temperature between 183 and 513 °C with a peak temperature found at 385 °C. A char content of 34.3 wt. % was found for the Organosolv lignin sample, which was the highest char content observed when compared to cellulose and xylan char yields. The Organosolv lignin can be considered one of the pure lignins, as no DTG shoulder was observed, that could indicate some possible traces of carbohydrates or extractives originating from the biomass material used for the lignin production [216].

Figure 38 shows the DTG profile all biomass and model components, which gives a good overview how biomass thermally degrades and how this can be compared with the biomass-derived model components. Furthermore, the shape of the DTG profile is reflective to the lignocellulosic content of the biomass.
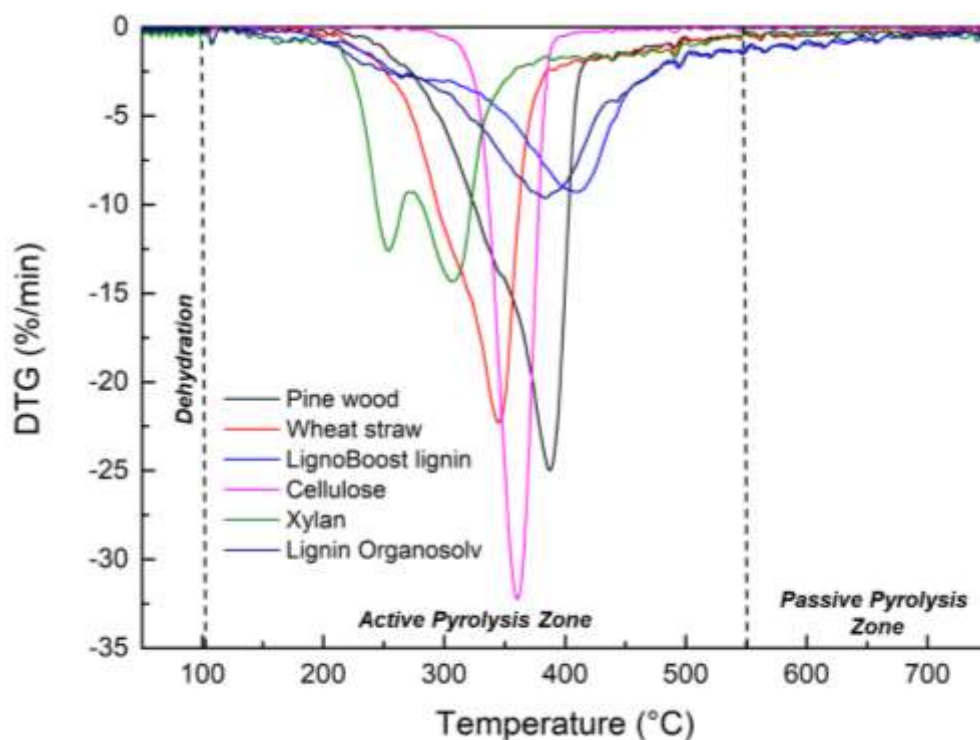
Figure 38. DTG curves of all biomass and biomass-derived model components at a heating rate of 25 °C min⁻¹.

All studied feedstock and model components were fully thermally decomposed up to the temperature of 550 °C that marked the end of the active pyrolysis zone. The passive pyrolysis zone involved only the char formation and carbonisation with release of non-condensable gases. The study revealed that xylan was one of the first feedstock to fully decompose starting at 162 °C and finishing at 388 °C. Similarly, wheat straw's decomposition was observed between 185 and 390 °C and was found with a peak temperature of 345 °C. This indicates that the thermal behaviour of wheat straw was similar to that of xylan's decomposition and explained that the DTG curve shifted towards a lower temperature range. The DTG curve of pine wood shifted towards a higher temperature range between 230 and 419 °C, which could be explained by a higher cellulose and lignin content found. As described above, cellulose and Organosolv lignin decomposed at a higher temperature. From the DTG profiles, both Lignoboost and Organosolv lignin decomposed over a wider temperature range with a peak temperature difference of 20 °C. Lignin Organosolv is an industrial lignin with traces of impurities, which shifted to a lower temperature when compared to LignoBoost lignin.

4.3.2.   Kinetic analysis

Model-free methods – Kissinger, Kissinger-Akahira-Sunose (KAS) and Flynn-Wall-Ozawa (FWO) – have been used to calculate the kinetic parameters of all feedstock from the data obtained using TGA experiments. These include the calculations of activation energy, pre-exponential factor and regression coefficient (R^2), which are presented in Table 11, Table 12 and Table 13 respectively.

Table 11. Kinetic parameters using the Kissinger method summarised of all feedstock with activation energy, pre-exponential factors and regression coefficients.

Feedstock	Activation Energy (kJ mol^{-1})	Pre-exponential factor (min^{-1})	R^2
Pine wood	183.49	$4.37e^{14}$	0.999
Wheat straw	172.30	$5.13e^{14}$	0.999
LignoBoost lignin	166.29	$7.11e^{12}$	0.983
Cellulose	155.87	$7.51e^{12}$	0.994
Xylan	165.27	$1.16e^{15}$	0.975
Lignin Organosolv	115.35	$1.09e^{9}$	0.980

Table 12. Kinetic parameters using the KAS method summarised with activation energy, pre-exponential factors and regression coefficients.

Conversion (α)	Pine wood			Wheat straw			LignoBoost lignin			Cellulose			Xylan			Lignin Organosolv		
	E_a	A_o	R^2	E_a	A_o	R^2	E_a	A_o	R^2	E_a	A_o	R^2	E_a	A_o	R^2	E_a	A_o	R^2
0.1	164.23	2.15×10^{15}	0.997	154.03	9.22×10^{14}	0.991	116.95	8.41×10^{10}	0.992	170.18	6.49×10^{14}	0.999	-	-	-	115.46	5.97×10^{10}	0.990
0.2	167.85	5.60×10^{14}	0.999	167.95	2.60×10^{15}	0.996	154.22	6.95×10^{12}	0.992	168.17	2.23×10^{14}	0.997	141.11	1.23×10^{14}	0.986	139.38	7.12×10^{11}	0.996
0.3	170.70	3.09×10^{14}	0.999	176.73	5.16×10^{15}	0.998	178.26	1.12×10^{14}	0.992	167.14	1.30×10^{14}	0.998	174.03	4.07×10^{16}	0.985	144.17	3.37×10^{11}	0.905
0.4	173.82	2.35×10^{14}	0.999	173.86	1.15×10^{15}	0.998	216.73	2.62×10^{16}	0.973	164.17	5.56×10^{13}	0.997	172.33	6.74×10^{15}	0.996	226.02	4.64×10^{17}	0.985
0.5	174.34	1.29×10^{14}	0.999	176.37	9.65×10^{14}	0.999	287.43	1.14×10^{20}	0.392	162.82	3.42×10^{13}	0.996	183.49	2.16×10^{16}	0.992	506.42	3.14×10^{37}	0.981
0.6	174.45	7.68×10^{13}	0.999	196.20	1.88×10^{16}	0.996				163.31	3.10×10^{13}	0.997	167.03	2.47×10^{13}	0.732			
0.7	173.55	3.64×10^{13}	0.999	346.81	1.02×10^{25}	0.899				161.48	1.73×10^{13}	0.996						
0.8										162.45	1.64×10^{13}	0.996						
0.9										161.74	1.42×10^{13}	0.997						
Average	171.28	5.00×10^{14}	0.999	198.85	1.46×10^{24}	0.982	190.72	2.28×10^{19}	0.868	164.61	1.30×10^{14}	0.997	167.60	1.38×10^{16}	0.938	226.29	6.27×10^{36}	0.971

Table 13. Kinetic parameters using the FWO method summarised with activation energy, pre-exponential factors and regression coefficients.

Conversion (α)	Pine wood			Wheat straw			LignoBoost lignin			Cellulose			Xylan			Lignin Organosolv		
	E_a	A_o	R^2	E_a	A_o	R^2	E_a	A_o	R^2	E_a	A_o	R^2	E_a	A_o	R^2	E_a	A_o	R^2
0.1	173.46	5.19×10^{21}	0.997	162.96	2.08×10^{21}	0.991	126.07	2.02×10^{17}	0.993	180.08	1.80×10^{21}	0.999	-	-	-	124.63	1.45×10^{17}	0.991
0.2	177.65	1.52×10^{21}	0.999	177.38	6.53×10^{21}	0.996	164.52	2.10×10^{19}	0.993	178.26	6.44×10^{20}	0.998	149.75	2.60×10^{20}	0.987	149.44	2.07×10^{18}	0.996
0.3	180.83	8.98×10^{20}	0.999	186.45	1.38×10^{22}	0.999	189.17	3.77×10^{20}	0.99.	177.34	3.85×10^{20}	0.998	183.13	9.49×10^{22}	0.987	152.99	7.59×10^{17}	0.904
0.4	184.21	7.18×10^{20}	0.999	183.82	3.22×10^{21}	0.998	228.15	9.64×10^{22}	0.975	174.44	1.67×10^{20}	0.997	181.75	1.69×10^{22}	0.996	237.12	1.60×10^{24}	0.987
0.5	184.94	4.12×10^{20}	0.999	186.52	2.81×10^{21}	0.999	299.87	4.92×10^{26}	0.412	173.16	1.04×10^{20}	0.997	193.20	5.73×10^{22}	0.993	518.24	1.20×10^{44}	0.982
0.6	185.21	2.53×10^{20}	0.999	206.62	5.74×10^{22}	0.997				173.71	9.53×10^{19}	0.997	177.50	7.70×10^{19}	0.755			
0.7	184.50	1.24×10^{20}	0.999	358.91	4.14×10^{31}	0.905				171.95	5.41×10^{19}	0.997						
0.8										173.00	5.20×10^{19}	0.997						
0.9										180.74	1.44×10^{20}	0.990						
Average	181.54	1.30×10^{21}	0.999	208.95	5.91×10^{30}	0.984	201.56	9.85×10^{25}	0.873	175.85	3.80×10^{20}	0.997	177.07	3.39×10^{22}	0.943	236.48	2.39×10^{43}	0.972

E_a values are reported in kJ mol^{-1}, A_o are reported in min^{-1}

The conversion values (α) of all feedstock were not normalised to 1, as to observe on how each biomass was devolatilised and how this can be compared with the biomass-derived model components. All calculated regression coefficients (R^2) outlined in Table 11, Table 12 and Table 13 corresponds with the linear plots in Figure 39, Figure 40 and Figure 41. Furthermore, Figure 42 displays a graphical comparison of the activation energy versus conversion values using KAS and FWO methods for all feedstock to give a better overview.
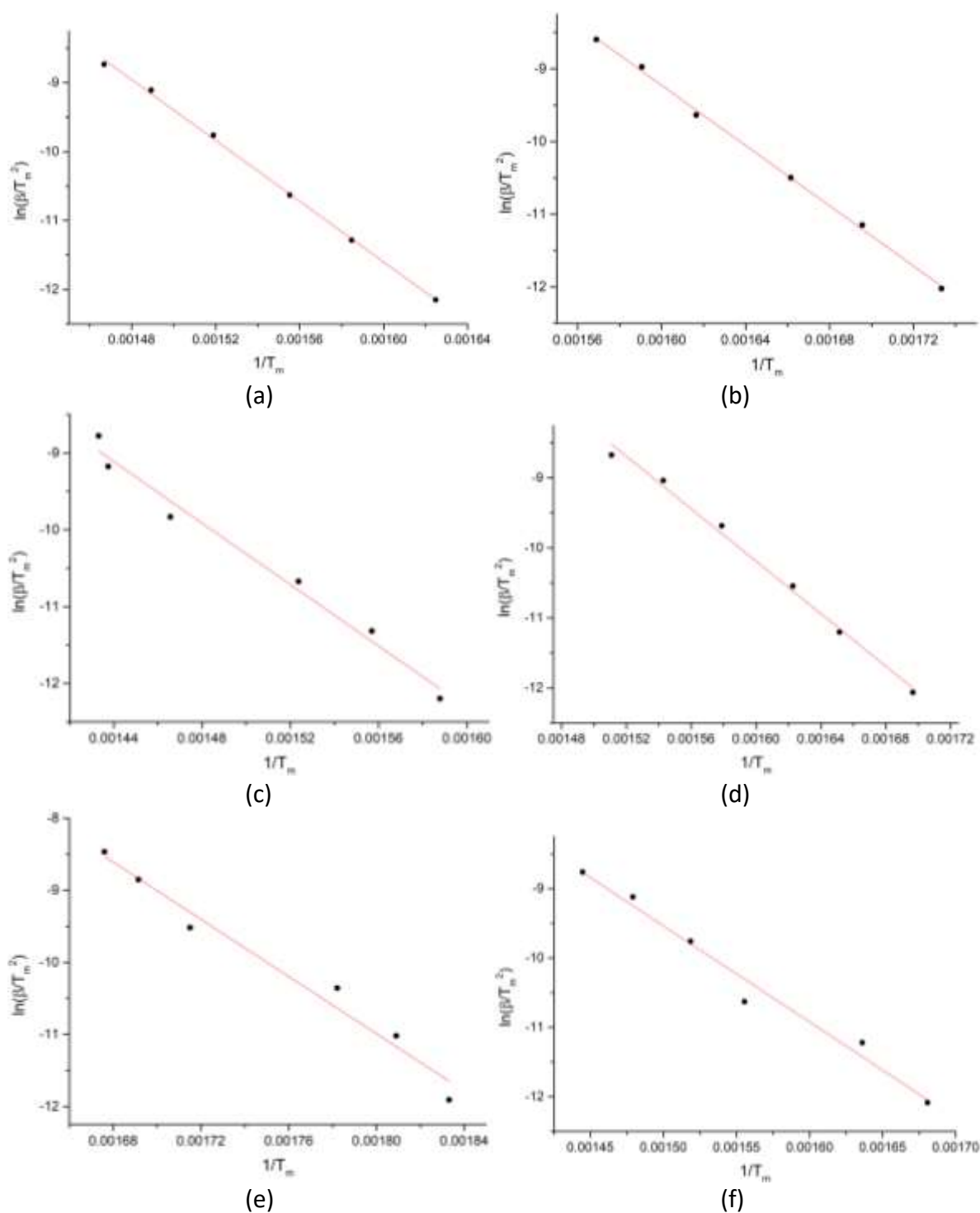
Figure 39. Kissinger method showing a plot of ln(β/Tm²) vs 1/Tm of (a) pine wood, (b) wheat straw, (c) LignoBoost lignin, (d) cellulose, (e) xylan and (f) Organosolv lignin.
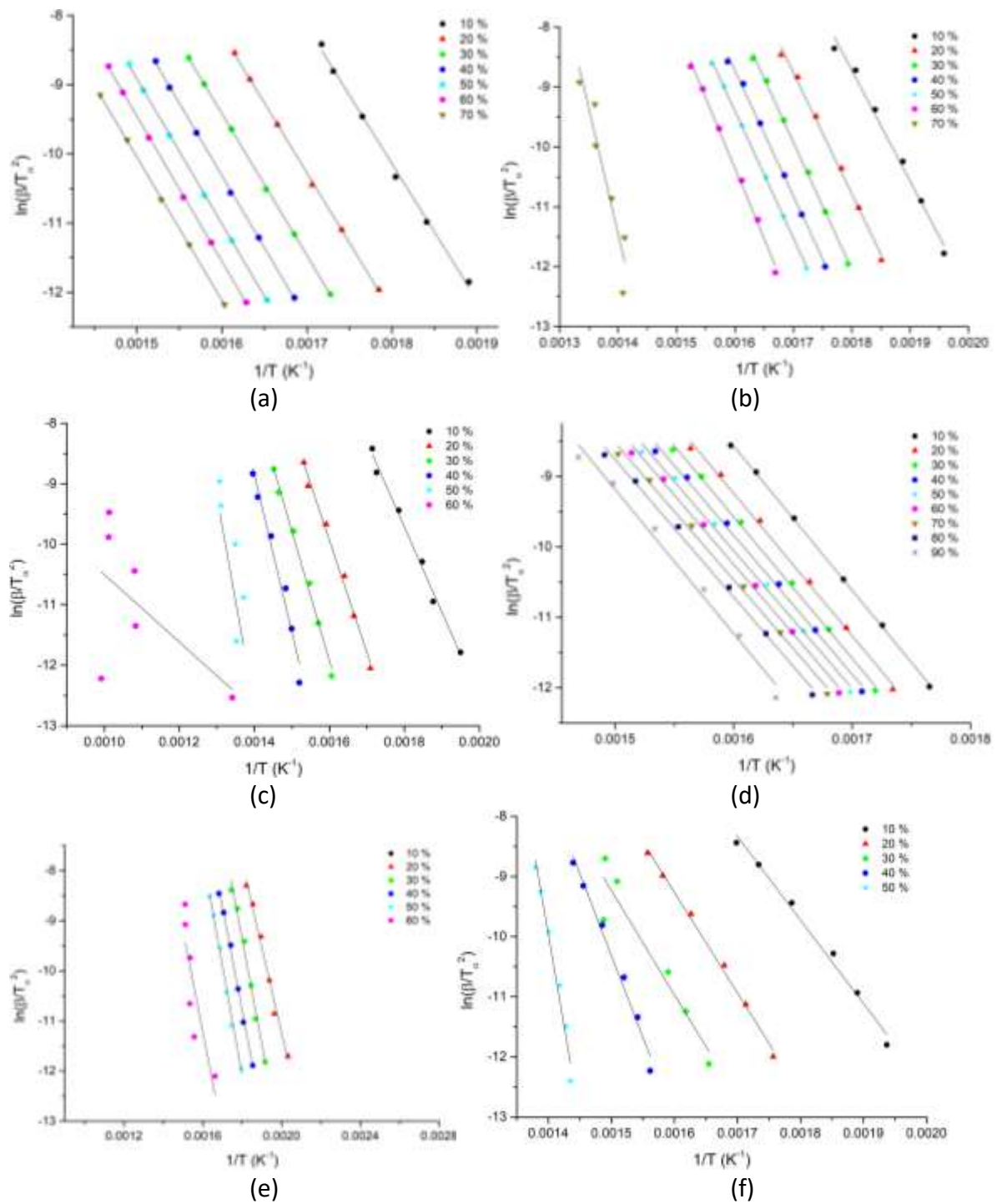
Figure 40. KAS method showing a plot of $\ln(\beta/T_\alpha^2)$ vs 1/T of (a) pine wood, (b) wheat straw, (c) LignoBoost lignin, (d) cellulose, (e) xylan and (f) Organosolv lignin.
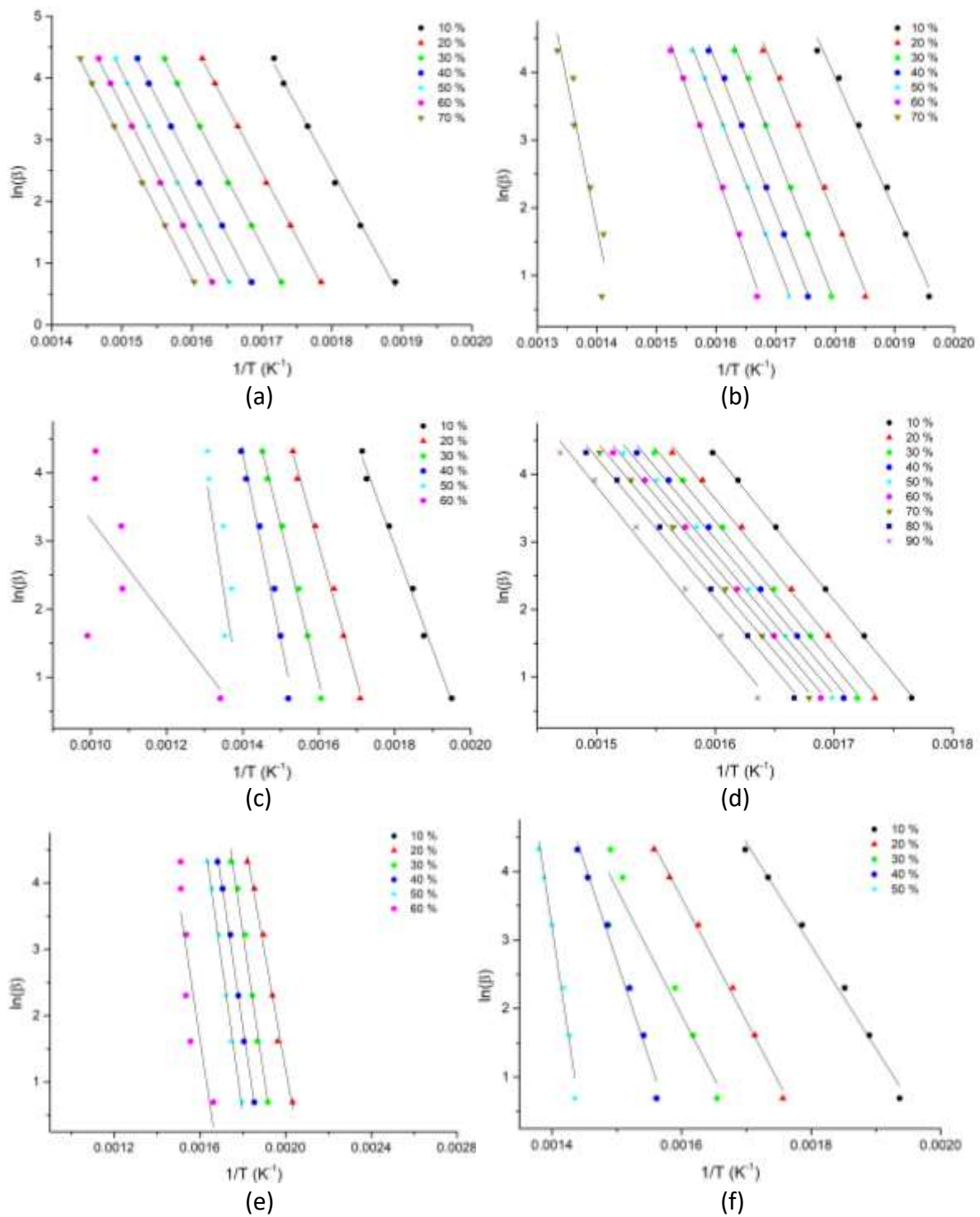
Figure 41. FWO method showing a plot of ln(β) vs 1/T of (a) pine wood, (b) wheat straw, (c) LignoBoost lignin, (d) cellulose, (e) xylan and (f) Organosolv lignin.

`
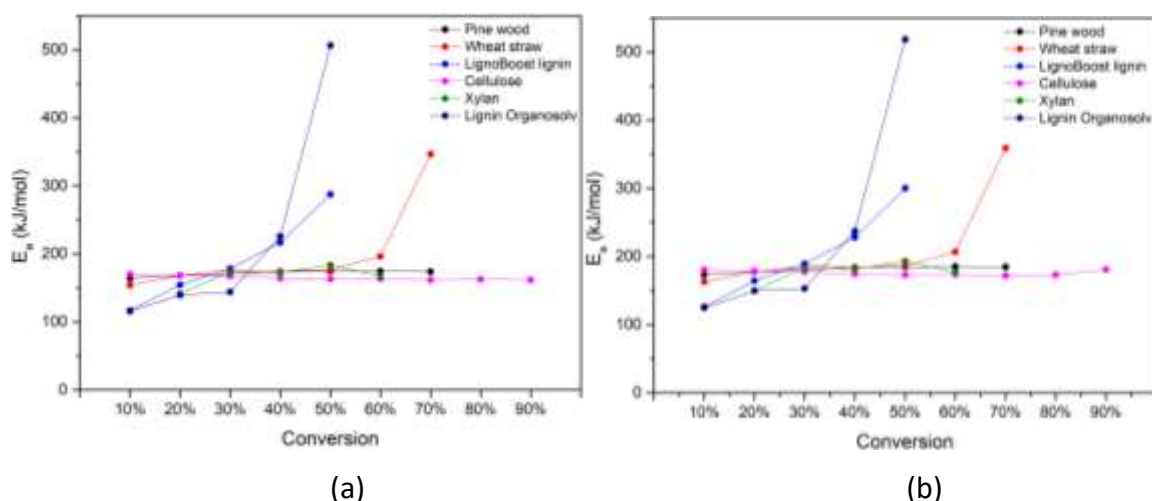
Figure 42. Activation energy vs conversion of all feedstock using (a) KAS method and (b) FWO method.

The activation energy values using the Kissinger method are 183.49 kJ mol^{-1} (pine wood), 172.30 kJ mol^{-1} (wheat straw), 166.29 kJ mol^{-1} (LignoBoost lignin), 155.87 kJ mol^{-1} (cellulose), 165.27 kJ mol^{-1} (xylan) and 155.35 kJ mol^{-1} (Organosolv lignin). The Kissinger method was a simple way to calculate the activation energy using different heating rates, which was a recommendation of the International Confederation for Thermal Analysis and Calorimetry (ICTAC) [211]. However, Kissinger method only assumed that the activation energy values were the same throughout the whole thermal degradation process. The method also assumed that there was only one T_m, which was challenging when xylan was observed with two major DTG peaks. This also explains why xylan's R^2 value was slightly lower and the linear plot was not "fitting". Therefore, KAS and FWO methods were utilised which were more detailed as the activation energy will vary at each α.

The average activation energy values using the KAS method was 171.28 kJ mol^{-1} (pine wood), 198.85 kJ mol^{-1} (wheat straw), 190.72 kJ mol^{-1} (LignoBoost lignin), 164.61 kJ mol^{-1} (cellulose), 167.60 kJ mol^{-1} (xylan) and 226.29 kJ mol^{-1} (Organosolv lignin). The FWO method's calculated average activation energy values were 181.54 kJ mol^{-1} (pine wood), 208.95 kJ mol^{-1} (wheat straw), 201.56 kJ mol^{-1} (LignoBoost lignin), 175.85 kJ mol^{-1} (cellulose), 177.07 kJ mol^{-1} (xylan) and 236.48 kJ mol^{-1} (Organosolv lignin). As observed in Table 12 and Table 13, the results of xylan conversion at 10 % are missing due to poor regression coefficient.

At the beginning of the degradation (α = 0.1), the activation energies (both KAS and FWO) of all feedstock were particularly low as the dehydration stage was occurring. At this stage, simple sugars are being decomposed at lower degradation temperature. Both LignoBoost and Organosolv lignins were difficult to pyrolytically decompose due to their complex structure when compared to cellulose and xylan. It can also be seen that at α = 0.5, Organosolv lignin required the highest activation energy

with 506.42 kJ mol^{-1} (KAS method) and 518.24 kJ mol^{-1} (FWO method) in order to break down its aromatic structures. Similarly, LignoBoost lignin required more energy of 287.43 kJ mol^{-1} (KAS method) and 299.87 9 kJ mol^{-1} (FWO method). Furthermore, a higher value of activation energy indicates a slower reaction [166]. At α = 0.7, wheat straw's activation energy was observed at 346.81 kJ mol^{-1} and 358.91 kJ mol^{-1} for KAS and FWO respectively. At α = 0.7 (460 °C), most of the hemicellulose and lignin was thermally degrading and could explain an increase in the activation energy in wheat straw [213]. Overall, an increase in activation energy of all studied feedstock showed with increasing α, which corresponded that the decomposition was not a single state reaction.

When comparing the activation energy values from Kissinger and the two isothermal methods (KAS and FWO), the cellulose values seemed to be lower when comparing the activation energy values reported by Di Blasi [217]. Di Blasi described an overall trend of 192-250 kJ mol^{-1} and 154-200 kJ mol^{-1} for cellulose and hemicellulose, respectively. However, the activation energy values of xylan from KAS and FWO methods seemed to be in the range from the same literature. Whereas, Zhu and Zhong [218] reported activation energy values of 168.61, 126.31 and 87.19 kJ mol^{-1} for cellulose, hemicellulose and lignin respectively. The activation energy values of cellulose were also in good agreement of Zhu and Zhong's [218] reported value. The reported activation energy values of hemicellulose and lignin were lower in the literature, since the values were only calculated in the temperature range of 200 to 400 °C. In contrast, the calculated values in this chapter considered the whole degradation from ambient to 750 °C which resulted in a higher activation energy. Chen et al reported a lower average of 155.83 kJ mol^{-1} (KAS) and 157.97 kJ mol^{-1} (FWO) for pine wood as well [219].

Mahmood et al [220] used KAS and FWO methods to calculate the activation energy values of wheat straw and described similar thermal behaviour as observed here in this chapter. An increase in the activation energy values was observed between $0.6 \leq \alpha \leq 0.7$, which are also stated in Table 12 and Table 13 [220]. The results for all feedstock obtained from KAS and FWO values were quite similar to each other and had negligible differences. Cortes and Bridgwater [197] also found that the kinetic parameters using KAS, FWO, Vyazovkin and Friedman methods were comparable and had minimal differences.

4.3.3. Thermodynamic analysis

The thermodynamic parameters, including enthalpy (ΔH), Gibbs free energy (ΔG) and entropy (ΔS) for the three biomass are obtained from equation 4.1.7, 4.1.8 and 4.1.9 (on page 94) presented in Table 14 (KAS method) and Table 16 (FWO method). The thermodynamic results of biomass constituents are presented in Table 15 (KAS method) and Table 17 (FWO method).

Table 14. KAS thermodynamic results of lignocellulosic biomass summarised including enthalpy, Gibbs free energy and entropy values.

Conversion (α)	Pine wood			Wheat straw			LignoBoost lignin		
	ΔH	ΔG	ΔS	ΔH	ΔG	ΔS	ΔH	ΔG	ΔS
0.1	159.52	170.20	-16.24	149.54	159.52	-16.29	112.29	122.16	-14.55
0.2	162.89	173.66	-16.47	163.30	173.40	-16.85	149.19	159.62	-16.01
0.3	165.54	176.50	-16.65	171.81	182.38	-17.20	172.81	184.07	-16.82
0.4	168.60	179.53	-16.80	168.76	179.47	-17.18	210.97	223.12	-17.92
0.5	169.04	179.98	-16.88	171.04	182.09	-17.33	281.28	294.45	-19.89
0.6	168.98	180.11	-16.94	191.00	201.87	-17.96			
0.7	168.04	179.10	-16.97	340.81	354.22	-22.02			
0.8									
0.9									
Average	166.09	177.01	-16.71	193.75	204.71	-17.83	153.23	164.49	-16.95

ΔH and ΔG are reported in kJ mol^{-1}, ΔS is reported in J mol^{-1}

Table 15. KAS thermodynamics results of biomass constituents summarised including enthalpy Gibbs free energy and entropy values.

Conversion (α)	Cellulose			Xylan			Lignin Organosolv		
	ΔH	ΔG	ΔS	ΔH	ΔG	ΔS	ΔH	ΔG	ΔS
0.1	170.16	175.82	-8.94	-	-	-	114.02	120.37	-10.05
0.2	166.95	173.55	-10.81	136.77	146.07	-16.25	136.98	144.44	-11.95
0.3	165.92	172.61	-10.76	169.51	179.41	-17.43	141.62	149.20	-12.09
0.4	162.94	169.43	-10.65	167.47	177.79	-17.45	222.45	232.24	-15.75
0.5	162.81	168.34	-8.52	178.62	188.86	-17.91	504.96	516.94	-18.55
0.6	163.30	168.81	-8.51	161.78	171.70	-17.93			
0.7	159.00	166.74	-12.61						
0.8	162.45	167.74	-8.41						
0.9	159.20	166.87	-12.69						
Average	163.64	169.99	-10.21	162.83	172.76	-17.39	224.01	232.64	-13.68

ΔH and ΔG are reported in kJ mol^{-1}, ΔS is reported in J mol^{-1}

Table 16. FWO thermodynamic results of lignocellulosic biomass summarised including enthalpy, Gibbs free energy and entropy values.

Conversion (α)	Pine wood			Wheat straw			LignoBoost lignin		
	ΔH	ΔG	ΔS	ΔH	ΔG	ΔS	ΔH	ΔG	ΔS
0.1	168.76	180.78	-18.28	158.46	169.69	-18.32	121.41	129.55	-11.94
0.2	172.69	184.80	-18.53	172.73	184.05	-18.89	159.49	169.59	-15.62
0.3	175.67	187.99	-18.71	181.53	193.33	-19.19	183.72	190.92	-10.76
0.4	178.99	191.26	-18.87	178.72	190.71	-19.23	222.40	232.13	-14.28
0.5	179.63	191.92	-18.95	181.19	193.55	-19.39	293.72	305.21	-17.50
0.6	179.74	192.24	-19.02	201.42	213.55	-20.03			
0.7	178.99	191.41	-19.06	352.91	367.51	-23.97			
0.8									
0.9									
Average	176.35	188.63	-18.77	203.85	216.06	-19.43	164.92	174.10	-13.84

ΔH and ΔG are reported in kJ mol^{-1}, ΔS is reported in J mol^{-1}

Table 17. FWO thermodynamic results of biomass constituents summarised including enthalpy, Gibbs free energy and entropy values.

Conversion (α)	Cellulose			Xylan			Lignin Organosolv		
	ΔH	ΔG	ΔS	ΔH	ΔG	ΔS	ΔH	ΔG	ΔS
0.1	180.06	187.02	-11.00	-	-	-	120.07	130.85	-16.75
0.2	177.05	184.92	-12.88	145.42	155.87	-18.27	144.47	155.81	-17.86
0.3	176.12	184.10	-12.82	178.61	189.66	-19.46	147.71	159.31	-18.16
0.4	173.21	180.98	-12.71	176.89	188.41	-19.49	231.62	244.65	-20.61
0.5	173.15	180.02	-10.59	188.32	199.74	-19.96	512.33	530.13	-27.35
0.6	173.70	180.55	-10.58	172.25	183.32	-20.00			
0.7	169.47	178.51	-14.69						
0.8	173.00	179.59	-10.48						
0.9	178.19	187.22	-14.93						
Average	174.88	182.54	-12.30	172.30	183.40	-19.43	231.24	244.15	-20.15

ΔH and ΔG are reported in kJ mol^{-1}, ΔS is reported in J mol^{-1}

All enthalpy values of all feedstock were positive, which indicated that the process was endothermic, and an additional heat source was required to initiate a pyrolytic reaction. The average enthalpy values from KAS method were 166.09 kJ mol^{-1} (pine wood), 193.75 kJ mol^{-1} (wheat straw), 153.23 kJ mol^{-1} (LignoBoost lignin), 163.64 kJ mol^{-1} (cellulose), 167.60 kJ mol^{-1} (xylan) and 224.01 kJ mol^{-1} (Organosolv lignin). The calculated enthalpy values using the FWO method were 176.35 kJ mol^{-1} (pine wood), 203.85 kJ mol^{-1} (wheat straw), 164.92 kJ mol^{-1} (LignoBoost lignin), 174.88 kJ mol^{-1} (cellulose), 177.07 kJ mol^{-1} (xylan) and 231.24 kJ mol^{-1} (Organosolv lignin). The calculated positive enthalpy values have shown that the pyrolytic thermal degradation reactions were endothermic and absorbed the energy in order to break down complex chemical structures of model components and biomass samples. Overall, the calculated enthalpy values do not differ from calculated activation energies. The difference between activation energy and enthalpy values is that the reaction reflects on the possibility of a pyrolysis reaction occurring. If the activation energy and the enthalpy values have a small difference, it means that product formation is favourable [213]. For both KAS and FWO values, a small difference of approximately ~ 5 kJ mol^{-1} was observed in all feedstock, except for LignoBoost lignin with a difference of 36 and 37.5 kJ mol^{-1} from KAS and FWO methods respectively. This indicated the potential energy barrier will be high in order to achieve product formation.

The Gibbs free energy describes the energy available from the feedstock upon the pyrolysis process. The calculated Gibbs free energy from the KAS method were 177.01 kJ mol^{-1} (pine wood), 204.71 kJ mol^{-1} (wheat straw), 164.49 kJ mol^{-1} (LignoBoost lignin), 169.99 kJ mol^{-1} (cellulose), 172.76 kJ mol^{-1} (xylan) and 232.64 kJ mol^{-1} (Organosolv lignin). For the FWO method, the average Gibbs free energy values were 188.63 kJ mol^{-1} (pine wood), 216.06 kJ mol^{-1} (wheat straw), 174.10 kJ mol^{-1} (LignoBoost lignin), 182.54 kJ mol^{-1} (cellulose), 183.40 kJ mol^{-1} (xylan) and 244.15 kJ mol^{-1} (Organosolv lignin). All the positive Gibbs free energy values indicated that the reaction is not spontaneous, which will equire additional heating as the reaction continued [221].

The entropy indicates the physical change and the chemical reactivity. A low value or negative entropy means that the reaction system will have little chemical reactivity and will reach thermal equilibrium after pyrolysis [221]. All calculated entropy values from both KAS and FWO methods for all feedstock were found to be negative, indicating that the reaction was moving from a disorderly state to an orderly state or getting closer to thermodynamic equilibrium [222]. The average entropy values using the KAS method were -16.71 J mol^{-1} (pine wood), -17.83 J mol^{-1} (wheat straw), -16.95 J mol^{-1} (LignoBoost lignin), -10.24 J mol^{-1} (cellulose), -17.39 J mol^{-1} (xylan) and -13.68 J mol^{-1} (Organosolv lignin). The average entropy value from FWO method were -18.77 J mol^{-1} (pine wood), -19.86 J mol^{-1} (wheat straw), -13.84 J mol^{-1} (LignBoost lignin), -12.30 J mol^{-1} (cellulose), -19.43 J mol^{-1}

(xylan) and -20.15 J mol^{-1} (Organosolv lignin). However, the entropy values of wheat straw, Lignoboost lignin, cellulose and Organosolv lignin decreased significantly at the end of the reaction. An increase in entropy change corresponded to an increased reactivity and more disorder in the structure of the biomass [223].

Chapter 5
Hydrothermal liquefaction of lignocellulosic biomass

5.1. Introduction

The selected lignocellulosic biomass was chosen to undergo thermochemical processing, specifically hydrothermal liquefaction (HTL). This chapter focused on the impact of the temperature of LignoBoost lignin and pine wood and how this affected the HTL product distribution (gases, liquids and chars). From the previous studies [86-88, 90], it was found that liquefaction using lignocellulosic biomass at a processing temperature of 300 °C is the optimum temperature to produce the maximum bio-crude yield. However, different processing temperatures might be preferred depending on the type of lignocellulosic biomass used and might not necessarily yield the maximum amount of bio-crude at 300 °C. Therefore, this chapter will concentrate on the processing of LignoBoost lignin and pine wood at different processing temperatures of 275, 300 and 325 °C. A mass balance is included to observe which lignocellulosic biomass and processing temperature will yield the most bio-crude.

This chapter also focused on the characterisation of the bio-products obtained from HTL. Particular attention was paid to the aqueous phase, as this often involves in complicated characterisation in the Gas Chromatography-Mass Spectrometry (GC-MS). Complicated sample preparation using standard derivatisation or extraction methods are commonly used before injecting into the GC-MS. Sample preparation including silylation require a complete water removal or chloroformates before derivatisation [224]. Literature review was conducted to observe common compounds found in the aqueous phase obtained from HTL. Standard characterisation (without any complicated sample preparation) will be injected in the GC-MS to detect the compounds found. Novel technique using High-Performance Liquid Chromatography (HPLC) was used to characterise the aqueous phase. Comparisons were made with the GC-MS and HPLC to see whether any undetected compounds (by GC-MS) were found in the HPLC.

5.2. Methodology

5.2.1. Materials

5.2.1.1. Biomass feedstock

All biomass, including LignoBoost lignin, pine wood and wheat straw, described in section 3.2.1.2 on page 58 were used in the HTL experimental work reported in this chapter. The biomass used in all HTL experimental run was in powdered form (below 0.25 mm) – as described in section 3.2.2 on page 58.

5.2.1.2. Solvents for the product separation and recovery

Acetone (C_3H_6O) (CAS: 67-64-1) 99% specified laboratory reagent (SLR) reagent grade was procured from Fisher Scientific UK Ltd and used for the HTL product separation and recovery of bio-crude. Acetone was also used remove any remaining residues on the 300 ml batch reactor.

5.2.1.3. Carboxylic acids, lignin and holocellulose markers, and alcohol for high performance liquid chromatography

For high performance liquid chromatography (HPLC) studies of the HTL aqueous phase chemical composition, the reference materials used were carboxylic acids, holocellulose markers, lignin markers and one alcohol marker. Carboxylic acids including formic acid (CH_2O_2) (CAS: 64-18-6), acetic acid ($C_2H_4O_2$) (CAS: 64-19-7), propionic acid ($C_3H_6O_2$) (CAS: 79-09-4) and levulinic acid ($C_5H_8O_3$) (CAS: 123-76-2), were all purchased from Sigma-Aldrich Ltd. Holocellulose markers were all acquired through Sigma-Aldrich Ltd, which were furfural ($C_5H_4O_2$) (CAS: 98-01-1) and 5-methylfurfural ($C_6H_6O_2$) (CAS: 620-02-0). Lignin markers used from Sigma-Aldrich Ltd were guaiacol ($C_7H_8O_2$) (CAS: 90-05-1) and 4-ethyl-2-methoxyphenol (4-ethylguaiacol) ($C_9H_{12}O_2$) (CAS: 2785-89-9). Whilst, methanol (CH_4OH) (CAS: 67-56-1) was acquired from Fisher Scientific UK Ltd.

5.2.2. Experimental set-up

Hydrothermal liquefaction (HTL) experiments were performed in a high-pressure 300 ml stainless steel (T316) Parr® Instrument Company (Moline, IL, USA) 5521 compact stirred batch autoclave reactor (see Figure 43).

Figure 43. 300 ml stainless steel (T316) Parr® 5521 compact batch autoclave reactor (left) with Parr® 4848 reactor controller (right).

The reactor design was equipped with gas inlet and outlet valves, a pressure gauge, a rupture disc and a J-type thermocouple (presented below in Figure 44).
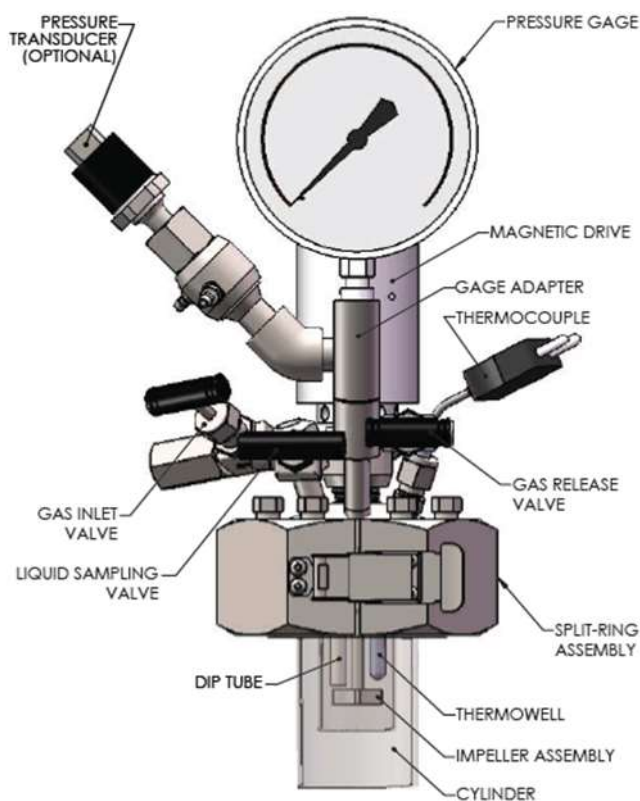
Figure 44. Parr batch reactor diagram.
[Public resource [225] – Image licence CC BY 4.0]

The reactor was fitted with a magnetic stainless steel (T316SS) stirrer designed to stir up to 1700 rpm and was equipped with a cooling sleeve. A turbine type four-blade impeller was used on the magnetic stirrer. The seal of the reactor was fitted with a PTFE flat gasket, which was rated to go up to 350 °C and 200 bar, as well as 6 compression bolts to ensure that there the reactor was sealed correctly. An alloy 600 rupture disc (Fike® Corporation, Blue Springs, MO, USA) was in place and was rated to go up to 207 bar at 22 °C. It was taken into consideration that the rupture disc recommended pressure should not exceed 90 % of its rating when heated from 22 to 500 °C. The temperature and pressure were measured and regulated using the Parr® 4848 Reactor Controller, which was connected to both the thermocouple and gas connection. The temperature and pressure were recorded throughout the experiment using a data-logging program. The 4848 Reactor Controller was also built with a high temperature built alarm. If the reactor surpasses the maximum temperature or pressure, a high limit reset will be triggered, which will prevent power from going to the heater as a safety measure.

Prior to experiments, a series of leak tests were performed. The reactor was pressurised with under inert (nitrogen) atmosphere to 25 bar and left for over an hour. A test run to 300 °C was also run using

deionised water and initially pressurised with nitrogen to 30 bars. A data log of the test run is presented in Figure 45.
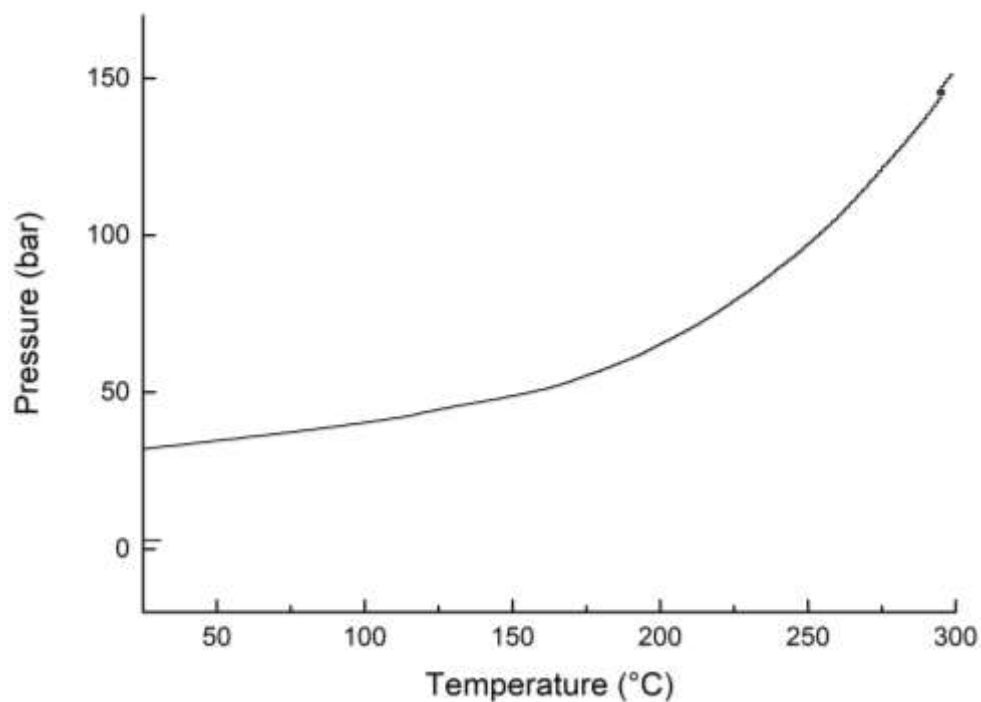
Figure 45. Data recorded for the HTL test run carried out with water only.

5.2.3. Experimental procedure

All hydrothermal liquefaction (HTL) experiments were conducted in a high-pressure 300 ml batch reactor. Approximately 1 g of biomass was placed in a Satorius MA35 moisture analyser to determine the moisture content, which was dried at 105 °C for 15 min. 10 g of feedstock and approximately 50 ml of deionised water (depending on the moisture of the feedstock) was weighed to reach a 1:5 biomass-to-solvent ratio. Three initial experiments to test the biomass and four additional experiments at different temperatures were carried out as outlined in Table 18.

Table 18. List of HTL experiment runs.

Experimental Run	Feedstock	Residence Time (min)	Reaction Temperature (°C)	Initial pressure (bar)
1	Pine wood	15	325	10
2	LignoBoost lignin	15	325	10
3	Wheat straw	15	325	10
4	LignoBoost lignin	15	300	10
5	LignoBoost lignin	15	275	10
6	Pine wood	15	300	10
7	Pine wood	15	275	10

Before each HTL experiment, the reactor was sealed and purged three times with nitrogen to ensure an inert atmosphere and weighed using a KERN D5 scale (maximum weight of 8000.00 g). An initial pressure of approximately 10 bar was introduced and weighed again. The reactor was then connected to the Parr 4848 Reactor Controller to set the desired temperature. The reactants inside the reactor were mixed using a magnetic stirrer at approximately 850 rpm and heated at the set-point temperature. Once the reactor had reached the desired temperature, the temperature was maintained at a residence time of 15 min. At the end of the reaction, the reactor controller and magnetic stirrer were switched off and cooled down to room temperature. Temperature and pressure were recorded using a data-logging program throughout the experimental run to ensure that it remained within the liquefaction region of the water-phase diagram.

5.2.4. Product recovery

A schematic diagram of how the HTL products were recovered is presented in Figure 46. After cooling and before opening the reactor, the pressure was recorded and the reactor was weighed to measure the total weight of the products (including gases, liquids and solids). Through the gas outlet, the gases were sampled in a one-litre Tedlar sampling gas bag. The remaining gases were purged safely using a vent system within the extraction compartment where the high-pressure reactor was placed. The weight of the reactor was recorded (liquid and solids) using the KERN D5 scale and the reactor was then opened afterwards. Water-soluble/aqueous fraction and char were carefully collected and

separated using a separation funnel using Whatman Type 1 filter paper (55 mm diameter) and a vacuum pump. The aqueous fraction was separated from the char and filtrate. Acetone was added to extract the organic phase (bio-crudes) from the char and filtrated. Acetone was then evaporated from the bio-crude and acetone at 40 °C, which was left with a very thick, viscous layer. The now-emptied reactor was weighed again to consider the losses. The wet filter paper was dried overnight at a low temperature of 40 °C and weighed afterwards to consider the losses.
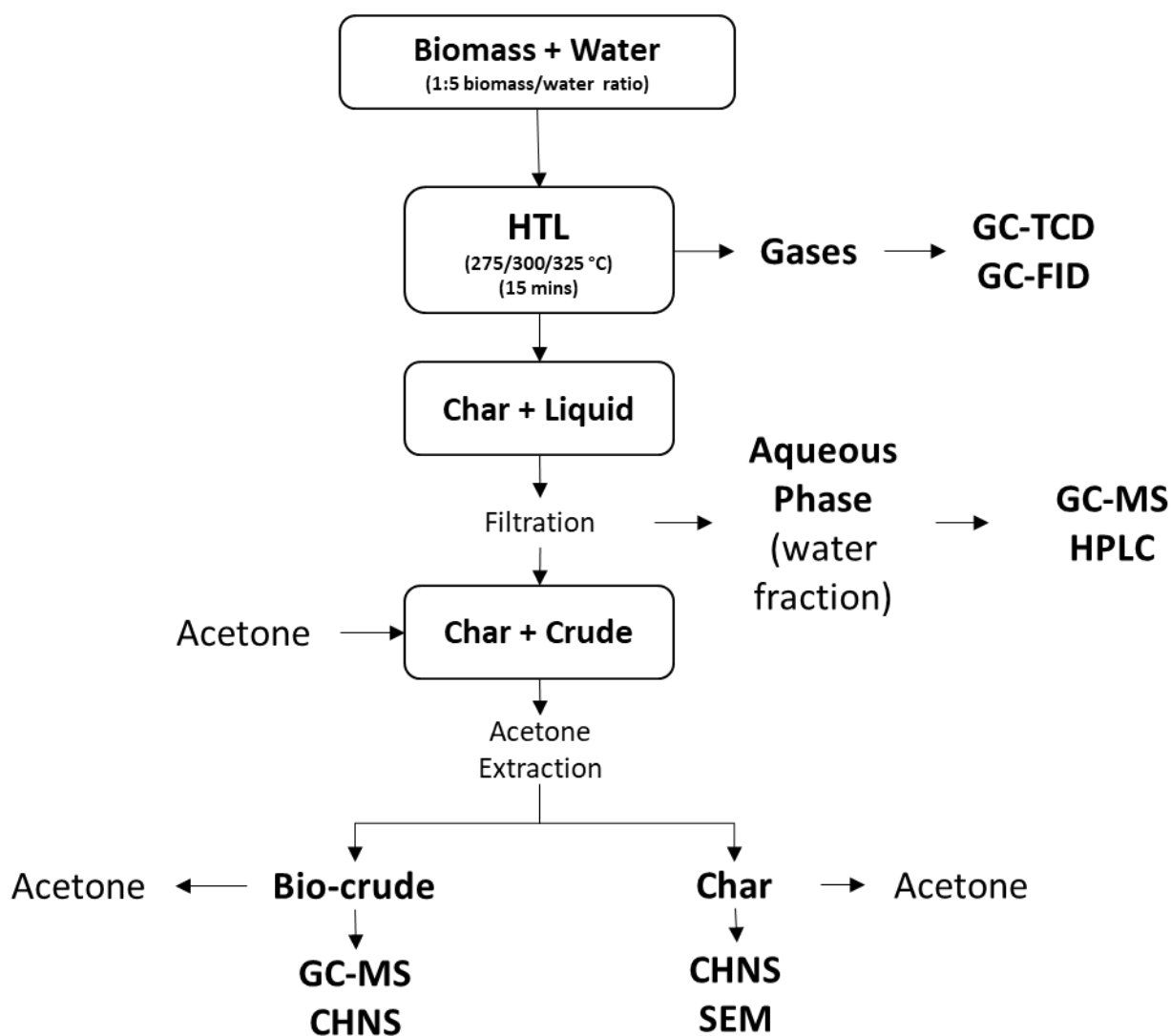
Figure 46. Product recovery after HTL experiments.

The following equations were used to calculate the product yields:

$$Y_{char}\ (\%) = \frac{W_{char}}{W_{biomass+water}} \times 100 \tag{5.2.1}$$

$$Y_{aqueous\ phase}(\%) = \frac{W_{aqueous\ phase}}{W_{biomass+water}} \times 100 \tag{5.2.2}$$

$$Y_{organic\ phase} = \frac{W_{organic}}{W_{biomass+water}} \times 100 \tag{5.2.3}$$

$$Y_{gases} = 100 - Y_{char} - Y_{aqueous\ phase} - Y_{organic\ phase} \tag{5.2.4}$$

5.2.5.   Gas Analysis

Gas products were analysed using a Shimadzu GC 2014 gas chromatograph. Permanent gases (hydrogen, nitrogen, oxygen and carbon monoxide) were separated on a molecular sieve column (2 m length, 2 mm diameter and 60-80 mesh) and analysed using a thermal conductivity detector (TCD). Hydrocarbon gases (C_1 to C_4) and carbon dioxide were separated on a Hayesep column (2 m length, 2 mm diameter and 80-100 mesh) and analysed using a flame ionisiation detector (FID). Using a gas-tight syringe, 0.5 ml of each sample was injected at 60 °C. Both TCD and FID detectors were set at 220 °C during the analysis. The column oven was set at 80 °C and ramped at a heating rate of 10 °C min^{-1} to 180 °C, which is held at 3 min.

5.2.6.   Elemental analysis of char and bio-crude

Carbon (C), hydrogen (H), nitrogen (N) and sulphur (S) content were analysed and improved by using the confidence intervals.

5.2.6.1.   Char analysis

All char and bio-crude samples were subjected to a ThermoFisher Scientific Flash 2000 Organic Elemental Analyser. Approximately 2.5 mg was analysed six times to ensure that the samples analysed were homogenous and combusted in excess oxygen at a maximum temperature of 900 °C. An average of five samples were taken where the results were reported at a 95 % confidence interval, using the following equation:

$$\bar{x} \pm \frac{ts}{\sqrt{n}} \tag{5.2.5}$$

Where x̄ is the sample mean, t is Student's t factor which is 2.78 (see Appendix C on page 284), s is the sample standard deviation, and n is the number of measurements/samples.

5.2.6.2. Bio-crude analysis

A 3.5 mm absorbent disc was inserted in a tin capsule and tared. Approximately 2 µl of the bio-crude (dissolved in GC-grade acetone (1:5 vol/vol)) was absorbed onto the disc. The prepared samples were left in a low-temperature oven at 40 °C to ensure all acetone was evaporated. The samples were weighed along with vanadium pentoxide (V_2O_5) and combusted at 900 °C.

5.2.6.3. Heating values and energy recovery

Carbon (C), hydrogen (H) and oxygen (O) content analysed from the elemental analyser were used to calculate the heating values of char and bio-crudes generated from the hydrothermal liquefaction (HTL) experiments using the Dulong's formula:

$$HHV \ (MJ \ kg^{-1}) = 0.3383C + 1.442\left(H - \frac{O}{8}\right) \tag{5.2.6}$$

The following energy recovery calculation for bio-crude was used:

$$Energy \ recovery \ (\%) = \frac{HHV_{bio-crude} \times Y_{bio-crude}}{HHV_{feedstock}} \tag{5.2.7}$$

5.2.7. Gas Chromatography-Mass Spectrometry analysis

The chemical components present in the HTL-derived bio-crude and aqueous phase samples were analysed by a gas chromatography-mass spectrometry (GC-MS) using a Shimadzu GC-MS-QP2010 system. A representative sample of bio-crude was dissolved in GC-grade acetone (1:100 vol/vol). Each sample (1 µl) was injected onto the GC column using an AOC-20i Autoinjector and the injector port was maintained at 300 °C. Helium was used as a carrier gas at a flow rate of 25 ml min^{-1}, and after injection and sample devolatilization, volatiles were split with set-up ratio of 25:1. All devolatilised

products were separated using the DB-5 (silica) capillary column (30 m length, 0.25 mm internal diameter, and 0.25 μm film thickness). The oven was programmed with the following temperature program: 5 °C min^{-1} from 45 °C up to 280 °C, which was held for 2.25 min at the final temperature of 280 °C. Separated components were individually identified in the MS detector with ionisation electron energy at 70 eV. The MS detector was operated in the molecular mass spectra detection range of *m/z* = 45-300. Peak assignments for individual components were based on the National Institute of Standards and Technology (NIST) 2010 MS library, taking into consideration best matches based on fragmentation patterns.

5.2.8. Aqueous phase analysis

The aqueous phase obtained from HTL experiments was analysed using the high-performance liquid chromatography (HPLC) using Shimadzu Prominence-i LC-2030. Prior injection, each aqueous phase sample was filtered using a Fisherbrand PTFE 0.2 μm syringe filter. 5 μl of the sample was injected into the Restek Ultra Aqueous C18 Column (250 x 4.6 mm, 5 μm particle size) equipped with a Restek Trident cartridge (10 x 4.0 mm) and filter (4 mm, 2.0 μm) which was selected as it was able to easily detect organic and carboxylic acids (see Figure 47). 0.005 M sulphuric acid mobile phase in deionised water was used at a flowrate of 1 ml min^{-1} and at 30 °C. The ultraviolet (UV) detector was set at 207 nm, as it gives a better overall absorption.

The following approach for the determination of individual carboxylic acids (formic, acetic, propionic and levulinic acids), holocellulose markers (furfural and 5-methylfurfural), lignin markers (guaiacol and 4-ethyl-2-methoxyphenol), and alcohol (methanol) were applied for the determination of chemical components in aqueous phases from HTL bio-liquids.

1) Carboxylic acids (formic, acetic, propionic and levulinic acids) were injected individually, which was to establish the retention time (for ultra the aqueous C18 column) and as a representative liquid chromatogram (LC).
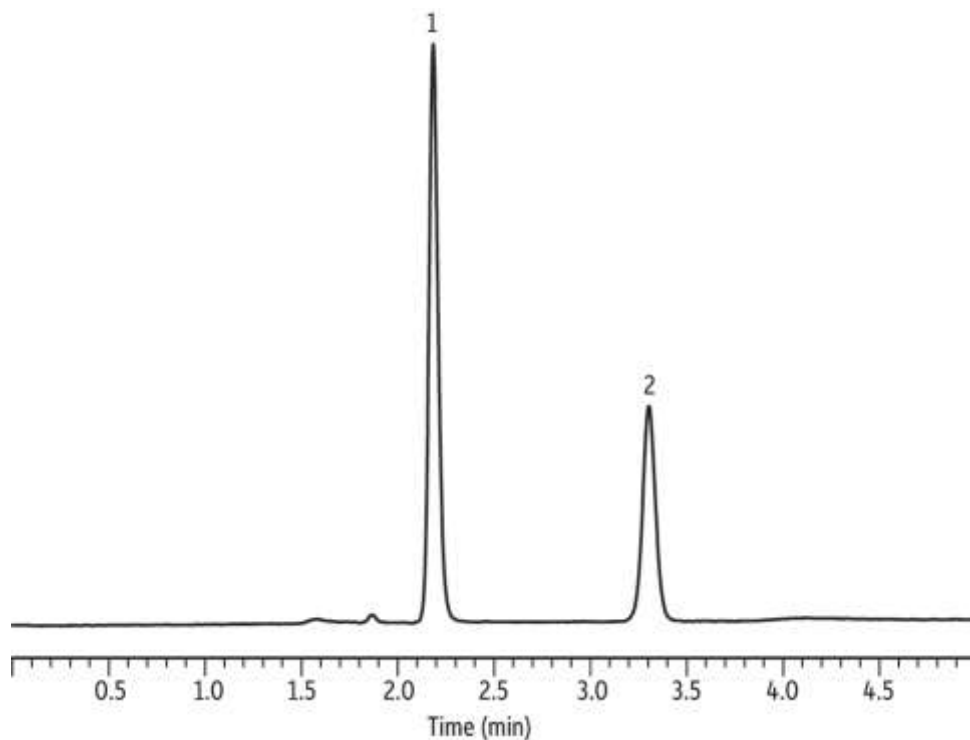
Figure 47. Carboxylic acids on Restek Ultra Aqueous C18 Column. (1) Formic acid; (2) Acetic Acid
Adapted from **[226].**

2) Lignin markers, including 2-methoxyphenol (guaiacol) and 4-ethyl-2-methoxyphenol (4-ethylguaiacol) standards were used in order to assess lignin markers presence in aqueous phases of HTL bio-crudes. The injected carbohydrate makers was to establish the retention time (for the ultra aqueous C18 column) and as a representative LC.

3) Furfural and 5-methylfurfural were also used in order to assess holocellulose degradation products in aqueous phase of HTL bio-crudes, which was to establish the retention time (for the ultra aqueous C18 column) as a representative LC.

4) Methanol was injected and used in order to assess the aqueous phase of HTL bio-crudes, which was to establish the retention time (for the ultra aqueous C18 column) as a representative LC.

5.2.9.   Scanning Electron Microscopic imaging of chars

Morphology images of the original LignoBoost lignin and pine wood samples along and HTL-generated bio-chars were obtained by a JEOL 7800F Prime Field Emission Scanning Electron Microscope (SEM) and used to evaluate the surface morphology and compared with each other.

5.3. Results and discussion

5.3.1. HTL product yields

The impact of temperature on the residual pressure in the reactor during the hydrothermal liquefaction (HTL) of the studied samples is presented in Figure 48. The pressure – temperature curves from all HTL runs were compared against the water saturation curve in order to validate that the process was maintained (at the set residence time) within the hydrothermal liquefaction region.
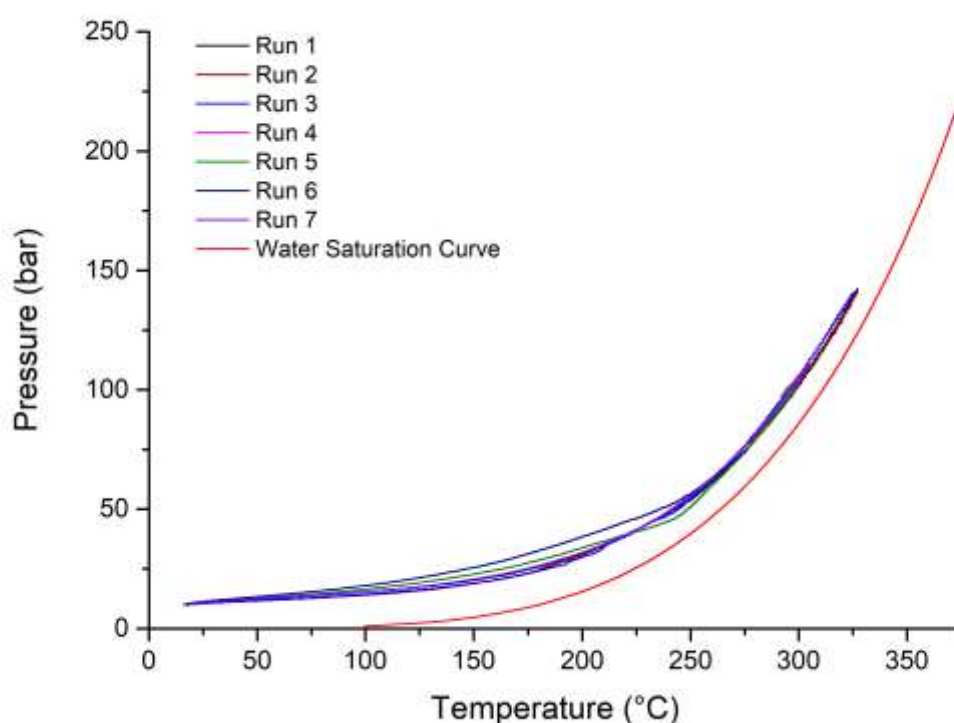
Figure 48. Pressure-temperature readings from HTL experimental runs 1-7.

Table 19 gives the details about the feedstock and process parameters used for hydrothermal liquefaction (HTL) experiments carried out. For all experiments, the residence time at the targeted temperature (275, 300 or 325 °C) was 15 min, as well as a starting pressure of 10 bar using nitrogen. Real-data was recorded for temperature and pressure. Table 19 shows achieved temperatures and indicates match to the targeted set-point, with a small difference at the level of 2 °C. This difference could be due to the thermocouple accuracy. The maximum pressures were recorded at the achieved temperature set-point, as well as after cooling of the entire reactor assembly to room temperature.

This allowed to detect the residual pressure difference (ΔP) before and after the experimental run. This indicated the generation of non-condensable components (gases) analysed by GC-FID in the post-run mode using Tedlar gas sampling bags.

Laboratory-scale processing started with the first set at 325 °C using all three lignocellulosic biomass samples with LignoBoost lignin, pine wood and wheat straw (Table 20 experimental runs 3, 6 and 7). This was in order to observe yields with the planned maximum temperature processing, as 325 °C is the maximum temperature at which the reactor is able to reach without triggering the rupture disc. A higher HTL processing temperature (350 °C) was attempted, but this triggered the rupture disc at approximately 340 °C. HTL yields of wheat straw processed at 325 °C are shown here for comparison only.

The second set was to use LignoBoost lignin and pine wood at different temperatures (275 and 300 °C) at a residence time of 15 min, which was to be in line with project partners carrying out hydro-pyrolysis experiments at this temperature process parameters.

Table 19. Recorded temperature and pressure data for HTL experiments.

Experimental run	Feedstock	Temperature (°C)		Pressure (bar)			
		Targeted reaction temperature	Achieved reaction temperature	Initial pressure	Final pressure	Pressure (after cooling)	ΔP
1	LignoBoost lignin	275	275	10.2	85.2	10.7	0.5
2	LignoBoost lignin	300	300	10.1	104.3	11.2	1.1
3	LignoBoost lignin	325	327	10.2	141.6	11.3	1.1
4	Pine wood	275	276	10.5	85.2	12.5	2.0
5	Pine wood	300	305	10.3	110.7	12.9	2.6
6	Pine wood	325	327	10.3	142.4	13.0	2.7
7	Wheat straw	325	325	10.1	140.8	12.5	2.4

The product yields of all experimental runs are presented in Table 20. The yields of the gaseous fraction were calculated by difference from the yield of char and liquid (crude) products using equation 5.2.4 (page 120).

Table 20. Mass balances from all HTL experiments.

HTL products with sub-fractions	Experimental Run						
	LignoBoost lignin			Pine wood			Wheat straw
Experimental run	1	2	3	4	5	6	7
Char (wt. %)	16.14	11.22	12.50	12.46	17.02	11.85	12.01
Liquids (wt. %)	73.15	80.62	81.32	72.05	71.52	70.80	79.25
Aqueous phase (wt. %)	*66.41*	*72.43*	*72.01*	*64.64*	*63.31*	*68.55*	*74.10*
Bio-crudes (wt. %)	*6.74*	*8.19*	*9.31*	*7.41*	*8.21*	*2.25*	*5.15*
Gases (wt. %)	10.71	8.16	6.18	15.49	11.46	17.35	8.74

Figure 49a and Figure 50a are given the graphical representation of mass balances (yield of crude, char and gases) achieved from HTL processing of LignoBoost lignin and pine wood respectively. Figure 49b and Figure 50b show the same mass balances but with clear distinction taking into consideration of crude and aqueous phase recovered from liquids.

(a)   (b)
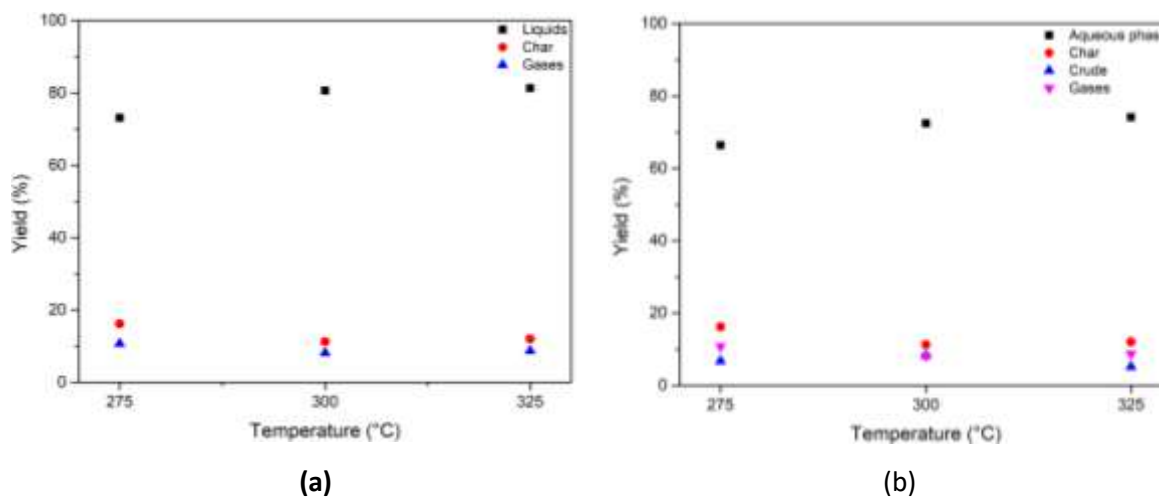
Figure 49. Yields of HTL products at different temperatures for LignoBoost lignin.
(a) product yields of liquids, char and gases, (b) products yield of aqueous phase, char, crude and gases

(a)   **(b)**
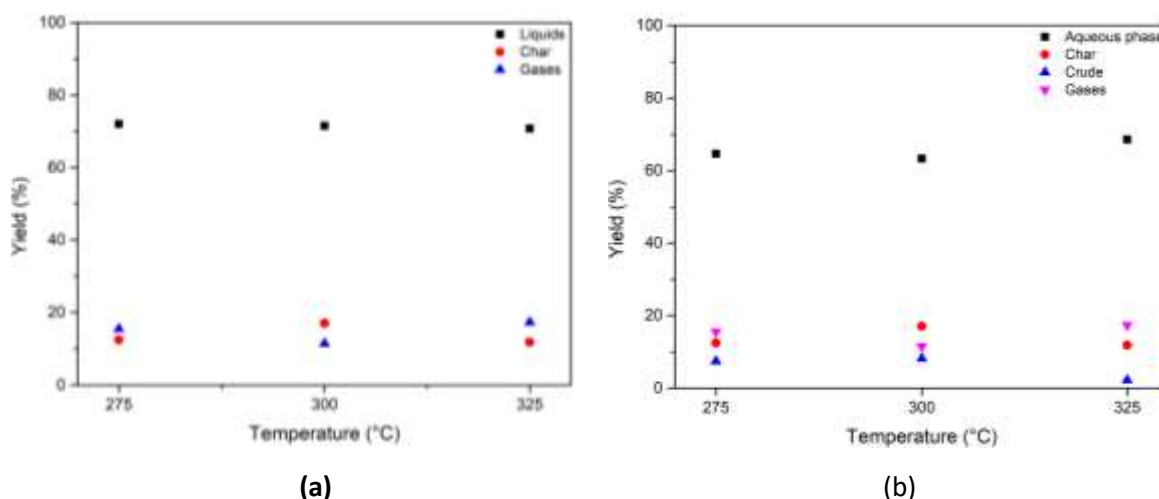
Figure 50. Yields of HTL product at different temperatures for pine wood.
(a) product yields of liquids, char and gases, (b) product yields of aqueous phase, char, crude and gases

The maximum liquid yield of 81.32 wt. % was obtained from LignoBoost lignin processed at a temperature of 325°C. Whilst pine wood and wheat straw processed at 325 °C had a total liquid yield of 70.80 and 79.25 wt.%, respectively. Most importantly, LignoBoost lignin also yielded the most bio-crudes with 9.31 wt.% obtained at 325 °C (experimental run 3). It was anticipated that pine wood and wheat straw would yield more bio-crudes than LignoBoost lignin due to different amount of biochemical components, i.e. holocellulose content, found in the lignocellulosic biomass. However, that is not the case in this study. Xu and Li [70] conducted a literature review stating that high cellulose and hemicellulose content in lignocellulosic biomass will yield more bio-crudes. The previous statement was also agreed upon by Akhtar and Amin [90]. However, the experimental results in this study contradicts the above statement and instead a higher bio-crude yield was obtained using LignoBoost lignin. Similar results achieved by de Caprariis et al [85] obtained the highest bio-crude yield from a lignin-rich feedstock using walnut shell. This could be further explained by the effect of temperature and the different biochemical compositions found in the biomass. Lignin depolymerisation favours higher processing temperature due to its stable structure, and as a result, it requires a higher temperature to break down the bonds. This can be observed from the yield of Lignoboost lignin-derived bio-crudes and increases with the increase of the HTL processing temperature. As mentioned above, the highest bio-crude yield obtained from LignoBoost lignin was 9.31 wt. % (325 °C), whilst the lowest bio-crude yield was 6.74 wt. % processed at a lower temperature of 275 °C (experimental run 1).

Pine wood, which has a higher cellulose and hemicellulose content than LignoBoost lignin (as confirmed in Chapter 3, section 3.3.5.5 on page 80), achieved a maximum bio-crude yield of 8.21 wt.

% processed at 300 °C (experimental run 5), which was an increase from 7.41 wt. % at 275 °C (experimental run 4). At 325 °C (experimental run 6), the bio-crude yield of 2.25 wt. % was dramatically decreased. This can be again explained by the difference in the biochemical content of LignoBoost lignin and pine wood. Pine wood with a higher holocellulose content favours lower processing temperature. According to Minowa et al [227], cellulose decomposes rapidly between 240 and 280 °C and no cellulose was found above 280 °C. It was also shown that the bio-crude yield of cellulose was at its maximum at 300 °C, and decreased above 300 °C. This explains why the bio-crude yield obtained from pine wood was significantly decreased at 325 °C, as most of the cellulose could have repolymerised into bio-char or into gaseous products. This was also confirmed with de Caprariis et al [85] and stated that the holocellulose content of the biomass feedstock would decompose at 250 °C which increases the bio-crude yields at a lower temperature. The biomass initially decomposes and depolymerises into smaller components, and these compounds may rearrange through different competitive reaction including condensation, cyclisation and polymerisation to generate heavy molecular weight products and may condense into bio-char [228].

The highest char yield of LignoBoost lignin was acquired at 275 °C as 16.14 wt. %, which could be due to the incomplete lignin matrix depolymerisation at this temperature. The LignoBoost lignin char yield (11.22 wt. %) was decreased when the temperature increased to 300 °C, but the char yield was slightly increased to 12.50 wt. % when processed at a higher temperature of 325 °C. An increase in char yield of lignin is often attributed by depolymerisation reaction and accompanied with a degradation reaction at higher temperatures, which explains a higher char yield at 325 °C than at 300 °C. However, pine wood char did not follow the same trend as LignoBoost lignin char. The summarised data showed that pine wood was found to have the highest char yield of 17.02 wt. % processed at 300 °C. Whereas, pine wood char processed at 275 and 325 °C was found with a lower char yield of 12.46 and 11.85 wt. %, respectively.

Interestingly, pine wood processed at 325 °C was observed with an increase in gas yield of 17.35 wt. % and less char yield of 11.85 wt. %. This was further confirmed in pressure difference (ΔP), which was found to have an additional of 2.7 bar generated after hydrothermal liquefaction (HTL) reaction. This could be due to cracking reactions occurring, which could transform the bio-crude and/or intermediates products into gas and char [104]. Furthermore, as the temperature and pressure increased, the HTL reaction was leaning toward a hydrothermal gasification reaction rather than hydrothermal carbonisation reaction. Hence, a decrease in char and crude yield was observed, and an increase in gas yield.

5.3.2. Gas analysis

Table 21 shows the detected by the GC/FID hydrocarbon gas products generated from hydrothermal liquefaction (HTL) experiments at different temperatures using LignoBoost lignin and pine wood as a feedstock. An exemplar gas chromatogram of detected hydrocarbon gases from pine wood processed at 325 °C is presented in Figure 51. A better overview of yields of detected hydrocarbon gases are presented in Figure 52 in the form of a bar chart.

Permanent gases, including hydrogen (H_2), carbon monoxide (CO) and CO_2, are not included in Table 21. However, these are presented in Table D.1 (on page 285) in Appendix D. A large amount of carbon dioxide was observed as this was calculated by difference, which resulted in inconsistencies and limitations of very small or near to zero percentage in the calibrated gases.

Table 21. Hydrocarbon gases produced at different temperature from HTL processing using LignoBoost lignin and pine wood.

Gases (%)	LignoBoost lignin			Pine wood		
	275 °C	300 °C	325 °C	275 °C	300 °C	325 °C
Methane	51.07	51.43	63.66	26.29	16.09	24.45
Ethene	9.74	8.69	5.94	13.27	6.01	8.00
Ethane	7.40	8.38	9.48	7.27	3.18	5.54
Propene	12.13	11.95	7.91	32.81	28.21	25.58
Propane	4.34	4.16	5.10	5.96	1.15	2.26
Butene	9.65	8.87	1.97	5.66	36.29	25.04
Butane	5.68	6.52	5.95	8.73	9.07	9.13
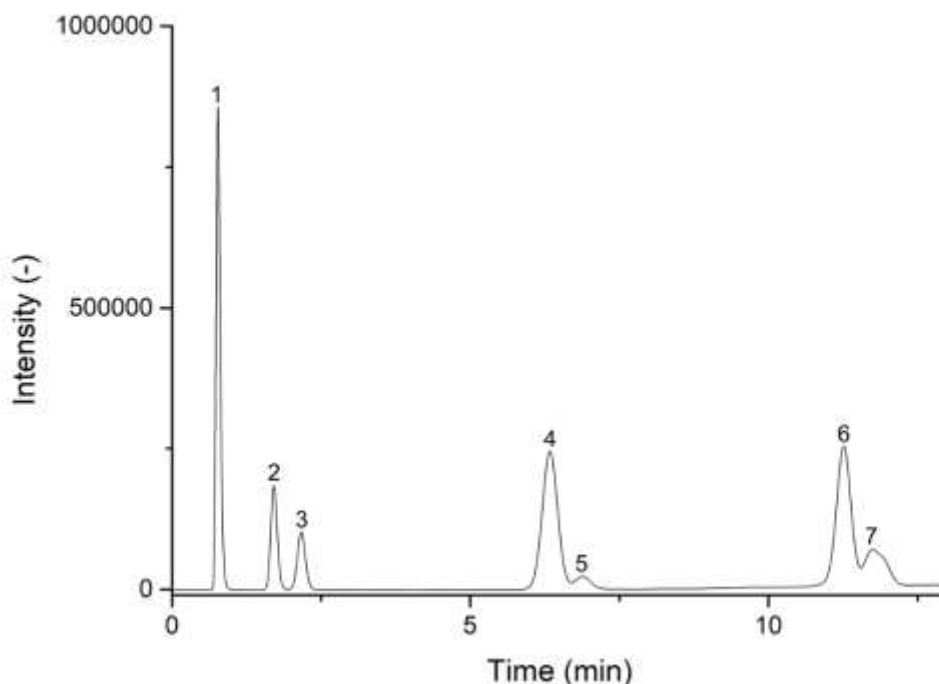
Figure 51. Hydrocarbon gases produced from HTL experiments of pine wood analysed by GC-FID.
Peak assignment: (1) methane; (2) ethene; (3) ethane; (4) propene; (5) propane; (6) butene; (7) butane
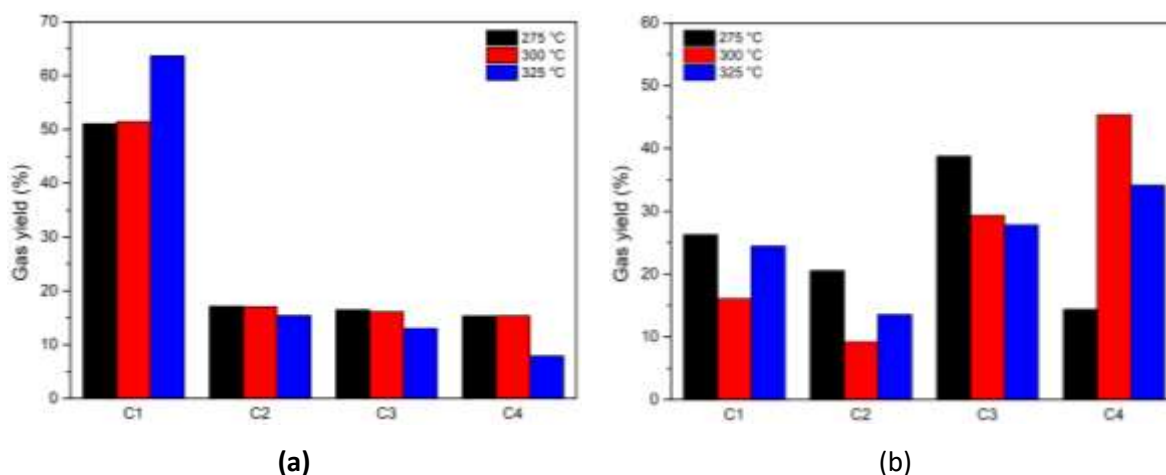
(a)	(b)

Figure 52. Overview of distribution in hydrocarbon gases (C_1, C_2, C_3 and C_4).
(a) LignoBoost lignin, (b) pine wood

The GC/TCD analyses of gases revealed that carbon dioxide (CO_2) was one of the main gaseous products in the HTL experimental runs. Beauchet et al [229] and Feng et al [230] have also found that the gaseous products obtained from HTL reaction mainly contain CO_2 which could be formed through decarboxylation reaction and through intermediates cracking.

Gas analysis results summarised in Table 21 revealed that higher HTL processing temperatures lead to an increase in CH_4 and ethane (C_2H_6) production from LignoBoost lignin HTL reaction. At 275 °C, CH_4 and C_2H_6 yields were observed to be 51.07 % and 7.40 %, respectively. Whilst at 325 °C, an increase in the yields of CH_4 and C_2H_6 was observed at 63.66 % and 9.48 %, respectively. CH_4 is typically formed from the degradation of methoxyl group (mainly found in lignin) through cleavage of O-C bond [231]. Furthermore, an increase in CH_4 and C_2H_6 production resulted in further cracking of other hydrocarbon gases. These include ethene (C_2H_4), propene (C_3H_6), propane (C_3H_8) and butene (C_4H_8), which saw a slight decrease at 300 °C. At 325 °C, a continued decrease of these gases were also observed.

A significant amount of CH_4 (26.29 %) and C_3H_6 (32.81 %) were found in gas products obtained during the HTL processing of pine wood at lower temperature of 275 °C. This could be explained by different biochemical compositions found when comparing the LignoBoost lignin and pine wood. At 300 °C, a decrease in nearly all gaseous products, with the exception of C_4H_8. Instead it saw a significant increase in C_4H_8 from 5.66 % to 36.29 %. The increase in CH_4 and C_2 gas yields were observed at 325 °C. In contrast, C_3H_6 continued to decrease at 300 °C and 325 °C and may be cracked into other hydrocarbon gases (CH_4 and C_2 gases). An increase in butane (C_4H_{10}) at 300 °C and 325 °C was also observed at 9.07 and 9.13 %, respectively.

5.3.3. Elemental analysis

The elemental composition (C, H, N, S and O) of all char and bio-crudes samples generated from LignoBoost lignin and pine wood, along with H/C and O/C molar ratio, and heating values are presented Table 22 and Table 23.

Table 22. Elemental analysis and heating value of LignoBoost and pine wood char generated from HTL processing.

Sample	C (%)	H (%)	N (%)	S (%)	O* (%)	H/C	O/C	HHV (MJ kg^{-1})
LignoBoost lignin char								
275	57.65 ± 1.99	5.05 ± 0.11	0.23 ± 0.01	1.21 ± 0.05	35.85 ± 2.11	1.04	0.47	20.32
300	59.55 ± 2.90	5.17 ± 0.14	0.22 ± 0.02	1.02 ± 0.02	34.05 ± 3.02	1.03	0.43	21.46
325	67.77 ± 4.55	4.96 ± 0.05	0.25 ± 0.02	1.27 ± 0.09	25.75 ± 4.70	0.87	0.24	25.44
Pine wood char								
275	70.44 ± 0.27	5.37 ± 0.06	0.24 ± 0.01	0.00	23.95 ± 0.32	0.91	0.26	27.26
300	71.93 ± 0.44	5.38 ± 0.03	0.24 ± 0.02	0.00	22.45 ± 0.46	0.89	0.23	28.04
325	71.50 ± 0.35	5.11 ± 0.06	0.35 ± 0.01	0.00	23.03 ± 0.37	0.85	0.24	27.41

*Oxygen content was calculated by difference

Table 23. Elemental analysis and heating values of LignoBoost and pine wood bio-crude generated from HTL processing.

Sample	C (%)	H (%)	N (%)	S (%)	O* (%)	H/C	O/C	HHV (MJ kg^{-1})	ER (%)
LignoBoost bio-crude									
275	80.69 ± 3.45	7.02 ± 0.45	0.00	1.83 ± 0.13	7.13 ± 2.14	1.04	0.07	36.14	9.4
300	79.98 ± 1.39	6.77 ± 0.27	0.88 ± 0.15	1.62 ± 0.09	7.83 ± 1.64	1.01	0.07	35.41	11.2
325	71.54 ± 1.74	6.05 ± 0.43	0.00	0.83 ± 0.15	17.43 ± 2.93	1.01	0.18	29.79	10.7
Pine wood bio-crude									
275	75.33 ± 0.98	6.90 ± 0.13	0.00	0.00	15.58 ± 1.10	1.11	0.16	32.29	12.1
300	74.62 ± 1.39	6.77 ± 0.27	0.88 ± 0.15	0.00	7.83 ± 1.64	1.03	0.16	31.66	13.2
325	68.98 ± 1.70	5.86 ± 0.19	0.56 ± 0.04	0.00	21.42 ± 1.81	1.01	0.23	27.92	3.2

*Oxygen content was calculated by difference

The elemental analysis provides the quality of the char and bio-crudes. Generally, a higher carbon (C) content is preferred, which will result in a higher HHV. The elemental analysis revealed that in both chars derived from LignoBoost lignin and pine wood had a lower carbon (C) content at lower HTL processing temperature. The lowest C value found in LignoBoost lignin char was obtained at 275 °C with 57.65 %, and the highest at 325 °C with 67.77 %. Pine wood char was found to have the lowest C content of 70.44 % processed at 275 °C, whilst the highest C content of 71.93 % was observed at 300 °C. At 325 °C, the C content of pine wood char slightly decreased to 71.50 %. Both LignoBoost lignin and pine wood bio-crudes did not follow the same trend as the char did. The elemental analysis revealed that the highest C value was observed at 275 °C, which was 80.69 and 75.33 % in LignoBoost lignin and pine wood bio-crudes, respectively.

Higher hydrogen (H) content was favoured at lower HTL processing temperatures. The highest H content in LignoBoost lignin and pine wood chars at 300 °C was found to be 5.17 and 5.38 %, respectively. Whilst the highest H content from LignoBoost lignin and pine wood bio-crudes processed at 275 °C was 7.02 and 6.90 % respectively.

A lower nitrogen (N) is preferred, since this will minimise the formation of NO_x emission when combusting the bio-crudes. The lowest N content was detected in LignoBoost lignin char (0.22 %) obtained at 300 °C. An increase in N content was found in all bio-crudes when increasing the temperature. The maximum N content was observed at 0.88 % in both bio-crudes obtained at 300 °C. At 325 °C, there was no N content found in LignoBoost lignin bio-crude, whilst the N content was decreased to 0.56 % in the pine wood bio-crude.

As anticipated, sulphur (S) content was observed in both LignoBoost lignin char and bio-crudes. S will create gaseous emission, syngas cleaning and corrosion problems during gasification and combustion processes [69].

The lowest oxygen (O) content found in LignoBoost lignin char was obtained at 325 °C with 25.75 %, whilst the lowest O content was 22.45 % found in pine wood char obtained at 300 °C. The O content is derived from depolymerisation of the biomass and generates organic acids, furans, phenolics, guaiacols and syringols in the bio-products [232]. The O content found in the LignoBoost lignin and pine wood bio-crudes was in the range of 7.13 and 21.42 %, which is considerably high when compared to conventional fuel oil. Therefore, the bio-crudes will need to have upgrading processes (such as hydrodeoxygenation) to be able to use it as a transportation fuel [233].

Using the C, H and O content obtained from the elemental analysis, the atomic ratios H/C and O/C were calculated for all HTL-generated chars and bio-crudes. Both H/C and O/C atomic ratios decreased

in LignoBoost lignin and pine wood chars produced at a higher HTL processing temperature. The lowest H/C and O/C ratios of LignoBoost lignin char obtained at 325 °C were 0.87 and 0.24, respectively. The lowest H/C and O/C ratios found in pine wood char obtained at 325 °C were 0.85 and 0.24, respectively. The H/C molar ratio of both LignoBoost lignin and pine wood bio-crudes decreased to 1.01 at a higher HTL processing temperature of 325 °C. A high H/C is preferred in the petroleum industry, as it suggests more aromatic products found in the bio-crudes [234]. However, the bio-crude's O/C ratio increased as the temperature increased to 325 °C, which was found with 0.18 and 0.23 processed from LignoBoost lignin and pine wood bio-crudes, respectively.

The atomic ratios of the HTL-generated chars and bio-crudes are plotted in a van Krevelen diagram in Figure 53, along with the values of the feedstock (obtained from Chapter 3, section 3.3.1 on page 62).
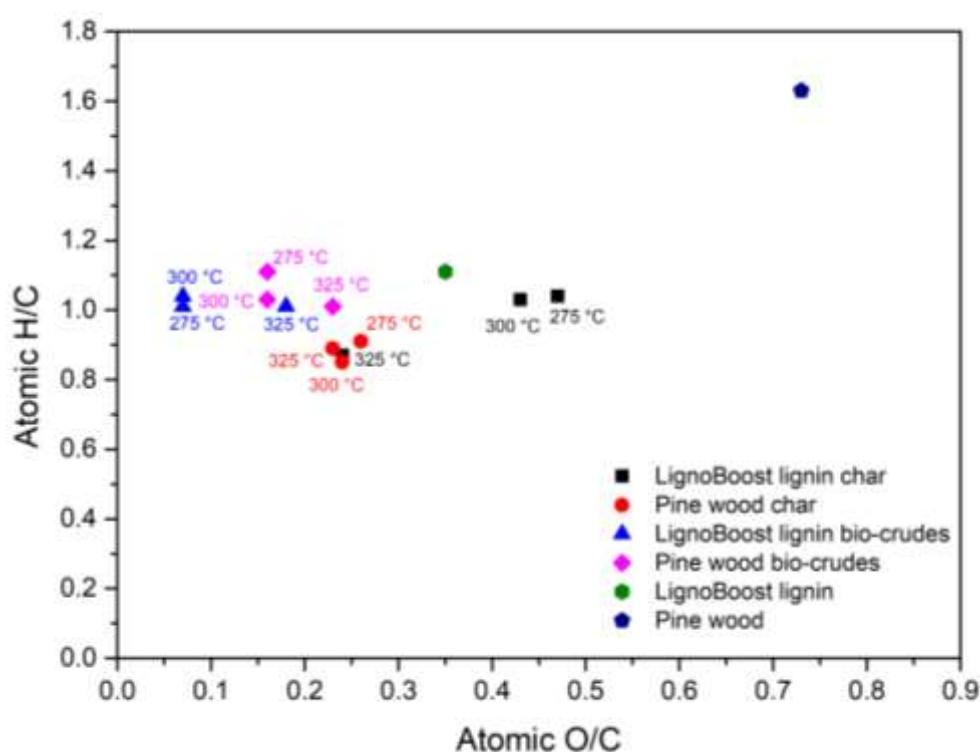
Figure 53. van Krevelen diagram plotted with LignoBoost lignin and pine wood, and HTL-generated chars and bio-crudes obtained at different reaction temperatures.

From Figure 53, the H/C atomic ratio of all HTL processed LignoBoost lignin char has been slightly reduced when compared to LignoBoost lignin as a feedstock, which was found to be 1.11. Whilst the O/C atomic ratio for the feedstock LignoBoost lignin was 0.35, and that has been increased for LignoBoost lignin chars processed at 275 and 300 °C. The LignoBoost lignin bio-crudes processed at 300 and 325 °C H/C ratio was also slightly decreased. For LignoBoost lignin bio-crudes obtained at all HTL processed temperatures, the O/C ratio has been reduced as well compared to its feedstock. HTL

processed at 325 °C did reduce the O/C ratio in both the LignoBoost lignin char and bio-crude, which showed that deoxygenation was taking place during HTL.

Pine wood as a feedstock was found to have a H/C atomic ratio of 1.63, whilst all HTL-processed pine wood char was significantly reduced and observed to be in the range of 0.85-0.91. The same observation was found in the pine wood bio-crudes, which were found in the range of 1.01-1.11. The O/C atomic ratio of pine wood chars was notably lower and was found within the range of 0.24-0.26 compared to its feedstock, which was 0.71. Whilst the bio-crudes from pine wood were in the range of 0.16-0.23. Deoxygenation occurred during HTL processing and was found to be more effective in pine wood than LignoBoost lignin.
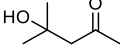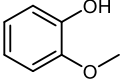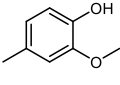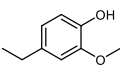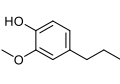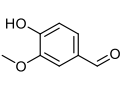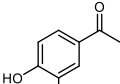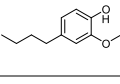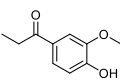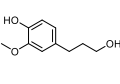
It has been observed that the heating values increased as the HTL processing temperature increased. The highest HHV from LignoBoost lignin and pine wood bio-crudes was in the range of 36.14 and 32.29 MJ kg^{-1} respectively, which is considered low when compared with conventional fuel – crude oil, gasoline and petroleum (42 to 44 MJ kg^{-1}) [235]. Furthermore, the elemental composition has a direct impact of the heating value, whereby carbon and hydrogen will increase the heating value as opposed to oxygen and nitrogen, which will have a negative effect [236]. Therefore, further upgrading will be necessary in order to remove oxygen. The energy recovery (ER) was also calculated for the bio-crudes, which shows whether it would lead to an economically viable process, as it is defined as the energy available in the biomass and converted into bio-crude [237]. The highest ER of 13.2 % was processed at 300 °C, and lowest 3.2 at 325 °C due to the low bio-crude yield obtained from pine wood.

5.3.4. Bio-crude analysis

GC-MS chromatograms obtained for bio-crudes derived from LignoBoost lignin and pine wood (at three different HTL processing temperatures) are presented from Figure 54 to Figure 59. Identified chemical components in HTL-derived bio-crudes from LignoBoost lignin and pine wood processed from 275 to 325 °C are listed in Table 24 and Table 25, respectively. The most abundant components identified with a peak area percentage value higher than 1 % are included in these tables. It should be taken into consideration that the peak area percentage values are not the actual representation of the overall concentration. The peak area percentage presented here shows the relative concentration of each component in the fraction of the bio-crude that was able to vaporise and pass through the GC column. Furthermore, the total area does not add up to 100 % as there were unidentified peaks.

Table 24. Chemical products found in all three temperatures of LignoBoost lignin bio-crudes.

Retention Time (min)	Name	Formula	MW	Structure	m/z	Area (%) 275 °C	Area (%) 300 °C	Area (%) 325 °C
5.44	4-hydroxy-4-methyl-2-pentanone	$C_6H_{12}O_2$	116		116.08 (100.0 %), 17.09 (6.5 %)	3.92	3.17	0.68
13.75	2-methoxyphenol (guaiacol)	$C_7H_8O_2$	124		124.05 (100.0 %), 125.06 (7.6 %)	12.11	13.55	30.82
17.64	2-methoxy-4-methylphenol (creosol)	$C_8H_{10}O_2$	138		138.07 (100.0 %), 139.07 (8.7 %)	3.67	6.88	18.41
20.77	4-ethyl-2-methoxyphenol	$C_9H_{12}O_2$	152		152.08 (100.0 %), 153.09 (9.7 %)	7.36	9.73	17.58
23.91	2-methoxy-4-propylphenol	$C_{10}H_{14}O_2$	166		166.10 (100.0 %), 167.10 (10.8 %)	8.41	9.80	12.25
24.97	3-hydroxy-4-methoxybenzaldehyde	$C_8H_8O_3$	152		152.05 (100.0 %), 153.05 (8.7 %)	6.28	4.8	-
27.84	1-(4-hydroxy-3-methoxyphenyl)-ethanone (apocynin)	$C_9H_{10}O_3$	166		166.06 (100.0 %), 167.07 (9.7 %)	6.55	5.62	2.52
29.26	4-butyl-2-methoxyphenol	$C_{11}H_{16}O_2$	180		180.12 (100.0 %), 181.12 (11.9 %)	5.11	3.58	2.38
30.91	1-(4-hydroxy-3-methoxyphenyl)-1-propanone	$C_{10}H_{12}O_3$	180		180.08 (100.0 %), 181.08 (10.8 %)	1.37	1.21	0.36
32.91	4-hydroxy-3-methoxybenzenepropanol	$C_{10}H_{14}O_3$	182		182.09 (100.0 %), 183.10 (10.8 %)	3.29	3.08	0.47
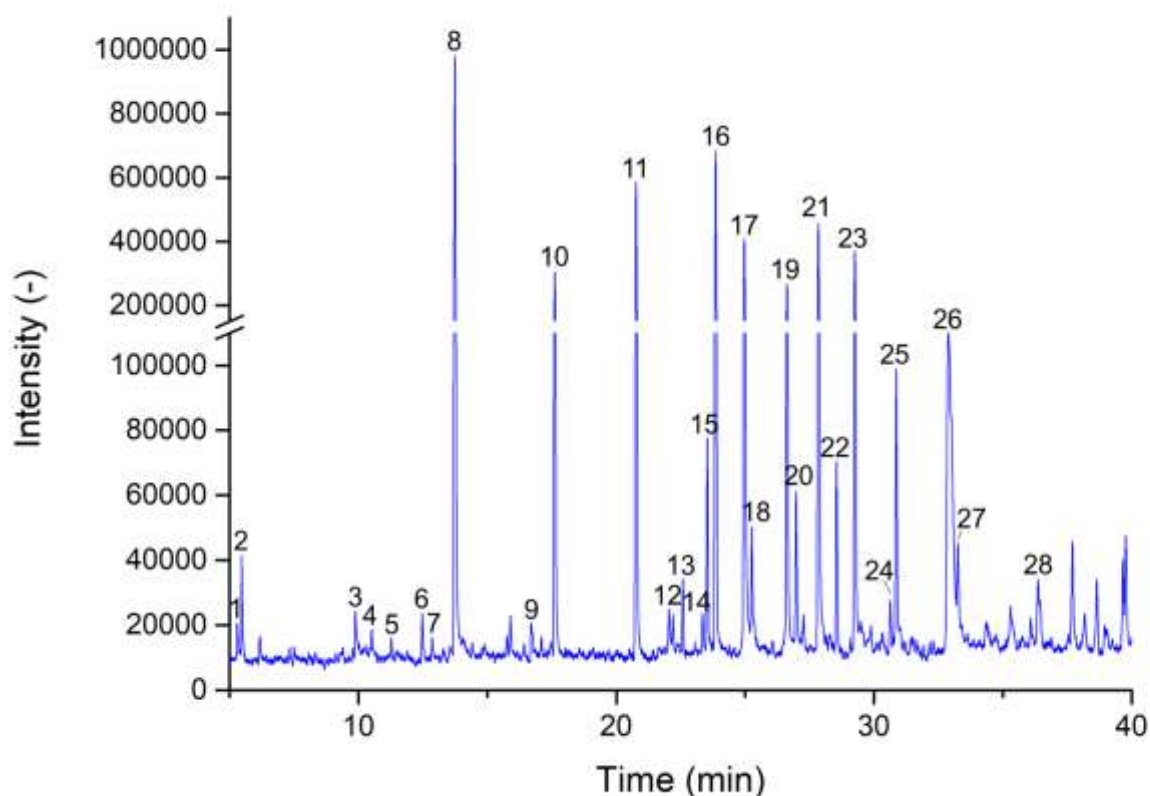
Figure 54. Chromatogram of HTL crude generated from LignoBoost lignin at 275 °C.
Peak assignment: (1) furfural; (2) 4-hydroxy-4-methyl-2-pentanone; (3) phenol; (4) 2-thiophenecarboxaldehyde; (5) 1-methyl-3-(1-methylethyl)-benzene; (6) 3-ethyl-2-hydroxy-2-cyclopentenone; (7) S-methyl methanethiosulphate; (8) 2-methoxyphenol (guaiacol); (9) 4-ethylphenol; (10) 2-methoxy-4-methylphenol (creosol); (11) 4-ethyl-2-methoxyphenol; (12) 2-methoxy-4-vinylphenol; (13) 5-acetyl-2-methoxyphenyl acetate; (14) 2,6-dimethoxyphenol; (15) 2-methoxy-4-(2-propenyl)phenol (eugenol); (16) 2-methoxy-4-propylphenol; (17) 4-hydroxy-3-methoxybenzaldehyde; (18) 2-methoxy-4-(1-propenyl)phenol (Isoeugenol); (19) 2-methoxy-4-(1-propenyl)phenol (trans-isoeugenol); (20) 2-methoxy-4-propylphenol; (21) 1-(4-hydroxy-3-methoxyphenyl)-ethanone (apocynin); (22) 1,2-dimethoxy-4—propylbenzene; (23) 4-butyl-2-methoxyphenol; (24) 4-(1-hydroxyallyl)-2-methoxyphenol; (25) 1-(4-hydroxy-3-methoxyphenyl)-1-propanol; (26) 4-hydroxy-3-methoxybenzenepropanol; (27) 3-methoxy-2-napthalenol; (28) 2,3-dimethoxynaphthalene
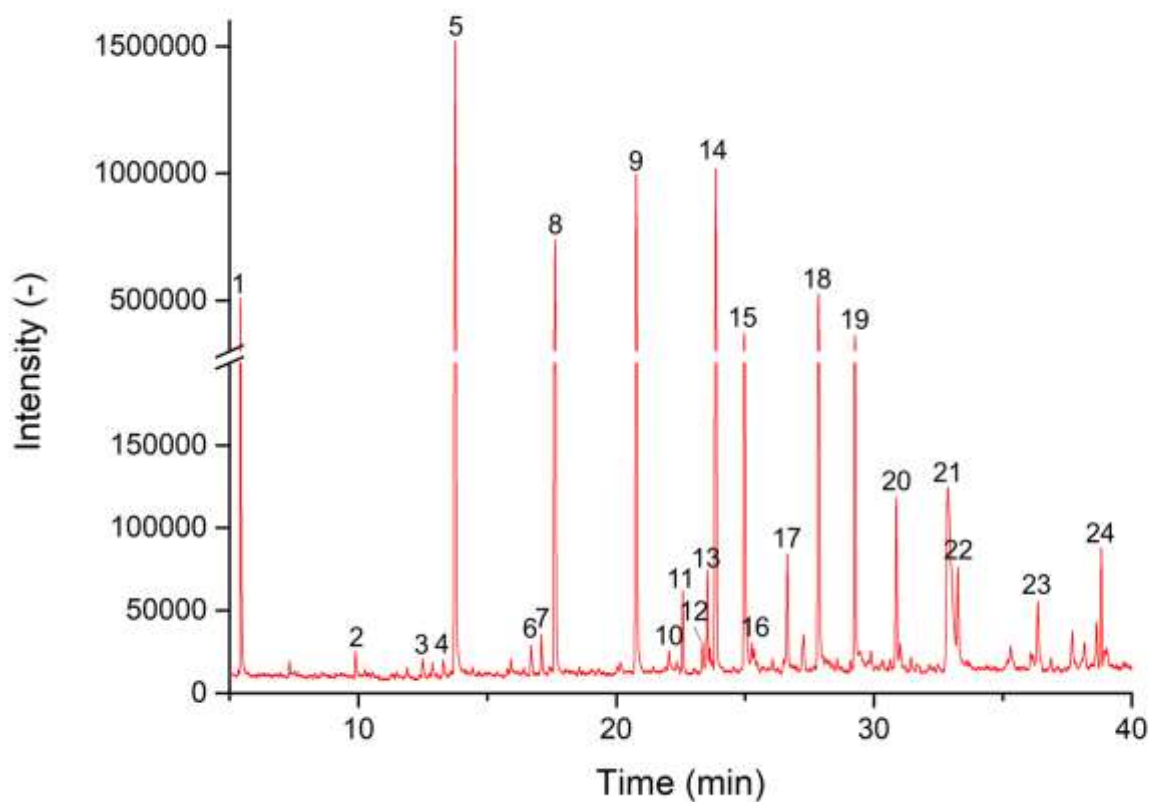
Figure 55. Chromatogram of HTL crude generated from LignoBoost lignin at 300 °C.
Peak assignment: (1) 4-hydroxy-4-methyl-2-pentanone; (2) phenol; (3) 3-ethyl-2-hydroxy-2-cyclopentenone; (4) S-methyl methanethiosulphate; (5) 2-methoxyphenol (guaiacol); (6) 4-ethylphenol; (7) 2-methoxy-3-methylphenol; (8) 2-methoxy-4-methylphenol (creosol); (9) 4-ethyl-2-methoxyphenol; (10) 2-methoxy-4-vinylphenol; (11) 5-acetyl-2-methoxyphenyl acetate; (12) 2,6-dimethoxyphenol; (13) 2-methoxy-4-(2-propenyl)phenol (eugenol); (14) 2-methoxy-4-propylphenol; (15) 4-hydroxy-3-methoxybenzaldehyde; (16) 2-methoxy-4-(1-propenyl)phenol (isoeugenol); (17) 2-methoxy-4-(1-propenyl)phenol (trans-isoeugenol); (18) 1-(4-hydroxy-3-methoxyphenyl)-ethanone (apocynin); (19) 4-butyl-2-methoxyphenol; (20) 1-(4-hydroxy-3-methoxyphenyl)-1-propanone; (21) 4-hydroxy-3-methoxybenzenepropanol; (22) 3-methoxy-2-napthalenol; (23) 2,3-dimethoxynaphthalene; (24) bis(2-methylpropyl) benzene-1,2-dicarboxylate
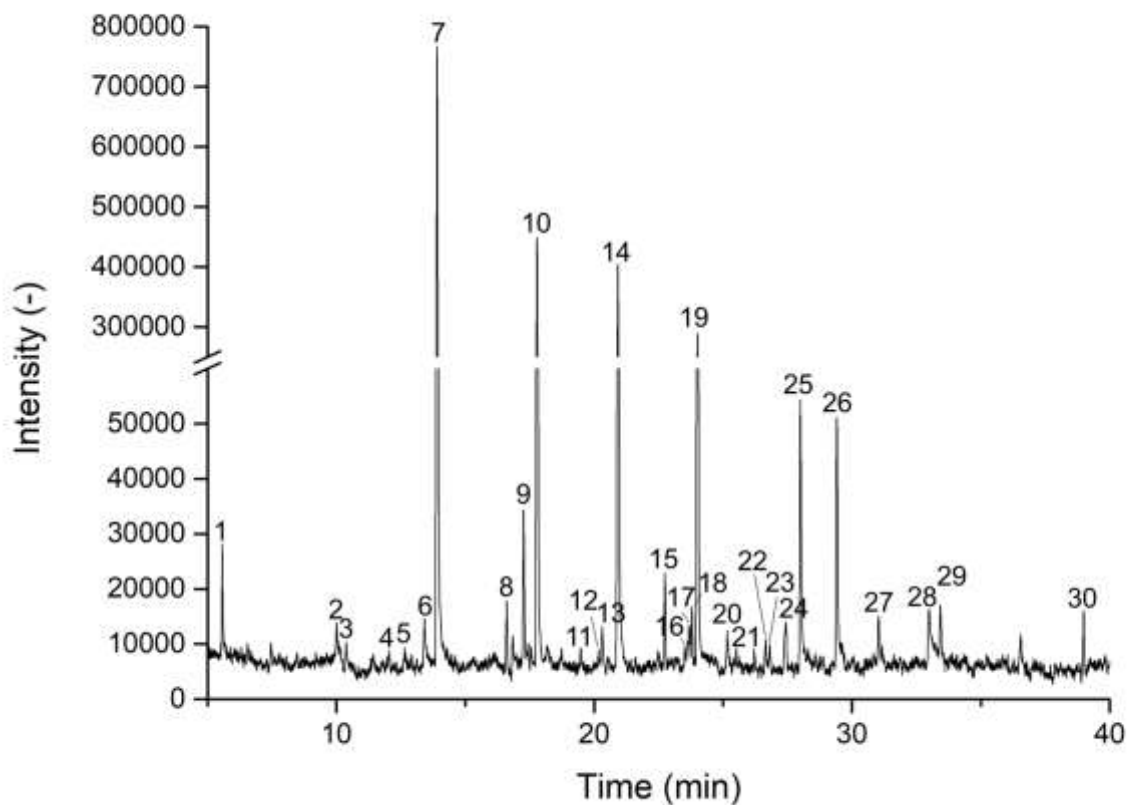
Figure 56. Chromatogram of HTL crude generated from LignoBoost lignin at 325 °C.
Peak assignment: (1) 4-hydroxy-4-methyl-2-pentanone; (2) phenol; (3) 3,4-dimethyl-2-cyclopentenone; (4) 2,3-dimethyl-2-cyclopentenone; (5) S-methyl methanethiosulphate; (6) 4-methylphenol (p-Cresol); (7) 2-methoxyphenol (guaiacol); (8) 1,2,3,4-tetranapthalene; (9) 2-methoxy-3-methylphenol; (10) 2-methoxy-4-methylphenol (creosol); (11) 3,4-dimethoxytoluene; (12) 4-propylphenol; (13) 1,4-dimethoxy-2-methylbenzene; (14) 4-ethyl-2-methoxyphenol; (15) 5-acetyl-2-methoxyphenyl acetate; (16) 2,6-dimethoxyphenol; (17) 2-methoxy-4-(2-propenyl)phenol (eugenol); (18) 1-(2-hydroxy-4-methoxyphenyl)-ethanone; (19) ; 2-methoxy-4-propylphenol; (20) 4-hydroxy-3-methoxybenzaldehyde; (21) 4-hydroxy-3-propyl-benzoic acid; (22) 1-(4-hydroxy-3-methoxyphenyl)-1-propane; (23) 2-methoxy-4-(2-propenyl)phenol (trans-isoeugenol); (24) 2-methoxy-5-(2-propenyl)phenol; (25) 1-(4-hydroxy-3-methoxyphenyl)-ethanone (apocynin); (26) 4-butyl-2-methoxyphenol; (27) 1-(4-hydroxy-3-methoxyphenyl)-1-propanone; (28) 4-hydroxy-3-methoxybenzenepropanol; (29) 3-methoxy-2-napthol; (30) bis(2-methylpropyl) benzene-1,2-dicarboxylate

The LignoBoost lignin is considered a pure industrial sample, where most of the holocellulose components have been removed during the delignification process using sulphuric acid [57]. Traces of holocellulose markers and sulphuric products were observed, including 4-hydroxy-4-methyl-2-pentanone, 3-ethyl-2-hydroxy-2-cyclopentenone, 3,4-dimethyl-2-cyclopentenone, 2,3-dimethyl-2-cyclopentenone, furfural and S-methyl methanethiosulphate. The distribution of chemical compounds present in the LignoBoost lignin HTL bio-crudes were found to be similar to the pyrolysis products identified during the analytical pyrolysis studies (section 3.3.5.4. on page 78 in Chapter 3). The

majority of the phenolic components were derived from the lignin decomposition, particularly methoxyphenols (including guaiacol, creosol, 4-ethyl-2-methoxyphenol, 2-methoxy-4-propylphenol and 4-butyl-2-methoxyphenol) which were formed from depolymerisation followed by hydrolysis of guaiacyl-lignin units [238]. Cleavage of aryl-ether (β-O-4) bonds occur easily at temperatures from 200 to 300 °C and will mainly yield guaiacol as well as other phenolic compounds [239]. This was further confirmed by a study done by Kawamoto [46], and explained that lignin will be dependent on the temperature and especially between temperatures 200 and 400 °C, which will yield more methoxy groups. Furthermore, the β-O-4 bond is the most common substructure, accounting 60 % of all linkages in lignin [240]. The study also showed that other linkages (e.g. 5-O-4 and α-o-4) and condensation bonds (β-1) between the lignin building blocks were cleaved in order to form lower molecular weight components (phenolics) [240]. The formation of phenolic compound originated from demethoxylation reaction, whereby the methoxy group will cleave to generate oxygen and methyl free radicals. The hydrogen from the methyl radical is abstracted to produce the phenol-type compounds along with the release of a methylene radical [241]. The creosol is generated via the coupling reaction of the phenolic and methyl radicals. However, the breakdown of β-O-4 bonds may also lead to a repolymerisation reaction via cross-linking with higher molecular weight fragments leading to char formation or produce coke simultaneously [238]. Whereas, propyl side chains (e.g. $C_α/C_β$ and $C_β/Cγ$) may generate the open-side chains including 4-hydroxy-4-methyl-2-pentanone [242]. During liquefaction processing, multiple reactions (including demethoxylation, alkylation, and condensation reactions) are compete against each other whilst cleaving of the C-O-C and C-C bonds [243].

Alhassan et al [244] showed that an increasing temperature reduced the yield of guaiacol to produce catechol, however the results here in this study seem to disagree with this statement. An increase in guaiacol production with a peak area of 30.82 % was observed at the highest HTL-processing temperature of 325 °C. Whilst a lower guaiacol peak area was observed to be 12.11 and 13.55 % processed at 275 and 300 °C, respectively. One explanation could be the fact that at high temperatures phenolic bonds are highly stable and resulting in a low yield of phenol production (of less than a peak area of 1 %) and therefore, no catechol was observed in this study. According to Schuler et al [245], catechol is an expected product from guaiacol degradation. In order to break down guaiacol and its derivatives (including 2-methoxy-4-proylphenol, 4-ethyl-2-methoxyphenol and creosol), a longer reaction time was needed to have phenol, *o*-cresol, catechol and its derivatives for products (as these are value-added intermediates in the chemical industry) [246].

As observed in Table 24, an increase in the temperature also saw a decrease in the peak areas of the larger molecular weight components. 3-hydroxy-4-methoxybenzaldehyde had a peak area of 6.28 % at 275 °C but was not detected by GC-MS with the crude sample generated at 325 °C. Similarly, apocynin had a peak area of 6.55 %, but decreased to a peak area of 2.52 % when the temperature increased to 325 °C. 4-butyl-2-methoxyphenol was found with a peak area of 5.11 % and decreased to 2.38 % at 325 °C. The smaller peak area of 1.37 and 3.29 % was obtained from 1-(4-hydroxy-3-methoxyphenyl)-1-propane and 4-hydroxy-3-methoxybenzenepropanol, respectively. These components were found with a peak area of 0.36 and 0.47 %, respectively, when the temperature was increased to 325 °C.

Table 25. Components found in all three temperatures of pine wood bio-crudes.

Retention Time (min)	Name	Formula	MW	Structure	m/z	Area (%)		
						275 °C	300 °C	325 °C
5.44	4-hydroxy-4-methyl-2-pentanone	$C_6H_{12}O_2$	116		116.08 (100.0 %), 17.09 (6.5 %)	8.39	3.12	3.17
7.98	2,5-hexandione	$C_6H_{10}O_2$	114		114.07 (100.0 %), 115.07 (6.5 %)	1.16	0.87	-
9.87	phenol	C_6H_6O	94		94.04 (100.0 %), 95.05 (6.5 %)	1.00	1.06	0.13
12.74	levulinic acid	$C_5H_8O_3$	116		116.05 (100.0 %), 117.05 (5.4 %)	2.78	1.49	-
13.77	2-methoxyphenol (guaiacol)	$C_7H_8O_2$	124		124.05 (100.0 %), 125.06 (7.6 %)	7.73	11.45	0.21
17.64	2-methoxy-4-methylphenol (creosol)	$C_8H_{10}O_2$	138		138.07 (100.0 %), 139.07 (8.7 %)	1.28	3.03	13.55
20.78	4-ethyl-2-methoxyphenol	$C_9H_{12}O_2$	152		152.08 (100.0 %), 153.09 (9.7 %)	2.05	3.39	9.73
23.38	2,6-dimethoxyphenol	$C_8H_{10}O_3$	154		154.06 (100.0 %), 155.07 (8.7 %)	1.16	1.07	0.12
23.87	2-methoxy-4-propylphenol	$C_{10}H_{14}O_2$	166		166.10 (100.0 %), 167.10 (10.8 %)	0.54	1.25	9.80
24.98	4-hydroxy-3-methoxybenzaldehyde (vanillin)	$C_8H_8O_3$	152		152.05 (100.0 %), 153.05 (8.7 %)	8.66	5.13	4.10
27.90	1-(4-hydroxy-3-methoxyphenyl)-ethanone (apocynin)	$C_9H_{10}O_3$	166		166.06 (100.0 %), 167.07 (9.7 %)	1.68	1.68	5.62
29.26	4-butyl-2-methoxyphenol	$C_{11}H_{16}O_2$	180		180.12 (100.0 %), 181.12 (11.9 %)	3.07	2.62	3.58
32.87	4-hydroxy-3-methoxybenzenepropanol	$C_{10}H_{14}O_3$	182		182.09 (100.0 %), 183.10 (10.8 %)	3.70	3.39	3.08
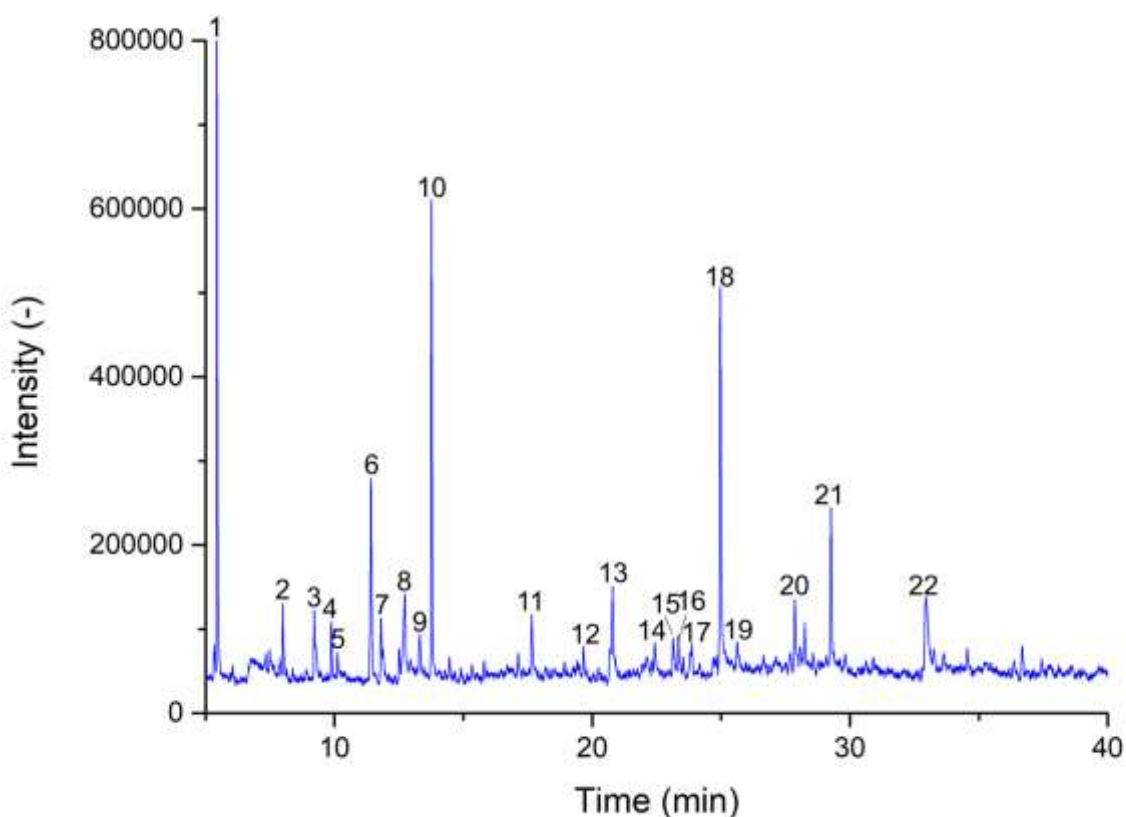
Figure 57. Chromatogram of HTL crude generated from pine wood at 275 °C.

Peak assignment: (1) 4-hydroxy-4-methyl-2-pentanone; (2) 2,5-hexadione; (3) 5-methyl-2-furancarboxaldehyde; (4) phenol; (5) 3-hydroxy-dihydro-2(3H)-furanone; (6) 3-methyl-1,2-cyclopentanedione; (7) 2-acetyl-5-methylfuran; (8) levulinic acid; (9) 3-methylphenol; (10) 2-methoxyphenol (guaiacol); (11) 2-methoxy-4-methylphenol (creosol); (12) 3,5-dimethylfuran; (13) 4-ethyl-2-methoxyphenol; (14) 2,3-dimethyl-2-cyclopentenone; (15) 2-methyl-1,4-benzenediol; (16) 2,6-dimethoxyphenol; (17) 2-methoxy-4-propylphenol; (18) 4-hydroxy-3-methoxybenzaldehyde (vanillin); (19) 2-methyl-5-hydroxybenzofuran; (20) 1-(4-hydroxy-3-methoxyphenyl)-ethanone (apocynin); (21) 4-butyl-2-methoxyphenol; (22) 4-hydroxy-3-methoxybenzenepropanol
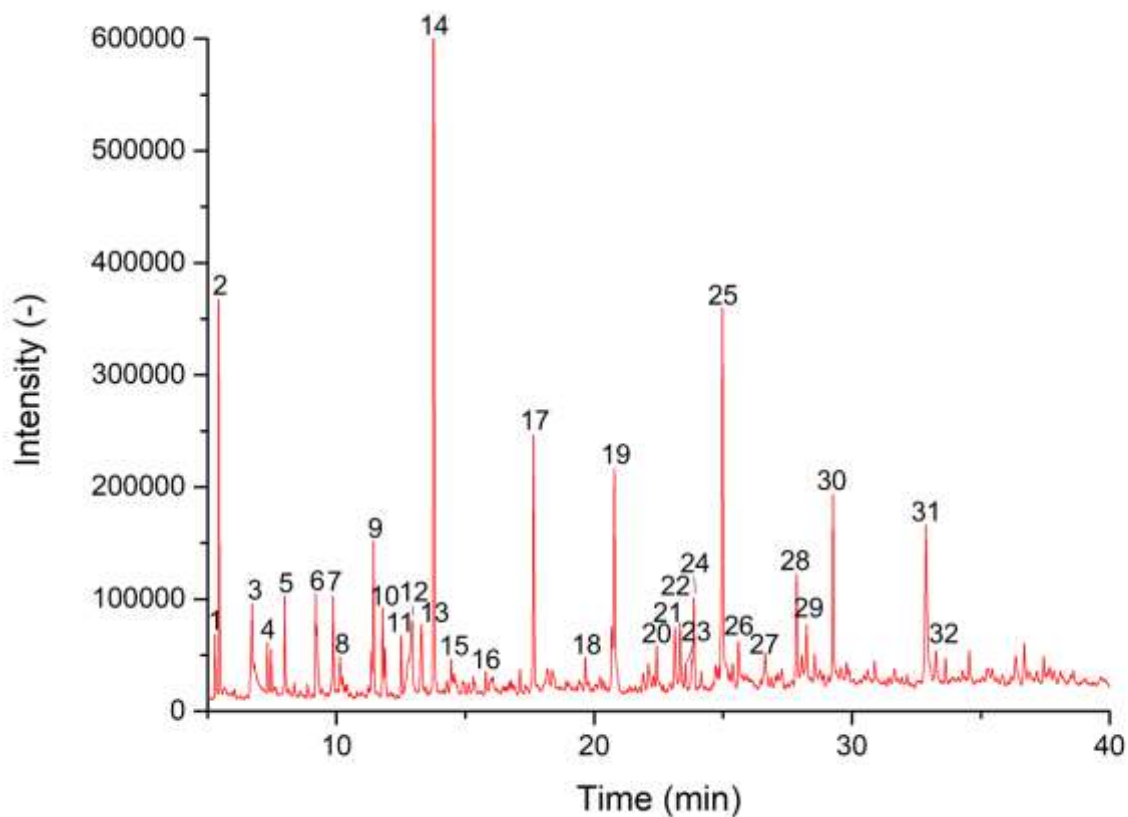
Figure 58. Chromatogram of HTL crude generated from pine wood at 300 °C.
Peak assignment: (1) 2-cyclopentenone; (2) 4-hydroxy-4-methyl-2-pentanone; (3) 2-methyl-2-cyclpentenone; (4) 1-(2-furanyl)-ethanone; (5) 2,5-hexandione; (6) 5-methyl-2-furancarboxaldehyde; (7) 3-methyl-2-cyclopentenone; (8) phenol; (9) 3-methyl-1,2-cyclopentanedione; (10) 2,3-dimethyl-2-cyclopentenone; (11) 2-methylphenol; (13) levulinic acid; (14) 2-methoxyphenol (guaiacol); (15) 2-methylbenzofuran; (16) (2Z)-3-propyl-2,4-pentandienol; (17) 2-methoxy-4-methylphenol (creosol); (18) 3,4-dimethylfuran; (19) 4-ethyl-2-methoxyphenol; (20) 2,3-dimethyl-2-cyclopentenone; (21) 2-methyl-1,4-benzenediol; (22) 2,6-dimethoxyphenol; (23) 2-methoxy-4-(2-propenyl)phenol (eugenol); (24) 2-methoxy-4-propylphenol; (25) 4-hydroxy-3-methoxybenzaldehyde (vanillin); (26) 2-methyl-5-hydroxybenzofuran; (27) (Z)-2-methoxy-4-(1-propenyl)phenol; (28) 1-(4-hydroxy-3-methoxyphenyl)-ethanone (apocynin); (29) 2,5-dimethyl-1,4-benzenedicarboxaldehyde; (30) 4-butyl-2-methoxyphenol; (31) 4-hydroxy-3-methoxybenzenepropanol; (32) 3-methoxy-2-naphthalenol
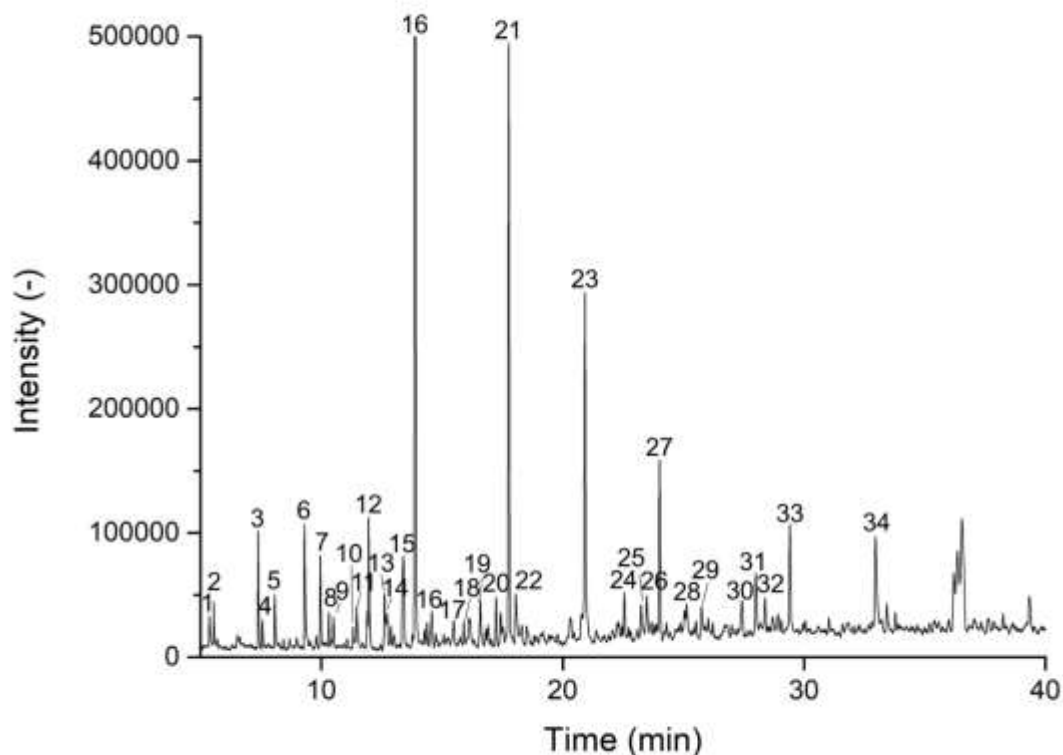
Figure 59. Chromatogram of HTL crude generated from pine wood at 325 °C.
Peak assignment: (1) 2-cyclopentenone; (2) 4-hydroxy-4-methyl-2-pentanone; (3) 2-methyl-2-cyclopentenone; (4) 1-(2-furanyl)-ethanone; (5) 2,5-hexandione; (6) 3-methyl-2-cyclopentanone; (7) phenol; (8) 3,4-dimethyl-2-cyclopentenone; (9) 6-methyl-3-heptyne; (10) (E,Z)-3,4-dimethyl-2,4-hexadiene; (11) 3,6-heptandione; (12) 2,3-dimethyl-2-cyclopentenone; (13) 2-methylphenol; (14) levulinic acid; (15) 3-methylphenol; (16) 2-methoxyphenol (guaiacol); (16) 2-ethyl-3-methylcyclopentenone; (17) 1-acetyl-1,2-epoxy-cyclopentenone; (18) 2,4-dimethylphenol; (19) 1,2,3,4-tetrahydronapthalene; (20) 2-methoxy-3-methylphenol; (21) 2-methoxy-4-methylphenol (creosol); (22) 1,2-dihydroxybenzenediol (catechol); (23) 4-ethyl-2-methoxyphenol; (24) 2,3-dimethyl-2-cyclopentenone (25) 2-methyl-1,4-benzenediol; (26) 2,6-dimethoxyphenol; (27) 2-methoxy-4-propylphenol; (28) 4-hydroxy-3-methoxybenzaldehyde (vanillin); (29) 2-methyl-5-hydroxybenzofuran; (30) 3-allyl-6-methoxyphenol; (31) 1-(4-hydroxy-3-methoxyphenyl)-ethanone (apocynin); (32) 2,3,4,5-tetramethylbenzaldehyde; (33) 4-butyl-2-methoxyphenol; (34) 1-(4-hydroxy-3-methoxyphenyl)-1-propanone; (35) 4-hydroxy-3-methoxybenzenepropanol

The most abundant holocellulose markers were found in all pine wood bio-crude degradation at all processed HTL temperatures (275, 300 and 325 °C), including 4-hydroxy-4-methyl-2-pentanone, 2,5-hexandione and levulinic acid. It was observed with particular attention that levulinic acid was present in all three bio-crudes processed from pine wood as a feedstock, but formic acid was not detected by GC-MS. Holocellulose components tend to be the first components that easily decompose and hydrolyse into lower molecular weight fragments and solvents starting at 250 °C but will also have enough time to repolymerise into char products [85, 247]. Hence 5-methyl-2-furancarboxaldehyde and 3-methyl-1,2-cyclopentanedione were not observed in the bio-crude generated at 325 °C, and

may have been broken down into smaller components or repolymerised into char. During the liquefaction run, the cellulose will undergo through hydrolysis reaction which will lead to glucose, followed by dehydration of glucose and 5-hydroxymethylfurfural. This will lead to a hydration reaction resulting in the formation of formic and levulinic acid [248].

Whereas hemicellulose was readily hydrolysed directly into acetic acid as a by-product which was formed from acetyl ester bonds. The acetic acid acts as a catalyst to degrade the hemicellulose into sugars such as pentose and hexoses from cleaving the glycosidic linkages. The sugars subsequently degrade into furfural and 5-hydroxymethylfurfural, and eventually leading to rehydration from the acids into levulinic acid and formic acid [39].

Lignin markers from all pine wood bio-crudes were also detected including guaiacol, creosol, 4-ethyl-2-methoxyphenol, 2,6-dimethoxyphenol, 2-methoxy-4-propylphenol, vanillin, apocynin and 4-butyl-2-methoxyphenol and 4-hydroxy-3-methoxybenzenepropanol. These were also observed in the LignoBoost lignin bio-crudes, as the feedstock LignoBoost lignin was produced from 50:50 pine wood and spruce. 2,6-dimethoxyphenol is also known as syringol, which is a derivative of sinapyl alcohol and precursor of hardwood lignin. Majority of these 2-methoxyphenol derivatives were observed in Cheng et al [104] and suggested that the depolymerised products went through substitution reactions to form a variety of phenolic compounds.

It was observed that at higher temperatures, a decrease in peak areas of holocellulose markers were decreased (e.g. 4-hydroxy-4-methyl-2-pentanone, 2,5-hexandione, and levulinic acid). 4-hydroxy-4-methyl-2-pentanone was observed with a peak area percentage of 8.39 at 275 °C, which was decreased to 3.17 at 325 °C. 2,5-hexandione and levulinic acid at 275 °C was found with 1.16 and 2.78 respectively. These compounds were not detected at 325 °C. Different thermal degradation behaviour from lignin markers is observed in the pine wood bio-crudes when comparing the bio-crudes from LignoBoost lignin. Large molecular weight products including creosol (13.55 %), 4-ethyl-2-methoxyphenol (9.73 %), 2-methoxy-4-propylphenol (9.80 %), apocynin (5.62 %) and 4-butyl-2-methoxyphenol (3.58 %), saw an increase in the peak area percentage at a higher HTL processed temperature of 325 °C. It was anticipated that these named lignin markers would have a decreased peak area percentage at higher temperatures, as this was similarly observed in the LignoBoost lignin bio-crudes. This could also be explained by the different biochemical compositions found in pine wood when compared to LignoBoost lignin.

5.3.5.　Aqueous phase analysis

Figure 60. Aqueous phase of pine wood, wheat straw and LignoBoost lignin processed at 325 °C.

The aqueous phases (as shown in Figure 60) present in HTL-derived liquids usually receive less attention as opposed to the bio-crude. Those are often considered a by-product or waste. In contrast, previous studies [249-251] have attempted to reuse the aqueous phase samples as HTL co-solvents to reduce the amount of wastewater and to improve bio-crude yield. However, it is advantageous to know what the aqueous phase samples contain and how this can be utilised in an efficient manner. As aqueous phase samples are made up of polar water-soluble molecules, this can lead to complicated sample preparation that requires derivatisation or extraction prior the analysis [224]. When analysing aqueous phase on GC-MS, mainly volatile components will be removed and unable to identify precisely the content of the aqueous phase. Therefore, high-performance liquid chromatography (HPLC) was selected to analyse the aqueous phase samples, which are able to analyse water-soluble components.

Before the HPLC analysis of all aqueous phase samples generated from HTL experiments were screened using GC-MS with particular attention to the presence of specific markers and presented in Figure 63 and Figure 66.
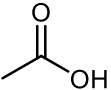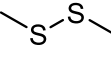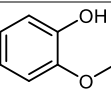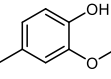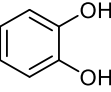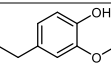
A literature review [252-256] was conducted and it mainly found mainly carboxylic acids in the aqueous phase along with guaiacol and methanol. Therefore, carboxylic acids (including formic, acetic, propionic and levulinic acids), lignin markers (guaiacol and 4-ethyl-2-methoxyphenol), holocellulose marker (furfural and 5-methylfurfural) and methanol were selected and injected into the Restek Ultra
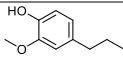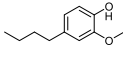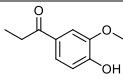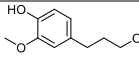
Aqueous C18 Column and analysed by the HPLC, and these HPLC chromatograms are presented from Figure 67 to Figure 70.

5.3.5.1. Gas Chromatography-Mass Spectrometry of aqueous phases

Prior to the HPLC analysis of selected carboxylic acids, lignin and holocellulose markers, and methanol, all aqueous phase from HTL experiments at 275, 300 and 325 °C of LignoBoost lignin and pine wood were analysed by GC-MS. GC-MS chromatograms from this analysis are presented from Figure 61 to Figure 66. Table 26 and Table 27 summarised the most abundant components identified in HTL aqueous phases for LignoBoost lignin and pine wood, respectively. Particular attention was paid to carboxylic acids that had peak areas of less than 1 %. It should be noted that the peak area percentage values are not the actual concentration, but only the relative concentration of each product in the fraction of the aqueous phase was able to be vaporised and passed through the GC column. The peak area percentage does not add up to 100 %, as there were unidentified peaks.

Table 26. Identified components in LignoBoost lignin aqueous phase from HTL at 275, 300 and 325 °C by GC-MS analysis.

Retention Time (min)	Name	Formula	MW	Structure	m/z	Area (%)		
						275 °C	300 °C	325 °C
2.38	acetic acid	$C_2H_4O_2$	60		60.02 (100.0 %), 61.02 (2.2 %)	0.68	0.82	1.70
3.56	dimethyl disulphide	$C_2H_6S_2$	93		93.99 (100.0 %), 95.99 (4.5 %), 94.99 (2.22 %), 94.99 (1.6 %)	1.00	0.86	0.19
13.91	2-methoxyphenol (guaiacol)	$C_7H_8O_2$	124		124.05 (100.0 %), 125.06 (7.6 %)	24.65	32.79	34.92
17.77	2-methoxy-4-methylphenol (creosol)	$C_8H_{10}O_2$	138		138.07 (100.0 %), 139.07 (8.7 %)	5.00	10.34	12.18
18.11	1,2-dihydroxybenzene (catechol)	$C_6H_6O_2$	110		110.04 (100.0 %), 111.04 (6.5 %)	-	0.57	6.79
20.92	4-ethyl-2-methoxyphenol	$C_9H_{12}O_2$	152		152.08 (100.0 %), 153.09 (9.7 %)	5.75	8.13	6.25

24.00	2-methoxy-4-propylphenol	$C_{10}H_{14}O_2$	166		166.10 (100.0 %), 167.10 (10.8 %)	3.27	3.65	1.80
29.41	4-butyl-2-methoxyphenol	$C_{11}H_{16}O_2$	180		180.12 (100.0 %), 181.12 (11.9 %)	10.84	9.44	8.79
31.02	1-(4-hydroxy-3-methoxyphenyl)-1-propane	$C_{10}H_{12}O_3$	180		180.08 (100.0 %), 181.08 (10.8 %)	1.14	0.87	0.46
32.95	4-hydroxy-3-methoxybenzenepropanol	$C_{10}H_{14}O_3$	182		182.09 (100.0 %), 183.10 (10.8 %)	18.01	12.63	9.00
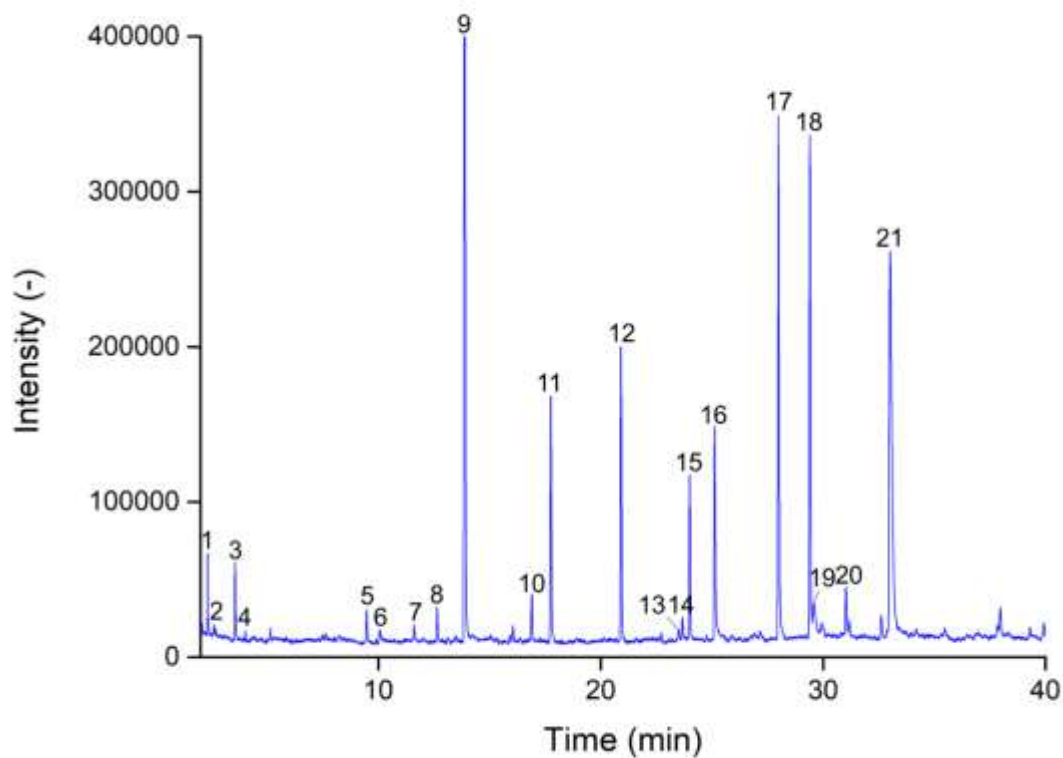
Figure 61. Gas chromatogram of LignoBoost lignin aqueous phase at 275 °C.
Peak assignment: (1) acetic acid; (2) thiophene; (3) dimethyl disulphide; (4) 3-methylthiophene; (5) dimethyl trisulphide; (6) phenol; (7) 3-methyl-1,2-cyclopentanedione; (8) 3-ethyl-2-hydroxy-2-cyclopentenone; (9) 2-methoxyphenol (guaiacol); (10) 1,1-bis(methylthio)-ethane; (11) 2-methoxy-4-methylphenol (creosol); (12) 4-ethyl-2-methoxyphenol; (13) 2,6-dimethoxyphenol; (14) 2-methoxy-4-(2-propenyl)phenol (eugenol); (15) 2-methoxy-4-propylphenol; (16) 3-hydroxy-4-methoxybenzaldehyde; (17) 1-(4-hydroxy-3-methoxyphenyl)-ethanone (apocynin); (18) 4-butyl-2-methoxyphenol; (19) 3-methoxy-4-hydroxyphenylethanol; (20) 1-(4-hydroxy-3-methoxyphenyl)-1-propanone; (21) 4-hydroxy-3-methoxy-benzenepropanol;
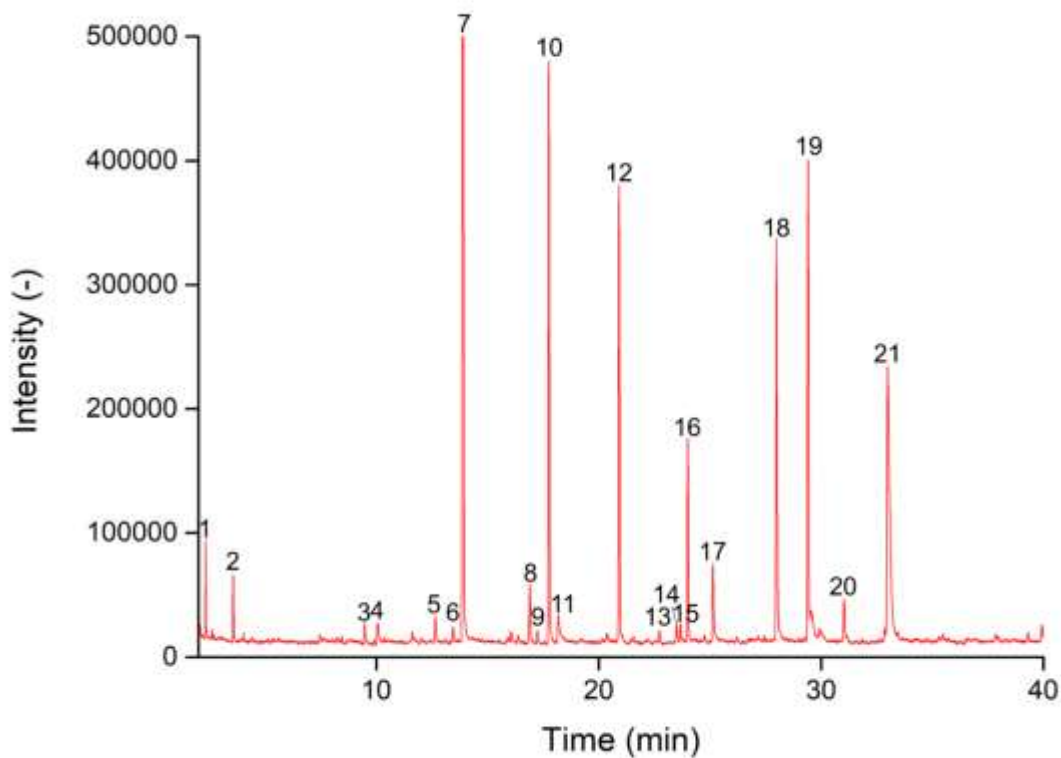
Figure 62. Gas chromatogram of LignoBoost lignin aqueous phase at 300 °C.
Peak assignment: (1) acetic acid; (2) dimethyl disulphide; (3) dimethyl trisuphide; (4) phenol; (5) 3-ethyl-2-hydroxy-2-cyclopentenone; (6) 4-methylphenol (p-Cresol); (7) 2-methoxyphenol (guaiacol); (8) 1,1-bis(methylthio)-ethane; (9) 2-methoxy-3-methylphenol; (10) 2-methoxy-4-methylphenol (creosol); (11) 1,2-dihydroxybenzene (catechol); (12) 4-ethyl-2-methoxyphenol; (13) 5-acetyl-2-methoxyphenyl acetate; (14) 2,6-dimethoxyphenol; (15) 2-methoxy-4-(2-propenyl)phenol (eugenol); (16) 2-methoxy-4-propylphenol; (17) 3-hydroxy-4-methoxybenzaldehyde; (18) 1-(4-hydroxy-3-methoxyphenyl)-ethanone (apocynin); (19) 4-butyl-2-methoxyphenol; (20) 1-(4-hydroxy-3-methoxyphenyl)-1-propanone; (21) 4-hydroxy-3-methoxybenzenepropanol
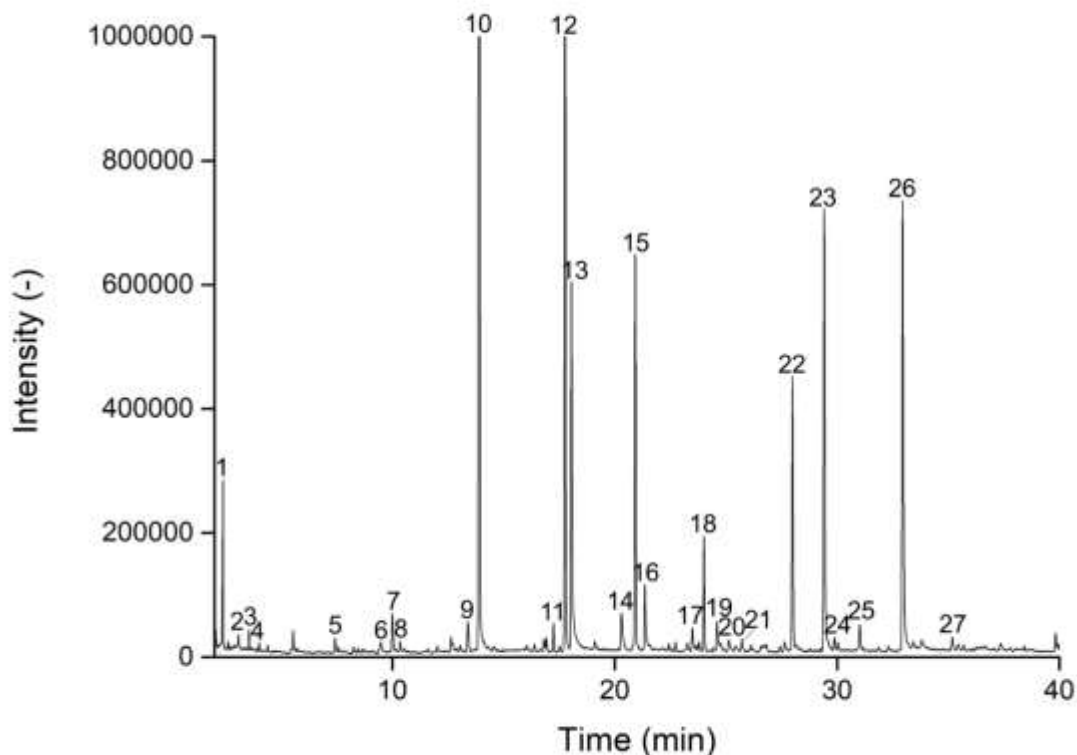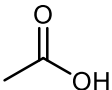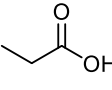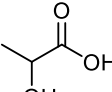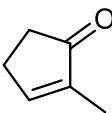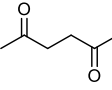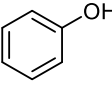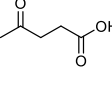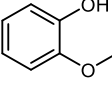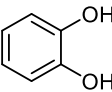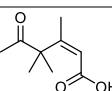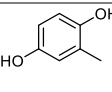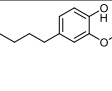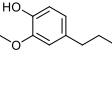
Figure 63. Gas chromatogram of LignoBoost lignin aqueous phase at 325 °C.
Peak assignment: (1) acetic acid; (2) propionic acid; (3) dimethyl disulphide; (4) 2-methylthiophene; (5) 2-methyl-2-cyclopentenone; (6) dimethyl trisulphide; (7) phenol; (8) 3,5-dimethyl-2-cyclopentenone; (9) 4-methylphenol (p-Cresol); (10) 2-methoxyphenol (guaiacol); (11) 2-methoxy-3-methylphenol; (12) 2-methoxy-4-methylphenol (creosol); (13) 1,2-dihydroxybenzene (catechol); (14) 3-methoxy-1,2-benzenediol; (15) 4-ethyl-2-methoxyphenol; (16) 4-methyl-1,2-benzenediol; (17) 2,6-dimethoxyphenol; (18) 2-methoxy-4-propylphenol; (19) 4-ethyl-1,2-benzenediol; (20) 2-methoxy-1,4-benzenediol; (21) 2,5-dimethyl-1,4-benzenediol; (22) 1-(3-hydroxy-4-methoxyphenyl)-ethanone; (23) 4-butyl-2-methoxyphenol; (24) 4-hydroxy-3-methoxybenzenepropanol; (25) 1-(4-hydroxy-3-methoxyphenyl)-1-propanone; (26) 4-hydroxy-3-methoxybenzenepropanol; (27) 3-(3,4-dimethoxyphenyl)-1-propanol

The only carboxylic acid identified in LignoBoost lignin aqueous phase was acetic acid. Very small quantity of acetic acid (of less than 1 % peak area) was identified at lower temperatures of 275 and 300 °C, which was found at 0.68 % and 0.82 %, respectively. An increase in HTL temperature to 325 °C did enhance the production of acetic acid at a peak area of 1.70 %. The acetic acid may have been formed from the traces of holocellulose content found in the LignoBoost lignin. The only sulphuric product observed was dimethyl disulphide and was derived from the delignification process, which used sulphur. A significant amount of lignin markers, including guaiacol, creosol, catechol, 4-ethyl-2methoxyphenol, 2-methoxy-4-propylphenol, 4-butyl-2-methoxyphenol, 1-(4-hydroxy-3-methoxyphenyl)-1-propane and 4-hydroxy-3-methoxybenzenepropanol were found in the aqueous phases. The most abundant product was guaiacol seen at increased abundance at higher

temperatures. It is believed that this occurs at higher temperature as the lignin bonding are broken down. According to Brebu and Vasile [257], the β-β and C-C linkages found in the lignin units will cleave at 275-350 °C to guaiacol and guaiacol-type compounds including creosol, 4-ethyl-2-methoxyphenol, 2-methoxy-4-propylphenol and 4-butyl-2-methoxyphenol. However, it can also be observed that higher molecular weight products like 4-ethyl-2-methoxyphenol, 2-methoxy-4-propylphenol and 4-butyl-2-methoxyphenol started to decrease at higher temperature and may have broken down into smaller fragments. Some of these phenolics may undergo a repolymerisation to produce coke [30]. Guaiacol will be broken down during hydrolysis reaction into important intermediates such as catechol and phenol. Although phenol is not included in the table, but is present in small quantities (< 1 % peak area). Studies [258, 259] have reported catechol or catechol derivatives found in the bio-crude and aqueous phase. In this study, catechol was not identified in the bio-crudes, and cannot be found in the aqueous phase at a lower temperature of 275 °C. The increase in the concentration of catechol was only found at 300 and 325 °C with a peak area of 0.57 % and 6.79 % respectively. However, it was also found that an increase in temperature and in residence time will promote the production of catechol [31]. Another explanation was that catechol and catechol derivatives are not directly present in natural lignin and are formed from secondary decomposition from guaiacol requiring longer residence times [257].

Table 27. Identified components in pine wood aqueous phase from HTL at 275, 300 and 325 °C by GC-MS analysis.

Retention Time (min)	Name	Formula	MW	Structure	*m/z*	Area (%) 275 °C	Area (%) 300 °C	Area (%) 325 °C
2.38	acetic acid	$C_2H_4O_2$	60		60.02 (100.0 %), 61.02 (2.2 %)	13.32	23.85	25.59
3.12	propionic acid	$C_3H_6O_2$	74		74.04 (100.0 %), 75.04 (3.2 %)	0.53	0.88	1.51
6.88	lactic acid	$C_3H_6O_3$	90		90.03 (100.0 %), 91.04 (3.2 %)	2.13	4.03	3.26
7.40	2-methyl-2-cyclopentanone	C_6H_8O	96		96.06 (100.0 %), 97.06 (6.5 %)	0.44	1.25	1.65
8.20	2,5-hexadione	$C_6H_{10}O_2$	114		114.07 (100.0 %), 115.07 (6.5 %)	0.89	1.60	1.55
10.02	phenol	C_6H_6O	94		94.04 (100.0 %), 95.05 (6.5 %)	0.24	0.59	1.02
13.09	levulinic acid	$C_5H_8O_3$	116		116.06 (100.0 %), 117.05 (5.4 %)	0.92	0.59	3.88
13.90	2-methoxyphenol (guaiacol)	$C_7H_8O_2$	124		124.05 (100.0 %), 125.06 (7.6 %)	1.81	5.33	10.00
18.14	1,2-dihydroxybenzene (catechol)	$C_6H_6O_2$	110		110.04 (100.0 %), 111.04 (6.5 %)	-	0.20	5.26
22.55	(Z)-3,4,4-trimethyl-5-oxo-2-hexenoic acid	$C_9H_{14}O_3$	170		170.09 (100.0 %), 171.10 (9.7 %)	0.19	0.35	1.13
23.24	2-methyl-1,4-benzenediol	$C_7H_8O_2$	124		124.05 (100.0 %), 125.06 (7.6 %)	0.33	0.76	2.26
29.42	4-butyl-2-methoxyphenol	$C_{11}H_{16}O_2$	180		180.12 (100.0 %), 181.12 (11.9 %)	0.55	0.87	1.65
32.96	4-hydroxy-3-methoxybenzenepropanol	$C_{10}H_{14}O_3$	182		182.09 (100.0 %), 183.10 (10.8 %)	1.06	2.16	2.55
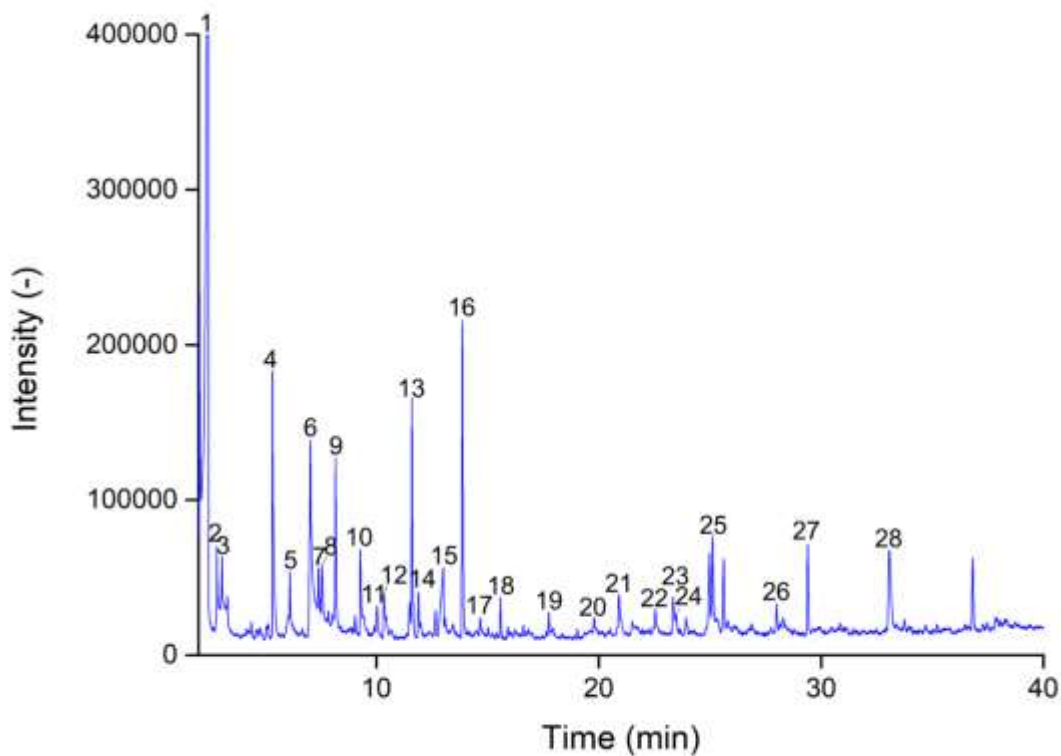
Figure 64. Gas chromatogram of pine wood aqueous phase at 275 °C.
Peak assignment: (1) acetic acid; (2) 1-acetate 1,2-propanediol; (3) propionic acid; (4) furfural; (5) butanal; (6) lactic acid; (7) 2-methyl-2-cylopentenone; (8) 1-(2-furanyl)-ethanone; (9) 2,5-hexandione; (10) 5-methyl-2-furancarboxaldehyde; (11) phenol; (12) cyclopentanol; (13) 3-methyl-1,2-cyclopentanedione; (14) 2-acetyl-5-methylfuran; (15) levulinic acid; (16) 2-methoxyphenol (guaiacol); (17) 2-methyl-4-oxopentanoic acid; (18) 3-ethyl-2-hydroxy-2-cyclopentenone; (19) 2-methoxy-4-methylphenol (creosol); (20) 3,4-dimethylfuran; (21) 3-hydroxyphenyl acetate; (22) (Z)-3,4,4-trimethyl-5-oxo-2-hexenoic acid; (23) 2-methyl-1,4-benzenediol; (24) 2,6-dimethoxyphenol; (25) 4-hydroxy-3-methoxybenzaldehyde (vanillin); (26) 1-(4-hydroxy-3-methoxyphenyl)-ethanone (apocynin); (27) 4-butyl-2-methoxyphenol; (28) 4-hydroxy-3-methoxybenzenepropanol
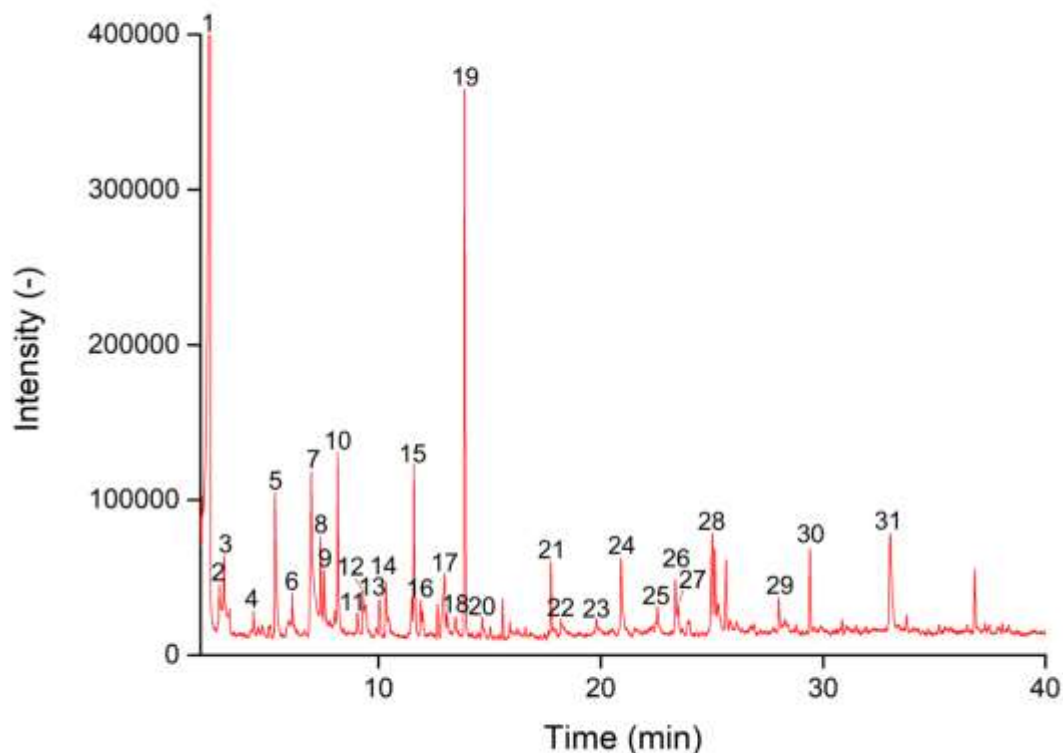
Figure 65. Gas chromatogram of pine wood aqueous phase at 300 °C.
Peak assignment: (1) acetic acid; (2) methyl 2-butyoxyacetate; (3) propionic acid; (4) cyclopentanone; (5) 2,5-dimethylfuran; (6) butanal; (7) lactic acid; (8) 2-methyl-2-cyclopentenone; (9) 1-(2-furanyl)-ethanone; (10) 2,5-hexandione; (11) dihydro-5-methyl-2(3H)-furanone; (12) 5-methyl-2-furancarboxaldehyde; (13) phenol; (14) cyclopentanol; (15) 3-methyl-1,2-cyclopentanedione; (16) 2,3-dimethyl-2-cyclopentenone; (17) levulinic acid; (18) 3-methylphenol; (19) 2-methoxyphenol (guaiacol); (20) 2-methyl-4-oxopentanoic acid; (21) 2-methoxy-4-methylphenol (creosol); (22) 1,2-dihydroxybenzenediol (catechol); (23) 3,4-dimethylfuran; (24) 3-hydroxyphenyl acetate; (25) (Z)-3,4,4-trimethyl-5-oxo-2-hexenoic acid; (26) 2-methyl-1,4-benzenediol; (27) 2,6-dimethoxyphenol; (28) 4-hydroxy-3-methoxybenzaldehyde (vanillin); (29) 1-(4-hydroxy-3-methoxyphenyl)-ethanone (apocynin); (30) 4-butyl-2-methoxyphenol; (31) 4-hydroxy-3-methoxybenzenepropanol
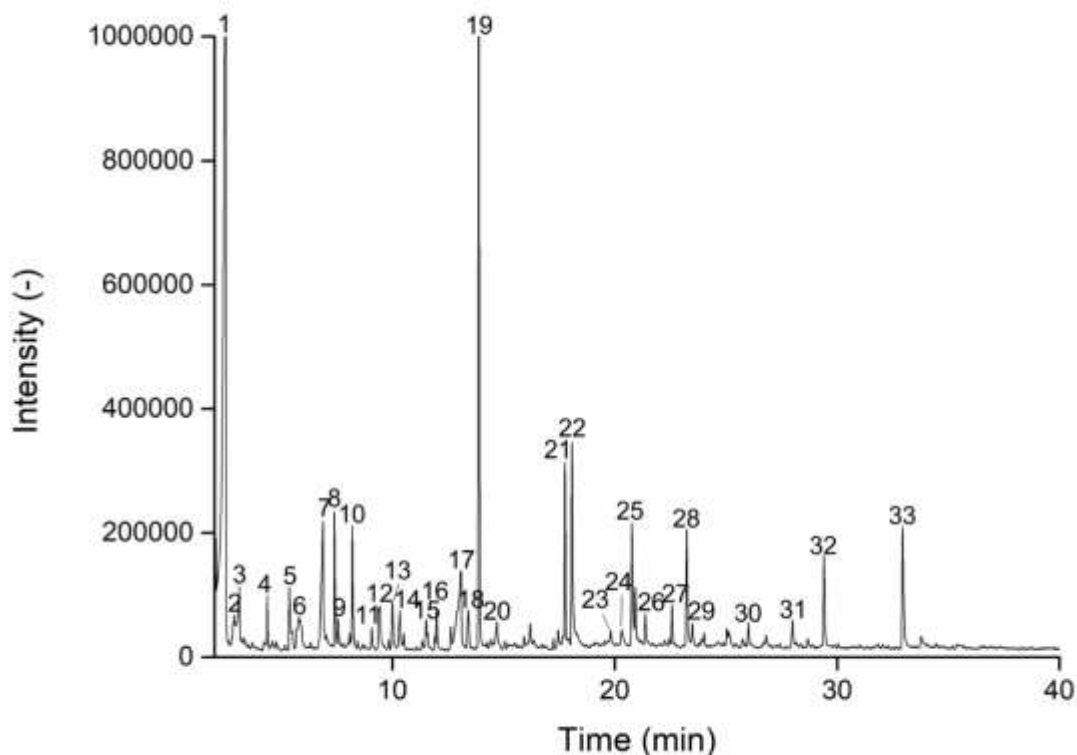
Figure 66. Gas chromatogram of pine wood aqueous phase at 325 °C.
Peak assignment: (1) acetic acid; (2) 3-pentanone; (3) propionic acid; (4) cyclopentanone; (5) 2-cyclopentenone; (6) ethyl formate; (7) lactic acid; (8) 2-methyl-2-cyclopentenone; (9) 1-(2-furanyl)-ethanone; (10) 2,5-hexandione; (11) dihydro-5-methyl-2(3H)-furanone; (12) 3-methyl-2-cyclopentenone; (13) phenol; (14) 4-methyl-1-penten-3-ol; (15) 3,4-dimethyl-2-cyclopentenone; (16) 2,3-dimethyl-2-cyclopentenone; (17) levulinic acid; (18) 3-methylphenol; (19) 2-methoxyphenol (guaiacol); (20) 2-methyl-4-oxopentanoic acid; (21) 2-methoxy-4-methylphenol (creosol); (22) 1,2-dihydroxybenzene (catechol); (23) 3,4-dimethylfuran; (24) 3-methoxy-1,2-benzenediol; (25) 4-methyl-1,4-benzenediol; (26) 4-methyl-1,2-benzenediol; (27) (Z)-3,4,4-trimethyl-5-oxo-2-hexenoic acid; (28) 2-methyl-1,4-benzenediol; (29) 2,6-dimethoxyphenol; (30) ethylparaben; (31) 1-(4-hydroxy-3-methoxyphenyl)-ethanone (apocynin); (32) 4-butyl-2-methoxyphenol; (33) 4-hydroxy-3-methoxybenzenepropanol

Most of the aqueous phase products were carboxylic acids, along with some holocellulose and lignin markers. Carboxylic acids, including acetic, propionic, lactic and levulinic acid were identified in all pine wood aqueous phases. The most prevalent carboxylic acid was found to be acetic acid with a maximum peak area of 25.59 % obtained at 325 °C. Whilst at lower HTL processing temperature, a peak area of 13.32 and 23.85 % was found in acetic acid at 275 and 300 °C, respectively. The similar upward trend was also found in the propionic acid when increasing the temperature from 275 to 325 °C and found an increasing peak area from 0.53 to 1.51 %. This observation was also found to be in line with the literature, and found an increase in concentration in the acetic acid and propionic acid using HTL from pine wood [260]. The increase of temperature will impact the holocellulose to breakdown into lower molecular weight products, including acetic and propionic acid [34]. Acetic acid

was mainly formed from the cleaving acetyl group linked to the xylose unit from hemicellulose [34]. Whereas, propionic acid was another components as a result from degradation of hemicellulose. Levulinic acid was the only carboxylic acid that was present in the bio-crudes and aqueous phase samples from pine wood. From cellulose degradation, the acidic condition in liquefaction processing will promote the production of 5-hydroxymethylfurfural and levulinic acid. Whereas under basic conditions, acetic and lactic acids are generated [70]. Lactic acid was also observed, and may be derived from dehydration rearrangement of pyruvaldehyde from holocellulose [261]. Interestingly, the concentration of lactic acid was slightly increased at 300 °C (4.03 %) and then decreased to 3.26 (%) at 325 °C.

Small quantities of holocellulose markers, 2-methyl-2-cyclopentanone and 2,5-hexandione, were also observed in the aqueous phases. 2,5-hexandione was also found in the pine wood bio-crudes. Both 2-methyl-2-cyclopentanone and 2,5-hexadione concentrations increased when the increasing temperature. However, 2,5-hexandione gained a maximum peak area of 1.60 % at 300 °C, which was then slightly decreased to 1.55 % at 325 °C.

Phenol, guaiacol, catechol, 2-methyl-1,4-benzenediol, 4-butyl-2-methoxyphenol and 4-hydroxy-3-methoxybenzenepropanol are typical lignin degradation markers that were also observed in the aqueous phase from pine wood. Phenol was observed in very small quantities with a maximum peak area of 1.02 % at 325 °C, which is derived from the degradation of guaiacol. Like phenol, increase in temperature also increased the production of guaiacol at a maximum peak area of 10.00 % at 325 °C. The catechol was not observed in either bio-crudes produced from LignoBoost lignin or pine wood, but observed in both feedstock aqueous phase samples. Similar trend was observed with catechol in both samples, where catechol was not observed at 275 °C. However, once the temperature increased to 300 °C, a small peak area of 0.20 % was observed and further increased to 5.26 % at 325 °C. Larger molecular weight products including 2-methyl-1,4-benzenediol, 4-butyl-2-methoxyphenol and 4-hydroxy-3-methoxybenzenepropanol were found in smaller quantities of 2.26, 1.65 and 2.55 % respectively.

5.3.5.2.   Method development and aqueous phase by high performance liquid chromatography

The GC-MS analysis and literature review conducted [252-256], mainly found carboxylic acids in the aqueous phase samples. Furthermore, it was further investigated that acids and alcohols have a higher affinity with water and mainly found in aqueous samples [262]. Therefore, each individual carboxylic acid (acetic, propionic, formic and levulinic acids), holocellulose and lignin markers, and one alcohol

were injected in the high-performance liquid chromatography (HPLC) and presented in Figure 67, Figure 68, Figure 69 and Figure 70 respectively. LignoBoost lignin and pine wood aqueous phase samples were injected in HPLC and compared with all individual carboxylic acid, holocellulose and lignin markers, and alcohol. The aqueous samples of LignoBoost and pine wood generated at 325 °C are presented in Figure 71. The peaks of both aqueous phase samples were identified using the individual compounds' retention times.
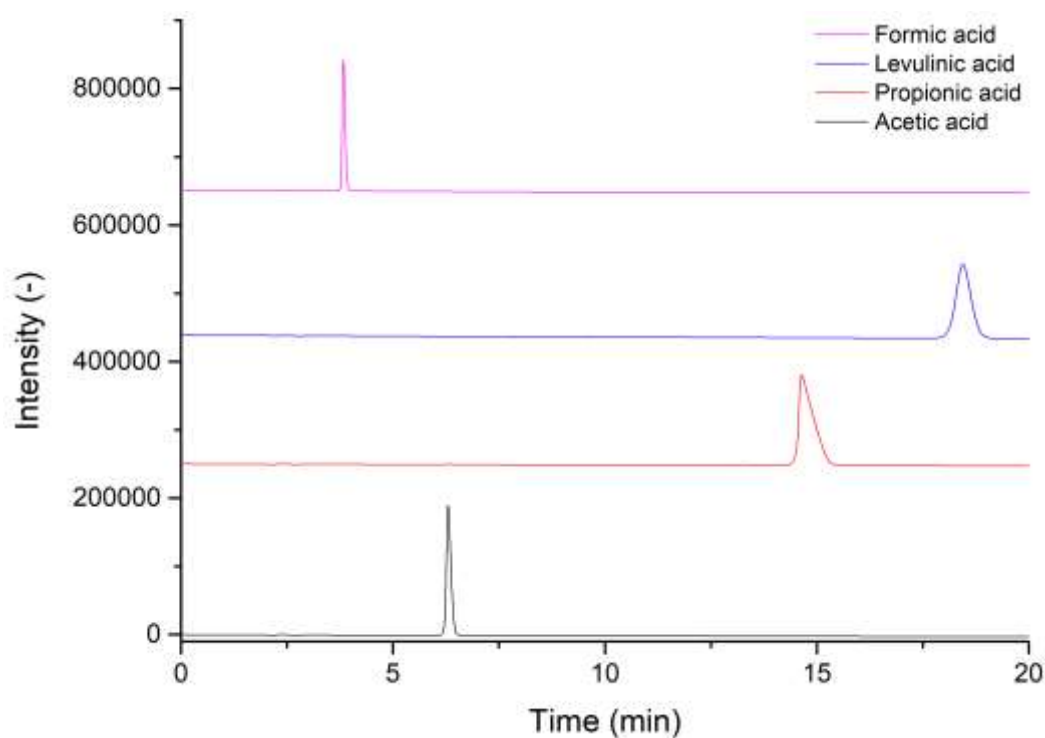
Figure 67. Liquid chromatogram of carboxylic acids, including acetic, propionic, formic and levulinic acid.
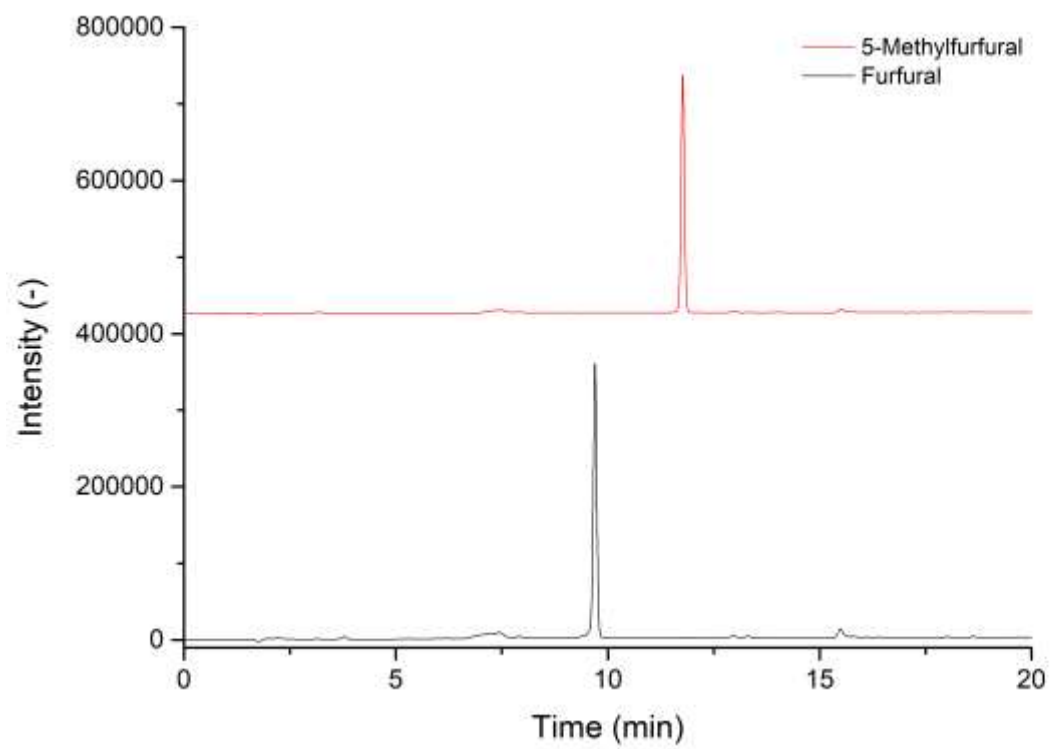
Figure 68. Liquid chromatogram of furfural and 5-methylfurfural.
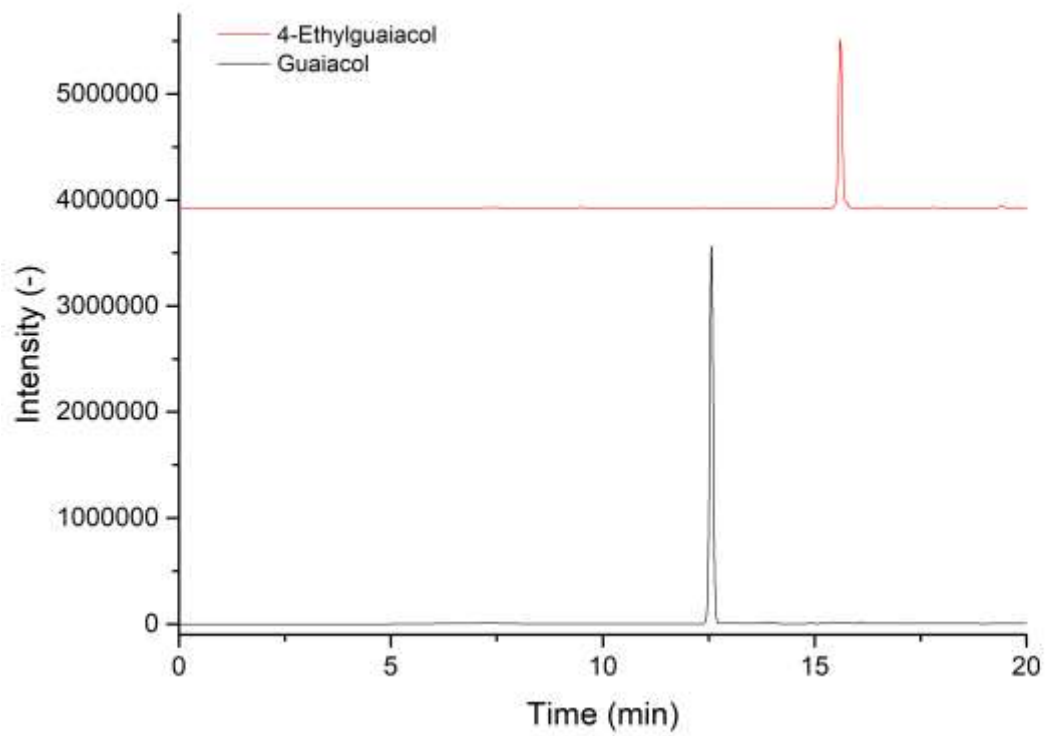
Figure 69. Liquid chromatogram of lignin markers, including 2-methoxyphenol (guaiacol) and 4-ethyl-2-methoxyphenol (4-ethylguaiacol).
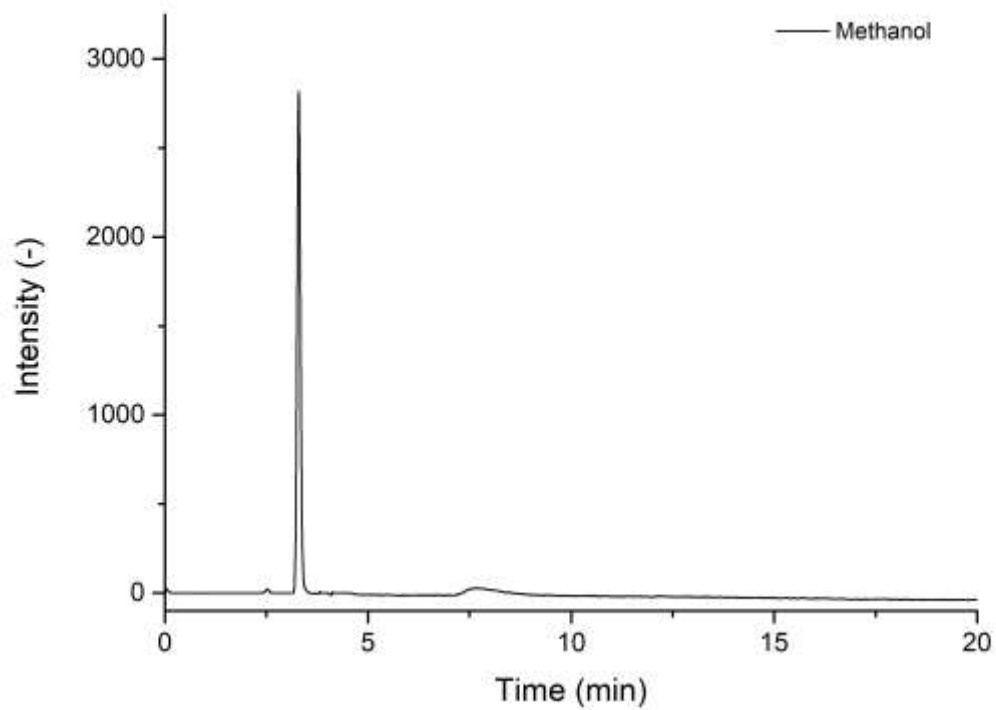
Figure 70. Liquid chromatogram of methanol.
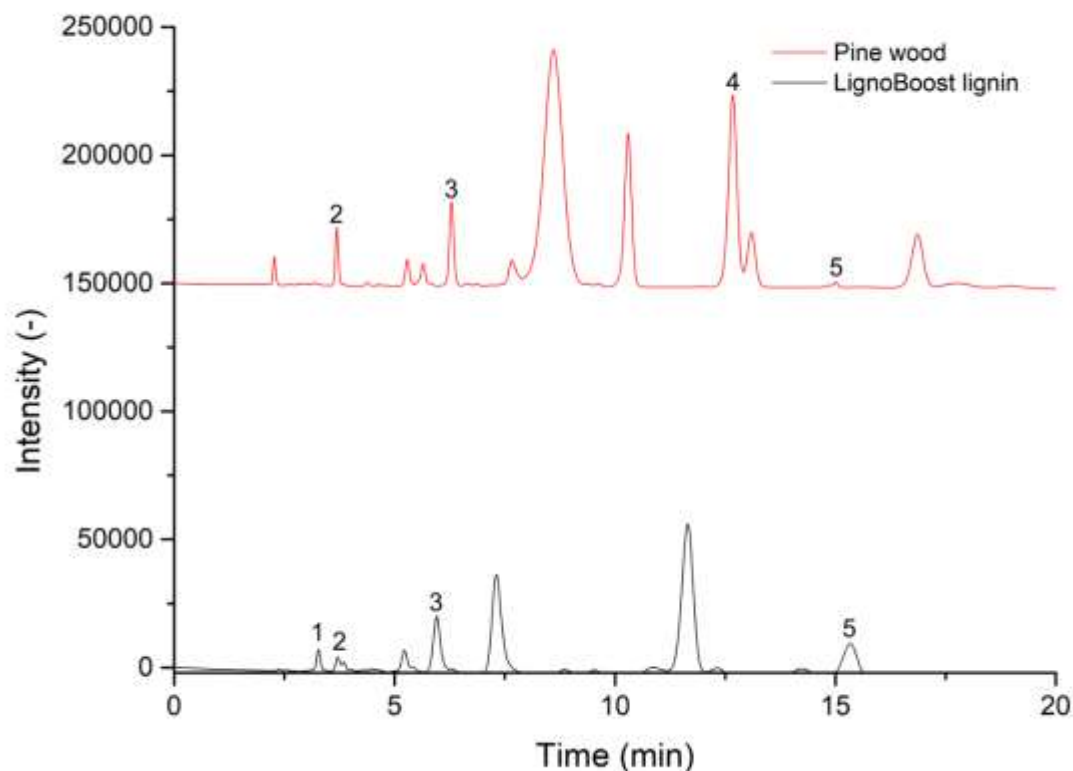
Figure 71. Liquid chromatogram of pine wood and LignoBoost lignin aqueous phase samples generated at 325 °C.

Peak assignment: (1) methanol; (2) formic acid; (3) acetic acid; (4) guaiacol; (5) propionic acid

The HPLC analysis has revealed that methanol, formic acid, acetic acid and propionic acid were found in the aqueous phase samples produced from LignoBoost lignin. In contrast, formic acid, acetic acid, guaiacol and propionic acid were found in the pine wood aqueous phase sample. Methanol and formic acid were previously not detected in LignoBoost lignin aqueous phase sample from GC-MS analysis, as it was easily devolatilised and a low molecular weight product. However, methanol, formic acid and acetic acid were detected in liquid samples using lignin decomposition processing from a study conducted by Beauchet et al [229]. Various competing reactions are occurring along with hydrolysis reactions of methoxyl groups and the cleaving in C-C bonds in the propanoid chains of lignin, which resulted in the formation of methanol, formic and acetic acids [229]. Formic and acetic acids can also be produced from the degradation of glucose in alkaline or neutral conditions. It was further confirmed that acetic acid can be formed from hydrothermal reactions, but biomass slurry will also contain acetic acid and could have been already dissolved in the water [262]. Guaiacol was only found in pine wood aqueous phase samples, which was previously identified as one of the main products found in both the bio-crude and aqueous phase samples. In both Lignoboost lignin and pine wood aqueous phase samples, propionic acid was observed, which was also identified in the GC-MS analysis.

5.3.6. Scanning Electron Microscopic imaging of biomass and bio-char

Scanning Electron Microscopic (SEM) images of the unprocessed biomass LignoBoost lignin and pine wood were compared with the HTL-generated LignoBoost lignin and pine wood bio-char obtained at 325 °C. These are presented in Figure 72.

(a)

(b)

(c)

(d)
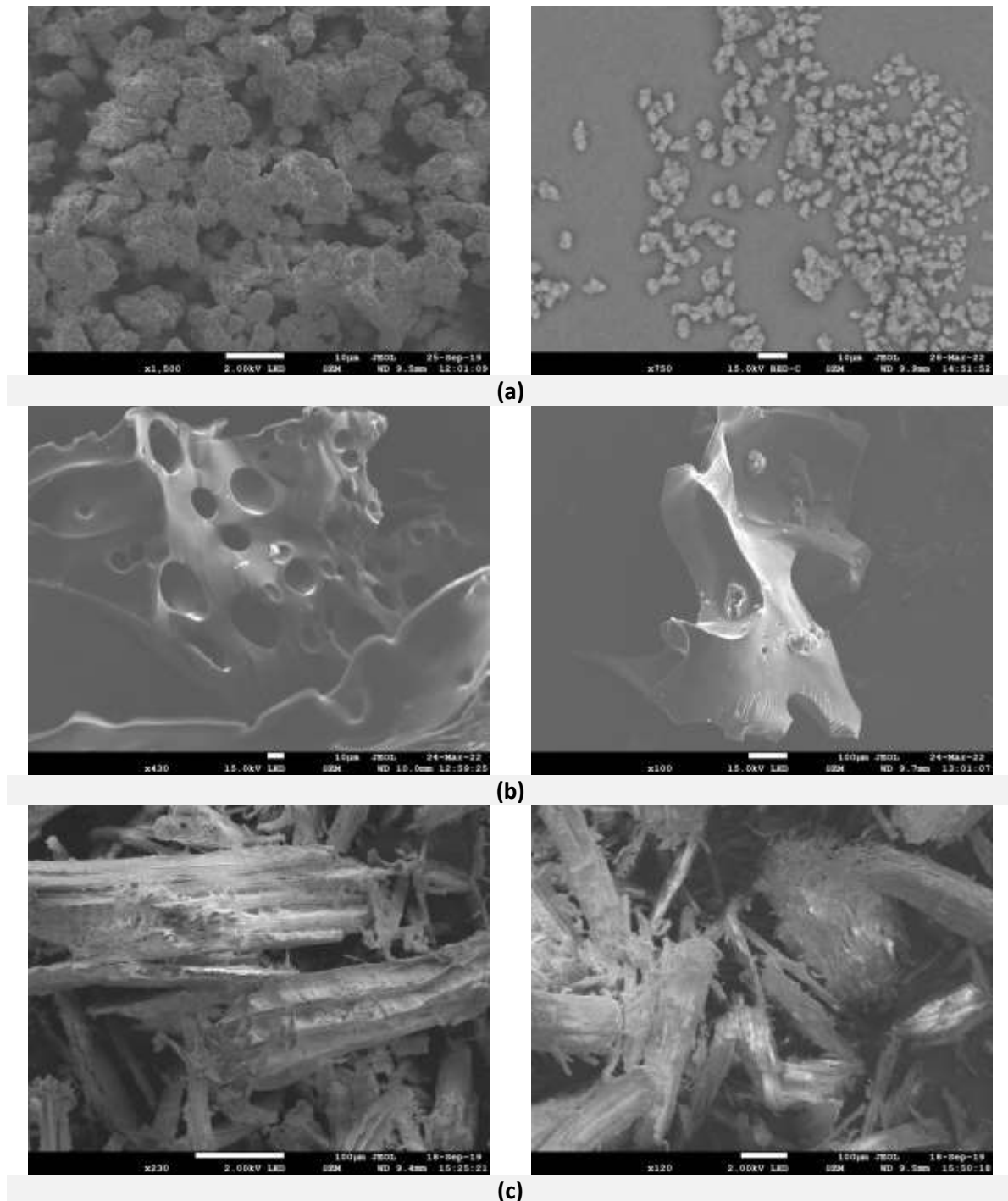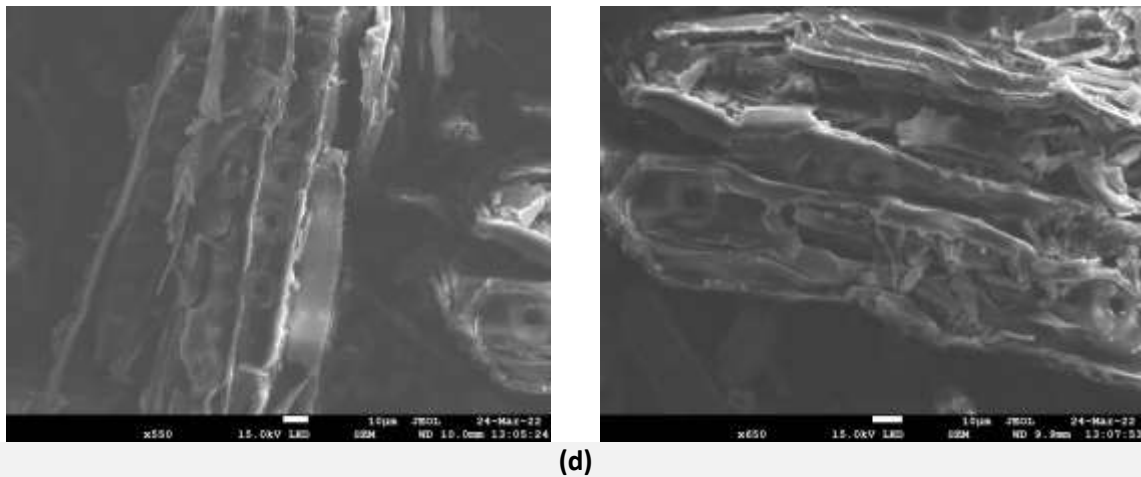
Figure 72. SEM of (a) LignoBoost lignin (b) LignoBoost lignin char and (c) pine wood (d) pine wood char.

The structure of the unprocessed (as received) LignoBoost lignin presented in Figure 72a appear to be granular-like and clustered together with friable, with rough surfaces and non-porous structure. Figure 72b shows the HTL-generated bio-char from LignoBoost lignin appeared to be completely different from its original structure. One explanation could be due to the HTL processing and the increase in temperature, which will go through the destruction and deformation. The LignoBoost lignin bio-char developed pores of different sizes and distributed all over the surface. Unlike its original structure, the char has a smooth surface with an uneven structure. During the char formation, the lignin undergoes through softening, melting, and fusing stages as well as the releasing of volatiles [263]. According to Hu et al [79], bio-char generated at elevated temperatures will produce a large surface area and large pore volume. Pores were created due to the release of volatiles and resulted in larger surface area or produced due to the water permeating into the pores [79].

The SEM images of the unprocessed pine wood (Figure 72c) had a longitudinal and rough morphological structure. The structure appeared to be destroyed and fragile, which could be due to the grinding and sieving of the biomass. Pine wood char (Figure 72d) obtained from the HTL experiment has shown to have pores as well. The pores could be formed at elevated temperatures, which also resulted in larger, visible pores due to the destruction and deformation of the lignocellulosic biomass [264]. The SEM images of pine wood char have shown the structure to be uneven and rough, but maintained the longitudinal structure.

Chapter 6

Product analysis of liquefaction in molten salts

6.1. Introduction

This chapter concentrates on characterisation of the individual salts, eutectic mixture of molten salt, recycled salts and recovered chars from liquefaction processing using molten salts with pine wood and LignoBoost lignin. The main stress was put on the characterisation of recycled (recovered) salts along with all its constituent prior application in the liquefaction process. The molten salt and recycled salts were characterised using a wide range of analytical methods including X-ray diffraction (XRD), differential scanning calorimetry (DSC) and X-ray fluorescence (XRF). Whilst the recovered chars were characterised using thermogravimetric analysis (TGA), elemental analysis, XRF and scanning electron microscopic-energy dispersive x-ray (SEM-EDX).

Recycled molten salts and recovered char samples were derived from the liquefaction of molten salts from pine wood and LignoBoost lignin processing. The recovered/recycled molten salt samples have been re-used twice under the same liquefaction conditions and these molten salts were recovered three times. The recovered chars were compared with the char produced from hydrothermal liquefaction (HTL) described in Chapter 5.

Individual salts including zinc chloride ($ZnCl_2$), potassium chloride (KCl), sodium chloride (NaCl), calcium chloride ($CaCl_2$), potassium carbonate (K_2CO_3) and calcium chloride ($CaCl_2$) were characterised using XRD to understand the crystallinity and the diffractogram patterns. The XRD analysis was also performed on the eutectic mixture of $ZnCl_2$:KCl:NaCl at a molar ratio of 44.3:41.9:13.8 respectively [6]. This particular eutectic was chosen as a desirable "molten salt" for the application in liquefaction of pine wood and LignoBoost lignin.

Part of this research chapter was to investigate the interaction of biomass' inorganic matter or 'impurities' with molten salts. Based on the inorganic elemental analysis in Chapter 3 as outlined in Table 28, wheat straw and its ashes were found with a significant amount of potassium (K), which was

found to be 0.905 and 18.37 % respectively. In comparison, large amounts of calcium (Ca) were identified in pine wood and pine wood ashes with 0.11 and 24.26, respectively.

Table 28. Inorganic elements found in pine wood, wheat straw and its ashes.

Feedstock	Most abundant elements found	Inorganic elements corresponding to element interaction studies with molten salt
Pine wood	Cl (0.14 %), Ca (0.11 %), K (0.03 %), Si (0.0266 %) and Mg (0.023 %)	$CaCl_2$ and $CaCO_3$
Pine wood ash	Ca (24.26 %), K (5.46 %), Mg (5.42 %) and Cl (0.10 %)	
Wheat straw	Si (0.95 %), K (0.91 %), Cl (0.51 %) and Ca (0.27 %)	K_2CO_3
Wheat straw ash	K (18.37 %), Si (9.81 %), Ca (5.67 %) and Cl (4.00 %)	

The selection of inorganic elements was selected compared with the literature resources [160, 265-267]. Both inorganics (K and Ca) exist in the form of carbonates and chlorides when processed, especially when interacting with the molten salts used during thermal treatment. This may be potentially problematic due to the possible change of molar ratios of the selected molten salt mixture, especially when recycled in the liquefaction process. Therefore, $CaCl_2$, $CaCO_3$ and K_2CO_3 were individually added to the molten salt mixture and mainly referred to as the added inorganics/impurities and analysed using the XRD.

The results from the characterisation of the molten salts were used as a baseline and compared with the salts with the added impurities ($CaCl_2$, $CaCO_3$ and K_2CO_3) and the recycled salt mixture. The XRD analysis of the recycled salts were analysed to confirm whether the structure was changed during the liquefaction process.

DSC analyses were performed on the molten salts to find out the thermal behaviour of the molten salt mixture, which included the glass transition and melting stages. Likewise, with the XRD analysis, the molten salt was also used as a baseline for the comparison of recycled salts. The DSC profiles of recycled salt samples were used to understand whether the melting temperature have shifted and compared with the unprocessed or 'pure' molten salt.

From the pine wood and LignoBoost lignin using molten salts liquefaction processing, the recovered char samples were analysed on the TGA to obtain the derivative thermogravimetric (DTG) combustion

profiles. Elemental analysis and SEM imaging were used to analyse the recovered char samples, which were compared with the chars derived from HTL processing in Chapter 5. XRF and SEM-EDX analysis was additionally used on a complementary basis to confirm the salt presence found in the recovered chars.

6.2. Methodology

6.2.1. Materials

6.2.1.1. Individual salts and molten salts preparation

The following individual salt samples were used for thermal, elemental and XRD analyses, zinc chloride ($ZnCl_2$) (CAS: 7646-85-7) 98.3 %; potassium chloride (KCl) (CAS: 7447-40-7) ≥ 99.5 %; sodium chloride (NaCl) (CAS: 7647-14-5) ≥ 99.8 %; calcium chloride ($CaCl_2$) (CAS: 10043-52-4); potassium chloride (K_2CO_3), (CAS: 585-08-7) ≥ 99.995 %; and calcium carbonate ($CaCO_3$) (CAS: 474-34-1) ≥ 99.0. $Zncl_2$ was obtained from VWR Chemicals Int., whilst the remaining salts were procured through Sigma-Aldrich Int.

For the liquefaction studies of lignocellulosic biomass and lignin with molten salts, a dedicated molten salt was proposed and prepared by the project partner Norwegian University of Life Sciences (NMBU) [6], Norway. This molten salt was a eutectic mixture of individual salts $ZnCl_2$, KCl and NaCl at a molar ratio of 44.3:41.9:13.8 %, respectively. Prior mixing, each individual salt was dried in a separate container at 200 °C for at least 24 hours ensuring that the residual water is removed. The salt mixture was inserted in nickel crucible and placed in a vertical tube furnace with radiation shield at the bottom, which was to minimise heat losses, and heated to 250 °C and held for 3 hours. LabVIEW 8.2 (National Instrument) was used to monitor and record the temperature profiles (using an S-type thermocouple) and measurements. Argon was introduced from the bottom of the furnace to provide an inert atmosphere. The salt mixture was continuously mixed in the final hour of this treatment. Then the mixture was cooled rapidly to 220 °C under controlled cooling at a rate at 0.5 °C min^{-1}. The prepared molten salt was crushed with a pestle and mortar into a powdered form in order to prepare a homogeneous sample for analytical characterisation.

6.2.1.2. Recovered char and recycled molten salts samples

Molten salt samples used for characterisation studies presented in this chapter were recovered from the liquefaction experiments carried out at Ghent University. A schematic diagram of the molten salt recovery (recycling) from the liquefaction process is outlined is outlined in Figure 73.
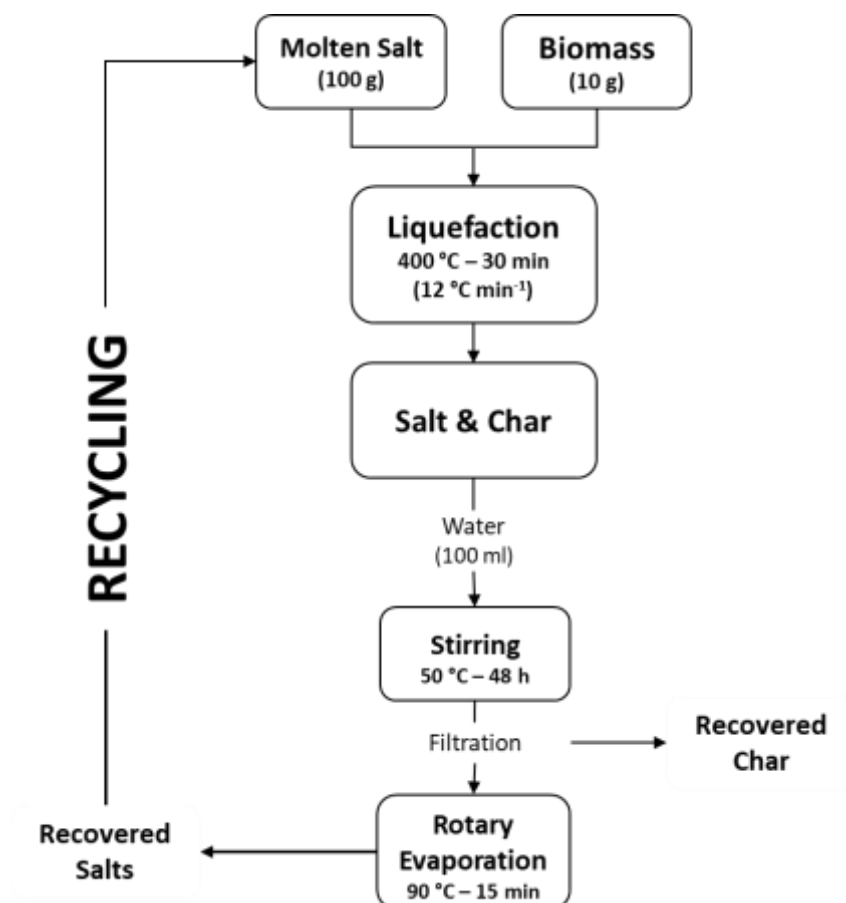
Figure 73. Schematic diagram of molten salts liquefaction with pine wood and LignoBoost lignin.

In each liquefaction experiment, 10 g of biomass (LignoBoost lignin or pine wood) was pre-mixed with 100 g of molten salt and inserted in the reactor vessel using a glass liner. The biomass molten salt mixture heated at a heating rate of 12 °C min^{-1} to a maximum temperature of 400 °C and maintained for 30 minutes in an inert environment (nitrogen). Once the reactor reached a temperature of 230 °C, the stirrer was switched on at a constant speed of 15 rpm to ensure the homogeneity of the sample. Once the reactor was cooled down, the char and spent molten salt (solid residue) samples were recovered.

Approximately 10 g of the recovered solid residue was then mixed with 100 ml of deionised water and stirred on a magnetic plate at 50 °C for 48 hours. The dissolved in water spent molten salts were separated from char by filtration on a filter paper. The recovered char and filter paper were dried at 105 °C to the constant weight and collected for further analyses. The water from filtrate was evaporated to retrieve molten salts. The separation was carried out in a rotary evaporator stirred at 100 rpm at 90 °C and held at 15 min at the final temperature. The dried recovered molten salt was re-used on the liquefaction process twice, and the same recovery process was applied after each liquefaction experiment.

6.2.2. X-Ray Diffraction

Before the XRD analysis, additional attention was paid to the potential interaction of some (most abundant) biomass inorganic constituents (calcium, chlorine and potassium) with the molten salt during the liquefaction process. From the metal analysis (section 3.3.2 on page 63 in Chapter 3) of biomass and biomass-derived ashes, the most abundant element for wheat straw was potassium and for pine wood – calcium. These individual elements in its respective chemical forms of $CaCl_2$, K_2CO_3, and $CaCO_3$ were selected for biomass inorganic matter interaction studies with molten salt [66, 160, 265, 267]. This involved physical mixing and melting of each above mentioned compound with 'pure' molten salt with further analysis of potentially created intermediates and new inorganic compounds. With the molten salts interaction, the potassium would be most likely form as carbonates (K_2CO_3).

XRD measurements of 'pure' molten salt along with its individual constituents and mixtures with compounds used for interaction studies were performed using a Bruker D8 Advance diffractometer with Cu Kα radiation source (λ = 1.5418 Å) operating at 40 mA and 40 kV. The X-ray intensity data were collected by a LynxeyePSD detector at 10-80 ° 2θ range with a step scan at 0.02 ° at 1 s per step.

The individual salt components (including NaCl, KCl, K_2CO_3, $CaCO_3$, and $CaCl_2$) were compared with the reference XRD database [268-273] to validate the results and ensure the diffraction peak profiles were within the expected range. The software Visualization for Electronic and STructural Analysis (VESTA) was also applied to visualise the crystal morphology of the salts and determine the powder diffraction patterns (presented in Figure 74 and Figure 75 for NaCl). This was done to distinguish individual peak assignments in each diffraction pattern and provide diffraction patterns for $ZnCl_2$, which could not be analysed by XRD due to its high volatility and hygroscopicity. The XRD peak intensity is the only

difference that can be observed, which corresponds to the differences in the total area of the crystal face of the samples.
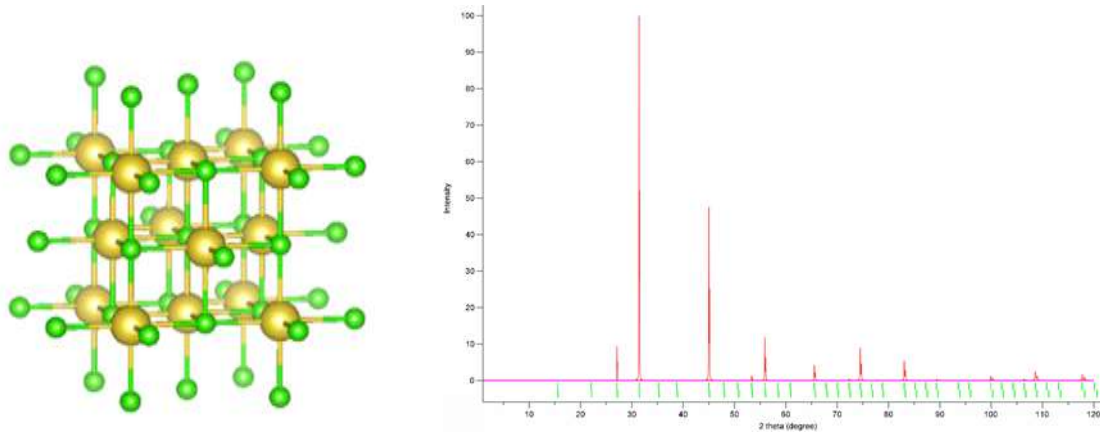
Figure 74. Crystal structure and powder diffraction pattern of NaCl in VESTA software [270].
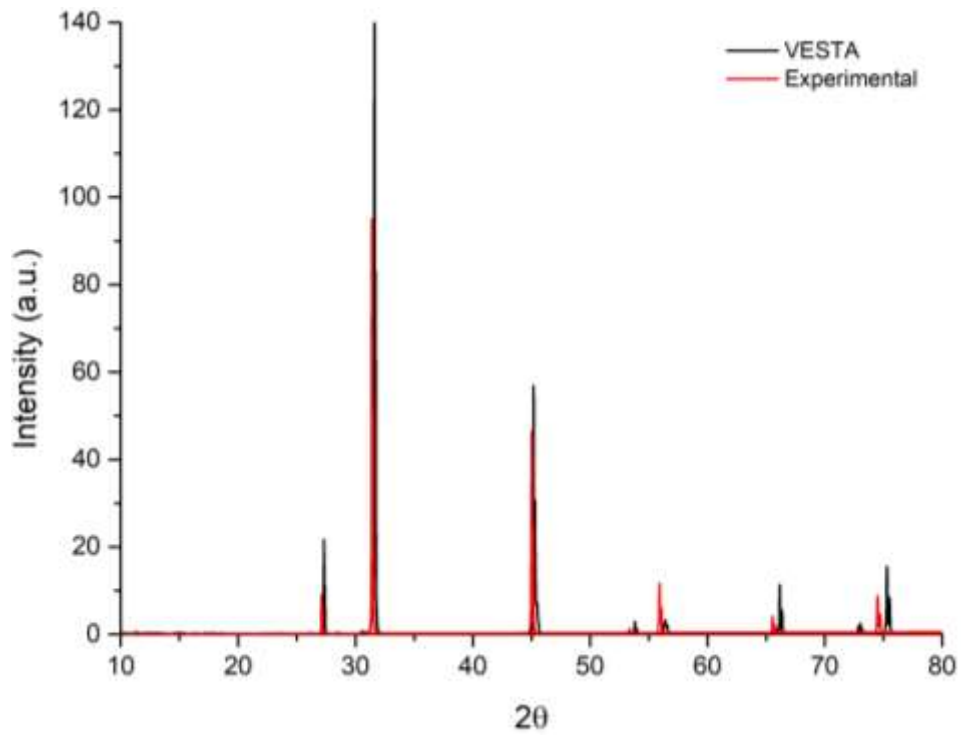
Figure 75. Comparison of NaCl using VESTA software [270] and experimental data.

6.2.3.   Differential Scanning Calorimetry

DSC characterisation of pure and recycled molten salts was carried out to assess the thermal stability of the molten salt mixture during the thermal treatment (liquefaction). The DSC melting temperature (along with the glass transition/softening temperature) was used as a "checkpoint" to assess the thermal stability of molten salts used in and recovered from the process.

The DSC characterisation of all molten salts samples was performed using a Mettler Toledo TGA/DSC^3 STAR^E System. Approximately 2-3 mg of feedstock samples were loaded and heated at a heating rate of 25 °C min^{-1} with the final temperature of 500 °C. Nitrogen at a flow rate of 30 ml min^{-1} was used as a carrier gas to provide an inert atmosphere. The temperature range was measured from 40 °C to 500 °C. All samples were enclosed in a covered aluminium crucible with a pierced lid, and an empty covered crucible was used as a reference. The following DSC temperature programme was applied:

1.   The sample was heated from 40 °C to 500 °C at a flowrate of 25°C min^{-1}

2.   The final temperature of 500 °C was maintained for 5 min.

3.   The sample is then cooled to 40 °C at a cooling rate of 25°C min^{-1}

6.2.4. Thermogravimetric analysis

The recovered char samples from liquefaction experiments with molten salts experiments were obtained from Ghent University for TGA characterisation. The TGA experiments were conducted in an oxidative atmosphere to observe any potential impact of the remaining traces of salts (as confirmed by XRF, SEM and XRD analysis) on char combustion profiles. The TGA programme can be found in section 3.2.3 on page 59.

6.2.5. Elemental Analysis

Elemental analysis of char samples from LignoBoost lignin and pine wood processed with molten salts were analysed six times in the elemental analyser. Detailed methodology is described in Chapter 5 (section 5.2.6) on page 121.

6.2.6. X-Ray Fluorescence

Wavelength-dispersive X-ray fluorescence (WDXRF) analysis was performed on the Bruker S8 Tiger X-ray fluorescence with TouchControl™ for elemental composition determination. The XRF was equipped with an X-ray tube with rhodium anode (end-window 4-kW) operated at 60 kV, 50 mA (Co) and 40 kV. Samples were analysed using an optimised analyser crystal (Co: LiF 200 crystal) and prepared as a loose powder in a sample cup mounted on Mylar™ film with a mask of 8 mm at acquisition time of 18 min. All analysis was performed under helium atmosphere at a flow rate of 0.7 l min^{-1}. The quantitive results were investigated on the SPECTRA^{plus} software.

6.2.7. Scanning Electron Microscopic-Energy Dispersive X-ray of recovered chars

Morphology of recovered chars from molten salt liquefaction process was studied using a JEOL 7800 FF Prime Field Emission Scanning Electron Microscope (SEM). The semi-quantification of inorganic matter occluded in the recovered char was carried out at the same time with the aid of Energy Dispersive X-ray (EDX) analyser (Oxford Instruments, UK).

6.3. Results and Discussion

6.3.1. X-Ray Diffraction of salts

The X-ray diffraction (XRD) characterisation was applied for molten salt and molten salt with 10 % inorganics added in order to assess the potential interaction of three components of the molten salt mixture with inorganics present in biomass/feedstock. The XRD pattern of the pure molten salt is presented in Figure 76. Whereas the molten salt mixed with the added 10 % of potassium carbonate (K_2CO_3), calcium chloride ($CaCl_2$) or calcium carbonate ($CaCO_3$) are presented in Figure 80-Figure 82, respectively. FactSage 7.2 was also utilised by NMBU to investigate the impact of the impurities on the melting point of the pure molten salt. FactPS and FT Salt database were used to determine each individual impurity, including K_2CO_3, $CaCl_2$ and $CaCO_3$. From the FactSage modelling, some intermediates were expected from melting the pure molten salts with each individual impurity. These additional intermediates were included by using the VESTA software, which are compared with the peaks obtained from XRD analysis to confirm the modelling results.
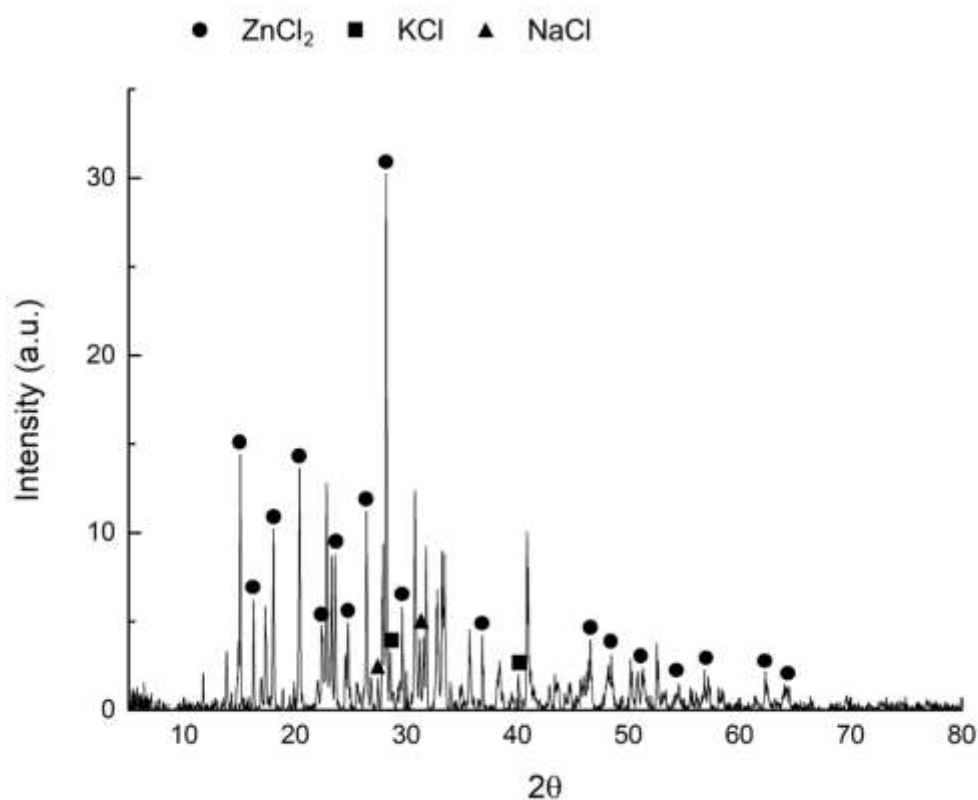
Figure 76. XRD pattern of 'pure' molten salt with peak assignment.

The XRD pattern of the pure molten salts revealed that most of the peaks corresponded mostly to zinc chloride. It should be taken into consideration that the molar ratio of $ZnCl_2$:KCl:NaCl is 44.3:41.9:13.8. Therefore, there will be fewer peaks identified as KCl and NaCl and most of these peaks will correspond mainly to $ZnCl_2$. The figure above of pure molten salts pattern was used as a baseline to compare with the molten salts with the added inorganics.

Figure 77 and Figure 78 shows results from the FactSage modelling and XRD analysis of molten salts and the addition of K_2CO_3 respectively.

(a)   (b)
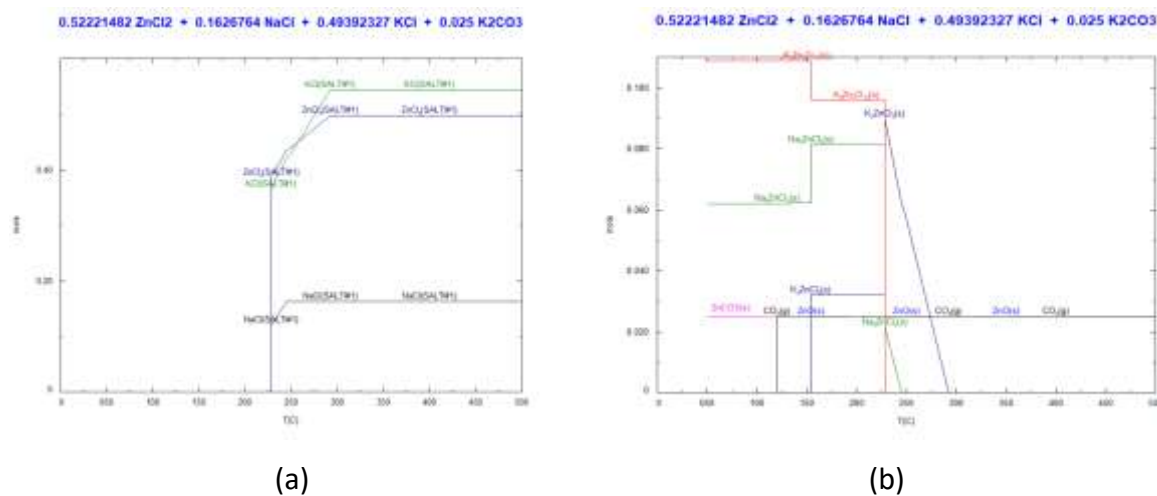
Figure 77. FactSage modelling results of molten salts with added 0.025 mol K_2CO_3.
(a) molar concentration of different molten salts, (b) molar concentration reduction of solid components through temperature increments
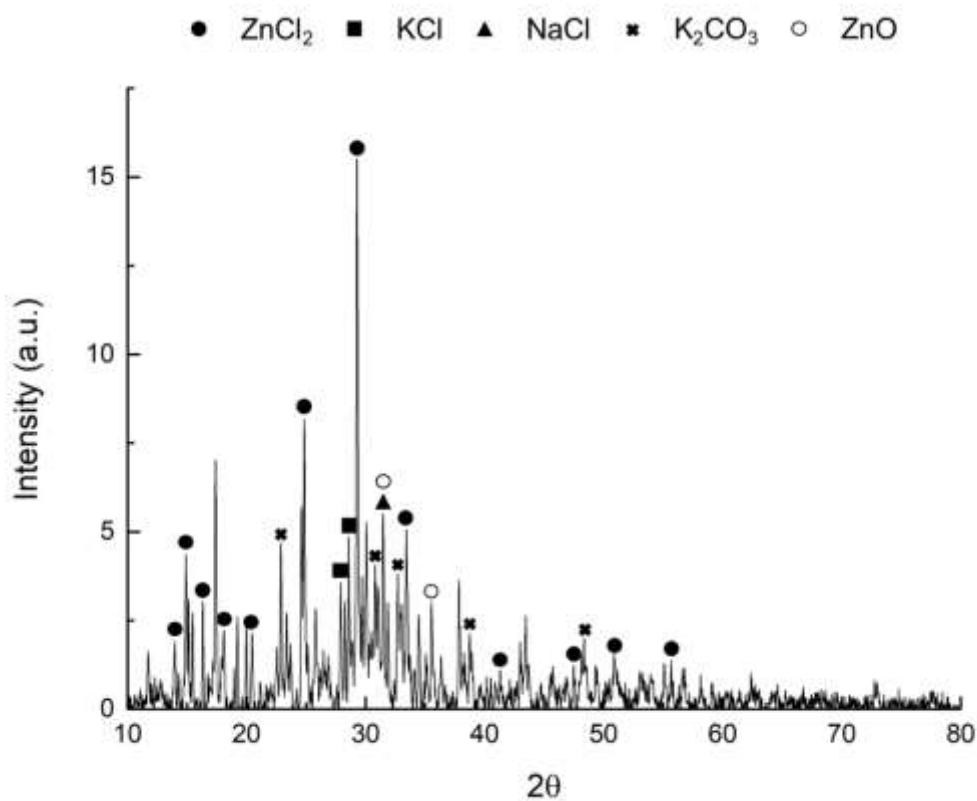
Figure 78. XRD data of molten salts mixed with K_2CO_3 with peak assignment.

From FactSage modelling, it was shown that K_2CO_3 was reacting with $ZnCl_2$ from the eutectic mixture molten salts. As the temperature was increased to melt the molten salts with K_2CO_3, the molar composition of molten salts was altered as well as forming zinc oxide (ZnO). When the temperature increased, Na_2ZnCl_4 decomposed into NaCl and $ZnCl_2$ in a liquid form and disappeared at 245 °C. K_2ZnCl_4 was also observed but disappeared at 292 °C. The decomposition of K_2CO_3 also increased the concentration of KCl, but this could not be confirmed by just XRD analysis alone. From the XRD analysis, the KCl did appear to be more defined and intense. Most of the peaks corresponded mainly to $ZnCl_2$ and K_2CO_3. From the model, some of the peaks did indeed match the intermediate ZnO that was formed during the melting of the molten salts and K_2CO_3. One of the peaks was observed to be either NaCl or ZnO. Like with all x-ray analysis, the overlapping of sodium and zinc will be inevitable when analysing molten salts.

Figure 79 and Figure 80 show results from the FactSage modelling and XRD analysis of molten salts with $CaCl_2$ respectively.

(a)   (b)
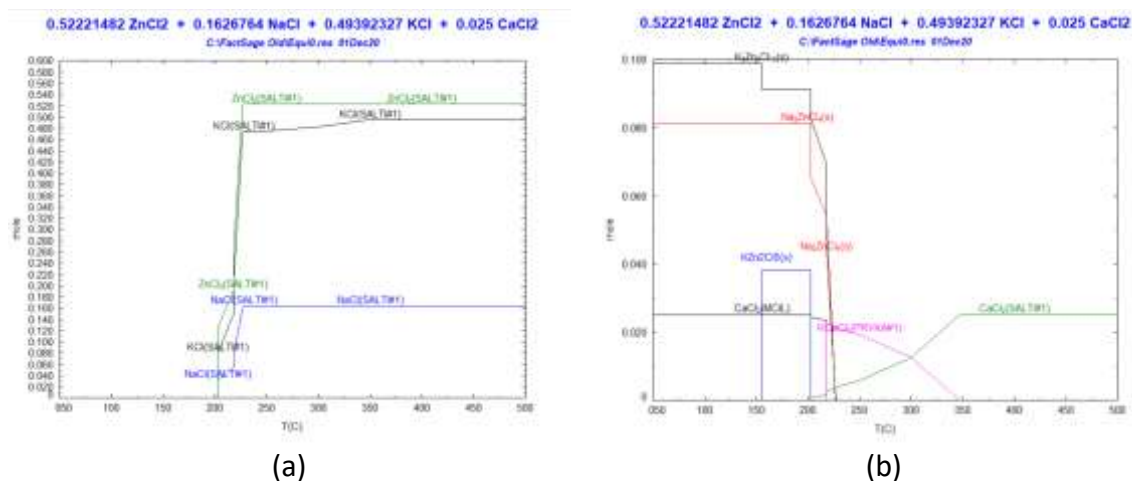
Figure 79. FactSage modelling results of molten salts with 0.025 mol $CaCl_2$.
(a) molar concentration of different molten salts, (b) molar concentration of impurities and formation of intermediate components including $KCaCl_3$ through chemical reactions
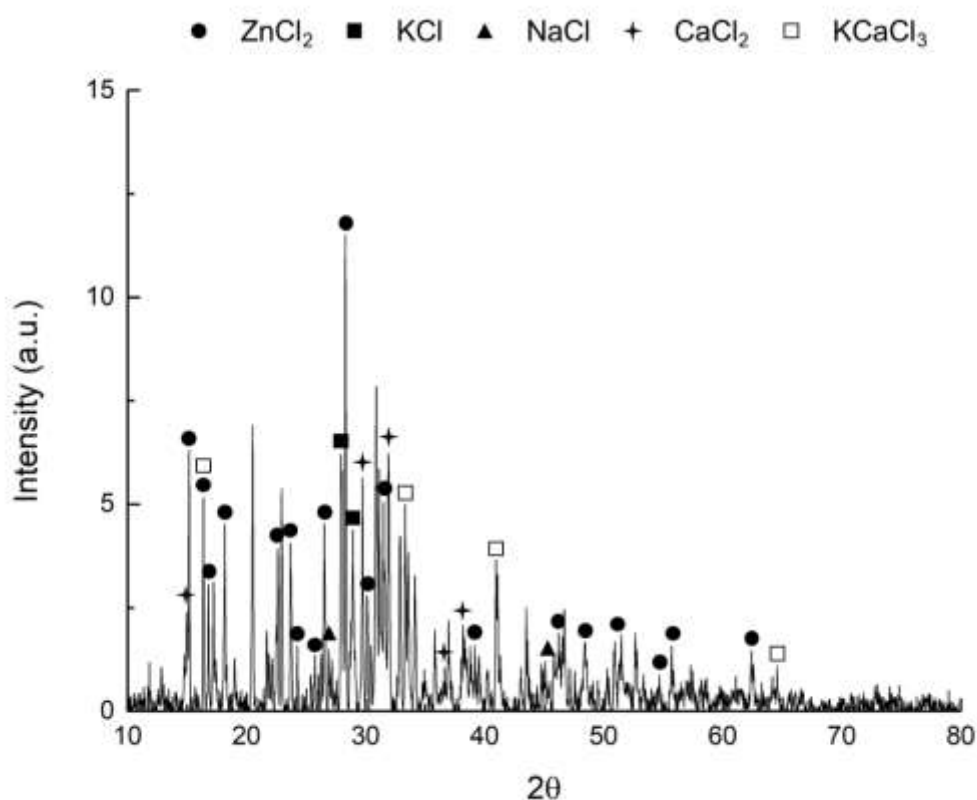
Figure 80. XRD data of molten salt mixed with CaCl₂ with peak assignment.

The FactSage modelling results revealed that the melting point did not have a major impact to the melting point of the eutectic salts. However, the KCl was reacting with $CaCl_2$ to form chlorocalcite ($KCaCl_3$). From the XRD analysis, it was observed that most of the peaks were detected to be $ZnCl_2$ along with a few peaks that corresponded to $CaCl_2$. $KCaCl_3$ was also included in this XRD analysis, and some of these peaks were identified as $KCaCl_3$.

FactSAge modelling results and XRD analysis of molten salts and the addition of $CaCO_3$ are shown in Figure 79 and Figure 82 respectively.
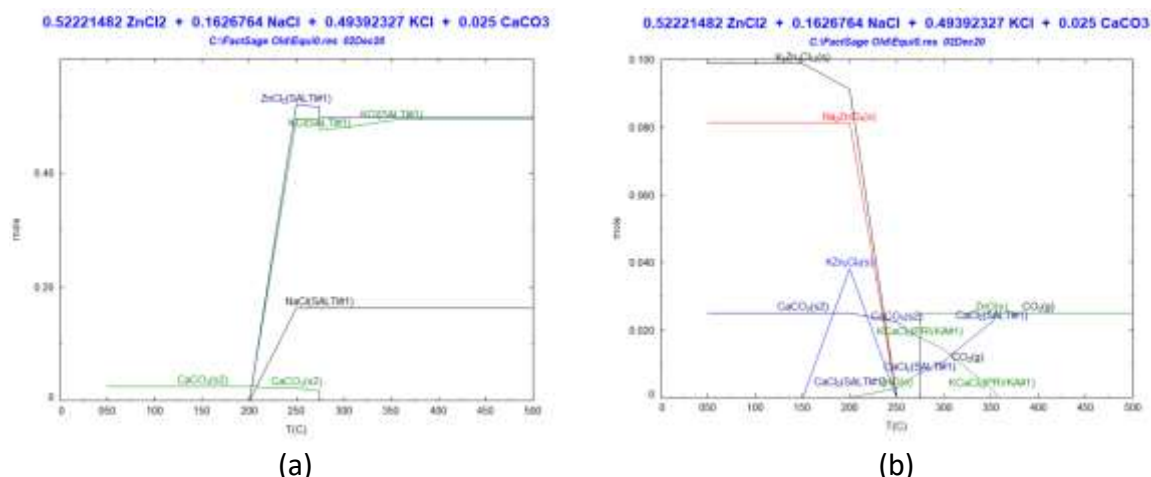
Figure 81. FactSage modelling of molten salts with added 0.025 mol of CaCO₃.
(a) molar concentration of the molten salts, (b) molar concentration of impurities and formation of intermediates including KCaCl3, CaCl2 and ZnO through chemical reaction
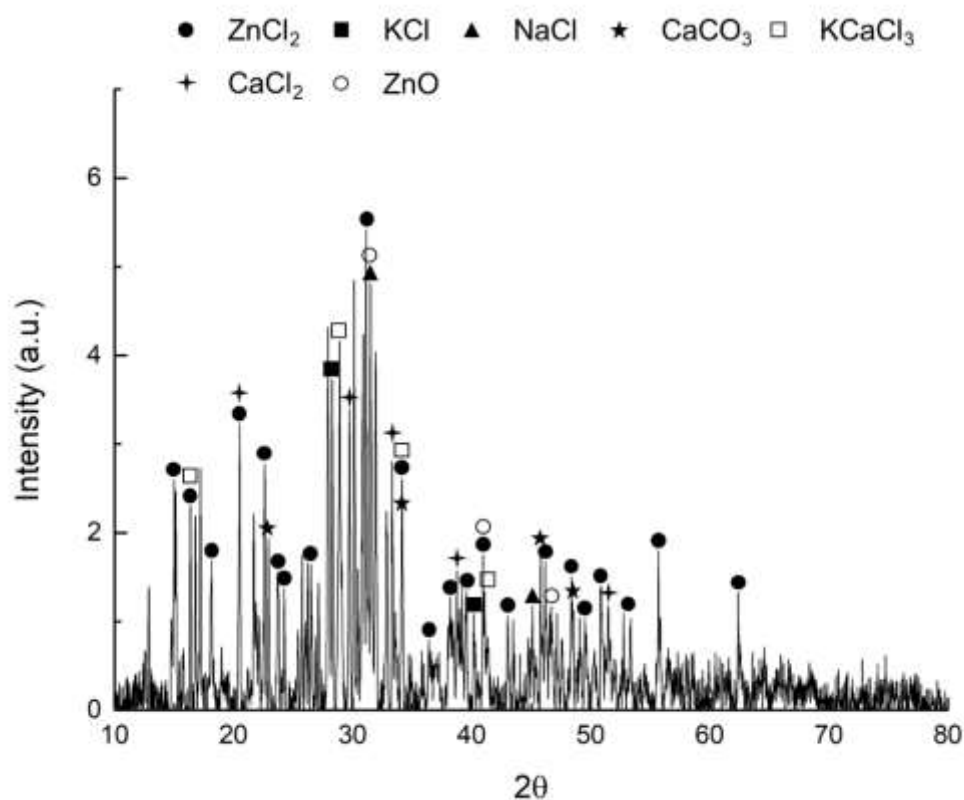
Figure 82. XRD data of molten salt mixed with CaCO₃ with peak assignment.

Similar to the previous analysis, it was observed from the FactSage modelling that $ZnCl_2$, KCl and $CaCO_3$ were reacting which produced some intermediates including chlorocalcite ($KCaCl_3$) and ZnO. At elevated temperature of 274 °C, the unstable $KCaCl_3$ was further decomposed to KCl and $CaCl_2$. It was

also discovered that $ZnCl_2$ and KCl were consumed in a chemical reaction up to 358 °C. From the XRD analysis, it was revealed that all intermediates including $KCaCl_3$, $CaCl_2$ and ZnO, were present as well as the molten salt components. Again, most of the XRD peaks corresponded to $ZnCl_2$. Similar issue with the ZnO and NaCl overlapping can be observed here as well. Furthermore, with the multiple components in the XRD analysis, there will bound to be peaks overlapping each other corresponding to a few components and therefore it cannot be distinguished which exact component is corresponding to that certain peak from the XRD diffractogram alone. Few detected peaks did correspond to $CaCO_3$, $KCaCl_3$.and $CaCl_2$. When comparing the XRD patterns with the 'pure' molten salt and the molten salts mixed with $CaCO_3$, the mixture here appeared to be less intense. One explanation could be the change in the molar compositions after adding $CaCO_3$ as well as the melting and cooling down the eutectic mixture.

6.3.2. Differential Scanning Calorimetry Analysis of molten and recycled salts

Differential scanning calorimetry (DSC) results for the pure molten salt is presented in Figure 83, which was recorded from 40 °C to 500 °C at a flowrate of 25°C min^{-1}.
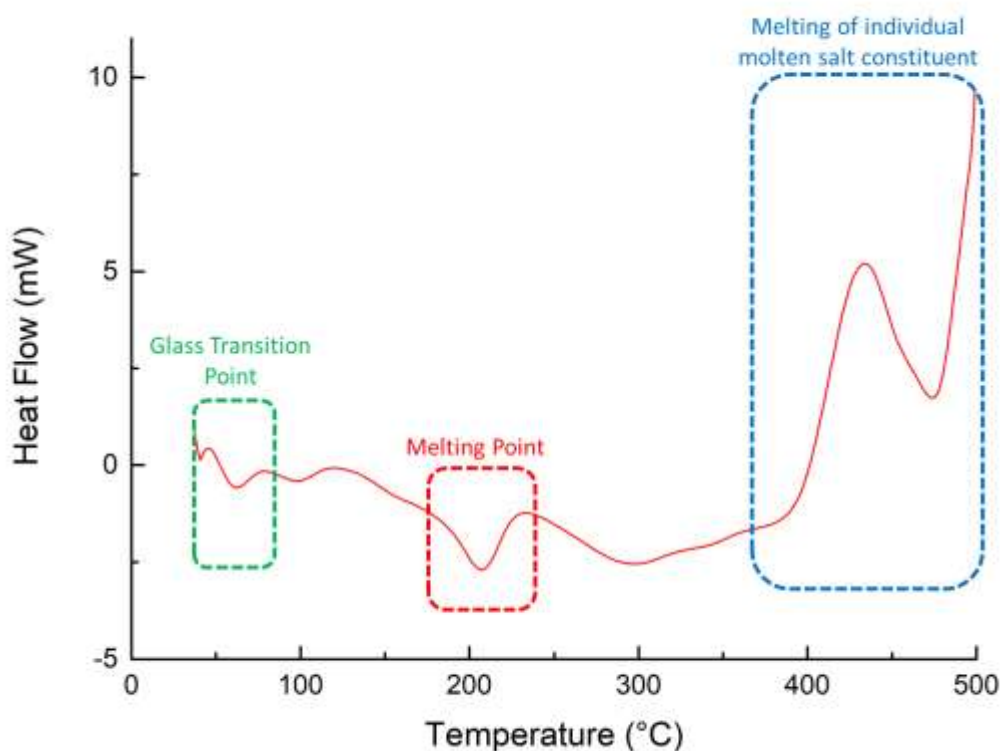
Figure 83. DSC characterisation of 'pure' molten salts.

As seen in Figure 83, around 70 °C, a subtle endothermic heat flow curve was observed corresponding to a glass transition (or softening) phase. As the molten salt was heated, a change of heat flow curve was reflected by the DSC where the molecules start to soften and move but not considered to be in a molten phase yet. It was then observed that the molten salts undergo through the melting transition phase from a 'more' defined endothermic curve. The molten salts' melting point was observed at 208 °C, which was in line with the theoretical solid-liquid transition/melting region (229 °C) calculated for this particular molten salts [6]. The melting point was also used to validate the thermal stability of molten salts. A good salt thermal stability is defined as no salt losses during pyrolysis, which can be used for the possibility of salt recycling. The slight temperature shift (difference of 21 °C) in molten salts was believed as a consequence of the applied DSC 'open crucible' method. In this method, some ZnCl$_2$ possibly evaporated (due to its extremely high volatility and hygroscopicity) during the DSC

analysis (with the applied final temperature of 500 °C). The last heat flow curve was assumed to be the melting of the individual molten salt constituents.

The 'pure' molten salts (salt #4) was then compared with the molten salt samples that have been recycled three times, which were separated from the LignoBoost lignin and pine wood chars, and shown in Figure 84 and Figure 85.
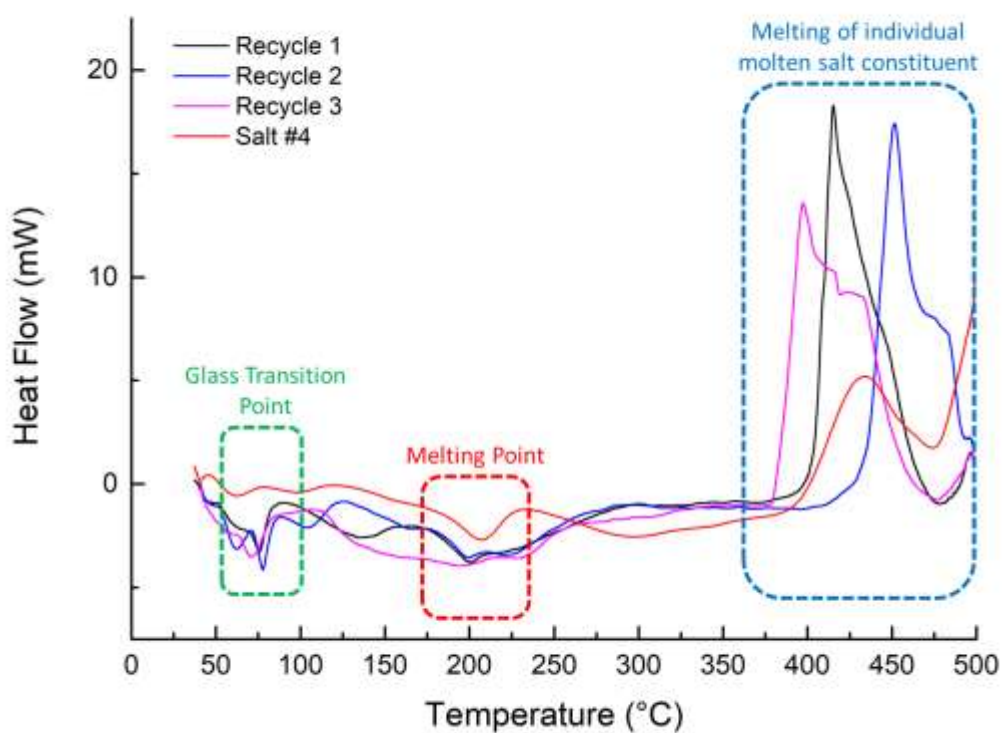
Figure 84. DSC characterisation of molten salts processed with LignoBoost lignin.
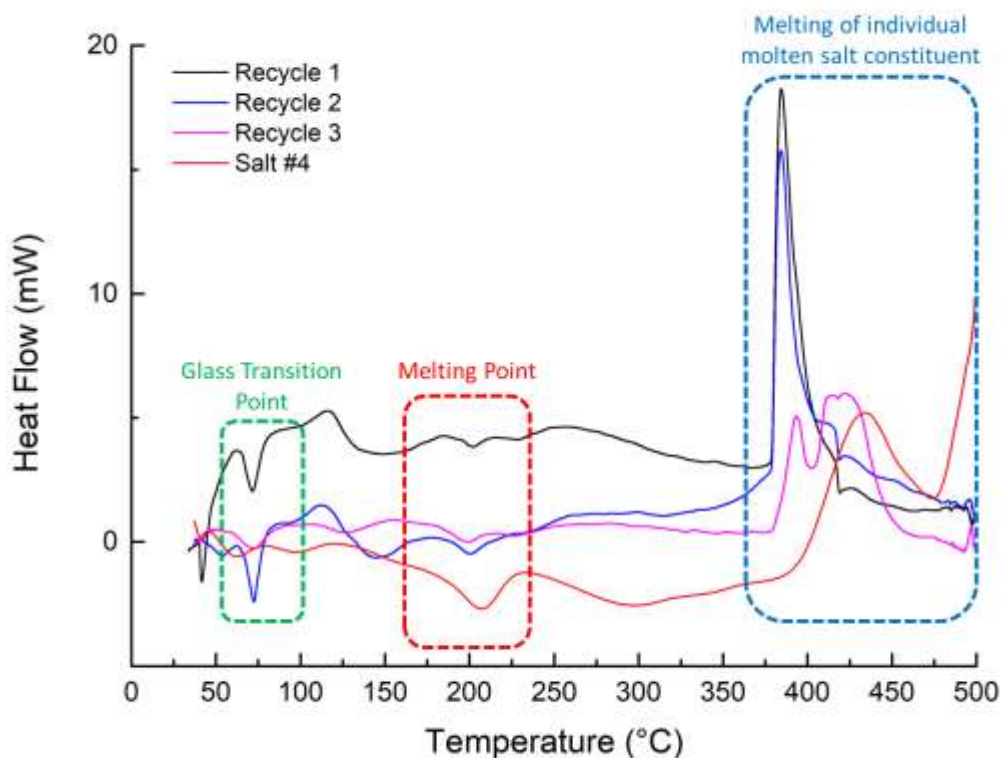
Figure 85. DSC characterisation of molten salts processed with pine wood.

The DSC characterisation was also used to assess the thermal stability of the recycled salts, which was compared with the 'pure' molten salt (salt #4). Figure 84 shows the DSC recycled spent salts from LignoBoost lignin. The glass transition point remained within the same region of 70 °C. However, a defined endothermic peak was observed rather than a subtle endothermic peak as observed in the 'pure' molten salt. This could be explained by the molar concentration of each individual salts and the crystallinity change of the molten salt. For salts from the first and second recovery trials, a less-defined melting point curve was observed. The melting temperature was shifted towards a lower temperature of 201 °C when compared to the 'pure' molten salt (salt #4) with its melting point at 208 °C. On the third recycling, no melting peak was detected at all, which was confirmed after two DSC analysis repetitions. Furthermore, it was observed and believed that the melting of each individual constituent from the molten salt in the third recycled molten salt was shifted to a lower temperature in the region of 400-460 °C.

Similar thermal behaviours were observed in the DSC analysis of recycled salts used in pine wood thermal processing (Figure 85). A defined glass transition phase was again observed in the first and second recycled salts, but the peak was very subtle in the third recycled salt. Both transition phase of first and second recovered salts occurred around the same temperature of 70 °C. The melting phase

showed a very subtle endothermic heat flow curve, which is explained by the molar concentration change in the molten salts. As expected, the molten salts are thermally behaving as in a similar way as the molten salts processed LignoBoost lignin, and shifted to a lower temperature but within the same region of 200 °C. The melting points for individual salts were shifted to a lower temperature in the region of 380-430 °C, due to the change in the molar concentration of the molten salts.

6.3.3.   Thermogravimetric analysis of recovered char

The derivative thermogravimetric (DTG) and mass loss profiles from the thermogravimetric analyses (TGA) of recovered char samples obtained from LignoBoost lignin and pine wood in liquefaction experiments are depicted in Figure 86 and Figure 87, respectively.
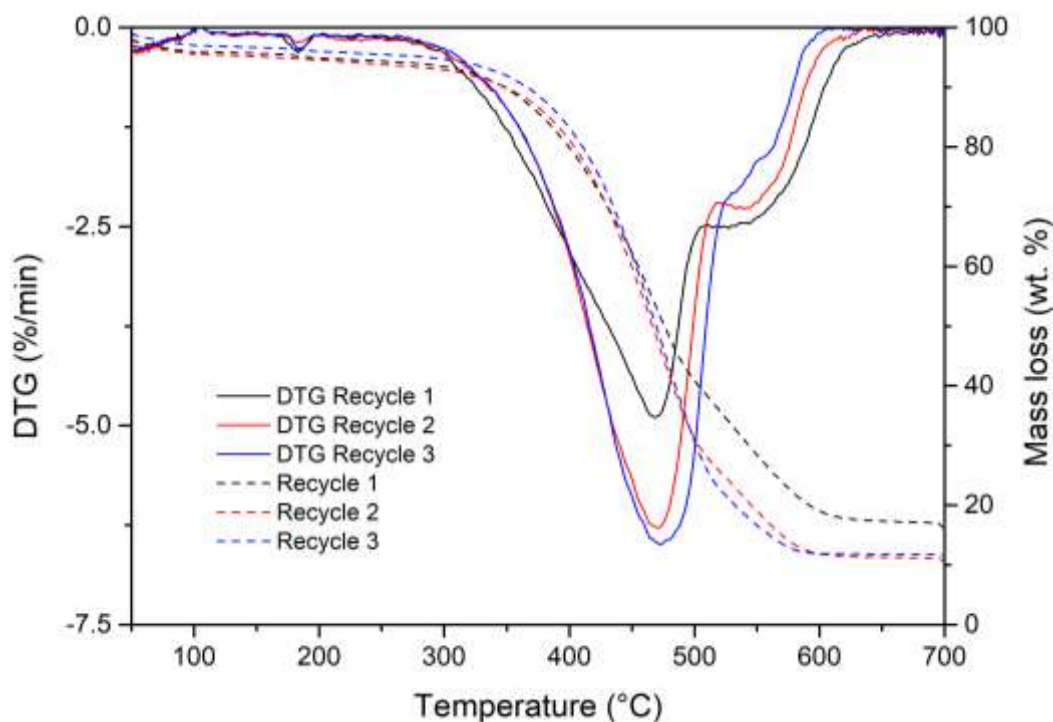
Figure 86. DTG combustion profile of LignoBoost lignin char.
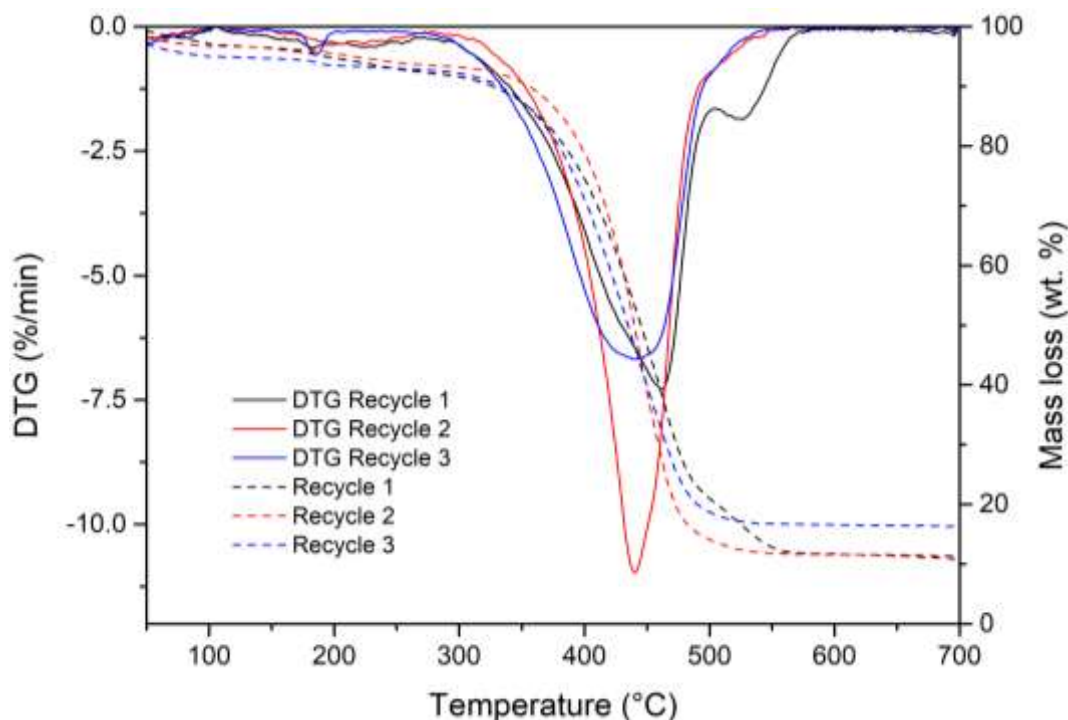
Figure 87. DTG combustion profile of pine wood char.

The main combustion peak (volatile combustion) of Lignoboost char (Figure 86) was observed between 469-475 °C. A shoulder can also be observed at approximately 537-543 °C for the first and second recovered char samples, which is associated with char burnout. It also revealed from the weight loss curve, the first recycled char had a solid residue of 16.5 % left when compared with the second and third recovered char which had 10-11 %. This could potentially indicate that most of the salts were removed during the second and third recycling process.

Figure 87 shows the DTG and mass loss profiles from combustion tests of recovered char samples processed from liquefaction of molten salt and pine wood. A DTG peak can be seen between 441-465 °C in all recovered char samples. From the second and third recycled char, char burnout shoulders were not observed as opposed to the first recycled char. For this, it is believed that the molten salts were more 'accurately' recovered. It is also noticeable that in the second recycled char DTG peak of volatile combustion was sharper and combusted at a faster rate, and can be explained due to the catalytic impact of inorganics traces present in the char. From the mass loss curves, a solid residue/ash in the first and second recycled char were observed at 9 % and 11 % respectively. Whereas 15 % solid residue/ash was found in the third recycled char and could suggest that there were remaining traces of salts left.

6.3.4. Elemental analysis of recovered char

Recovered char samples from LignoBoost lignin and pine wood processed with molten salts were analysed in an elemental analyser to determine carbon (C), hydrogen (H), nitrogen (N) and sulphur (S) content, which are presented in Table 29. Oxygen (O) content was determined by difference. The elemental analysis was also done in order to compare with the elemental results obtained from the HTL experiments (Chapter 5). An overview of the average results of C, H, N, S and O content from HTL (Chapter 5) versus liquefaction with molten salts are presented in Figure 52. Furthermore, the results in this section were compared with pyrolysis studies done previously, as there are no results (as of 2022) could be found with HTL in molten salts.

Table 29. Elemental analysis of char from LignoBoost lignin and pine wood processed with molten salts.

Sample	C (%)	H (%)	N (%)	S (%)	O* (%)
LignoBoost lignin char *(a.r.)*					
Recycle 1	53.81 ± 1.86	3.04 ± 0.25	0.31 ± 0.05	0.70 ± 0.10	42.22 ± 1.39
Recycle 2	61.82 ± 1.06	2.93 ± 0.16	0.27 ± 0.01	0.94 ± 0.04	34.07 ± 1.10
Recycle 3	64.16 ± 2.10	2.94 ± 0.07	0.24 ± 0.01	0.92 ± 0.07	31.69 ± 2.15
Pine wood char *(a.r.)*					
Recycle 1	61.02 ± 1.88	3.13 ± 0.22	0.58 ± 0.01	0.00	35.27 ± 1.90
Recycle 2	64.28 ± 1.92	2.84 ± 0.36	0.23 ± 0.05	0.00	35.88 ± 1.98
Recycle 3	58.36 ± 0.93	2.89 ± 0.12	0.23 ± 0.03	0.00	38.50 ± 1.03

a.r. = as received
*Oxygen was calculated by difference

(a)   (b)
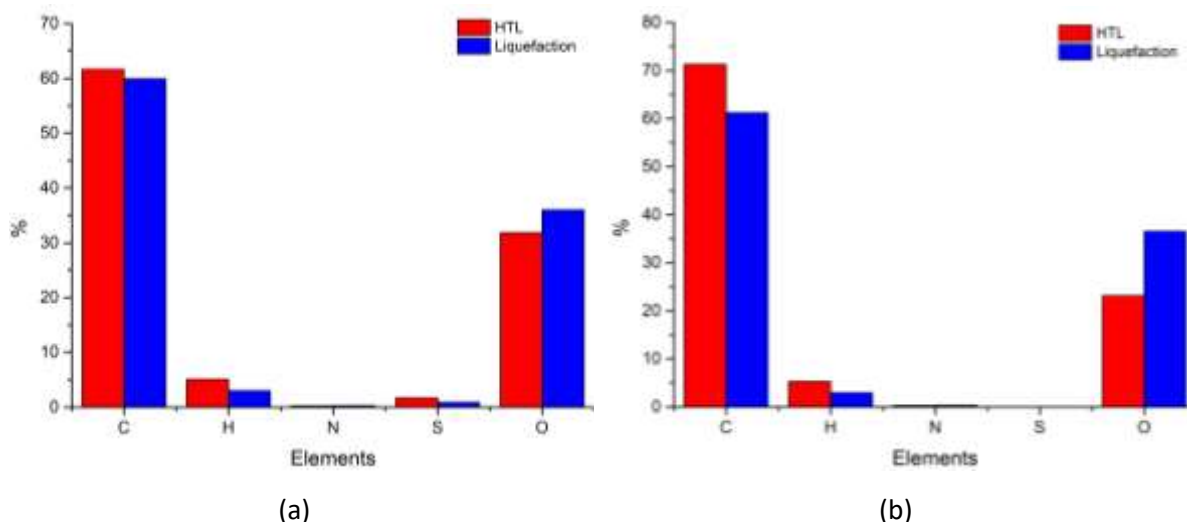
Figure 88. Overview of C, H, N, S and O content of HTL and liquefaction with molten salts.
(a) LignoBoost lignin, (b) pine wood

The LignoBoost lignin char's C content has slightly increased after every recycle. This could be assumed due to more salts washed out and filtered from the char. When comparing the results from Chapter 5 (section 5.3.3 on page 132), a higher content of C and H were found on average (61.66 and 5.06 % respectively) from HTL processing. The N content was found to be on a similar range of 0.21-0.26 %. While the H and S content found in the LignoBoost lignin char was slightly lower from molten salt liquefaction processing. This implies that the molten salt liquefaction processing could have catalysed the decomposition of S. Furthermore, a previous study conducted by Siefert et al [274] found that alkali metal salt was able to capture acid gases (H_2S and CO_2). This was further confirmed by Tang et al [275] and compared the conventional pyrolysis char with char processed from molten salts (using Li_2CO_3-Na_2CO_3-K_2CO_3 eutectic mixture) in pyrolysis, which successfully reduced the S content found in the chars. However, higher O content was found in the char from the liquefying and molten salt processing which were in the range of 31.69-42.22 %. The O content found in the char from conventional HTL was between 20.32 and 25.44 %. There is also a trend observed when the char has a decrease in salt content there will be a decrease in the O content.

Similar elemental components were also observed in pine wood, where on average the C (61.22 %) and H (2.59 %) content is significantly lower from biomass liquefaction in molten salt in contrast to conventional HTL processing (71.29 and 5.29 % respectively). Furthermore, the C content was higher in the first and second recycled char, except in the third recycling where C content was decreased. This suggests that there may be lower salt content found in the first and second recovered char. The results seem to agree with the TGA (section 6.3.3) and XRF results in the following section (section

6.3.5), since an increase in salt content was observed in the third recovered pine wood char. Comparable results of nitrogen content was found in both chars processed from HTL and liquefaction with molten salts in the range of 0.24-0.35 % and 0.23-0.58 % respectively. There was no S content present in both chars from HTL and liquefaction with molten salt processing. Increased O content was detected due to the additional salt found in the third recycled char, which was also seen in the recovered LignoBoost lignin char. In comparison, the O content of char is on average (23.14 %) lower found in the conventional HTL processed from pine wood.

6.3.5. X-Ray fluorescence of recovered char and recycled molten salts

This particular x-ray fluorescence (XRF) analytical method was applied in order to verify the type and level of molten salts originated in inorganic impurities after salts recycling in the recovered char and recycled molten salt samples. Distribution of individual elements detected in recovered char samples and recycled salt samples are presented in Table 30.

Table 30. Pine wood and LignoBoost lignin char samples processed with recycled molten salts.

Sample	Zn (%)	Cl (%)	K (%)	S (%)	Ba (%)	Fe (%)	Si (%)	Ca (%)	Mg (%)
LignoBoost lignin char (a.r.)									
Recycle 1	30.30	11.70	2.80	2.15	1.43	0.36	0.11	n/d	n/d
Recycle 2	18.50	8.42	1.56	2.30	1.49	0.33	n/d	0.78	0.24
Recycle 3	18.10	4.25	0.41	2.50	n/d	0.47	0.16	0.85	0.24
Pine wood char (a.r.)									
Recycle 1	19.60	7.89	1.30	n/d	n/d	0.30	n/d	0.27	0.12
Recycle 2	16.80	7.38	1.29	n/d	0.43	1.38	1.06	0.43	0.41
Recycle 3	23.90	7.45	1.22	n/d	0.15	1.03	0.22	0.32	0.24

a.r.= as received
n/d = not detected

Large concentrations of zinc (Zn), chlorides (Cl) and potassium (K) were detected in the first recovered chars in both LignoBoost lignin and pine wood. These individual elements originate from the molten salt samples applied in liquefaction experiments. The salt concentration was washed out and separated from the char in the second and third, which can be especially seen in the LignoBoost char. These results are in agreement with the TGA and elemental analysis, where both analyses assumed to have more salt content in the first recovered char. The TGA found more solid residue content, whereas in the elemental analysis there was less carbon content found. The sulphur content of LignoBoost lignin was in the range of 2.15-2.50 % slightly more than that was found from the elemental analyser. However, it should be taken into consideration that the XRF only analysed the inorganic content of the samples and does not take into account of the organic content. Therefore, the XRF analysed 'more' sulphur content in the LignoBoost lignin char. A slight amount of barium was also detected by XRF, which was previously not found in the biomass or in the biomass-derived ashes. A possible explanation

for these results may occur during the mechanical recovery of salt samples from the experimental work, the trace elements/cross-contaminants originate from the body of stainless-steel reactor used for molten salt studies. Aside from the detected salt elements, biomass-ash elements were also detected including iron (Fe), silica (Si), calcium (Ca) and magnesium (Mg). There has been an increase in the biomass-ash elements including Fe, Si, Ca and Mg in the third recovered chars when comparing these with the first and second recovered chars (as some of these elements were unable to be detected by XRF).

The characterisation of the recycled molten salts recovered from liquefaction experiments with pine wood and LignoBoost lignin are shown in Table 31.

Table 31. Recycled molten salts washed from the pine wood and LignoBoost lignin char.

Sample	Zn (%)	Cl (%)	K (%)	S (%)	Ba (%)	Fe (%)	Si (%)	Ca (%)	Mg (%)
Recycled molten salts processed with LignoBoost lignin (a.r.)									
Recycle 1	11.60	17.20	4.82	n/d	n/d	n/d	n/d	0.11	0.15
Recycle 2	20.50	39.50	10.60	n/d	n/d	n/d	n/d	0.25	0.20
Recycle 3	18.50	26.70	8.46	n/d	n/d	n/d	n/d	0.14	n/d
Recycled molten salts processed with pine wood (a.r.)									
Recycle 1	18.50	25.90	8.04	n/d	n/d	n/d	n/d	0.13	0.20
Recycle 2	19.10	26.70	8.14	n/d	n/d	n/d	n/d	0.13	n/d
Recycle 3	20.90	30.30	10.10	n/d	n/d	n/d	n/d	0.22	0.13

As confirmed in the previous TGA and elemental analyses, where it was assumed that the third recovered char may have more salt traces. As revealed in Table 31, there was a considerable amount of 23.90 % zinc found in the third recovered char as opposed to the first and second recovered char. This could be explained by the change in the molar concentration of the molten salt composition. However, there were no significant differences of Cl and K detected, which were found in the range of 7.38-7.89 % and 1.22-1.30 % respectively. Sulphur was not detected, which is in agreement with the elemental analysis conducted. Barium was observed, but substantially less than what was identified in LignoBoost lignin. Small amounts of biomass-ash related elements (Fe, Si, Ca and Mg)

were identified in all recovered chars. These were also identified in the biomass and ash-derived biomass in Chapter 3 (section 3.3.2 on page 63).

The increase in concentration of individual salts, particularly Zn, Cl and K, after each recycle was observed in both molten salts processed from LignoBoost lignin and pine wood. There were particularly more Zn, Cl and K of 20.50, 39.50 and 10.60 % detected in the second recycled salt processed from LignoBoost lignin respectively. It was assumed that there would be more salts recovered in the third recycled salts, however it could be due to the change in the molar concentration of salts. Whereas, an increase in the salt detection was observed in the molten salt from pine wood after each recycle processing. Furthermore, there would be more salts recovered as the recycled molten salts were reused. Small quantities of biomass-ash elements (including Ca and Mg) were observed in all molten salts.

One of the noticeable issues is that one of individual salt found in the molten salt – sodium, was not included in Table 30 and Table 31. As observed in Figure 89, the XRF was unable to detect any sodium due to the small concentration amount used in the molar ratio of molten salts ($ZnCl_2$:KCl:$NaCl_2$ at a molar ratio of 44.3:41.9:13.8) when compared to zinc and potassium. Sodium is considered one of the most "light" elements along with lithium, beryllium, magnesium, aluminium, silicon and phosphorus, which the XRF is incapable to accurately quantify or in some cases unable to detect. Furthermore, there have been overlapping energies with the spectral lines K-alpha ($K\alpha$) and L-alpha ($L\alpha$) of sodium and zinc respectively. The spectral line $K\alpha$ of sodium is 1.040 keV while the $L\alpha$ of zinc is 1.012 keV, which are relatively close to each other leading to any x-ray (including XRD, XRF and SEM-EDX) detectors unable to differentiate between the two overlapping energies. Whilst sodium is characterised by the $K\alpha$ spectral line, the innermost K shell emits the lowest energy and characterised by fewer spectral lines compared to zinc's $L\alpha$ line. The further the shell is away from the nucleus, the higher the electron energy and the better for the x-ray detector to identify and characterise the sample. This also explains why there was a better detection in zinc.
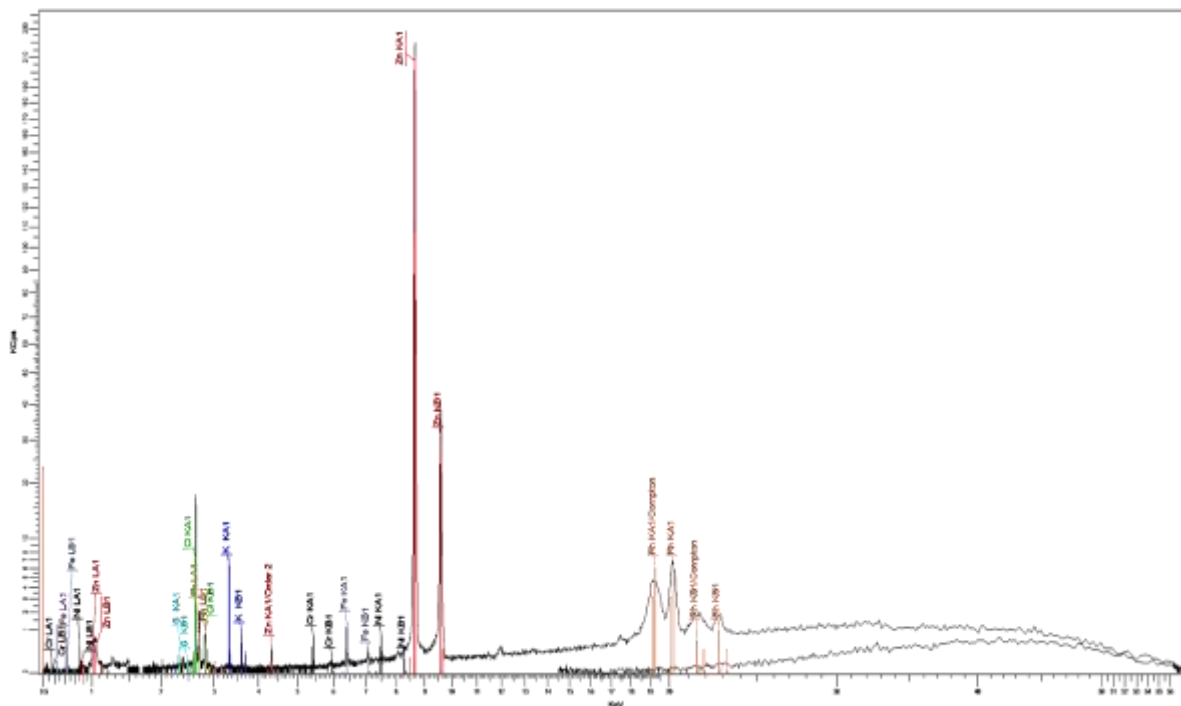
Figure 89. XRF analysis using SPECTRA^{plus} software to analyse the elemental composition.

6.3.6. Scanning Electron Microscopic-Energy Dispersive X-ray on recovered char

Recovered LignoBoost lignin and pine wood chars were subjected to Scanning Electron Microscopic-Energy Dispersive X-ray (SEM-EDX) to observe the presence of the molten salts. Table 32 and Table 33 summarises the semi-quantification of key elements detected in the recovered char samples. Images of those samples are presented in Figure 90 and Figure 91.

Table 32. SEM-EDX analysis for char samples from LignoBoost lignin.

Elements	Recycle 1	Recycle 2	Recycle 3
C (%)	52.19	58.04	72.17
O (%)	9.56	10.28	21.53
S (%)	0.82	0.84	0.56
Cl (%)	6.99	2.67	1.01
K (%)	0.70	0.65	n/d
Zn (%)	8.72	6.74	1.01
Si (%)	n/d	n/d	0.3

n/d = not detected

(a)

(b)

(c)

(d)

(e)
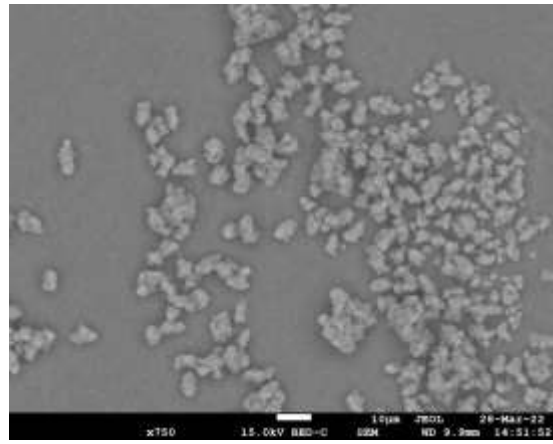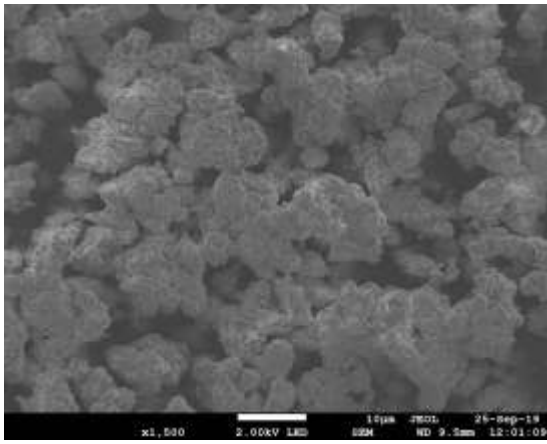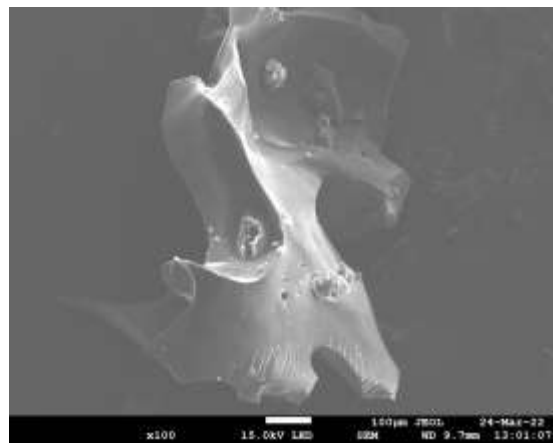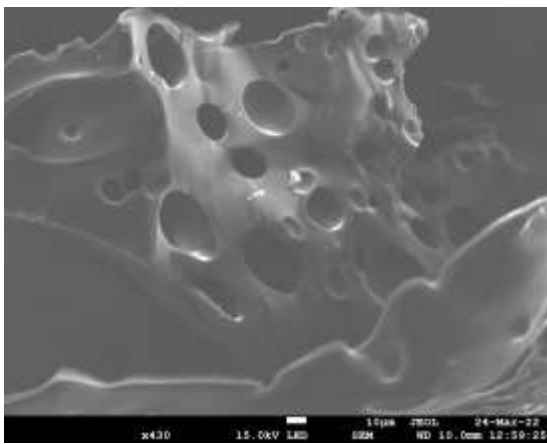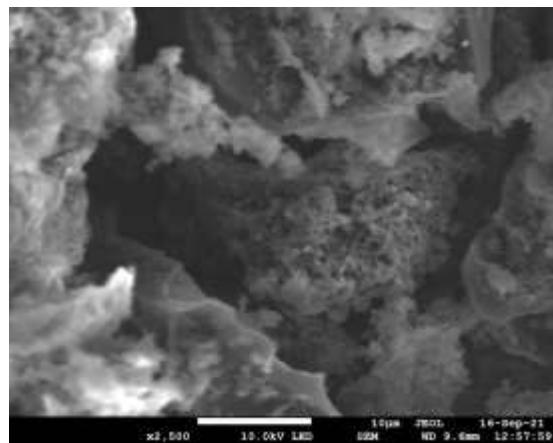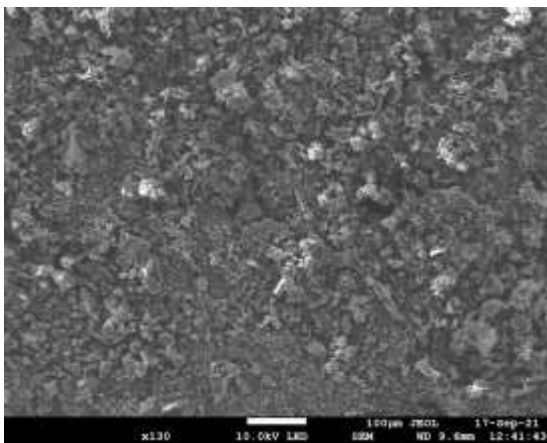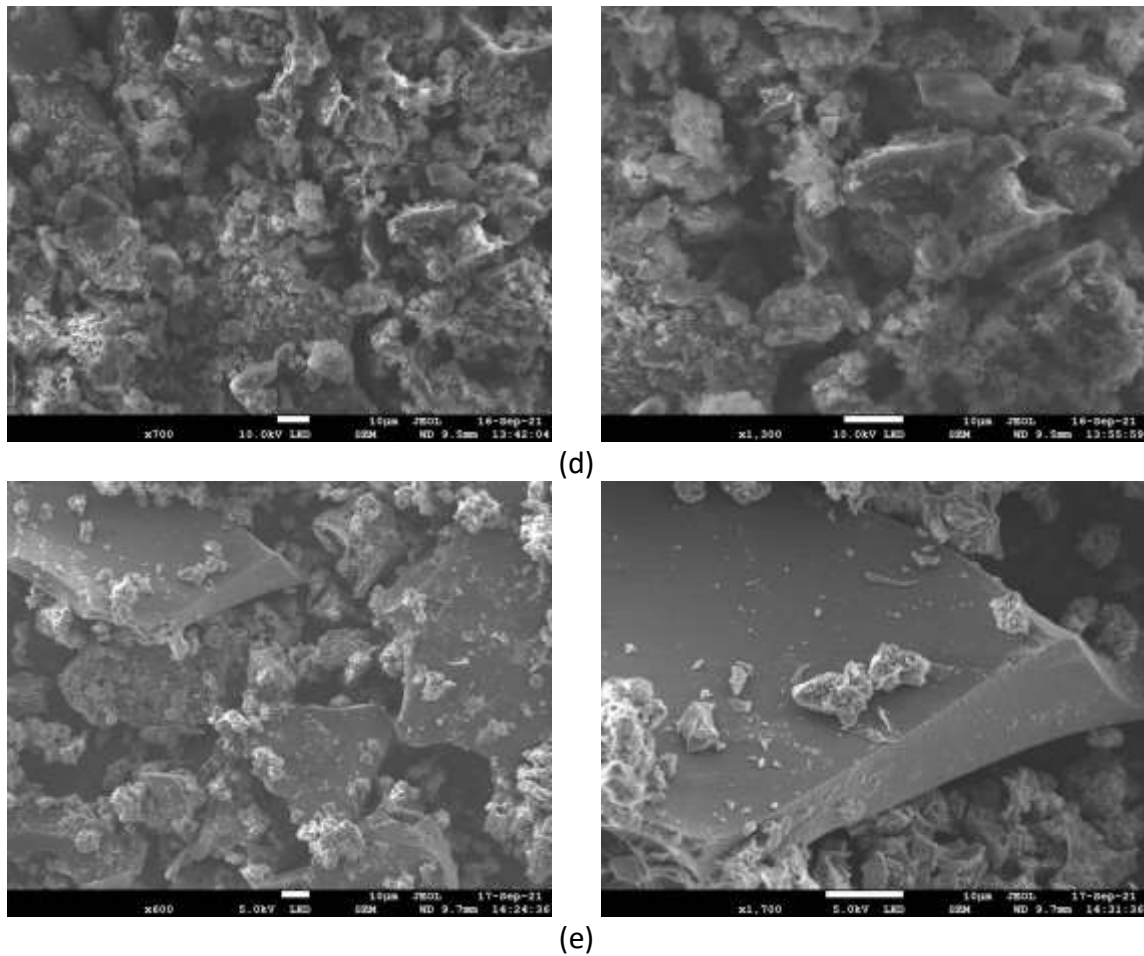
Figure 90. SEM images for LignoBoost lignin and chars from HTL and liquefaction treatment with recycled molten salts.
(a) LignoBoost lignin (b) LignoBoost lignin char from HTL, (c) first recycling, (d) second recycling and (e) third recycling

Table 33 SEM-EDX analysis of for char samples from pine wood

Elements	Recycle 1	Recycle 2	Recycle 3
C (%)	51.04	59.11	64.62
O (%)	5.89	6.00	10.49
Mg (%)	n/d	0.13	n/d
Cl (%)	2.11	1.25	1.90
K (%)	0.36	0.28	0.38
Zn (%)	5.95	2.49	7.04
Si (%)	n/d	n/d	n/d

n/d = not detected

(a)

(b)

(c)

(d)

(e)
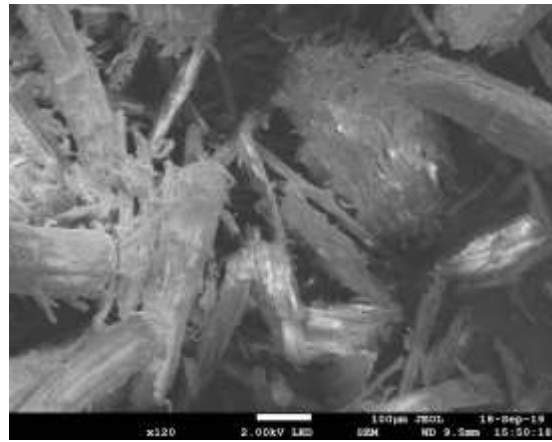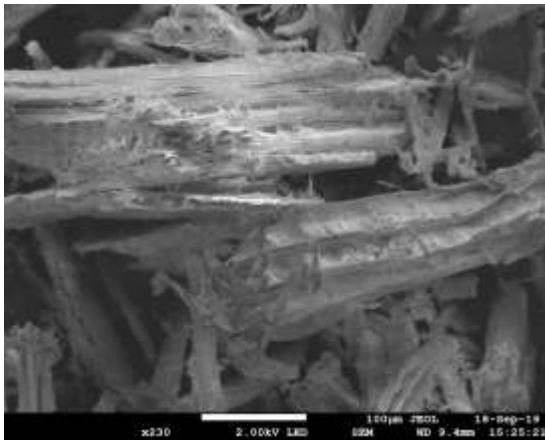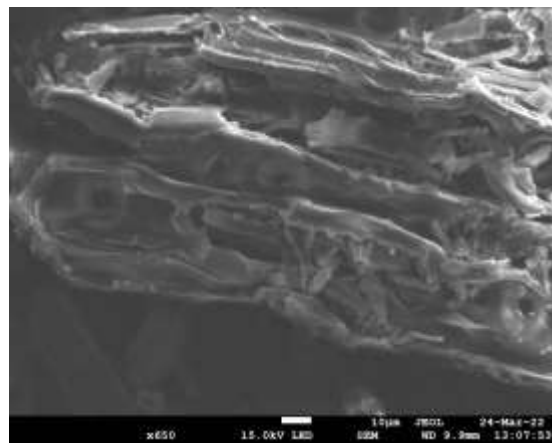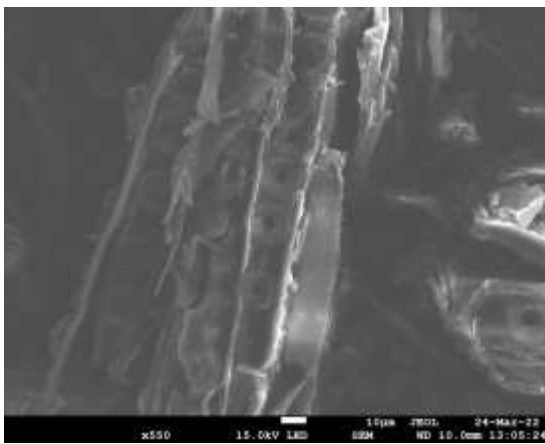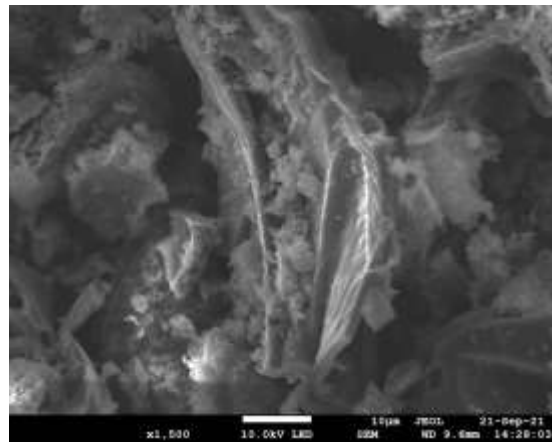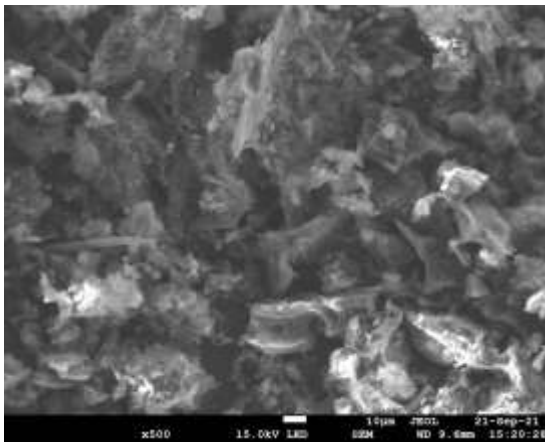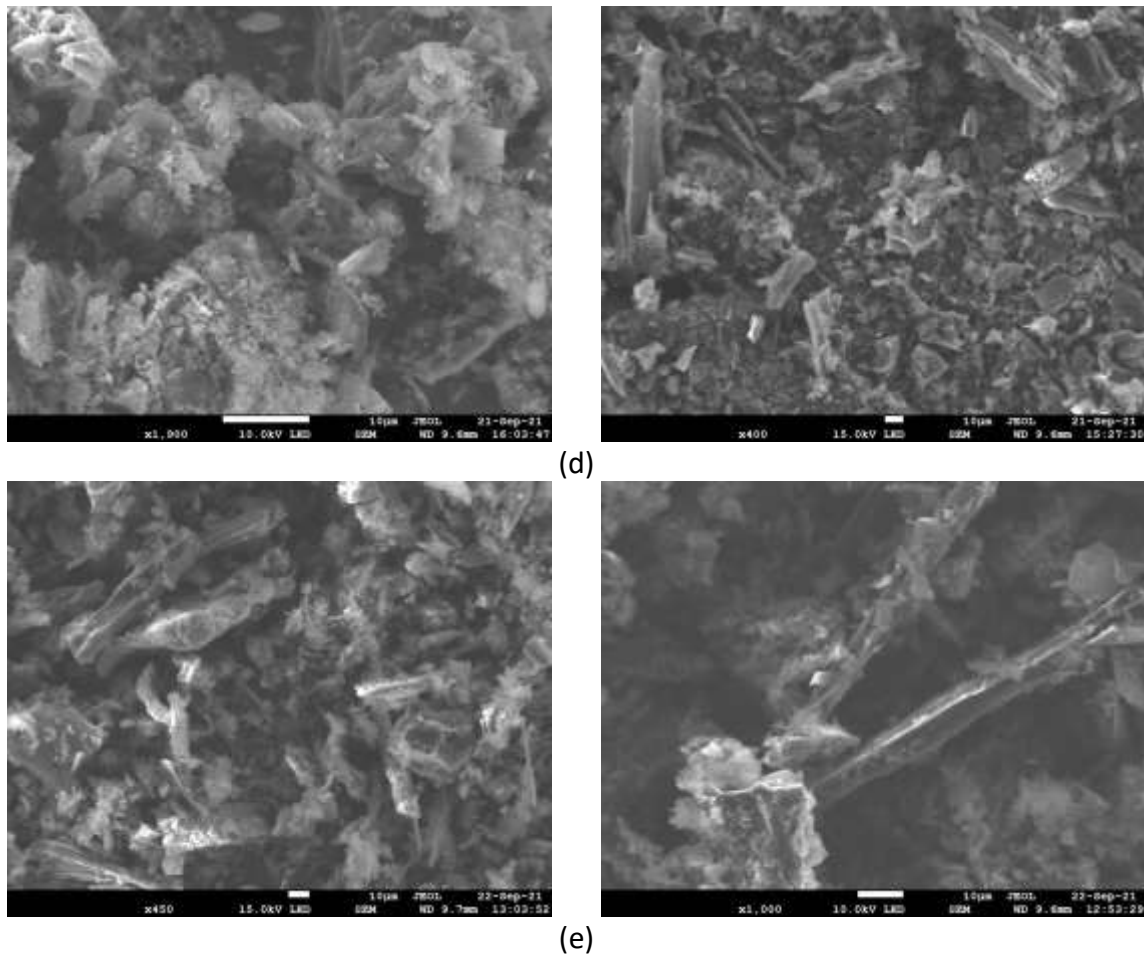
Figure 91. SEM images for pine wood and pine wood chars from HTL and liquefaction treatment with recycled molten salts.
(a) pine wood, (b) pine wood char from HTL, (c) first recycling, (d) second recycling and (e) third recycling

The recovered char results from the SEM-EDX and XRF were compared. Both LignoBoost lignin and pine wood char have traces of salts detected, including zinc, potassium and chlorides. Similar trend was also observed in XRF and in SEM-EDX where the concentration of zinc was found with a considerable amount followed by chlorides and potassium. Low amounts of organics were also identified in both recovered char samples, which are comparable with the elemental analysis. Low concentration of sulphur was also detected in the recovered LignoBoost lignin char samples. Small quantities of biomass-ash elements including magnesium (Mg) and silica (Si) were detected, which are comparable with the results from XRF. However, Si could not be detected in pine wood char.

SEM images for the recovered LignoBoost lignin and pine wood char samples from liquefaction experiments with the application of the recycled salts (three cycles) are presented in Figure 90 and Figure 91 respectively. The morphology of LignoBoost lignin chars was observed to be rough, which is

explained by a previous research that it was due to its delignification process from black liquor [276]. Pores could not be clearly observed in the SEM images of both LignoBoost lignin and pine wood chars, which could be due to the presence of salts. The pores have an important role for promoting electrode surface areas as previously described by literature [47]. The presence of pores was further confirmed by the HTL-generated LignoBoost lignin and pine wood char as seen in Figure 90b and Figure 91b. It was explained previously in Chapter 5 (section 5.3.6 on page 165) that the pores were formed due to the release of volatiles or water permeating into the pores. Furthermore, the morphology of both chars processed with molten salts were completely destroyed and mainly covered with salts when compared with the raw feedstock.

Same overlapping issue with zinc and sodium have occurred with the SEM-EDX, as described in section 6.3.5 above and can be seen in Figure 92. From SEM-EDX analysis alone, it would be impossible to tell whether it was a zinc or sodium peaks as the elements were overlapping, which is not uncommon and will be difficult to identify [277]. Furthermore, it should be taken into consideration how the results are interpreted, as these are semi-quantitative results and the purpose was to confirm whether there were any salts present.
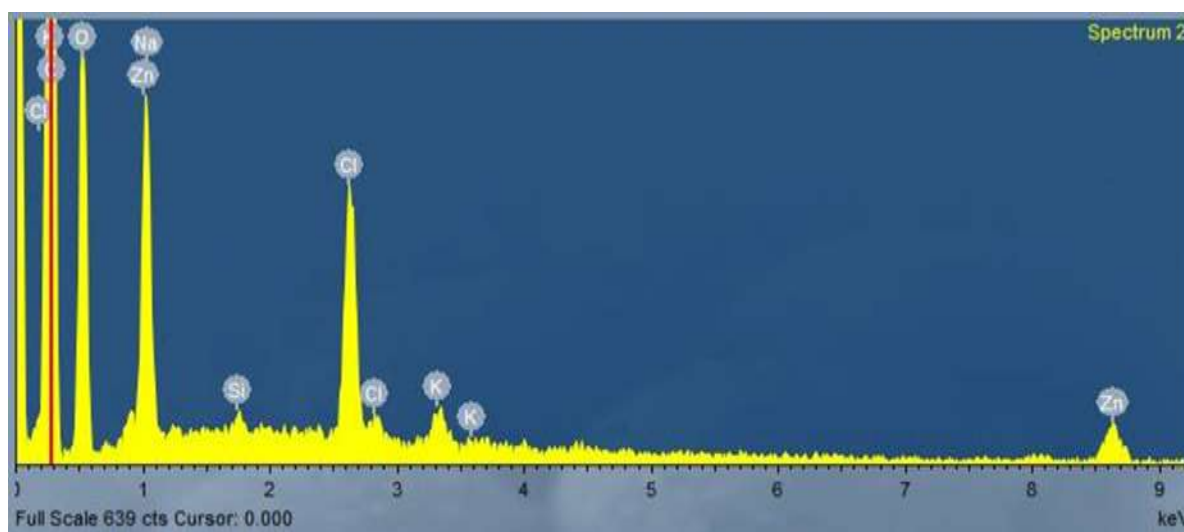
Figure 92. EDX characterisation of char samples where sodium and zinc are overlapping each other

Chapter 7

Conclusion and future work

The overall aim of this PhD research project was to produce HTL-derived bio-liquids, char and gas products from lignocellulosic biomass and waste lignin, whilst comparing them with those obtained from liquefaction experiments in molten salts carried out by ABC-Salt project partners. The bio-liquids obtained from liquefaction processing were targeted to meet specification for middle-range distillates that could be used in the conventional biorefinery streams. The main PhD project aim was met by successful completion of planned research tasks related to the ABC-Salt project along with a set of agreed measurable objectives. These included: (i) characterisation of potential lignocellulose and lignin for feedstock for application in thermochemical degradation via hydrothermal liquefaction; (ii) thermal degradation studies using TGA and Py-GC-MS techniques for assessment of potential end-products; (iii) assessment of feedstock thermal degradation kinetics; (iv) application of HTL processing to the selected feedstock; and (v) characterisation of products from the experimental work carried out at Aston (conventional HTL) and by the ABC-Salt project partners (liquefaction in molten salts). The research findings from this PhD are presented in four chapters (Chapter 3-6) and will describe the overall conclusion, future research works and planned dissemination.

7.1. Conclusion

Three lignocellulosic feedstock, including pine wood, wheat straw and LignoBoost lignin, were characterised and selected using a wide range of analytical methods to determine the suitability for hydrothermal liquefaction (HTL) and liquefaction in molten salts. From the conducted analytical methods, it was shown that both pine wood and LignoBoost lignin were seen as desirable feedstock for further processing. Both feedstock have shown to have a low ash content and low moisture content. Whereas, wheat straw had a high ash content and high moisture, which will give a good comparison with the pine wood and LignoBoost lignin when processing. Metal analysis on both the feedstock and the ashes produced from all the feedstock were conducted to observe whether there would be potential interaction with the molten salts, which was investigated in Chapter 6. The application of analytical pyrolysis was conducted on three feedstock and model components, as it was

an efficient and quick assessment for the thermal degradation of the feedstock and to fully understand the reaction network from the three model components.

Thermogravimetric analysis (TGA) was utilised to understand how lignocellulosic biomass was thermally decomposed by using the three selected feedstock and three model components. The derivative thermogravimetry of the feedstock were compared with the model components, but were also used to calculate activation energy by using Kissinger, Kissinger-Akahira-Sunose (KAS) and Flynn-Wall-Ozawa (FWO) methods. All calculated activation energy, using KAS and FWO, for all the feedstock and model components showed an increasing trend with conversion, which indicated that the reaction was not a single state reaction. Thermodynamic parameters, including enthalpy, Gibbs free energy and entropy, were all successfully calculated from the kinetic parameters. From the enthalpy and Gibbs free energy, all studied feedstock required additional heat source during the reaction as the thermal decomposition progressed. All entropy results were negative revealing that the reaction was moving from a disorderly state to get closer to a thermodynamic equilibrium.

As LignoBoost lignin and pine wood were seen as the most desirable feedstock in Chapter 3. Both biomass were investigated using HTL at processing temperatures of 275, 300 and 325 °C in Chapter 5. Particular attention was paid to the bio-crude yields from the HTL processing. The highest bio-crude yield of 9.31 wt.% was obtained at processing temperature of 325 °C using LignoBoost lignin. LignoBoost lignin, mainly consisting out of lignin, had a stable structure and needed a higher processing temperature (i.e. 325 °C) to breakdown the lignin. Hence, it was able to achieve a higher bio-crude yield. From the elemental analysis, the highest HHV of pine wood was obtained at a lower processing temperature of 275 °C of 36.14 MJ kg^{-1}. HTL processing has shown a great potential for the production for biofuels using LignoBoost lignin and pine wood. However, further upgrading is essential for both bio-crudes to improve the quality of the fuel. Further analysis was done on the bio-crudes using GC-MS. Guaiacol were observed to be the main product, as well as phenolic components, found in the LignoBoost lignin bio-crudes. Pine wood bio-crudes were observed with both holocellulose and lignin-derived products, such as 4-hydroxy-2-methyl-pentanone, levulinic acid, guaiacol, creosol and 2-methoxy-4-propylphenol. Most of these products were anticipated, which were already identified in the 'raw' feedstock from the Py-GC-MS analysis in Chapter 3.

Gaseous products were characterised using GC-FID where significant methane and ethane were obtained from HTL processing from both feedstock. Higher processing temperature resulted in an increase in methane (63.66 %) and ethane (9.48 %) production from LignoBoost lignin. Whilst, pine wood favoured a lower processing temperature of 275 °C and a maximum methane and ethane

production were found at 26.29 % and 7.27 %, respectively. Aqueous phases from the liquid products obtained from HTL were analysed using GC-MS and HPLC. Acetic acid was the only carboxylic acid detected in the aqueous phase from LignoBoost lignin using the GC-MS. Pine wood aqueous phase samples were found with acetic, propionic, lactic and levulinic acids. Low molecular weight products were revealed with the aid of HPLC, as additional carboxylic acids were found in both aqueous phase samples. LignoBoost lignin was found with methanol, formic and acetic acid. Pine wood was found with formic, acetic, propionic acids and guaiacol.

DSC analysis was a reliable method to identify the melting point and to validate the thermal stability of the 'pure' molten and recycled salts. The 'pure' molten salts were identified to have a melting point of 208 °C. Recycled salts, from the first and second recovery, processed with LignoBoost lignin were identified to have a melting point region of around 200 °C. Similar thermal behaviour were observed from the recovered salts processed with pine wood. Proving that the molten salts with biomass processed during the liquefaction, recovery and purification steps, were not affected and thermally stable. The metal analysis, conducted in Chapter 3, identified calcium and potassium to be the most abundant metals which could potentially interact with the molten salts. Therefore, XRD analyses were conducted on the 'pure' molten salts with added 10 % of potassium carbonate, calcium chloride or calcium carbonate. With the help of FactSage modelling, the 10 % added 'impurities' lead to the formation of intermediates such as zinc oxide, chlorocalcite and calcium chloride. These were further confirmed by XRD analysis, which were detected in the diffractogram. It also showed that individual molten salt constituents do interact with the inorganic matter from the biomass during liquefaction processing and impacting the crystallinity of the molten salt sample. This could be a potential reason why there was an observed decrease in the melting point of the recycled salts from the DSC analysis.

Lastly, char products were recovered along with the (recycled) molten salts and were characterised using elemental and SEM analyses. LignoBoost lignin and pine wood char were found on average to have a lower carbon and hydrogen content when compared to the conventional HTL chars (from Chapter 5). It should be noted that the products obtained from liquefaction in molten salts will be further processed in hydro-pyrolysis. Therefore, the carbon and hydrogen content will be increased after hydro-pyrolysis. SEM imaging showed that the structure of recovered chars were destroyed when comparing it to the unprocessed biomass and could be due to the presence of the salts.

7.2. Future work

This section provides suggestions on further investigations into HTL of lignocellulosic biomass and waste lignin, which are based on this research:

- Analytical pyrolysis (Py-GC-MS) was used to identify potential end-products from the thermal degradation of feedstock selected for conventional and molten salt liquefaction. The Py-GC-MS analysis gave only type (qualitative analysis) of thermal degradation components without quantification (quantitative analysis). The introduction of the flame ionisation detector (FID) is proposed for quantification of key markers with the aid of dedicated GC standards. Targeting markers of potential end-products that can be seen in the bio-liquids, including syringol-lignin, guaiacol-lignin, p-hydroxyphenyl lignin, cyclopentanes, and furfurals.

- The model-free Kissinger model was chosen as a starting point for kinetic parameters from the thermal degradation of studied feedstock. The thermodynamic results were used to be applied to study the interaction of biomass inorganic components (such as calcium, potassium and chloride) with molten salts. The thermodynamic results were used to be applied to study the interaction of biomass inorganic components (such as calcium, potassium and chloride) with molten salts. The Kissinger model takes only the peak temperature obtained from the DTG mass profile reflecting a simple thermal degradation model proposed by Shafizadeh. Two other kinetic models (KAS and FWO) were selected to reflect the conversion rates during thermal degradation and were used for thermodynamic assessment contributing to better understanding of process dynamics. Other kinetic methods such as model-fitting (Coats-Redfern) or model-free isothermal (such as Friedman) methods can be further used to calculate the kinetic parameters. The wider use of other kinetic models can be compared with the model-free and non-isothermal models to allow further validation on the thermal decomposition of biomass.

- The introduction of a wider range of process parameters, which could include lower and/or higher HTL processing temperature, starting pressure, different heating rates and atmosphere (hydrogen) to achieve the HTL temperature as well as different resident times are proposed to study the improvement of bio-liquid yields. Furthermore, it should not be limited to only softwood-based feedstock, as both LignoBoost lignin (delignified from pine wood and spruce wood at 50:50 ratio) and pine wood. The difference in the application of hardwood or softwood would be an interesting comparison to observe similarities or differences in the end-

product distribution (quantity and composition of bio-liquids/bio-crudes) along with the impact of different processing parameters.

- The HTL-generated bio-crudes require further upgrading as it was concluded that the HHV were low when compared to the conventional fuel. Using an inexpensive catalyst (such as potassium carbonate) could potentially improve the bio-crude yield, HHV and/or deoxygenate the bio-crudes and could possibly avoid the HDO upgrading step to minimise the costs. The use of (co-)solvents, such as tetralin, could enhance the bio-crude quality and lower the oxygen content found in the bio-crudes. Tetralin is a hydrogen donor solvent and promotes the *in-situ* hydrogenation within the process.

- The DSC analysis of all molten salts was only investigated up to 500 °C as aluminium crucible were used. Few attempts of using an alumina crucible were made, which allowed the TGA/DSC equipment to go above the 500 °C limit. However, the DSC was unable to detect the thermal behaviour of the molten salt. Different crucible material, such as platinum crucibles, could potentially detect the molten salt thermal behaviour above 500 °C.

- Solid products (chars) obtained from the conventional HTL process and liquefaction in molten salts were compared. However, a direct comparison was not done for bio-liquids. This could be interesting to investigate which process will improve the quality and quantity of the liquids, further needs for upgrading in order to meet the specification of middle-range distillates and most importantly, process economics.

7.3. Research outputs

7.3.1. Up-to-date disseminated items

During this PhD research projects, the following items were disseminated showing research outputs from experimental work between 2018 and 2022.

R.H.M. Siu, D.J. Nowakowski and A.V. Bridgwater; *Production of Biofuels from Various Lignocellulosic Waste Streams by Liquefaction and Hydropyrolysis*; 27th EU Biomass Conference and Exhibition – EUBCE 2019, Lisbon (Portugal), 27-30 May 2019. [conference poster]

D.J. Nowakowski, R.H.M. Siu and A.V. Bridgwater; *Deliverable 3.2 Biomass and ash characteristics and analyses*; 29 May 2019. [project deliverable]

R.H.M. Siu, J. Cherukkattu Manayil and D.J. Nowakowski; *Deliverable 4.1 Kinetic model of the thermal decomposition of biomass in molten-salt hydro-pyrolysis*; 29 October 2019. [project deliverable]

R.H.M Siu, D.J. Nowakowski and A.V. Bridgwater; *Py-GC-MS Characterisation and TGA Kinetics of Lignocellulosic Biomass*; 23rd edition of International eConference on Analytical and Applied Pyrolysis (ePYRO2021), Ghent (Belgium), on-line conference 12-13 April 2021. [e-conference presentation]

D.J. Nowakowski, R.H.M. Siu, A. Estrada Leon, F. Ronsse, S. Niazi and H.S. Nygård; *Deliverable 4.6 Thermodynamic models recommendations for molten salt recycling system*; 17 August 2021 [project deliverable]

R.H.M. Siu, J. Cherukkattu Manayil, D.J. Nowakowski and A.V. Bridgwater; *Hydrothermal liquefaction of lignocellulosic biomass for fuels: Influence of temperature and co-solvents*; 23rd edition of International Conference on Analytical and Applied Pyrolysis (PYRO2022), Ghent (Belgium), 15-20 May 2022. [conference poster]

R.H.M. Siu, J. Cherukkattu Manayil, D.J. Nowakowski and A.V. Bridgwater; *Kinetic and thermodynamic assessment of lignin and lignocellulosic biomass pyrolysis*; 23rd edition of International Conference on Analytical and Applied Pyrolysis (PYRO2022), Ghent (Belgium), 15-20 May 2022. [conference poster]

7.3.2.   Planned dissemination

The following research outputs would be published as a peer-reviewed papers (Open Access) disseminating findings from this PhD (paper 1) and collaborative research with the ABC-Salt project partners (paper 2).

1. R.H.M. Siu, J. Cherukkattu Manayil, D.J. Nowakowski; *Kinetic and thermodynamic assessment of lignin and lignocellulosic biomass pyrolysis*.
2. A. Estrada Leon, R.H.M. Siu, F. Ronsse, D.J. Nowakowski and A.V. Bridgwater; *Characterisation and thermal properties of spent molten salts by differential scanning calorimetry (DSC).*

References

1. *Framing and Context*, in *Global Warming of 1.5°C: IPCC Special Report on Impacts of Global Warming of 1.5°C above Pre-industrial Levels in Context of Strengthening Response to Climate Change, Sustainable Development, and Efforts to Eradicate Poverty*, Ipcc, Editor. 2022, Cambridge University Press: Cambridge. p. 49-92.

2. Lamb, W.F., et al., *A review of trends and drivers of greenhouse gas emissions by sector from 1990 to 2018.* Environmental Research Letters, 2021. **16**(7): p. 073005.

3. Allen, S.K., et al., *Summary for Policymakers*, in *Managing the Risks of Extreme Events and Disasters to Advance Climate Change Adaptation: Special Report of the Intergovernmental Panel on Climate Change*, C.B. Field, et al., Editors. 2012, Cambridge University Press: Cambridge. p. 3-22.

4. Government, H., *Net Zero Strategy: Build Back Greener*, E.a.I.S. Department for Business, Editor. 2021, Open Government Licence v3.0.

5. Moodley, P., *1 - Sustainable biofuels: opportunities and challenges*, in *Sustainable Biofuels*, R.C. Ray, Editor. 2021, Academic Press. p. 1-20.

6. Niazi, S., E. Olsen, and H.S. Nygård, *Hydrolysis of eutectic compositions in the ZnCl2:KCl:NaCl ternary system and effect of adding ZnO.* Journal of Molecular Liquids, 2020. **317**: p. 114069.

7. Wang, S.R., et al., *Lignocellulosic biomass pyrolysis mechanism: A state-of-the-art review.* Progress in Energy and Combustion Science, 2017. **62**: p. 33-86.

8. Tekin, K., M.K. Akalin, and S. Karagoz, *The effects of water tolerant Lewis acids on the hydrothermal liquefaction of lignocellulosic biomass.* Journal of the Energy Institute, 2016. **89**(4): p. 627-635.

9. Saini, J.K., R. Saini, and L. Tewari, *Lignocellulosic agriculture wastes as biomass feedstocks for second-generation bioethanol production: concepts and recent developments.* 3 Biotech, 2015. **5**(4): p. 337-353.

10. Merino, S.T. and J. Cherry, *Progress and Challenges in Enzyme Development for Biomass Utilization*, in *Biofuels*, L. Olsson, Editor. 2007, Springer Berlin Heidelberg: Berlin, Heidelberg. p. 95-120.

11. Ballesteros, M., et al., *Ethanol from lignocellulosic materials by a simultaneous saccharification and fermentation process (SFS) with Kluyveromyces marxianus CECT 10875.* Process Biochemistry, 2004. **39**(12): p. 1843-1848.

12. Naik, S., et al., *Characterization of Canadian biomass for alternative renewable biofuel.* Renewable Energy, 2010. **35**(8): p. 1624-1631.

13. Rowell, R.M., *Opportunities for Lignocellulosic Materials and Composites*, in *Emerging Technologies for Materials and Chemicals from Biomass*. 1992, American Chemical Society. p. 12-27.

14. Taherzadeh, M.J., et al., *Characterization and Fermentation of Dilute-Acid Hydrolyzates from Wood.* Industrial & Engineering Chemistry Research, 1997. **36**(11): p. 4659-4665.

15. *Index*, in *Fuels of Opportunity*, D.A. Tillman and N. Stanley Harding, Editors. 2004, Elsevier: Oxford. p. 305-312.

16. Huber, G.W., S. Iborra, and A. Corma, *Synthesis of transportation fuels from biomass: Chemistry, catalysts, and engineering.* Chemical Reviews, 2006. **106**(9): p. 4044-4098.

17. Shen, D.K. and S. Gu, *The mechanism for thermal decomposition of cellulose and its main products.* Bioresource Technology, 2009. **100**(24): p. 6496-6504.

18. Brosse, N., et al., *Dilute Sulphuric Acid and Ethanol Organosolv Pretreatment of Miscanthus x Giganteus.* Cellulose Chemistry and Technology, 2010. **44**: p. 71-78.

19. Rabemanolontsoa, H. and S. Saka, *Comparative study on chemical composition of various biomass species.* RSC Advances, 2013. **3**(12): p. 3946-3956.

20. Nanda, S., et al., *Characterization of North American Lignocellulosic Biomass and Biochars in Terms of their Candidacy for Alternate Renewable Fuels.* BioEnergy Research, 2013. **6**(2): p. 663-677.

21. Tang, J., et al., *Characterization of the pretreatment liquor of biomass from the perennial grass, Eulaliopsis binata, for the production of dissolving pulp.* Bioresource Technology, 2013. **129**: p. 548-552.

22. Shafiei, M., K. Karimi, and M.J. Taherzadeh, *Pretreatment of spruce and oak by N-methylmorpholine-N-oxide (NMMO) for efficient conversion of their cellulose to ethanol.* Bioresource Technology, 2010. **101**(13): p. 4914-4918.

23. Demirbaş, A., *Thermochemical Conversion of Biomass to Liquid Products in the Aqueous Medium.* Energy Sources, 2005. **27**(13): p. 1235-1243.

24. Cherubini, F. and A.H. Strømman, *Production of Biofuels and Biochemicals from Lignocellulosic Biomass: Estimation of Maximum Theoretical Yields and Efficiencies Using Matrix Algebra.* Energy & Fuels, 2010. **24**(4): p. 2657-2666.

25. Qu, T., et al., *Experimental Study of Biomass Pyrolysis Based on Three Major Components: Hemicellulose, Cellulose, and Lignin.* Industrial & Engineering Chemistry Research, 2011. **50**.

26. Li, H., et al., *Simultaneous saccharification and fermentation of lignocellulosic residues pretreated with phosphoric acid–acetone for bioethanol production.* Bioresource Technology, 2009. **100**(13): p. 3245-3251.

27.   Kumar, A., A. Gautam, and D. Dutt, *Biotechnological Transformation of Lignocellulosic Biomass in to Industrial Products: An Overview.* Advances in Bioscience and Biotechnology, 2016. **7**: p. 149-168.

28.   Sánchez, C., *Lignocellulosic residues: Biodegradation and bioconversion by fungi.* Biotechnology Advances, 2009. **27**(2): p. 185-194.

29.   Dhyani, V. and T. Bhaskar, *A comprehensive review on the pyrolysis of lignocellulosic biomass.* Renewable Energy, 2018. **129**: p. 695-716.

30.   Rowell, R., *Handbook Of Wood Chemistry And Wood Composites*. 2005.

31.   Ximenes, E., et al., *Hydrothermal Pretreatment of Lignocellulosic Biomass for Bioethanol Production*, in *Hydrothermal Processing in Biorefineries: Production of Bioethanol and High Added-Value Compounds of Second and Third Generation Biomass*, H.A. Ruiz, M. Hedegaard Thomsen, and H.L. Trajano, Editors. 2017, Springer International Publishing: Cham. p. 181-205.

32.   El-Sakhawy, M. and M.L. Hassan, *Physical and mechanical properties of microcrystalline cellulose prepared from agricultural residues.* Carbohydrate Polymers, 2007. **67**(1): p. 1-10.

33.   Bradbury, A.G.W., Y. Sakai, and F. Shafizadeh, *Kinetic-Model for Pyrolysis of Cellulose.* Journal of Applied Polymer Science, 1979. **23**(11): p. 3271-3280.

34.   Demirbas, A., *Pyrolysis Mechanisms of Biomass Materials.* Energy Sources, Part A: Recovery, Utilization, and Environmental Effects, 2009. **31**(13): p. 1186-1193.

35.   Piskorz, J., D. Radlein, and D.S. Scott, *On the mechanism of the rapid pyrolysis of cellulose.* Journal of Analytical and Applied Pyrolysis, 1986. **9**(2): p. 121-137.

36.   Wang, Q., et al., *Initial pyrolysis mechanism and product formation of cellulose: An Experimental and Density functional theory(DFT) study.* Scientific Reports, 2020. **10**(1): p. 3626.

37.   Liao, Y.-F., S. Wang, and X.Q. Ma, *Study of reaction mechanisms in cellulose pyrolysis.* ACS Division of Fuel Chemistry, Preprints, 2004. **49**.

38.   Scheller, H.V. and P. Ulvskov, *Hemicelluloses.* Annual Review of Plant Biology, Vol 61, 2010. **61**: p. 263-289.

39.   Xiao, L.-P., G.-Y. Song, and R.-C. Sun, *Effect of Hydrothermal Processing on Hemicellulose Structure*, in *Hydrothermal Processing in Biorefineries: Production of Bioethanol and High Added-Value Compounds of Second and Third Generation Biomass*, H.A. Ruiz, M. Hedegaard Thomsen, and H.L. Trajano, Editors. 2017, Springer International Publishing: Cham. p. 45-94.

40.   Sjöström, E., *Chapter 3 - Wood Polysaccharides*, in *Wood Chemistry (Second Edition)*, E. Sjöström, Editor. 1993, Academic Press: San Diego. p. 51-70.

41.   Ebringerova, A., *Structural diversity and application potential of hemicelluloses.* Macromolecular Symposia, 2006. **232**: p. 1-12.

42.   Fushimi, C., S. Katayama, and A. Tsutsumi, *Elucidation of interaction among cellulose, lignin and xylan during tar and gas evolution in steam gasification.* Journal of Analytical and Applied Pyrolysis, 2009. **86**(1): p. 82-89.

43.   Lafarguette, F., et al., *Poplar genes encoding fasciclin-like arabinogalactan proteins are highly expressed in tension wood.* New Phytologist, 2004. **164**(1): p. 107-121.

44.   Shimizu, K., *Wood and cellulosic chemistry*. Chemistry of hemicelluloses. 2001, New York: M. Dekker.

45.   Wool, R.P., *16 - LIGNIN POLYMERS AND COMPOSITES*, in *Bio-Based Polymers and Composites*, R.P. Wool and X.S. Sun, Editors. 2005, Academic Press: Burlington. p. 551-598.

46.   Kawamoto, H., *Lignin pyrolysis reactions.* Journal of Wood Science, 2017. **63**(2): p. 117-132.

47.   Li, W., et al., *Linking lignin source with structural and electrochemical properties of lignin-derived carbon materials.* RSC Advances, 2018. **8**(68): p. 38721-38732.

48.   Roudier, S.K., Ioanna ; Delgado Sancho, Luis ; Rodrigo Gonzalo, Miguel ; Suhr, Michael ; Giner Santonja, Germán ; Klein, Gabriele, *Best Available Techniques (BAT) reference document for the production of pulp, paper and board*. 2015, Publications Office of the European Union.

49.   Lin, S.Y. and I.S. Lin, *Lignin*, in *Ullmann's Encyclopedia of Industrial Chemistry*.

50.   Elumalai, S. and X.J. Pan, *Chemistry and Reactions of Forest Biomass in Biorefining*, in *Sustainable Production of Fuels, Chemicals, and Fibers from Forest Biomass*. 2011, American Chemical Society. p. 109-144.

51.   Matsushita, Y., *Conversion of technical lignins to functional materials with retained polymeric properties.* Journal of Wood Science, 2015. **61**(3): p. 230-250.

52.   Aro, T. and P. Fatehi, *Production and Application of Lignosulfonates and Sulfonated Lignin.* ChemSusChem, 2017. **10**(9): p. 1861-1877.

53.   Calvo-Flores, F.G., Dobado, J.A., Isac-García, J. and Martín-Martínez, F.J., *Isolation of Lignins*, in *Lignin and Lignans as Renewable Raw Materials*. 2015. p. 113-144.

54.   Theliander, H., *The lignoboost process: Solubility of lignin.* International Chemical Recovery Conference, 2010. **2**: p. 33-42.

55.   Chakar, F.S. and A.J. Ragauskas, *Review of current and future softwood kraft lignin process chemistry.* Industrial Crops and Products, 2004. **20**(2): p. 131-141.

56.   Bajwa, D.S., et al., *A concise review of current lignin production, applications, products and their environmental impact.* Industrial Crops and Products, 2019. **139**: p. 111526.

57.   Tomani, P., *The Lignoboost Process.* Cellulose Chemistry and Technology, 2010. **44**(1-3): p. 53-58.

58. Paridah, M.T., et al., *Alkaline Sulfite Anthraquinone and Methanol (ASAM) Pulping Process of Tropical Bamboo (Gigantochloa scortechinii)*, in *Bamboo*, H.P.S. Abdul Khalil, Editor. 2018, IntechOpen: Rijeka. p. 7-10.

59. Lindner, A. and G. Wegener, *Characterization of Lignins from Organosolv Pulping According to the Organocell Process Part 1. Elemental Analysis, Nonlignin Portions and Functional Groups.* Journal of Wood Chemistry and Technology, 1988. **8**(3): p. 323-340.

60. Pye, E.K. and J.H. Lora, *The Alcell Process - a Proven Alternative to Kraft Pulping.* Tappi Journal, 1991. **74**(3): p. 113-118.

61. Li, T. and S. Takkellapati, *The current and emerging sources of technical lignins and their applications.* Biofuels, Bioproducts and Biorefining, 2018. **12**(5): p. 756-787.

62. Hidayati, S., et al., *Isolation and characterization of formacell Lignins from oil empty fruits bunches.* IOP Conference Series: Materials Science and Engineering, 2018. **344**: p. 012006.

63. Ligero, P., A. Vega, and J.J. Villaverde, *Delignification of Miscanthus×Giganteus by the Milox process.* Bioresource Technology, 2010. **101**(9): p. 3188-3193.

64. Mohan, D., C.U. Pittman, and P.H. Steele, *Pyrolysis of wood/biomass for bio-oil: A critical review.* Energy & Fuels, 2006. **20**(3): p. 848-889.

65. Wang, S. and Z. Luo, *1. Biomass components and characteristics*, in *Pyrolysis of Biomass*. 2017, De Gruyter: Berlin, Boston. p. 1-32.

66. Vassilev, S.V., et al., *Ash contents and ash-forming elements of biomass and their significance for solid biofuel combustion.* Fuel, 2017. **208**: p. 377-409.

67. Yang, C., et al., *Hydrothermal liquefaction and gasification of biomass and model compounds: a review.* Green Chemistry, 2020. **22**(23): p. 8210-8232.

68. Shuping, Z., et al., *Production and characterization of bio-oil from hydrothermal liquefaction of microalgae Dunaliella tertiolecta cake.* Energy, 2010. **35**(12): p. 5406-5411.

69. Gollakota, A.R.K., N. Kishore, and S. Gu, *A review on hydrothermal liquefaction of biomass.* Renewable & Sustainable Energy Reviews, 2018. **81**: p. 1378-1392.

70. Xu, Y.-H. and M.-F. Li, *Hydrothermal liquefaction of lignocellulose for value-added products: Mechanism, parameter and production application.* Bioresource Technology, 2021. **342**: p. 126035.

71. Lange, J.-P., *Lignocellulose Liquefaction to Biocrude: A Tutorial Review.* ChemSusChem, 2018. **11**(6): p. 997-1014.

72. Demirbaş, A., *Mechanisms of liquefaction and pyrolysis reactions of biomass.* Energy Conversion and Management, 2000. **41**(6): p. 633-646.

73. Möller, M., F. Harnisch, and U. Schröder, *Hydrothermal liquefaction of cellulose in subcritical water—the role of crystallinity on the cellulose reactivity.* RSC Advances, 2013. **3**(27): p. 11035-11044.

74. Möller, M., et al., *Subcritical Water as Reaction Environment: Fundamentals of Hydrothermal Biomass Transformation.* ChemSusChem, 2011. **4**(5): p. 566-579.

75. Gagić, T., et al., *Hydrothermal Degradation of Cellulose at Temperature from 200 to 300 °C.* Industrial & Engineering Chemistry Research, 2018. **57**(18): p. 6576-6584.

76. TAKEUCHI, Y., et al., *CONVERSION OF GLUCOSE TO 5-HYDROXYMETHYL-2-FURALDEHYDE AND 2-FURALDEHYDE BY HYDROTHERMAL REACTION*, in *Hydrothermal Reactions and Techniques*. 2003. p. 67-73.

77. Gao, Y., et al., *Hydrothermal degradation of hemicelluloses from triploid poplar in hot compressed water at 180–340 °C.* Polymer Degradation and Stability, 2016. **126**: p. 179-187.

78. Zhang, L., et al., *Advance in Hydrothermal Bio-Oil Preparation from Lignocellulose: Effect of Raw Materials and Their Tissue Structures.* 2021. **1**(2): p. 74-93.

79. Hu, J., et al., *Effect of temperature on structure evolution in char from hydrothermal degradation of lignin.* Journal of Analytical and Applied Pyrolysis, 2014. **106**: p. 118-124.

80. Yahaya, A., H. Ursel, and M.B. Idris, *Lignin Hydrothermal Liquefaction into Bifunctional Chemicals: A Concise Review*, in *Biorefinery Concepts, Energy and Products*, B. Venko, Editor. 2020, IntechOpen: Rijeka. p. 71-92.

81. Yong, T.L.-K. and Y. Matsumura, *Kinetic Analysis of Lignin Hydrothermal Conversion in Sub- and Supercritical Water.* Industrial & Engineering Chemistry Research, 2013. **52**(16): p. 5626-5639.

82. Shimizu, N., B. Zeng, and K. Kushima, *Hydrothermal liquefaction of wood chips under supercritical and subcritical water reaction conditions.* SN Applied Sciences, 2021. **3**(5): p. 577.

83. Kim, J.Y., et al., *Overview of the recent advances in lignocellulose liquefaction for producing biofuels, bio-based materials and chemicals.* Bioresour Technol, 2019. **279**: p. 373-384.

84. Dimitriadis, A. and S. Bezergianni, *Hydrothermal liquefaction of various biomass and waste feedstocks for biocrude production: A state of the art review.* Renewable & Sustainable Energy Reviews, 2017. **68**: p. 113-125.

85. de Caprariis, B., et al., *Hydrothermal liquefaction of biomass: Influence of temperature and biomass composition on the bio-oil production.* Fuel, 2017. **208**: p. 618-625.

86. Mathanker, A., et al., *Hydrothermal liquefaction of lignocellulosic biomass feedstock to produce biofuels: Parametric study and products characterization.* Fuel, 2020. **271**: p. 117534.

87. Zhu, Z., et al., *Hydrothermal liquefaction of barley straw to bio-crude oil: Effects of reaction temperature and aqueous phase recirculation.* Applied Energy, 2015. **137**: p. 183-192.

88.   Sun, P., et al., *Direct liquefaction of paulownia in hot compressed water: Influence of catalysts.* Energy, 2010. **35**(12): p. 5421-5429.

89.   Ogi, T. and S.-y. Yokoyama, *Liquid Fuel Production from Woody Biomass by Direct Liquefaction.* Journal of The Japan Petroleum Institute, 1993. **36**(2): p. 73-84.

90.   Akhtar, J. and N.A.S. Amin, *A review on process conditions for optimum bio-oil yield in hydrothermal liquefaction of biomass.* Renewable and Sustainable Energy Reviews, 2011. **15**(3): p. 1615-1624.

91.   Mathanker, A., et al., *A Review of Hydrothermal Liquefaction of Biomass for Biofuels Production with a Special Focus on the Effect of Process Parameters, Co-Solvents and Extraction Solvents.* Energies, 2021. **14**: p. 4916.

92.   Jindal, M.K. and M.K. Jha, *Hydrothermal liquefaction of wood: a critical review.* Reviews in Chemical Engineering, 2016. **32**(4): p. 459-488.

93.   Durak, H. and T. Aysu, *Structural analysis of bio-oils from subcritical and supercritical hydrothermal liquefaction of Datura stramonium L.* The Journal of Supercritical Fluids, 2016. **108**: p. 123-135.

94.   Qian, L., S. Wang, and P.E. Savage, *Hydrothermal liquefaction of sewage sludge under isothermal and fast conditions.* Bioresource Technology, 2017. **232**: p. 27-34.

95.   Kruse, A. and A. Gawlik, *Biomass Conversion in Water at 330–410 °C and 30–50 MPa. Identification of Key Compounds for Indicating Different Chemical Reaction Pathways.* Industrial & Engineering Chemistry Research, 2003. **42**(2): p. 267-279.

96.   Yang, L., et al., *Hydrothermal liquefaction of spent coffee grounds in water medium for bio-oil production.* Biomass and Bioenergy, 2016. **86**: p. 191-198.

97.   Isa, K.M., T.A.T. Abdullah, and U.F.M. Ali, *Hydrogen donor solvents in liquefaction of biomass: A review.* Renewable and Sustainable Energy Reviews, 2018. **81**: p. 1259-1268.

98.   Toor, S.S., L. Rosendahl, and A. Rudolf, *Hydrothermal liquefaction of biomass: A review of subcritical water technologies.* Energy, 2011. **36**(5): p. 2328-2342.

99.   Blaschek, H.P., T.C. Ezeji, and J. Scheffran, *Biofuels from agricultural wastes and byproducts*. 2010: John Wiley & Sons.

100.   Perkins, G., et al., *Recent advances in liquefaction technologies for production of liquid hydrocarbon fuels from biomass and carbonaceous wastes.* Renewable and Sustainable Energy Reviews, 2019. **115**: p. 109400.

101.   Han, Y., et al., *Use of Co-Solvents in Hydrothermal Liquefaction (HTL) of Microalgae.* Energies, 2020. **13**(1): p. 124.

102.   Zhao, B., et al., *Promotion effects of metallic iron on hydrothermal liquefaction of cornstalk in ethanol-water mixed solvents for the production of biocrude oil.* Fuel, 2021. **285**: p. 119150.

103. Alper, K., K. Tekin, and S. Karagöz, *Hydrothermal Liquefaction of Lignocellulosic Biomass Using Potassium Fluoride-Doped Alumina.* Energy & Fuels, 2019. **33**(4): p. 3248-3256.

104. Cheng, S., et al., *Highly Efficient Liquefaction of Woody Biomass in Hot-Compressed Alcohol–Water Co-solvents.* Energy & Fuels, 2010. **24**(9): p. 4659-4667.

105. Xue, Y., et al., *A review on the operating conditions of producing bio-oil from hydrothermal liquefaction of biomass.* International Journal of Energy Research, 2016. **40**(7): p. 865-877.

106. Bayat, H., et al., *Hydrothermal Liquefaction of Food Waste: Effect of Process Parameters on Product Yields and Chemistry.* Frontiers in Sustainable Food Systems, 2021. **5**.

107. Eboibi, B.E., et al., *Effect of operating conditions on yield and quality of biocrude during hydrothermal liquefaction of halophytic microalga Tetraselmis sp.* Bioresource Technology, 2014. **170**: p. 20-29.

108. Cao, L.C., et al., *Hydrothermal liquefaction of agricultural and forestry wastes: state-of-the-art review and future prospects.* Bioresource Technology, 2017. **245**: p. 1184-1193.

109. Tian, Y., et al., *Hydrothermal liquefaction of crop straws: Effect of feedstock composition.* Fuel, 2020. **265**: p. 116946.

110. de Caprariis, B., et al., *Enhanced bio-crude yield and quality by reductive hydrothermal liquefaction of oak wood biomass: Effect of iron addition.* Journal of Analytical and Applied Pyrolysis, 2019. **139**: p. 123-130.

111. Ding, Y.-J., C.-X. Zhao, and Z.-C. Liu, *Catalytic hydrothermal liquefaction of rice straw for production of monomers phenol over metal supported mesoporous catalyst.* Bioresource Technology, 2019. **294**: p. 122097.

112. Cheng, S., L. Wei, and M. Rabnawaz, *Catalytic liquefaction of pine sawdust and in-situ hydrogenation of bio-crude over bifunctional Co-Zn/HZSM-5 catalysts.* Fuel, 2018. **223**: p. 252-260.

113. Yerrayya, A., et al., *Optimization of bio-crude yield and its calorific value from hydrothermal liquefaction of bagasse using methanol as co-solvent.* Energy, 2022. **244**: p. 123192.

114. Song, L., et al., *Insight into liquefaction process of sawdust with hydrogen donor solvents.* Biomass and Bioenergy, 2022. **160**: p. 106444.

115. Gopal, P.M., N.M. Sivaram, and D. Barik, *Chapter 7 - Paper Industry Wastes and Energy Generation From Wastes*, in *Energy from Toxic Organic Waste for Heat and Power Generation*, D. Barik, Editor. 2019, Woodhead Publishing. p. 83-97.

116. Bridgwater, A.V., *Review of fast pyrolysis of biomass and product upgrading.* Biomass & Bioenergy, 2012. **38**: p. 68-94.

117. Resende, F.L.P., *Recent advances on fast hydropyrolysis of biomass.* Catalysis Today, 2016. **269**: p. 148-155.

118. Marker, T.L., et al., *Integrated Hydropyrolysis and Hydroconversion (IH2) for the Direct Production of Gasoline and Diesel Fuels or Blending Components from Biomass, Part 1: Proof of Principle Testing.* Environmental Progress & Sustainable Energy, 2012. **31**(2): p. 191-199.

119. Venkatakrishnan, V.K., et al., *High-pressure fast-pyrolysis, fast-hydropyrolysis and catalytic hydrodeoxygenation of cellulose: production of liquid fuel from biomass.* Green Chemistry, 2014. **16**(2): p. 792-802.

120. Meesuk, S., et al., *Fast Pyrolysis of Rice Husk in a Fluidized Bed: Effects of the Gas Atmosphere and Catalyst on Bio-oil with a Relatively Low Content of Oxygen.* Energy & Fuels, 2011. **25**(9): p. 4113-4121.

121. Dayton, D.C., et al., *Biomass Hydropyrolysis in a Fluidized Bed Reactor.* Energy & Fuels, 2016. **30**(6): p. 4879-4887.

122. Zhang, H., et al., *Biomass fast pyrolysis in a fluidized bed reactor under N2, CO2, CO, CH4 and H2 atmospheres.* Bioresour Technol, 2011. **102**(5): p. 4258-64.

123. He, Y., et al., *Comparative study of fast pyrolysis, hydropyrolysis and catalytic hydropyrolysis of poplar sawdust and rice husk in a modified Py-GC/MS microreactor system: Insights into product distribution, quantum description and reaction mechanism.* Renewable and Sustainable Energy Reviews, 2020. **119**: p. 109604.

124. Beims, R.F., et al., *Hydrothermal liquefaction of biomass to fuels and value-added chemicals: Products applications and challenges to develop large-scale operations.* Biomass and Bioenergy, 2020. **135**: p. 105510.

125. Benés, M., et al., *Hydrodeoxygenation of Lignocellulosic Fast Pyrolysis Bio-Oil: Characterization of the Products and Effect of the Catalyst Loading Ratio.* Energy & Fuels, 2019. **33**(5): p. 4272-4286.

126. Elkasabi, Y., et al., *Hydrodeoxygenation of fast-pyrolysis bio-oils from various feedstocks using carbon-supported catalysts.* Fuel Processing Technology, 2014. **123**: p. 11-18.

127. Yue, Y., J.R. Kastner, and S. Mani, *Two-Stage Hydrothermal Liquefaction of Sweet Sorghum Biomass—Part II: Production of Upgraded Biocrude Oil.* Energy & Fuels, 2018. **32**(7): p. 7620-7629.

128. Tran, Q.K., et al., *Catalytic hydrodeoxygenation of guaiacol as a model compound of woody bio-oil over Fe/AC and Ni/γ-Al2O3 catalysts.* Renewable Energy, 2021. **173**: p. 886-895.

129. Oh, S., J.H. Lee, and J.W. Choi, *Hydrodeoxygenation of crude bio-oil with various metal catalysts in a continuous-flow reactor and evaluation of emulsion properties of upgraded bio-oil with petroleum fuel.* Renewable Energy, 2020. **160**: p. 1160-1167.

130. Bharath, G., et al., *Catalytic hydrodeoxygenation of biomass-derived pyrolysis oil over alloyed bimetallic Ni3Fe nanocatalyst for high-grade biofuel production.* Energy Conversion and Management, 2020. **213**: p. 112859.

131. Nygård, H.S. and E. Olsen, *Review of thermal processing of biomass and waste in molten salts for production of renewable fuels and chemicals.* International Journal of Low-Carbon Technologies, 2012. **7**(4): p. 318-324.

132. Coscia, K., et al., *Binary and Ternary Nitrate Solar Heat Transfer Fluids.* Journal of Solar Energy Engineering, 2013. **135**(2).

133. Cabeza, L.F., *2 - Advances in thermal energy storage systems: methods and applications*, in *Advances in Thermal Energy Storage Systems (Second Edition)*, L.F. Cabeza, Editor. 2021, Woodhead Publishing. p. 37-54.

134. Kim, J.S., Y.Y. Lee, and T.H. Kim, *A review on alkaline pretreatment technology for bioconversion of lignocellulosic biomass.* Bioresource Technology, 2016. **199**: p. 42-48.

135. Sada, E., H. Kumazawa, and M. Kudsy, *Pyrolysis of lignins in molten salt media.* Industrial & Engineering Chemistry Research, 1992. **31**(2): p. 612-616.

136. Kudsy, M. and H. Kumazawa, *Pyrolysis of kraft lignin in the presence of molten ZnCl2-KCl mixture.* The Canadian Journal of Chemical Engineering, 1999. **77**(6): p. 1176-1184.

137. Datta, R.D., J.P.;, *Molten salt pyrolysis for bio-oil and chemicals*, in *PCT*, WIPO, Editor. 2017.

138. Robelin, C. and P. Chartrand, *Thermodynamic evaluation and optimization of the (NaCl+KCl+MgCl2+CaCl2+ZnCl2) system.* The Journal of Chemical Thermodynamics, 2011. **43**(3): p. 377-391.

139. Xu, X., et al., *Basic properties of eutectic chloride salts NaCl-KCl-ZnCl2 and NaCl-KCl-MgCl2 as HTFs and thermal storage media measured using simultaneous DSC-TGA.* Solar Energy, 2018. **162**: p. 431-441.

140. Shen, D.K., S. Gu, and A.V. Bridgwater, *Study on the pyrolytic behaviour of xylan-based hemicellulose using TG-FTIR and Py-GC-FTIR (vol 87, pg 199, 2009).* Journal of Analytical and Applied Pyrolysis, 2010. **88**(2): p. 213-213.

141. Yang, H.P., et al., *Characteristics of hemicellulose, cellulose and lignin pyrolysis.* Fuel, 2007. **86**(12-13): p. 1781-1788.

142. *ASTM E1755-01(2015) Standard Test Method for Ash in Biomass*. 2015, ASTM International: West Conshohocken, PA.

143. Cai, J.M., et al., *Review of physicochemical properties and analytical characterization of lignocellulosic biomass.* Renewable & Sustainable Energy Reviews, 2017. **76**: p. 309-322.

144. Channiwala, S.A. and P.P. Parikh, *A unified correlation for estimating HHV of solid, liquid and gaseous fuels.* Fuel, 2002. **81**(8): p. 1051-1063.

145.   Singh, Y.D., P. Mahanta, and U. Bora, *Comprehensive characterization of lignocellulosic biomass through proximate, ultimate and compositional analysis for bioenergy production.* Renewable Energy, 2017. **103**: p. 490-500.

146.   Garcia, R., et al., *Characterization of Spanish biomass wastes for energy use.* Bioresource Technology, 2012. **103**(1): p. 249-258.

147.   Nagy, M., et al., *Characterization of CO2 precipitated Kraft lignin to promote its utilization.* Green Chemistry, 2010. **12**(1): p. 31-34.

148.   Gordobil, O., et al., *Assesment of technical lignins for uses in biofuels and biomaterials: Structure-related properties, proximate analysis and chemical modification.* Industrial Crops and Products, 2016. **83**: p. 155-165.

149.   Demirbas, A., *Relationships between heating value and lignin, moisture, ash and extractive contents of biomass fuels.* Energy Exploration & Exploitation, 2002. **20**(1): p. 105-111.

150.   Werkelin, J., B.J. Skrifvars, and M. Hupa, *Ash-forming elements in four Scandinavian wood species. Part 1: Summer harvest.* Biomass & Bioenergy, 2005. **29**(6): p. 451-466.

151.   Pogrzeba, M., S. Rusinowski, and J. Krzyzak, *Macroelements and heavy metals content in energy crops cultivated on contaminated soil under different fertilization-case studies on autumn harvest.* Environ Sci Pollut Res Int, 2018. **25**(12): p. 12096-12106.

152.   Zajac, G., et al., *Chemical Characteristics of Biomass Ashes.* Energies, 2018. **11**(11).

153.   Baxter, L.L., et al., *The behavior of inorganic material in biomass-fired power boilers: field and laboratory experiences.* Fuel Processing Technology, 1998. **54**(1-3): p. 47-78.

154.   Yao, X.W., K.L. Xu, and Y. Liang, *Comparative Analysis of the Physical and Chemical Properties of Different Biomass Ashes Produced from Various Combustion Conditions.* Bioresources, 2017. **12**(2): p. 3222-3235.

155.   Zevenhoven-Onderwater, M., et al., *The ash chemistry in fluidised bed gasification of biomass fuels. Part I: predicting the chemistry of melting ashes and ash–bed material interaction.* Fuel, 2001. **80**(10): p. 1489-1502.

156.   Robbins, M.P., et al., *New opportunities for the exploitation of energy crops by thermochemical conversion in Northern Europe and the UK.* Progress in Energy and Combustion Science, 2012. **38**(2): p. 138-155.

157.   Monti, A., N. Di Virgilio, and G. Venturi, *Mineral composition and ash content of six major energy crops.* Biomass and Bioenergy, 2008. **32**(3): p. 216-223.

158.   Shao, Y., et al., *Ash Deposition in Biomass Combustion or Co-Firing for Power/Heat Generation.* Energies, 2012. **5**(12): p. 5171-5189.

159.   Dayton, D.C., et al., *Release of Inorganic Constituents from Leached Biomass during Thermal Conversion.* Energy & Fuels, 1999. **13**(4): p. 860-870.

160.   Thy, P., et al., *Inorganic Composition of Saline-Irrigated Biomass.* Water, Air and Soil Pollution, 2013. **224**(7): p. 1-17.

161. Sánchez, J., et al., *Biomass Resources*, in *The Role of Bioenergy in the Bioeconomy Resources, Technologies, Sustainability and Policy*, C. Lago, Editor. 2019, Academic Press: Amsterdam, Netherlands. p. 34.

162. Caillat, S., E. Vakkilainen, and L. Rosendahl, *9 - Large-scale biomass combustion plants: an overview*, in *Biomass Combustion Science, Technology and Engineering*. 2013, Woodhead Publishing. p. 189-224.

163. Chouhan, A. and A. Sarma, *Critical Analysis of Process Parameters for Bio-oil Production via Pyrolysis of Biomass: A Review.* Recent Patents on Engineering, 2013. **7**: p. 98-114.

164. Greenhalf, C.E., et al., *Thermochemical characterisation of straws and high yielding perennial grasses.* Industrial Crops and Products, 2012. **36**(1): p. 449-459.

165. Hodgson, E.M., et al., *Variation in Miscanthus chemical composition and implications for conversion by pyrolysis and thermo-chemical bio-refining for fuels and chemicals.* Bioresource Technology, 2011. **102**(3): p. 3411-3418.

166. Mishra, R.K. and K. Mohanty, *Pyrolysis kinetics and thermal behavior of waste sawdust biomass using thermogravimetric analysis.* Bioresource Technology, 2018. **251**: p. 63-74.

167. Sanchez-Silva, L., et al., *Thermogravimetric–mass spectrometric analysis of lignocellulosic and marine biomass pyrolysis.* Bioresource Technology, 2012. **109**: p. 163-172.

168. Asadieraghi, M. and W.M.A. Wan Daud, *Characterization of lignocellulosic biomass thermal degradation and physiochemical structure: Effects of demineralization by diverse acid solutions.* Energy Conversion and Management, 2014. **82**: p. 71-82.

169. Gronli, M.G., G. Varhegyi, and C. Di Blasi, *Thermogravimetric analysis and devolatilization kinetics of wood.* Industrial & Engineering Chemistry Research, 2002. **41**(17): p. 4201-4208.

170. Quan, C., N.B. Gao, and Q.B. Song, *Pyrolysis of biomass components in a TGA and a fixed-bed reactor: Thermochemical behaviors, kinetics, and product characterization.* Journal of Analytical and Applied Pyrolysis, 2016. **121**: p. 84-92.

171. Fan, Y.S., et al., *Effects of the cellulose, xylan and lignin constituents on biomass pyrolysis characteristics and bio-oil composition using the Simplex Lattice Mixture Design method.* Energy Conversion and Management, 2017. **138**: p. 106-118.

172. Yeo, J.Y., et al., *Comparative studies on the pyrolysis of cellulose, hemicellulose, and lignin based on combined kinetics.* Journal of the Energy Institute, 2019. **92**(1): p. 27-37.

173. Wang, S., et al., *Mechanism research on cellulose pyrolysis by Py-GC/MS and subsequent density functional theory studies.* Bioresource Technology, 2012. **104**: p. 722-728.

174. Li, S., et al., *Real-time evolved gas analysis by FTIR method: an experimental study of cellulose pyrolysis.* Fuel, 2001. **80**(12): p. 1809-1817.

175. Lin, Y.-C., et al., *Kinetics and Mechanism of Cellulose Pyrolysis.* The Journal of Physical Chemistry C, 2009. **113**(46): p. 20097-20107.

176. Wang, C., et al., *Oriented valorization of cellulose and xylan into anhydrosugars by using low-temperature pyrolysis.* Fuel, 2021. **291**: p. 120156.

177. Shen, D.K., S. Gu, and A.V. Bridgwater, *The thermal performance of the polysaccharides extracted from hardwood: Cellulose and hemicellulose.* Carbohydrate Polymers, 2010. **82**(1): p. 39-45.

178. Shafizadeh, F. and Y.Z. Lai, *Thermal degradation of 1,6-anhydro-.beta.-D-glucopyranose.* The Journal of Organic Chemistry, 1972. **37**(2): p. 278-284.

179. Rick, S., A. Wille, and A. Steinbach, *Determining Saccharidic Tracers in Atmospheric Aerosols.* LC GC Europe, 2010: p. 1-6.

180. Evans, R.J. and T.A. Milne, *Molecular characterization of the pyrolysis of biomass.* Energy & Fuels, 1987. **1**(2): p. 123-137.

181. Kačuráková, M., et al., *Hydration properties of xylan-type structures: an FTIR study of xylooligosaccharides.* Journal of the Science of Food and Agriculture, 1998. **77**(1): p. 38-44.

182. Wang, S.-r., et al., *Mechanism of xylan pyrolysis by Py-GC/MS.* Chemical Research in Chinese Universities, 2013. **29**(4): p. 782-787.

183. Zhou, X., et al., *A mechanistic model of fast pyrolysis of hemicellulose.* Energy & Environmental Science, 2018. **11**(5): p. 1240-1260.

184. Ponder, G.R. and G.N. Richards, *Thermal synthesis and pyrolysis of a xylan.* Carbohydrate Research, 1991. **218**: p. 143-155.

185. Zhou, X., et al., *A Critical Review on Hemicellulose Pyrolysis.* Energy Technology, 2017. **5**(1): p. 52-79.

186. Peng, Y. and S. Wu, *The structural and thermal characteristics of wheat straw hemicellulose.* Journal of Analytical and Applied Pyrolysis, 2010. **88**(2): p. 134-139.

187. Zadeh, Z.E., et al., *Recent Insights into Lignocellulosic Biomass Pyrolysis: A Critical Review on Pretreatment, Characterization, and Products Upgrading.* Processes, 2020. **8**(7): p. 799.

188. Kosa, M., et al., *Pyrolysis oils from CO2 precipitated Kraft lignin.* Green Chemistry, 2011. **13**(11): p. 3196-3202.

189. Liu, C., et al., *Catalytic fast pyrolysis of lignocellulosic biomass.* Chemical Society reviews, 2014. **43**(22): p. 7457–7956.

190.   Nanayakkara, B., M. Riddell, and J. Harrington, *Screening of juvenile Pinus radiata wood by means of Py-GC/MS for compression wood focussing on the ratios of p-hydroxyphenyl to guaiacyl units (H/G ratios).* Holzforschung, 2016. **70**(4): p. 313-321.

191.   Subagyono, R.R.D.J.N., et al., *Pyrolysis-GC/MS analysis of biomass and the bio-oils produced from CO/H2O reactions.* Journal of Analytical and Applied Pyrolysis, 2016. **120**: p. 154-164.

192.   Banks, S.W., D.J. Nowakowski, and A.V. Bridgwater, *Impact of Potassium and Phosphorus in Biomass on the Properties of Fast Pyrolysis Bio-oil.* Energy & Fuels, 2016. **30**(10): p. 8009-8018.

193.   White, J.E., W.J. Catallo, and B.L. Legendre, *Biomass pyrolysis kinetics: A comparative critical review with relevant agricultural residue case studies.* Journal of Analytical and Applied Pyrolysis, 2011. **91**(1): p. 1-33.

194.   Saddawi, A., et al., *Kinetics of the Thermal Decomposition of Biomass.* Energy & Fuels, 2010. **24**(2): p. 1274-1282.

195.   Luo, Z. and J. Zhou, *Thermal Conversion of Biomass*, in *Handbook of Climate Change Mitigation*, W.-Y. Chen, et al., Editors. 2012, Springer US: New York, NY. p. 1001-1042.

196.   Anca-Couce, A., *Reaction mechanisms and multi-scale modelling of lignocellulosic biomass pyrolysis.* Progress in Energy and Combustion Science, 2016. **53**: p. 41-79.

197.   Cortés, A.M. and A. Bridgwater, *Kinetic study of the pyrolysis of miscanthus and its acid hydrolysis residue by thermogravimetric analysis.* Fuel Processing Technology, 2015. **138**: p. 184-193.

198.   Slopiecka, K., P. Bartocci, and F. Fantozzi, *Thermogravimetric analysis and kinetic study of poplar wood pyrolysis.* Applied Energy, 2012. **97**: p. 491-497.

199.   Khawam, A. and D.R. Flanagan, *Complementary use of model-free and modelistic methods in the analysis of solid-state kinetics.* Journal of Physical Chemistry B, 2005. **109**(20): p. 10073-10080.

200.   Opfermann, J.R., E. Kaisersberger, and H.J. Flammersheim, *Model-free analysis of thermoanalytical data-advantages and limitations.* Thermochimica Acta, 2002. **391**(1-2): p. 119-127.

201.   Flynn, J.H. and L.A. Wall, *A quick, direct method for the determination of activation energy from thermogravimetric data.* Journal of Polymer Science Part B: Polymer Letters, 1966. **4**(5): p. 323-328.

202.   Akahira, T. and T. Sunose, *Trans. Joint convention of four electrical institutes*. 1969, Chiba Institute of Technology: Chiba. p. 22-31.

203.   Kissinger, H.E., *Variation of peak temperature with heating rate in differential thermal analysis.* Journal of research of the National Bureau of Standards, 1956. **57**(4): p. 217-221.

204. Raveendran, K., A. Ganesh, and K.C. Khilar, *Pyrolysis characteristics of biomass and biomass components.* Fuel, 1996. **75**(8): p. 987-998.

205. Sokoto, M.A., et al., *Non-isothermal kinetic study of de-oiled seeds cake of African star apple (Chrosophyllum albidum) using thermogravimetry.* Heliyon, 2016. **2**(10): p. e00172.

206. Kissinger, H.E., *Reaction Kinetics in Differential Thermal Analysis.* Analytical Chemistry, 1957. **29**(11): p. 1702-1706.

207. Denshi Tsūshin, G., G. Shōmei, and G. Terebijon, *1976 Joint Convention record of Four Institutes of Electrical Engineers, Japan*. 1976: Denki Shigakkai Jōchi Rengō Taikai Kikaku Iinkai.

208. Cai, J., et al., *Processing thermogravimetric analysis data for isoconversional kinetic analysis of lignocellulosic biomass pyrolysis: Case study of corn stalk.* Renewable and Sustainable Energy Reviews, 2018. **82**: p. 2705-2715.

209. Vyazovkin, S., *Kissinger Method in Kinetics of Materials: Things to Beware and Be Aware of.* Molecules, 2020. **25**(12).

210. Balart, R., et al., *Kinetic Analysis of the Thermal Degradation of Recycled Acrylonitrile-Butadiene-Styrene by non-Isothermal Thermogravimetry.* Polymers (Basel), 2019. **11**(2).

211. Vyazovkin, S., et al., *ICTAC Kinetics Committee recommendations for analysis of multi-step kinetics.* Thermochimica Acta, 2020. **689**: p. 178597.

212. Xu, Y. and B. Chen, *Investigation of thermodynamic parameters in the pyrolysis conversion of biomass and manure to biochars using thermogravimetric analysis.* Bioresource Technology, 2013. **146**: p. 485-493.

213. Ahmad, M.S., et al., *Pyrolysis, kinetics analysis, thermodynamics parameters and reaction mechanism of Typha latifolia to evaluate its bioenergy potential.* Bioresource Technology, 2017. **245**: p. 491-501.

214. Yu, J., et al., *Cellulose, xylan and lignin interactions during pyrolysis of lignocellulosic biomass.* Fuel, 2017. **191**: p. 140-149.

215. Chen, W.-H., et al., *Torrefaction, pyrolysis and two-stage thermodegradation of hemicellulose, cellulose and lignin.* Fuel, 2019. **258**: p. 116168.

216. Trubetskaya, A., et al., *Structural and Thermal Characterization of Novel Organosolv Lignins from Wood and Herbaceous Sources.* Processes, 2020. **8**(7): p. 860.

217. Di Blasi, C., *Modeling chemical and physical processes of wood and biomass pyrolysis.* Progress in Energy and Combustion Science, 2008. **34**(1): p. 47-90.

218. Zhu, L. and Z. Zhong, *Effects of cellulose, hemicellulose and lignin on biomass pyrolysis kinetics.* Korean Journal of Chemical Engineering, 2020. **37**(10): p. 1660-1668.

219. Chen, R., et al., *Combustion characteristics, kinetics and thermodynamics of Pinus Sylvestris pine needle via non-isothermal thermogravimetry coupled with model-free and model-fitting methods.* Case Studies in Thermal Engineering, 2020. **22**: p. 100756.

220. Mahmood, H., et al., *A Comparative Study on Suitability of Model-Free and Model-Fitting Kinetic Methods to Non-Isothermal Degradation of Lignocellulosic Materials.* Polymers, 2021. **13**(15): p. 2504.

221. Kong, W., et al., *Pyrolysis of Spirulina platensis, Tetradesmus obliquus and Chlorella vulgaris by TG-FTIR and Py-GC/MS: Kinetic analysis and pyrolysis behaviour.* Energy, 2022. **244**: p. 123165.

222. Ruvolo, A. and P.S. Curti, *Chemical kinetic model and thermodynamic compensation effect of alkaline hydrolysis of waste poly(ethylene terephthalate) in nonaqueous ethylene glycol solution.* Industrial & Engineering Chemistry Research, 2006. **45**(24): p. 7985-7996.

223. Khan, A.S., et al., *Kinetics and thermodynamic parameters of ionic liquid pretreated rubber wood biomass.* Journal of Molecular Liquids, 2016. **223**: p. 754-762.

224. Madsen, R.B., et al., *Using design of experiments to optimize derivatization with methyl chloroformate for quantitative analysis of the aqueous phase from hydrothermal liquefaction of biomass.* Analytical and Bioanalytical Chemistry, 2016. **408**(8): p. 2171-2183.

225. Company, P.I., *5500 Compact Micro Reactors Operating Instruction Manual*. Parr Instrument Company: Moline, Illinois.

226. Corporation, R. *Carboxylic Acids on Ultra Aqueous C18*. 2022 [cited 2022 07/03/2022].

227. Minowa, T., F. Zhen, and T. Ogi, *Cellulose decomposition in hot-compressed water with alkali or nickel catalyst.* The Journal of Supercritical Fluids, 1998. **13**(1): p. 253-259.

228. Zhong, C. and X. Wei, *A comparative experimental study on the liquefaction of wood.* Energy, 2004. **29**(11): p. 1731-1741.

229. Beauchet, R., F. Monteil-Rivera, and J.M. Lavoie, *Conversion of lignin to aromatic-based chemicals (L-chems) and biofuels (L-fuels).* Bioresource Technology, 2012. **121**: p. 328-334.

230. Feng, S.H., et al., *Hydrothermal liquefaction of barks into bio-crude - Effects of species and ash content/composition.* Fuel, 2014. **116**: p. 214-220.

231. Marx, S. and R.J. Venter, *5.09 - Alternative Bio-Refinery Products From Hydrothermal Liquefaction of Waste☆*, in *Comprehensive Renewable Energy (Second Edition)*, T.M. Letcher, Editor. 2022, Elsevier: Oxford. p. 187-212.

232. Ramirez, J.A., R.J. Brown, and T.J. Rainey, *A Review of Hydrothermal Liquefaction Bio-Crude Properties and Prospects for Upgrading to Transportation Fuels.* Energies, 2015. **8**(7): p. 6765-6794.

233. Speight, J.G., *Chapter 6 - Refining Shale Oil*, in *Shale Oil Production Processes*, J.G. Speight, Editor. 2012, Gulf Professional Publishing: Boston. p. 139-163.

234. Brown, T.M., P. Duan, and P.E. Savage, *Hydrothermal Liquefaction and Gasification of Nannochloropsis sp.* Energy & Fuels, 2010. **24**(6): p. 3639-3646.

235. GREET, *Lower and Higher Heating Values of Gas, Liquid and Solid Fuels*, A.N. Laboratory, Editor. 2010: Argonne, IL.

236. Demirbas, A., et al., *Estimation of Calorific Values of Fuels from Lignocellulosics.* Energy Sources, 1997. **19**(8): p. 765-770.

237. Couto, E.A., et al., *Hydrothermal liquefaction of biomass produced from domestic sewage treatment in high-rate ponds.* Renewable Energy, 2018. **118**: p. 644-653.

238. Ciuffi, B., et al., *Towards a better understanding of the HTL process of lignin-rich feedstock.* Scientific Reports, 2021. **11**(1): p. 15504.

239. Liu, H.-M., H.-Y. Li, and M.-F. Li, *Cornstalk liquefaction in sub- and super-critical ethanol: Characterization of solid residue and the liquefaction mechanism.* Journal of the Energy Institute, 2017. **90**(5): p. 734-742.

240. Faravelli, T., et al., *Detailed kinetic modeling of the thermal degradation of lignins.* Biomass and Bioenergy, 2010. **34**(3): p. 290-301.

241. Shen, D., et al., *An overview on fast pyrolysis of the main constituents in lignocellulosic biomass to valued-added chemicals: Structures, pathways and interactions.* Renewable and Sustainable Energy Reviews, 2015. **51**: p. 761-774.

242. Yang, S., et al., *Hydrothermal degradation of lignin: Products analysis for phenol formaldehyde adhesive synthesis.* International Journal of Biological Macromolecules, 2015. **72**: p. 54-62.

243. Kang, S., et al., *Hydrothermal conversion of lignin: A review.* Renewable and Sustainable Energy Reviews, 2013. **27**: p. 546-558.

244. Yahaya, A., H. Ursel, and M.B. Idris, *Lignin Hydrothermal Liquefaction into Bifunctional Chemicals: A Concise Review.* 2020.

245. Schuler, J., et al., *Hydrothermal Liquefaction of Lignin.* Papers of the 24th European Biomass Conference: Setting the Course for a Biobased Economy, 2016: p. 985-989.

246. Wahyudiono, et al., *Decomposition of a Lignin Model Compound under Hydrothermal Conditions.* Chemical Engineering & Technology, 2007. **30**(8): p. 1113-1122.

247. Jin, F.M., et al., *Conversion mechanism of cellulosic biomass to lactic acid in subcritical water and acid-base catalytic effect of subcritical water.* Chemistry Letters, 2004. **33**(2): p. 126-127.

248. Jin, F., et al., *Water Under High Temperature and Pressure Conditions and Its Applications to Develop Green Technologies for Biomass Conversion*, in *Application of Hydrothermal Reactions to Biomass Conversion*, F. Jin, Editor. 2014, Springer Berlin Heidelberg: Berlin, Heidelberg. p. 3-28.
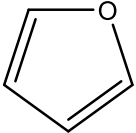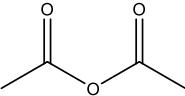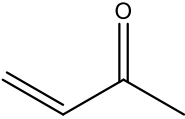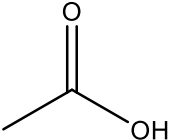
249.   Chen, H., et al., *Effects of the aqueous phase recycling on bio-oil yield in hydrothermal liquefaction of Spirulina Platensis, α-cellulose, and lignin.* Energy, 2019. **179**: p. 1103-1113.

250.   Biller, P., et al., *Effect of hydrothermal liquefaction aqueous phase recycling on bio-crude yields and composition.* Bioresource Technology, 2016. **220**: p. 190-199.

251.   Hu, Y., et al., *Investigation of aqueous phase recycling for improving bio-crude oil yield in hydrothermal liquefaction of algae.* Bioresource Technology, 2017. **239**: p. 151-159.

252.   Madsen, R.B., et al., *Predicting the Chemical Composition of Aqueous Phase from Hydrothermal Liquefaction of Model Compounds and Biomasses.* Energy & Fuels, 2016. **30**(12): p. 10470-10483.

253.   Panisko, E., et al., *Characterization of the aqueous fractions from hydrotreatment and hydrothermal liquefaction of lignocellulosic feedstocks.* Biomass and Bioenergy, 2015. **74**: p. 162-171.

254.   Maddi, B., et al., *Quantitative Characterization of Aqueous Byproducts from Hydrothermal Liquefaction of Municipal Wastes, Food Industry Wastes, and Biomass Grown on Waste.* ACS Sustainable Chemistry & Engineering, 2017. **5**(3): p. 2205-2214.

255.   Zhang, X., et al., *Advanced treatment of hydrothermal liquefaction wastewater with nanofiltration to recover carboxylic acids.* Environmental Science: Water Research & Technology, 2018. **4**(4): p. 520-528.

256.   Pipitone, G., et al., *Aqueous phase reforming of the residual waters derived from lignin-rich hydrothermal liquefaction: investigation of representative organic compounds and actual biorefinery streams.* Catalysis Today, 2020. **345**: p. 237-250.

257.   Brebu, M. and C. Vasile, *Thermal degradation of lignin – A Review.* Cellulose Chemistry and Technology, 2010. **44**: p. 353-363.

258.   Belkheiri, T., et al., *Hydrothermal liquefaction of kraft lignin in sub-critical water: the influence of the sodium and potassium fraction.* Biomass Conversion and Biorefinery, 2018. **8**(3): p. 585-595.

259.   Pińkowska, H., P. Wolak, and A. Złocińska, *Hydrothermal decomposition of alkali lignin in sub- and supercritical water.* Chemical Engineering Journal, 2012. **187**: p. 410-414.

260.   Tungal, R. and R.V. Shende, *Hydrothermal liquefaction of pinewood (Pinus ponderosa) for H2, biocrude and bio-oil generation.* Applied Energy, 2014. **134**: p. 401-412.

261.   Zhu, G., et al., *Kinetics of peanut shell pyrolysis and hydrolysis in subcritical water.* Journal of Material Cycles and Waste Management, 2014. **16**(3): p. 546-556.

262.   Dell'Orco, S., et al., *Hydrothermal Depolymerization of Biorefinery Lignin-Rich Streams: Influence of Reaction Conditions and Catalytic Additives on the Organic Monomers Yields in Biocrude and Aqueous Phase.* Energies, 2020. **13**(5): p. 1241.

263.   Jayathilake, M., et al., *Characterization and Evaluation of Hydrothermal Liquefaction Char from Alkali Lignin in Subcritical Temperatures.* Materials, 2021. **14**(11): p. 3024.

264. Zubbri, N.A., et al., *Enhancement of CO2 adsorption on biochar sorbent modified by metal incorporation.* Environmental Science and Pollution Research, 2020. **27**(11): p. 11809-11829.

265. Vassilev, S.V., et al., *An overview of the organic and inorganic phase composition of biomass.* Fuel, 2012. **94**: p. 1-33.

266. !!! INVALID CITATION !!! {}.

267. Jiang, L., et al., *Formation, fates and roles of catalytic precursors generated from the K2CO3-carbon interactions in the K2CO3-catalyzed CO2 gasification of coal char.* Journal of Analytical and Applied Pyrolysis, 2017. **124**: p. 384-392.

268. Persson, K., *Materials Data on ZnO (SG:186) by Materials Project*. 2014: United States.

269. Persson, K., *Materials Data on K2ZnCl4 (SG:33) by Materials Project*. 2014: United States.

270. Persson, K., *Materials Data on NaCl (SG:225) by Materials Project*. 2014: United States.

271. Persson, K., *Materials Data on KCl (SG:225) by Materials Project*. 2014: United States.

272. Persson, K., *Materials Data on ZnCl2 (SG:137) by Materials Project*. 2014: United States.

273. Persson, K., *Materials Data on ZnCl2 (SG:122) by Materials Project*. 2014: United States.

274. Siefert, N., et al., *Molten catalytic coal gasification with in situ carbon and sulphur capture.* Energy & Environmental Science, 2012. **5**(9): p. 8660-8672.

275. Tang, H., et al., *In-situ removal of sulfur from high sulfur solid waste during molten salt pyrolysis.* Fuel, 2018. **231**: p. 489-494.

276. Pua, F.-l., et al., *Direct production of biodiesel from high-acid value Jatrophaoil with solid acid catalyst derived from lignin.* Biotechnology for Biofuels, 2011. **4**(1): p. 56.

277. Wolfgong, W.J., *Chapter 14 - Chemical analysis techniques for failure analysis: Part 1, common instrumental methods*, in *Handbook of Materials Failure Analysis with Case Studies from the Aerospace and Automotive Industries*, A.S.H. Makhlouf and M. Aliofkhazraei, Editors. 2016, Butterworth-Heinemann: Boston. p. 279-307.

278. Harris, D.C., *Quantitative Chemical Analysis*. 2010: W. H. Freeman and Company.
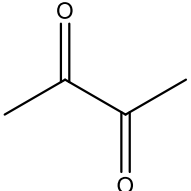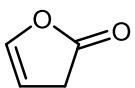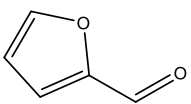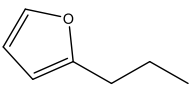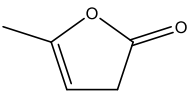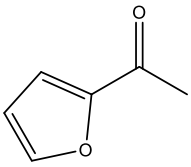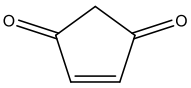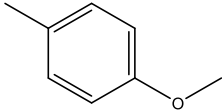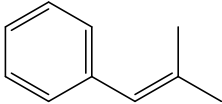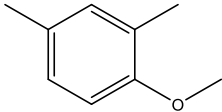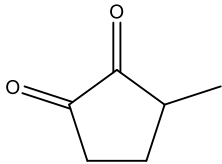
Appendices
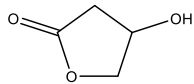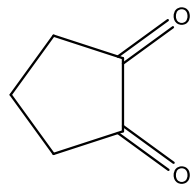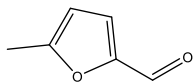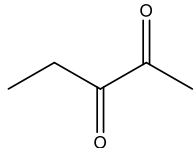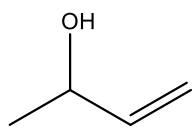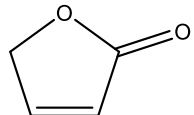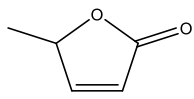
Appendix A
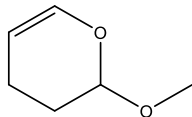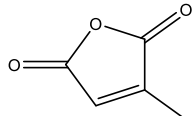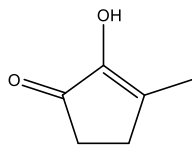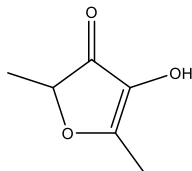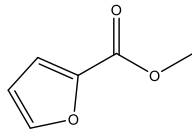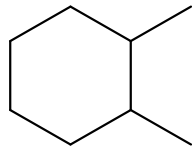
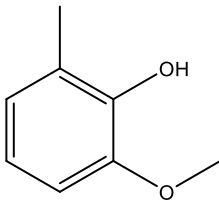**Table A.1 Full list of all Py-GC-MS identified components found in cellulose**
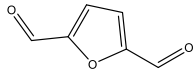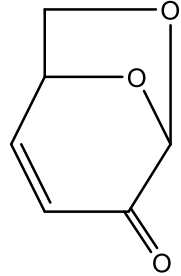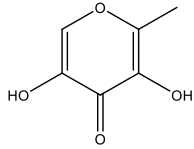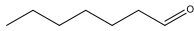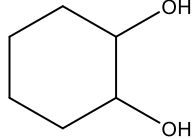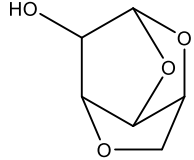
Retention Time (min)	Name	Formula	MW	Structure	m/z	Key Precursor
1.96	furan	C_4H_4O	68		68.03 (100.0 %), 69.03 (4.3 %)	Holocellulose
2.09	acetic anhydride	$C_4H_6O_3$	102		102.03 (100.0%), 103.04 (4.3 %)	Holocellulose
2.50	methyl vinyl ketone	C_4H_6O	60		70.04 (100.0 %), 71.05 (4.3 %)	Cellulose
3.77	acetic acid	$C_2H_4O_2$	60		60.02 (100.0 %), 61.02 (2.2 %)	Holocellulose
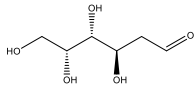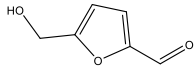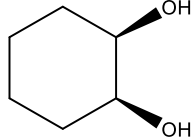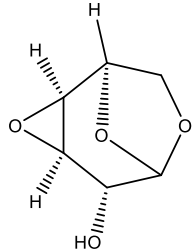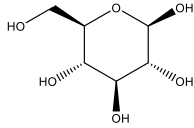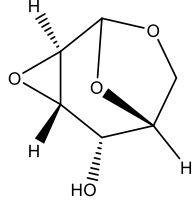
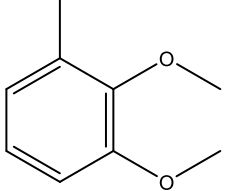| 4.19	2,3-butanedione	$C_4H_6O_2$	86		86.04 (100.0 %), 87.04 (4.3%)	Cellulose
8.03	2(3H)-furanone	$C_4H_4O_2$	84		84.02 (100.0 %), 85.02 (4.3 %)	Holocellulose
9.32	furfural	$C_5H_4O_2$	96		96.02 (100.0 %), 97.02 (5.4 %)	Holocellulose
9.98	2-propylfuran	$C_7H_{10}O$	110		110.07 (100.0 %), 111.08 (7.6 %)	Holocellulose
11.13	5-methyl-2(3H)-furanone	$C_5H_6O_2$	98		98.04 (100.0 %), 99.04 (5.4 %)	Holocellulose
12.61	1-(2-furanyl)-ethanone	$C_6H_6O_2$	110		110.04 (100.0 %), 111.04 (6.5 %)	Holocellulose
13.34	4-cyclopenten-1,3-dione	$C_5H_4O_2$	96		96.02 (100.0 %), 97.02 (5.4 %)	Holocellulose
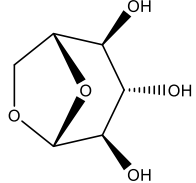
14.49	dihydro-4-hydroxy-2(3H)-furanone	$C_4H_6O_3$	102		102.03 (100.0 %), 103.04 (4.3 %)	Holocellulose
14.38	1,2-cyclopentanedione	$C_5H_6O_3$	98		98.04 (100.0 %), 99.04 (5.4 %)	Xylan
16.09	5-methyl-2-furancarboxaldehyde	$C_6H_6O_2$	110		110.04 (100.0 %), 111.04 (6.5 %)	Cellulose
16.62	2,3-pentadione	$C_5H_8O_2$	100		100.05 (100.0 %), 101.06 (5.4 %)	Cellulose
16.80	3-buten-2-ol	C_4H_8O	72		72.06 (100.0 %), 73.06 (4.3 %)	Cellulose
17.54	2(5H)-furanone	$C_4H_4O_2$	84		84.02 (100.0 %), 85.02 (4.3 %)	Holocellulose
18.29	5-methyl-2(5H)-furanone	$C_5H_6O_2$	98		98.04 (100.0 %), 99.04 (5.4 %)	Holocellulose

18.96	3,4-dihydro-2-methoxy-2H-pyran	$C_6H_{10}O_2$	114		114.07 (100.0 %), 115.07 (6.5 %)	Holocellulose
19.08	3-methyl-2,5-furandione	$C_5H_4O_3$	112		112.02 (100.0 %), 113.02 (5.4 %)	Cellulose
20.33	2-hydroxy-3-methyl-2-cyclopenten-1-one	$C_6H_8O_2$	112		112.05 (100.0 %), 113.06 (6.5 %)	Holocellulose
22.70	2,5-dimethyl-4-hydroxy-3(2H)-furanone	$C_6H_8O_3$	128		128.05 (100.0 %), 129.05 (6.5 %)	Cellulose
24.25	methyl 2-furoate	$C_6H_6O_3$	126		126.03 (100.0 %), 127.04 (6.5 %)	Holocellulose
24.59	2,3-dimethylcyclohexane	$C_8H_{16}O$	128		112.13 (100.0 %), 113.13 (8.7 %)	Cellulose

25.99	2,5-furandicarboxaldehyde	$C_6H_4O_3$	124		124.02 (100.0 %), 125.02 (6.5 %)	Cellulose
28.17	1,6-anhydro-3,4-dideoxy-β-D-pyranosen-2-one (levoglucosenone)	$C_6H_6O_3$	126		126.03 (100.0 %), 127.04 (6.5 %)	Cellulose
30.00	3,5-dihydroxy-2-methyl-4H-pyran-4-one	$C_6H_6O_4$	142		142.03 (100.0 %), 143.03 (6.5 %)	Cellulose
33.16	heptanal	$C_7H_{14}O$	114		114.10 (100.0 %), 115.11 (7.6 %)	Cellullose
33.68	1,2-cyclohexanediol	$C_6H_{12}O_2$	116		116.08 (100.0 %), 117.09 (6.5 %)	Cellulose
35.25	1,4:3,6-dianhydro-α-D-glucopyranose	$C_6H_8O_4$	144		144.04 (100.0 %), 145.05 (6.5 %)	Cellulose
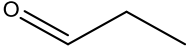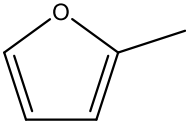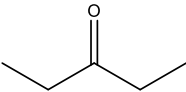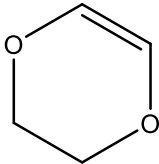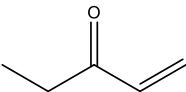
36.16	2-deoxy-D-galactose	$C_6H_{12}O_6$	164		164.07 (100.0 %), 165.07 (6.5 %), 166.07 (1.0 %)	Xylan
39.02	5-hydroxymethylfurfural	$C_6H_6O_3$	126		126.03 (100.0 %), 127.04 (6.5 %)	Cellulose
40.17	cis-1,2-cyclohexanediol	$C_6H_{12}O_2$	116		116.08 (100.0 %), 117.09 (6.5 %)	Cellulose
42.56	3,4-anhydro-D-galactosan	$C_6H_8O_4$	144		144.04 (100.0 %), 145.05 (6.5 %)	Xylan
44.19	β-D-glucopyranose	$C_6H_{12}O_6$	180		180.06 (100.0 %), 181.07 (6.5 %), 182.07 (1.2 %)	Cellulose
44.65	2,3-anhydro-D-galactosan	$C_6H_8O_4$	144		144.04 (100.0 %), 145.05 (6.5 %)	Xylan
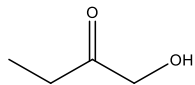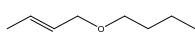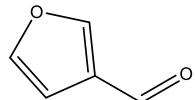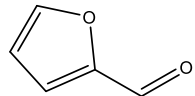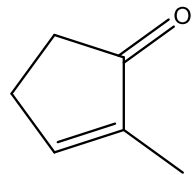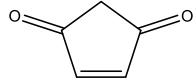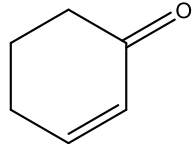
| 52.16 | 1,6-anhydro-β-D-glucopyranose (levoglucosan) | $C_6H_{10}O_5$ | 162 | | 162.05 (100.0 %), 163.06 (6.5 %), 164.06 (1.0 %) | Cellulose |
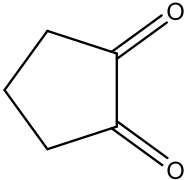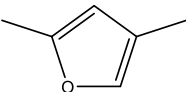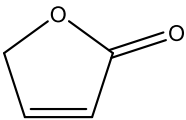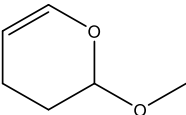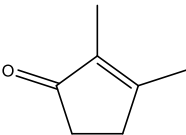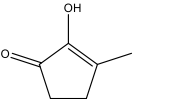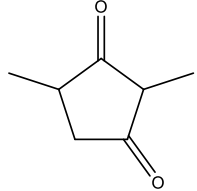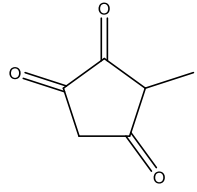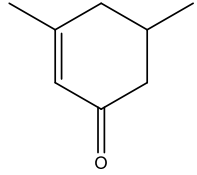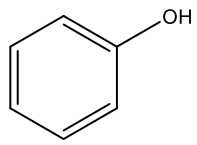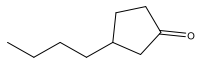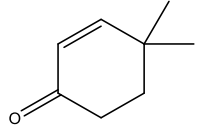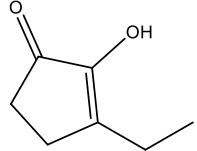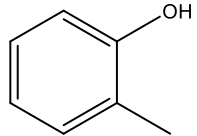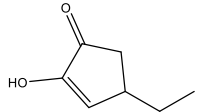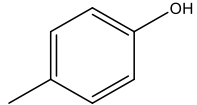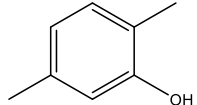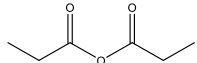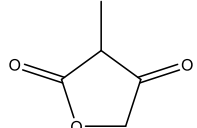
Retention Time (min)	Name	Formula	MW	Structure	m/z	Key Precursor
2.08	propanal	C_3H_6O	58		58.04 (100.0 %), 59.05 (3.2 %)	Xylan
2.33	2-methylfuran	C_5H_6O	82		82.04 (100.0 %), 83.05 (5.4 %)	Holocellulose
2.72	3-pentanone	$C_5H_{10}O$	86		86.07 (100.0 %), 87.08 (5.4 %)	Xylan
3.77	methyl formate	$C_2H_4O_2$	60		60.02 (100.0 %), 61.02 (2.2 %)	Xylan
4.35	2,3-dihydro-1,4-dioxin	$C_4H_6O_2$	86		86.04 (100.0 %), 87.04 (4.3 %)	Xylan
6.56	1-penten-3-one	C_5H_8O	84		84.06 (100.0 %), 85.06 (5.4 %)	Xylan
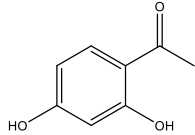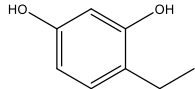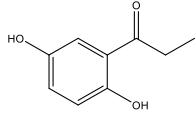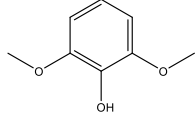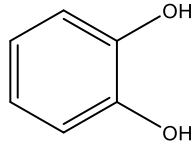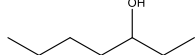
7.11	1-hydroxy-2-butanone	C_4H_8O	88		88.05 (100.0 %), 89.06 (4.3 %)	Xylan
7.34	1-butoxy-2-butene	$C_8H_{16}O$	128		128.12 (100.0%), 129.12 (8.7 %)	Xylan
8.34	3-furaldehyde	$C_5H_4O_2$	96		96.02 (100.0 %), 97.02 (5.4 %)	Holocellulose
9.57	furfural	$C_5H_4O_2$	96		96.02 (100.0 %), 97.02 (5.4 %)	Holocellulose
11.89	2-methyl-2-cyclopenten-1-one	C_6H_8O	96		96.06 (100.0 %), 97.06 (6.5 %)	Holocellulose
13.48	4-cyclopentene-1,3-dione	$C_5H_4O_2$	96		96.02 (100.0 %), 97.02 (5.4 %)	Xylan
13.83	2-cyclohexen-1-one	C_6H_8O	96		96.06 (100.0 %), 97.06 (6.5 %)	Xylan
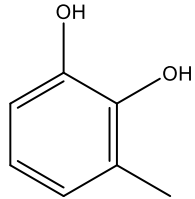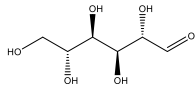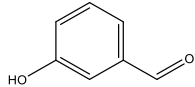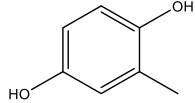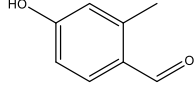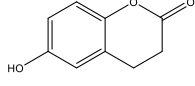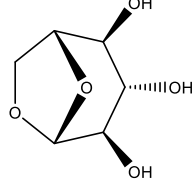
15.28	1,2-cyclopentanedione	$C_5H_6O_2$	98		98.04 (100.0 %), 99.04 (5.4 %)	Xylan
16.90	2,4-dimethylfuran	C_6H_8O	96		96.06 (100.0 %), 97.06 (6.5 %)	Xylan
17.76	2(5H)-furanone	$C_4H_4O_2$	84		84.02 (100.0 %), 85.02 (4.3 %)	Holocellulose
19.26	3,4-dihydro-2-methoxy-2H-pyran	$C_6H_{10}O_2$	114		114.07 (100.0 %), 115.07 (6.5 %)	Holocellulose
19.65	2,3-dimethyl-2-cyclopenten-1-one	$C_7H_{10}O$	110		110.07 (100.0%), 110.08 (7.6 %)	Holocellulose
20.87	2-hydroxy-3-methyl-2-cyclopenten-1-one	$C_6H_8O_2$	112		112.05 (100.0 %), 113.06 (6.5 %)	Holocellulose

21.47	2,4-dimethyl-1,3-cyclopentanedione	$C_7H_{10}O_2$	126		126.07 (100.0 %), 127.07 (7.6 %)	Holocellulose
21.95	3-methyl-1,2,4-cyclopentanetrione	$C_6H_6O_3$	126		126.03 (100.0 %), 127.04 (6.5 %)	Holocellulose
22.57	3,5-dimethyl-2-cyclohexen-1-one	$C_8H_{12}O$	124		124.09 (100.0 %), 125.09 (8.7 %)	Holocellulose
22.85	phenol	C_6H_6O	94		94.04 (100.0 %), 95.05 (6.5 %)	Lignin
23.76	3-butylcyclopentanone	$C_9H_{16}O$	140		140.12 (100.0 %), 141.12 (9.7 %)	Holocellulose
24.76	4,4-dimethyl-2-cyclohexen-1-one	$C_8H_{12}O$	124		124.09 (100.0 %), 125.09 (8.7 %)	Holocellulose

25.30	3-ethyl-2-hydroxy-2-cyclopenten-1-one	$C_7H_{10}O_2$	126		126.07 (100.0 %), 127.07 (7.6 %)	Holocellulose
25.47	2-methylphenol (o-Cresol)	C_7H_8O	108		108.06 (100.0 %), 109.06 (7.6 %)	p-Hydroxyphenyl lignin
25.95	4-ethyl-2-hydroxycyclopent-2-en-1-one	$C_7H_{10}O_2$	126		126.07 (100.0 %), 127.07 (7.6 %)	Holocellulose
27.62	4-methylphenol (p-Cresol)	C_7H_8O	108		108.06 (100.0 %), 109.06 (7.6 %)	p-Hydroxyphenyl lignin
29.97	2,5-dimethylphenol	$C_8H_{10}O$	122		122.07 (100.0 %), 123.08 (8.7 %)	Lignin
31.93	methyl acetic anhydride	$C_6H_{10}O_3$	130		130.06 (100.0 %), 131.07 (6.5 %)	Holocellulose
33.78	3-Methylfuran-2,4-dione	$C_5H_6O_3$	113		114.03 (100.0 %), 115.04 (5.4 %)	Holocellulose

34.05	1-(2,4-dihydroxyphenyl)-ethanone	$C_8H_8O_3$	152		152.05 (100.0 %), 135.05 (8.7 %)	p-Hydroxyphenyl lignin
35.41	4-ethyl-1,3-benzenediol	$C_8H_{10}O_2$	138		138.07 (100.0 %), 139.07 (8.7)	Lignin
38.81	2,5-dihydroxypropiophenone	$C_9H_{10}O_3$	166		166.06 (100.0 %), 167.07 (9.7 %)	p-Hydroxyphenyl lignin
39.04	2,6-dimethoxyphenol (syringol)	$C_8H_{10}O_3$	154		154.06 (100.0%), 155.07 (8.7 %)	Syringol lignin
39.44	1,2-dihydroxybenzene (catechol)	$C_6H_6O_2$	110		110.04 (100.0 %), 111.04 (6.5 %)	Lignin
40.41	3-heptanol	$C_7H_{16}O$	116		116.12 (100.0 %), 117.12 (7.6 %)	Xylan

41.13	3-methyl-1,2-benzenediol	$C_7H_8O_2$	124		124.05 (100.0 %), 125.06 (7.6 %)	Lignin
44.03	d-Mannose	$C_6H_{12}O_6$	180		180.06 (100.0 %), 181.07 (6.5 %), 182.07 (1.2 %)	Xylan
45.48	3-hydroxybenzaldehyde	$C_7H_6O_2$	122		122.04 (100.0 %), 123.04 (7.6 %)	p-Hydroxyphenyl lignin
47.20	2-methyl-1,4-benzenediol	$C_7H_8O_2$	124		124.05 (100.0 %), 125.06 (7.6 %)	p-Hydroxyphenyl lignin
49.49	4-hydroxy-2methylbenzaldehyde	$C_8H_8O_2$	136		136.05 (100.0 %), 137.06 (8.7 %)	p-Hydroxyphenyl lignin
51.06	3,4-dihydro-6-hydroxy-2H-1-benzopyran-2-one	$C_9H_8O_3$	164		164.05 (100.0 %), 165.05 (9.7 %)	p-Hydroxyphenyl lignin
57.28	1,6-anhydro-β-D-glucopyranose (levoglucosan)	$C_6H_{10}O_5$	162		162.05 (100.0 %), 163.06 (6.5 %), 164.06 (1.0 %)	Cellulose

| 62.55 | 1,6-anhydro-α-D-galactofuranose | $C_6H_{10}O_5$ | 162 | | 162.05 (100.0 %), 163.06 (6.5 %), 164.06 (1.0 %) | Xylan |
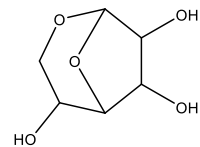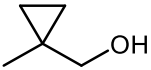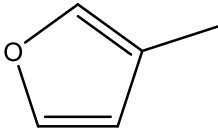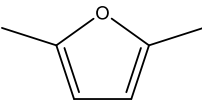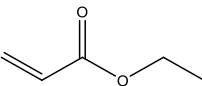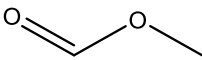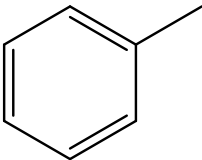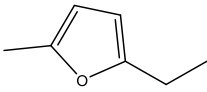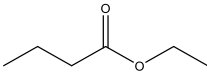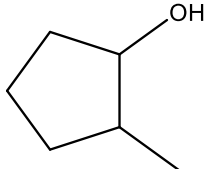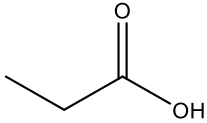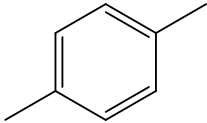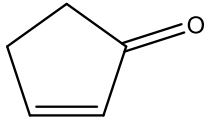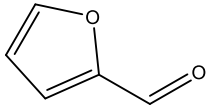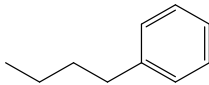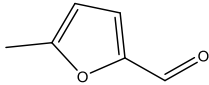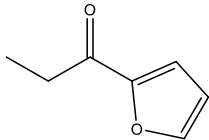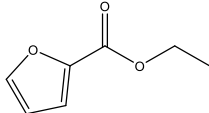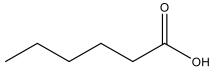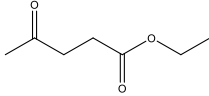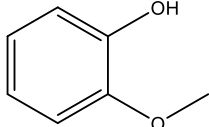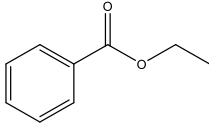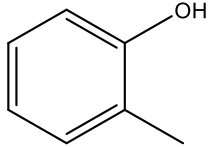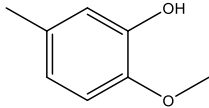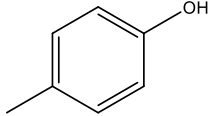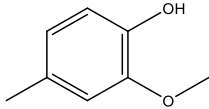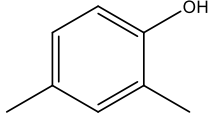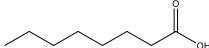
Table A.3 Full list of all Py-GC-MS identified components found in Organosolv lignin
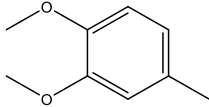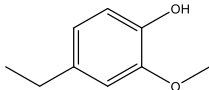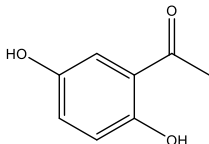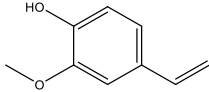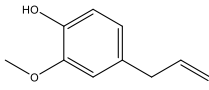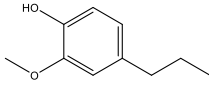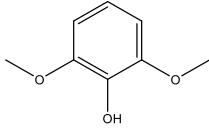
Retention Time (min)	Name	Formula	MW	Structure	m/z	Key Precursor
2.04	1-methylcyclopropanemethanol	$C_5H_{10}O$	86		86.07 (100.0 %), 87.08 (5.4 %)	Holocellulose
2.29	3-methylfuran	C_5H_6O	82		82.04 (100.0 %), 83.05 (5.4 %)	Holocellulose
3.10	2,5-dimethylfuran	C_6H_8O	96		96.06 (100.0 %), 97.06 (6.5 %)	Holocellulose
3.31	ethyl acrylate	$C_5H_8O_2$	100		100.05 (100.0 %), 101.06 (5.4 %)	Holocellulose
3.67	methyl formate	$C_2H_4O_2$	60		60.02 (100.0 %), 61.02 (2.2 %)	Xylan
4.23	toluene	C_7H_8	92		92.06 (100.0 %), 93.07 (7.6 %)	Lignin
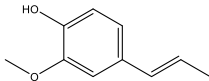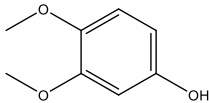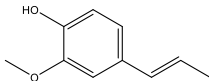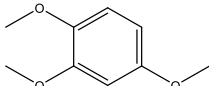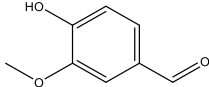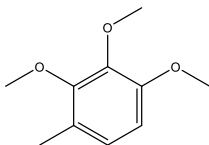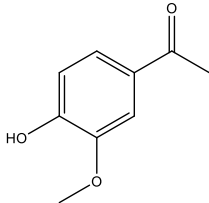
4.74	2-ethyl-5-methylfuran	$C_7H_{10}O$	110		110.07 (100.0 %), 111.08 (7.6 %)	Holocellulose
5.33	ethyl butanoate	$C_6H_{12}O_2$	116		116.08 (100.0 %), 117.09 (6.5 %)	Holocellulose
5.96	2-methylcyclopentanol	$C_6H_{12}O_2$	100		100.09 (100.0 %), 101.09 (6.5 %)	Holocellulose
6.29	propanoic acid	C_3H_6O	74		74.04 (100.0 %), 75.04 (3.2 %)	Holocellulose
7.11	1,4-dimethylbenzene (p-Xylene)	C_8H_{10}	106		106.08 (100.0 %), 107.08 (8.7 %)	Lignin
9.08	2-cyclopenten-1-one	C_5H_6O	82		82.04 (100.0 %), 83.05 (5.4 %)	Holocellulose
9.28	furfural	$C_5H_4O_2$	96		96.02 (100.0 %), 97.02 (5.4 %)	Holocellulose
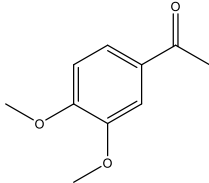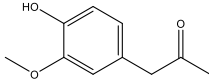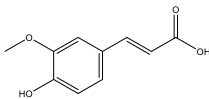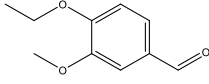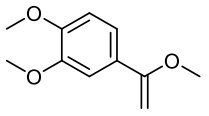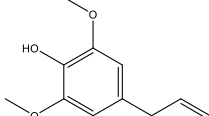
15.71	butyl benzene	$C_{10}H_{14}$	134		134.11 (100.0 %), 135.11 (10.8 %)	Lignin
16.00	5-methyl-2-furancarboxaldehyde	$C_6H_6O_2$	110		110.04 (100.0 %), 111.04 (6.5 %)	Holocellulose
17.40	1-(2-furanyl)-1-propanone	$C_7H_8O_2$	124		124.05 (100.0 %), 125.06 (7.6 %)	Holocellulose
19.71	ethyl furan-2-carboxylate	$C_7H_8O_3$	140		140.05 (100.0 %), 141.05 (7.6 %)	Holocellulose
19.97	hexanoic acid	$C_6H_{12}O_2$	116		116.08 (100.0 %), 117.09 (6.5 %)	Holocellulose
21.70	levulinic acid, ethyl ester	$C_7H_{12}O_3$	144		144.08 (100.0 %), 145.08 (7.6 %)	Holocellulose
22.69	2-methoxyphenol (guaiacol)	$C_7H_8O_2$	124		124.05 (100.0 %), 125.06 (7.6 %)	Guaiacol lignin
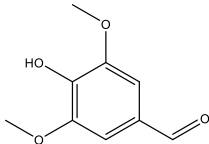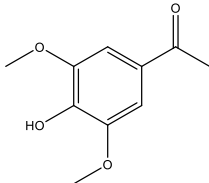
24.99	ethyl benzoate	$C_9H_{10}O_2$	150		150.07 (100.0 %0, 151.07 (9.7 %)	Lignin
25.21	2-methylphenol (o-Cresol)	C_7H_8O	108		108.06 (100.0 %), 109.06 (7.6 %)	p-Hydroxyphenyl lignin
26.55	2-Methoxy-5-methylphenol	$C_8H_{10}O_2$	138		138.07 (100.0 %), 139.07 (8.7 %)	Guaiacol lignin
27.25	4-methylphenol (p-Cresol)	C_7H_8O	108		108.06 (100.0 %), 109.06 (7.6 %)	p-Hydroxyphenyl lignin
28.48	2-methoxy-4-methylphenol (Creosol)	$C_8H_{10}O_2$	138		138.07 (100.0 %), 139.07 (8.7 %)	Guaiacol lignin
29.70	2,4-dimethylphenol	$C_8H_{10}O$	122		122.07 (100.0 %), 123.08 (8.7 %)	p-Hydroxyphenyl lignin
30.24	octanoic acid	$C_8H_{16}O_2$	144		144.12 (100.0 %), 145.12 (8.7 %)	Lignin

31.86	3,4-dimethoxytoluene	$C_9H_{12}O_2$	152		152.08 (100.0 %), 153.09 (9.7 %)	Lignin
32.91	4-ethyl-2-methoxyphenol	$C_9H_{12}O_2$	152		152.08 (100.0 %), 153.09 (9.7 %)	Guaiacol lignin
33.79	1-(2,5-dihydroxyphenyl)-ethanone	$C_8H_8O_3$	152		152.05 (100.0 %), 153.05 (8.7 %)	p-Hydroxyphenyl lignin
36.02	2-methoxy-4-vinylphenol	$C_9H_{10}O_2$	150		150.07 (100.0 %), 151.07 (9.7 %)	Guaiacol lignin
37.16	2-methoxy-4-(2-propenyl)phenol (eugenol)	$C_{10}H_{12}O_2$	164		164.08 (100.0 %), 165.09 (10.8 %)	Guaiacol lignin
37.28	2-methoxy-4-propylphenol	$C_{10}H_{14}O_2$	166		166.10 (100.0 %), 167.10 (10.8 %)	Guaiacol lignin
39.07	2,6-dimethoxyphenol (syringol)	$C_8H_{10}O_3$	154		154.06 (100.0 %), 155.07 (8.7 %)	Syringol lignin

40.01	2-methoxy-4-propenylphenol (isoeugenol)	$C_{10}H_{12}O_2$	164		164.08 (100.0 %), 165.09 (10.8 %)	Guaiacol lignin
40.65	3,4-dimethoxyphenol	$C_8H_{10}O_3$	154		154.06 (100.0 %), 155.07 (8.7 %)	Guaiacol lignin
42.72	(E)-2-methoxy-4-(2-propenyl)phenol (trans-isoeugenol)	$C_{10}H_{12}O_2$	164		164.08 (100.0 %), 165.09 (10.8 %)	Guaiacol lignin
43.75	1,2,4-trimethoxybenzene	$C_9H_{12}O_3$	168		168.08 (100.0 %), 169.08 (9.7 %)	Syringol lignin
44.02	4-hydroxy-3-methoxybenzaldehyde (vanillin)	$C_8H_8O_3$	152		152.05 (100.0 %), 153.05 (8.7 %)	Guaiacol lignin
47.13	1,2,3-trimethoxy-4-methylbenzene	$C_{10}H_{14}O_3$	182		182.09 (100.0 %), 183.10 (10.8 %)	Syringol lignin
47.60	1-(4-hydroxy-3-methoxyphenyl)-ethanone (apocynin)	$C_9H_{10}O_3$	166		166.06 (100.0 %), 167.07 (9.7 %)	Guaiacol lignin
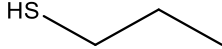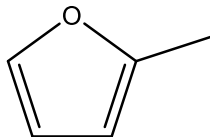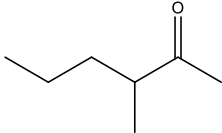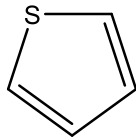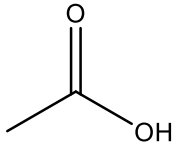
49.93	3,4-dimethoxyacetophenone	$C_{10}H_{12}O_3$	180		180.08 (100.0 %), 181.08 (10.8 %)	Guaiacol lignin
50.15	1-(4-hydroxy-3-methoxyphenyl)-2-propanone	$C_{10}H_{12}O_3$	180		180.08 (100.0 %), 181.08 (10.8 %)	Guaiacol lignin
50.72	3-(4-hydroxy-3-methoxyphenyl)-2-propenoic acid	$C_{10}H_{10}O_4$	194		194.06 (100.0 %), 195.06 (10.8 %)	Guaiacol lignin
51.41	4-ethoxy-3-anisaldehyde	$C_{10}H_{12}O_3$	180		180.08 (100.0 %), 181.08 (10.8 %)	Lignin
52.92	1,2-dimethoxy-4-(1-methoxyethenyl)benzene	$C_{11}H_{14}O_3$	194		194.09 (100.0 %), 195.10 (11.9 %)	Lignin
55.74	2,6-dimethoxy-4-(2-propenyl)-phenol	$C_{11}H_{14}O_3$	194		194.09 (100.0 %), 195.10 (11.9 %)	Syringol lignin
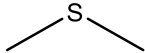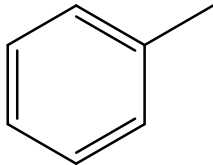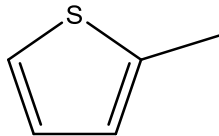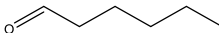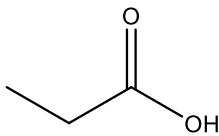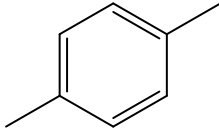
| 57.00 | 4-hydroxy-3,5-dimethoxy-benzaldehyde | $C_9H_{10}O_4$ | 196 | | 182.06 (100.0 %), 183.06 (9.7 %) | Syringol lignin |
| 59.67 | 1-(4-hydroxy-3,5-dimethoxyphenyl)-ethanone | $C_{10}H_{12}O_4$ | 196 | | 196.07 (100.0 %), 197.08 (10.8 %) | Syringol lignin |
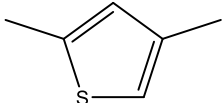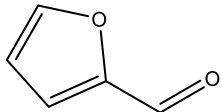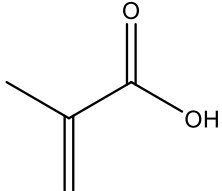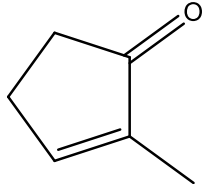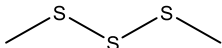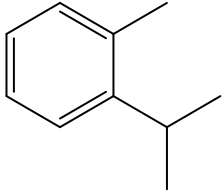
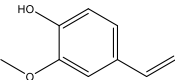**Table A.4 Full list of all Py-GC-MS identified components found in LignoBoost lignin**
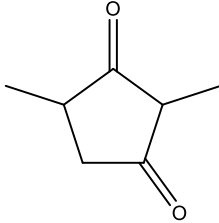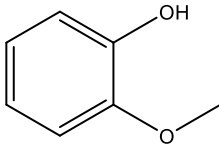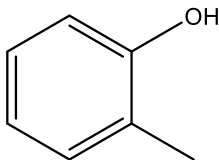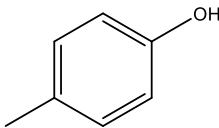
Retention Time (min)	Name	Formula	MW	Structure	m/z	Key Precursor
2.06	propyl mercaptan	C_3H_8S	76		76.03 (100.0 %), 78.03 (4.5 %), 77.04 (3.2 %)	LignoBoost process
2.31	2-methylfuran	C_5H_6O	82		82.04 (100.0 %), 83.05 (5.4 %)	Holocellulose
2.56	3-methyl-2-hexanone	$C_7H_{14}O$	114		114.10 (100.0 %), 115.11 (7.6 %)	Holocellulose
2.96	thiophene	C_4H_4S	84		84.00 (100.0 %), 86.00 (4.5 %), 85.01 (4.3 %)	LignoBoost process
3.79	acetic acid	$C_2H_4O_2$	60		60.02 (100.0 %), 61.02 (2.2 %)	Holocellulose

247
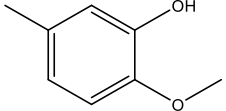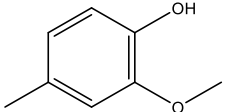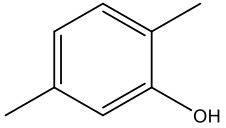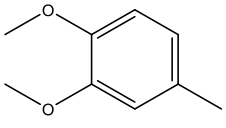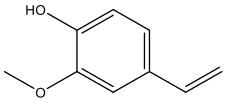
4.19	dimethyl sulphide	$C_2H_6S_2$	94		62.02 (100.0 %), 64.01 (4.5 %), 63.02 (2.2 %)	LignoBoost process
4.29	toluene	C_7H_8	92		92.06 (100.0 %), 93.07 (7.6 %)	Lignin
4.82	2-methylthiophene	C_5H_6S	98		98.02 (100.0 %), 99.02 (5.4 %), 100.01 (5.4 %)	LignoBoost process
6.09	hexanal	$C_6H_{12}O$	100		100.09 (100.0 %), 101.09 (6.5 %)	Holocellulose
6.30	propanoic acid	$C_3H_6O_2$	74		74.04 (100.0 %), 75.04 (3.2 %)	Holocellulose
7.24	1,4-dimethylbenzene (p-Xylene)	C_8H_{10}	106		106.08 (100.0 %), 107.08 (8.7 %)	Lignin
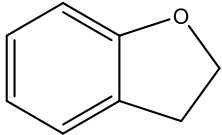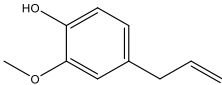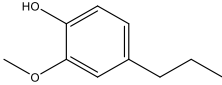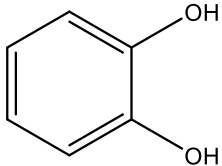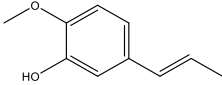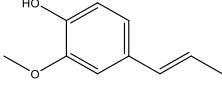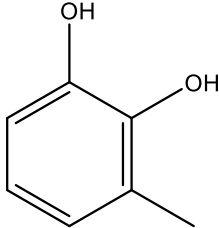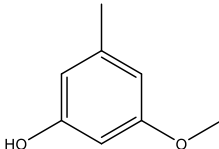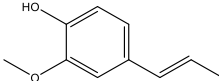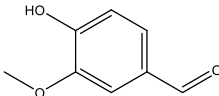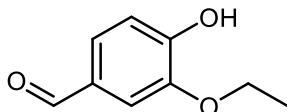
7.80	2,4-dimethylthiophene	C$_6$H$_8$S	112		112.03 (100.0 %), 113.04 (6.5 %), 114.03 (4.5 %)	LignoBoost process
9.36	furfural	C$_5$H$_4$O$_2$	96		96.02 (100.0 %), 97.02 (5.4 %)	Holocellulose
10.72	2-methyl-2-propenoic acid	C$_4$H$_6$O$_2$	86		86.04 (100.0 %), 87.04 (4.3 %)	Holocellulose
11.86	2-methyl-2-cyclopenten-1-one	C$_6$H$_8$O	96		96.06 (100.0 %), 97.06 (6.5 %)	Holocellulose
12.54	dimethyl trisulfide	C$_2$H$_6$S$_3$	126		125.96 (100.0 %), 127.96 (9.0 %), 127.96 (4.5 %), 126.96 (2.4 %), 126.97 (2.2 %)	LignoBoost process
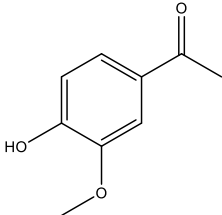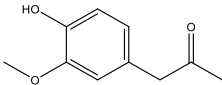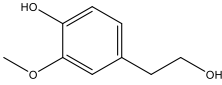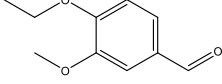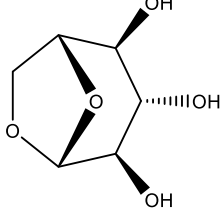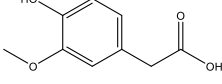
14.06	o-Cymene	$C_{10}H_{14}$	134		134.11 (100.0 %), 135.11 (10.8 %)	Lignin
15.82	1-methoxy-4-methylbenzene	$C_8H_{10}O$	122		122.07 (100.0 %), 123.08 (8.7 %)	Lignin
18.48	2-methyl-1-phenylpropene	$C_{10}H_{12}$	132		132.09 (100.0 %), 133.10 (10.8 %)	Lignin
20.31	2,4-dimethylanisole	$C_9H_{12}O$	136		136.09 (100.0 %), 137.09 (9.7 %)	Lignin
20.55	3-methyl-1,2-cyclopentanedione	$C_6H_8O_2$	112		112.05 (100.0 %), 113.06 (6.5 %)	Xylan

21.47	2,4-dimethyl-1,3-cyclopentanedione	$C_7H_{10}O_2$	126		126.07 (100.0 %), 127.07 (7.6 %)	Holocellulose
23.13	2-methoxyphenol (guaiacol)	$C_7H_8O_2$	124		124.05 (100.0 %), 125.06 (7.6 %)	Guaiacol lignin
25.34	2-methylpenol (o-cresol)	C_7H_8O	108		108.06 (100.0 %), 109.06 (7.5 %)	p-Hydroxyphenyl lignin
26.76	2-methoxy-6-methylphenol	$C_8H_{10}O_2$	138		138.07 (100.0 %), 139.07 (8.7 %)	Guiacol lignin
27.40	4-methylphenol (p-Cresol)	C_7H_8O	108		108.06 (100.0 %), 109.06 (7.6 %)	p-Hydroxyphenyl lignin

27.98	2-methoxy-5-methylphenol	$C_8H_{10}O_2$	138		138.07 (100.0 %), 139.07 (8.7 %)	Guaiacol lignin
29.01	2-methoxy-4-methylphenol (Creosol)	$C_8H_{10}O_2$	138		138.07 (100.0 %), 139.07 (8.7 %)	Guaiacol lignin
29.85	2,5-dimethylphenol	$C_8H_{10}O$	122		122.07 (100.0 %), 123.08 (8.7 %)	p-Hydroxyphenyl lignin
30.16	2,3-dimethoxytoluene	$C_9H_{12}O_2$	152		152.08 (100.0 %), 153.09 (9.7 %)	Lignin
32.13	3,4-dimethoxytoluene	$C_9H_{12}O_2$	152		152.08 (100.0 %), 153.09 (9.7 %)	Lignin
36.42	2-methoxy-4-vinylphenol	$C_9H_{10}O_2$	150		150.07 (100.0 %), 151.07 (9.7 %)	Guaiacol lignin

36.78	2,3-dihydrobenzofuran	C_8H_8O	120		120.06 (100.0 %), 121.06 (8.7 %)	Lignin
37.48	2-methoxy-4-(2-propenyl)phenol (eugenol)	$C_{10}H_{12}O_2$	164		164.08 (100.0 %), 165.09 (10.8 %)	Guaiacol lignin
37.60	2-methoxy-4-propylphenol	$C_{10}H_{14}O_2$	166		166.10 (100.0 %), 167.10 (10.8 %)	Guaiacol lignin
39.23	1,2-dihydroxybenzene (catechol)	C_6H6O_2	110		110.04 (100.0 %), 111.04 (6.5 %)	Lignin
39.56	2-methoxy-5-(1-propenyl)-phenol	$C_{10}H_{12}O_2$	164		164.08 (100.0 %), 165.09 (10.8 %)	Guaiacol lignin
40.29	2-methoxy-4-propenylphenol (isoeugenol)	$C_{10}H_{12}O_2$	164		164.08 (100.0 %), 165.09 (10.8 %)	Guaiacol lignin

41.02	3-methyl-1,2-benzenediol	$C_7H_8O_2$	124		124.05 (100.0 %), 125.06 (7.6 %)	Lignin
41.68	3-methoxy-5-methylphenol	$C_8H_{10}O_2$	138		138.07 (100.0 %), 139.07 (8.7 %)	Lignin
43.09	(E)-2-methoxy-4-(2-propenyl)phenol (trans-isoeugenol)	$C_{10}H_{12}O_2$	164		164.08 (100.0 %), 165.09 (10.8 %)	Guaiacol lignin
44.11	4-hydroxy-3-methoxybenzaldehyde (vanillin)	$C_8H_8O_3$	152		152.05 (100.0 %), 153.05 (8.7 %)	Guaiacol lignin
46.81	3-ethoxy-4-hydroxybenzaldehyde (ethyl vanillin)	$C_9H_{10}O_3$	166		166.06 (100.0 %), 167.07 (9.7 %)	Guaiacol lignin

47.99	1-(4-hydroxy-3-methoxyphenyl)-ethanone (apocynin)	$C_9H_{10}O3$	166		166.06 (100.0 %), 167.07 (9.7 %)	Guaiacol lignin
50.35	1-(4-hydroxy-3-methoxyphenyl)-2-propanone	$C_{10}H_{12}O_3$	180		180.08 (100.0 %), 181.08 (10.8 %)	Guaiacol lignin
50.84	homovanillyl alcohol	$C_9H_{12}O_3$	168		168.08 (100.0 %), 169.08 (9.7 %)	Guaiacol lignin
51.71	4-ethoxy-3-anisaldehyde	$C_{10}H_{12}O_3$	180		180.08 (100.0 %), 181.08 (10.8 %)	Lignin
55.27	1,6-anhydro-β-D-glucopyranose (levoglucosan)	$C_6H_{10}O_5$	162		162.05 (100.0 %), 163.06 (6.5 %), 164.06 (1.0 %)	Cellulose
56.20	2-(4-hydroxy-3-methoxyphenyl)acetic acid (homovanillic acid)	$C_9H_{10}O_4$	182		182.06 (100.0 %), 183.06 (9.7 %)	Guaiacol lignin
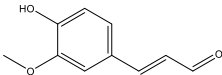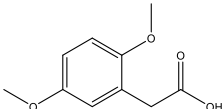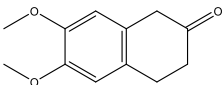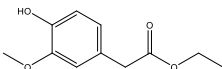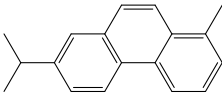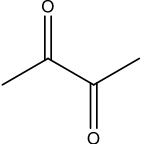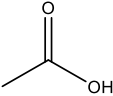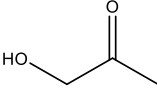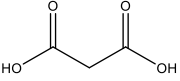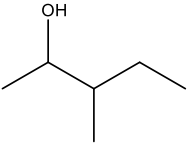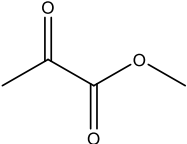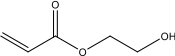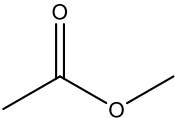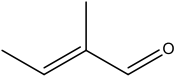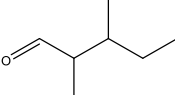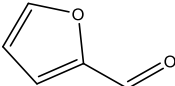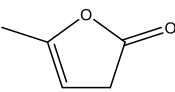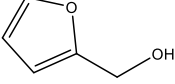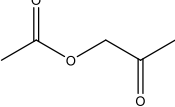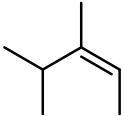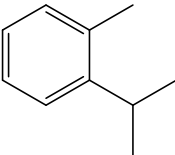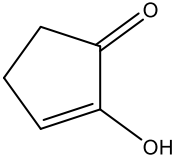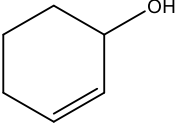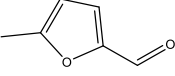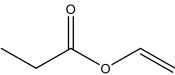
61.42	3-(4-hydroxy-3-methoxyphenyl)-2-propenal	$C_{10}H_{10}O_3$	178		178.06 (100.0 %), 179.07 (10.8 %)	Guaiacol lignin
61.64	2,5-dimethoxybenzeneacetic acid	$C_{10}H_{12}O_4$	196		196.07 (100.0 %), 197.08 (10.8 %)	Lignin
62.78	6,7-dimethoxy-2-tetralone	$C_{12}H_{14}O_3$	206		206.09 (100.0 %), 207.10 (13.0 %)	Lignin
66.05	ethyl homovanillate	$C_{11}H_{14}O_4$	210		210.09 (100.0 %), 211.09 (11.9 %)	Guaiacol lignin
72.87	retene	$C_{18}H_{18}$	234		234.14 (100.0 %), 235.14 (19.5 %), 236.15 (1.8 %)	Lignin
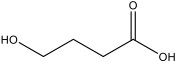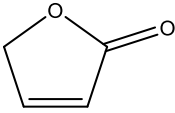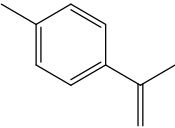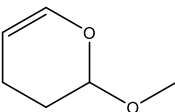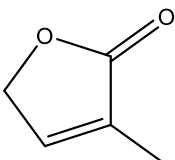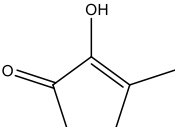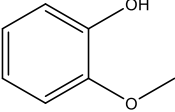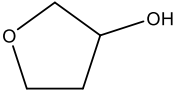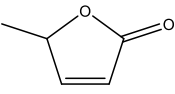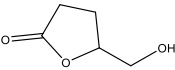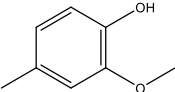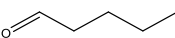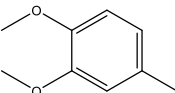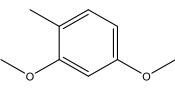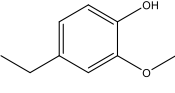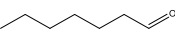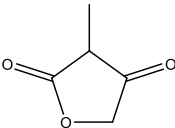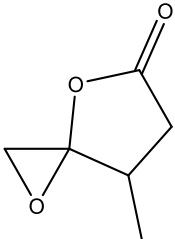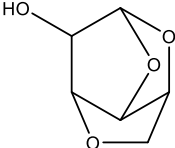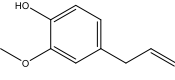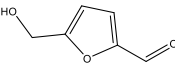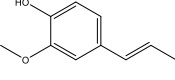
Retention Time (min)	Name	Formula	MW	Structure	m/z	Key precursor
2.56	2,3-butanedione	$C_4H_6O_2$	86		86.04 (100.0 %), 87.04 (4.3%)	Cellulose
3.72	acetic acid	$C_2H_4O_2$	60		60.02 (100.0 %), 61.02 (2.2 %)	Holocellulose
4.35	1-hydroxy-2-propanone (hydroyxacetone)	$C_3H_6O_2$	74		74.04 (100.0 %), 75.04 (3.2 %)	Cellulose
4.91	propanedioc acid	$C_3H_4O_4$	104		104.01 (100.0 %), 105.01 (3.2 %)	Holocellulose
5.16	3-methyl-2-pentanol	$C_6H_{14}O$	102		102.10 (100.0 %), 103.11 (6.5 %)	Holocellulose
5.37	methyl pyruvate	$C_4H_6O_3$	102		102.03 (100.0 %), 103.04 (4.3 %)	Holocellulose
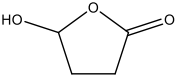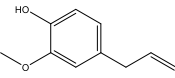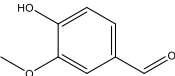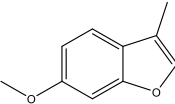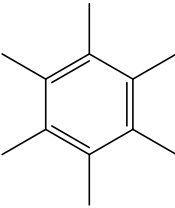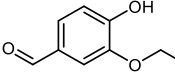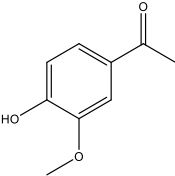
6.29	2-propenoic acid, 2-hydroxyethyl ester	$C_5H_8O_3$	116		116.05 (100.0 %), 117.05 (5.4 %)	Holocellulose
7.30	methyl acetate	$C_3H_6O_2$	74		74.05 (100.0 %), 75.04 (3.2 %)	Holocellulose
7.46	2-methyl-2-butenal	C_5H_8O	84		84.06 (100.0 %), 85.06 (5.4 %)	Holocellulose
8.81	2,3-dimethylpentanal	$C_7H_{14}O$	114		114.10 (100.0 %), 115.11 (7.6 %)	Holocellulose
9.44	furfural	$C_5H_4O_2$	96		96.02 (100.0 %), 97.02 (5.4 %)	Holocellulose
11.17	5-methyl-2(3H)-furanone	$C_5H_6O_2$	98		98.04 (100.0 %), 99.04 (5.4 %)	Holocellulose
11.78	2-furanmethanol	$C_5H_6O_2$	98		98.04 (100.0 %), 99.04 (5.4 %)	Holocellulose
12.05	1-(acetyloxy)-2-propanone	$C_5H_8O_3$	116		116.05 (100.0 %), 117.04 (5.4 %)	Holocellulose
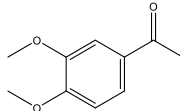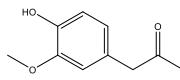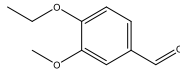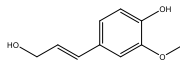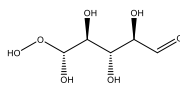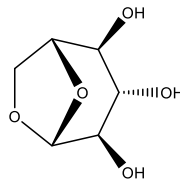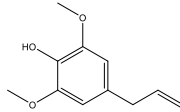
12.56	cis-3,4-dimethyl-2-pentene	C_7H_{14}	98		98.11 (100.0 %), 99.11 (7.6 %)	Holocellulose
13.37	4-cyclopenten-1,3-dione	$C_5H_4O_2$	96		96.02 (100.0 %), 97.02 (5.4 %)	Holocellulose
14.02	o-Cymene	$C_{10}H_{14}$	134		134.11 (100.0 %), 135.11 (10.8 %)	Lignin
15.15	2-hydroxy-2-cyclopenten-1-one	$C_5H_6O_2$	98		98.04 (100.0 %), 99.04 (5.4 %)	Holocellulose
16.02	2-cyclohexen-1-ol	$C_6H_{10}O$	98		98.07 (100.0 %), 99.08 (6.5 %)	p-Hydroxyphenyl lignin
16.15	5-methyl-2-furancarboxaldehyde	$C_6H_6O_2$	110		110.04 (100.0 %), 111.04 (6.5 %)	Holocellulose
16.69	vinyl propionate	$C_5H_8O_2$	100		100.05 (100.0 %), 101.06 (5.4 %)	Holocellulose

17.03	4-hydroxybutanoic acid	$C_4H_8O_3$	104		104.05 (100.0 %), 105.05 (4.3 %)	Holocellulose
17.75	2(5H)-furanone	$C_4H_4O_3$	84		84.02 (100.0 %), 85.02 (4.3 %)	Holocellulose
18.41	1-methyl-4-(1-methylethenyl)-benzene	$C_{10}H_{12}$	132		132.09 (100.0 %), 133.10 (10.8 %)	Lignin
19.07	3,4-dihydro-2-methoxy-2H-pyran	$C_6H_{10}O_2$	114		114.07 (100.0 %), 115.07 (6.5 %)	Holocellulose
20.08	3-methyl-2(5H)-furanone	$C_5H_6O_2$	98		98.04 (100.0 %), 99.04 (5.4 %)	Holocellulose
20.53	2-hydroxy-3-methyl-2-cyclopenten-1-one	$C_6H_8O_2$	112		112.05 (100.0 %), 113.06 (6.5 %)	Holocellulose
22.85	2-methoxyphenol (guaiacol)	$C_7H_8O_2$	124		124.05 (100.0 %), 125.06 (7.6 %)	Guaiacol lignin

26.01	tetrahydro-3-furanol	$C_4H_8O_2$	88		88.05 (100.0 %), 89.06 (4.3 %)	Holocellulose
26.23	5-methyl-5H-furan-2-one	$C_5H_6O_2$	98		98.04 (100.0 %), 99.05 (5.4 %)	Holocellulose
27.55	5-hydroxy-methyldihydrofuran-2-one	$C_5H_8O_3$	116		116.05 (100.0 %), 117.05 (5.4 %)	Holocellulose
28.64	2-methoxy-4-methylphenol (Creosol)	$C_8H_{10}O_2$	138		138.07 (100.0 %), 139.07 (8.7 %)	Guaiacol lignin
28.78	pentanal	$C_5H_{10}O$	86		86.07 (100.0 %), 87.08 (5.4 %)	Holocellulose
30.12	3,4-dimethoxytoluene	$C_9H_{12}O_2$	152		152.08 (100.0 %), 153.09 (9.7 %)	Lignin
32.04	1,5-dimethoxy-2-methyl-benzene	$C_9H_{12}O_2$	152		152.08 (100.0 %), 153.09 (9.7 %)	Lignin
33.06	4-ethyl-2-methoxyphenol	$C_9H_{12}O_2$	152		152.08 (100.0 %), 153.09 (9.7 %)	Guaiacol lignin
33.21	heptanal	$C_7H_{14}O$	114		114.10 (100.0 %), 151.11 (7.6 %)	Holocellulose

33.75	3-methyl-2,4(3H,5H)-furandione	$C_5H_6O_3$	114		114.03 (100.0 %), 115.04 (5.4 %)	Holocellulose
34.11	7-methyl-1,4-dioxaspiro[2,4]heptan-5-one	$C_6H_8O_3$	128		128.05 (100.0 %), 129.05 (6.5 %)	Holocellulose
35.07	1,4:3,6-dianhydro-α-D-glucopyranose	$C_6H_8O_4$	144		144.04 (100.0 %), 145.05 (6.5 %)	Cellulose
36.20	2-methoxy-4-vinylphenol	$C_9H_{10}O_2$	150		150.07 (100.0 %), 151.07 (9.7 %)	Guaiacol lignin
37.36	2-methoxy-4-(2-propenyl)phenol (eugenol)	$C_{10}H_{12}O_2$	164		164.08 (100.0 %), 165.09 (10.8 %)	Guaiacol lignin
38.94	5-hydroxymethylfurfural	$C_6H_6O_3$	126		126.03 (100.0 %), 127.04 (6.5 %)	Cellulose
40.17	2-methoxy-4-propenylphenol (isoeugenol)	$C_{10}H_{12}O_2$	164		164.08 (100.0 %), 165.09 (10.8 %)	Guaiacol lignin

40.79	dihydro-5-hydroxy-2(3H)-furanone	$C_4H_8O_3$	104		102.03 (100.0 %), 103.04 (4.3 %)	Holocellulose
42.93	(E)-2-methoxy-4-(2-propenyl)phenol (trans-isoeugenol)	$C_{10}H_{12}O_2$	164		164.08 (100.0 %), 165.09 (10.8 %)	Guaiacol lignin
43.87	4-hydroxy-3-methoxybenzaldehyde (vanillin)	$C_8H_8O_3$	152		152.05 (100.0 %), 153.05 (8.7 %)	Guaiacol lignin
44.21	6-methoxy-3-methylbenzofuran	$C_{10}H_{10}O_2$	162		162.07 (100.0 %), 163.07 (10.08 %)	Lignin
44.73	Hexamethylbenzene	$C_{12}H_{18}$	162		162.14 (100.0 %), 163.14 (13.0 %)	Lignin
46.72	3-ethoxy-4-hydroxybenzaldehyde (ethyl vanillin)	$C_9H_{10}O_3$	166		166.06 (100.0 %), 167.07 (9.7 %)	Guaiacol lignin
47.73	1-(4-hydroxy-3-methoxyphenyl)-ethanone (apocynin)	$C_9H_{10}O_3$	166		166.06 (100.0 %), 167.07 (9.7 %)	Guaiacol lignin

49.90	1-(3,4-dimethoxyphenyl)-ethanone	$C_{10}H_{12}O_3$	180		180.08 (100.0 %), 181.08 (10.8 %)	Lignin
50.15	1-(4-hydroxy-3-methoxyphenyl)-2-propanone	$C_{10}H_{12}O_3$	180		180.08 (100.0 %), 181.08 (10.8 %)	Guaiacol lignin
51.56	4-ethoxy-3-anisaldehyde	$C_{10}H_{12}O_3$	180		180.08 (100.0 %), 181.08 (10.8 %)	Lignin
52.17	4-(3-hydroxy-1-propenyl)-2-methoxyphenol	$C_{10}H_{12}O_3$	180		180.08 (100.0 %), 181.08 (10.8 %)	Guaiacol lignin
52.44	d-Allose (hexose)	$C_6H_{12}O_6$	180		180.06 (100.0 %), 181.07 (6.5 %), 182.07 (1.2 %)	Xylan
54.24	1,6-anhydro-β-D-glucopyranose (levoglucosan)	$C_6H_{10}O_5$	162		162.05 (100.0 %), 163.06 (6.5 %), 164.06 (1.0 %)	Cellulose
55.74	2,6-dimethoxy-4-(2-propenyl)-phenol	$C_{11}H_{14}O_3$	194		194.09 (100.0 %), 195.10 (11.9 %)	Syringol lignin
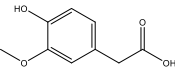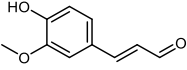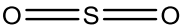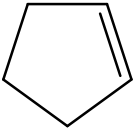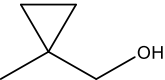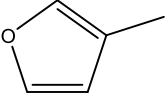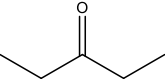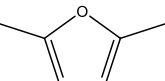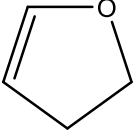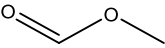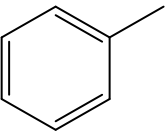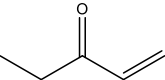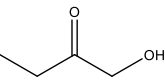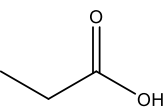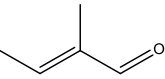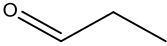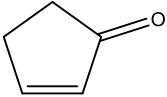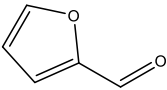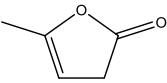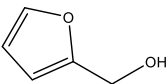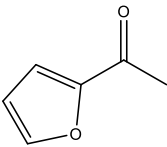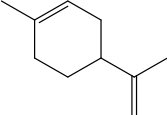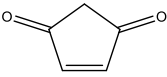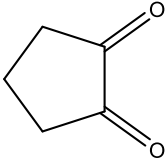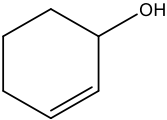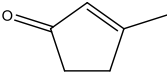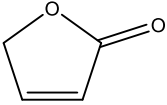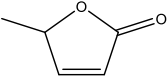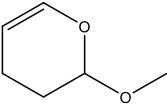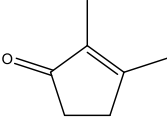
55.98	2-(4-hydroxy-3-methoxyphenyl)acetic acid (homovanillic acid)	$C_9H_{10}O_4$	182		182.06 (100.0 %), 183.06 (9.7 %)	Guaiacol lignin
61.44	3-(4-hydroxy-3-methoxyphenyl)-2-propenal	$C_{10}H_{10}O_3$	178		178.06 (100.0 %), 179.07 (10.8 %)	Guaiacol lignin
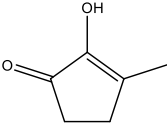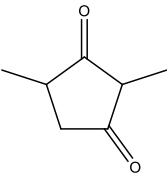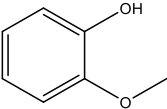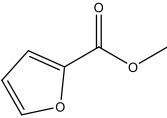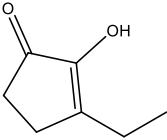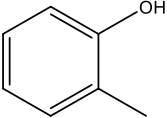
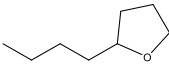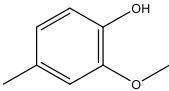**Table A.6 Full list of all Py-GC-MS identified components found in wheat straw**
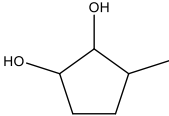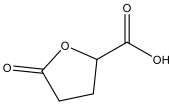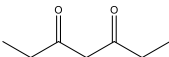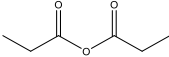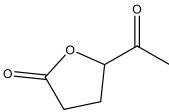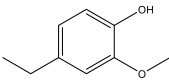
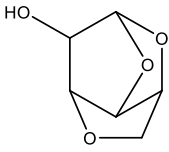| Retention Time (min)	Name	Formula	MW	Structure	m/z	Key Precursor
1.74	sulphur dioxide	O_2S	64	O=S=O	63.96 (100.0 %), 65.96 (4.5 %)	Holocellulose
1.93	cyclopentene	C_5H_8	68		68.06 (100.0 %), 69.07 (5.4 %)	Holocellulose
2.05	1-methylcyclopropanemethanol	$C_5H_{10}O$	86		86.07 (100.0 %), 87.08 (5.4 %)	Holocellulose
2.29	3-methylfuran	C_5H_6O	82		82.04 (100.0 %), 83.05 (5.4 %)	Holocellulose
2.57	3-pentanone	$C_5H_{10}O$	86		86.07 (100.0 %), 87.08 (5.4 %)	Holocellulose
3.11	2,5-dimethylfuran	C_6H_8O	96		96.06 (100.0 %), 97.06 (6.5 %)	Holocellulose
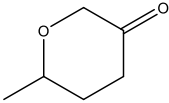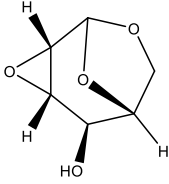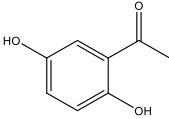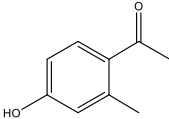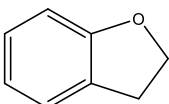
3.29	2,3-dihydrofuran	C_4H_6O	70		70.04 (100.0 %), Holocellulose 71.05 (4.3 %)
3.71	methyl formate	$C_2H_4O_2$	60		60.02 (100.0 %), Xylan 61.02 (2.2 %)
4.25	toluene	C_7H_8	92		92.06 (100.0 %), Lignin 93.07 (7.6 %)
6.31	1-penten-3-one	C_5H_8O	84		84.06 (100.0 %), Holocellulose 85.06 (5.4 %)
6.97	1-hydroxy-2-butanone	$C_4H_8O_2$	88		88.05 (100.0 %), Holocellulose 89.06 (4.3 %)
7.20	propanoic acid	$C_3H_6O_2$	74		74.04 (100.0 %), Holocellulose 75.04 (3.2 %)
7.42	2-methyl-2-butenal	C_5H_8O	84		84.06 (100.0 %), Holocellulose 85.06 (5.4 %)

8.77	propanal	C_3H_6O	58		58.04 (100.0 %), Holocellulose 59.05 (3.2 %)
9.19	2-cyclopenten-1-one	C_5H_6O	82		82.04 (100.0 %), Holocellulose 83.05 (5.4 %)
9.36	furfural	$C_5H_4O_2$	96		96.02 (100.0 %), Holocellulose 97.02 (5.4 %)
11.07	5-methyl-2(3H)-furanone	$C_5H_6O_2$	98		98.04 (100.0 %), Holocellulose 99.04 (5.4 %)
11.75	2-furanmethanol	C_5H_6O	98		98.04 (100.0 %), Holocellulose 99.04 (5.4 %)
12.55	1-(2-furanyl)-ethanone	$C_6H_6O_2$	110		110.04 (100.0 %), Holocellulose 111.04 (6.5 %)
13.00	limonene	$C_{10}H_{16}$	136		136.13 (100.0 %), Lignin 137.13 (10.8 %)
13.28	4-cyclopenten-1,3-dione	$C_5H_4O_2$	96		96.02 (100.0 %), Holocellulose 97.02 (5.4 %)
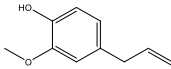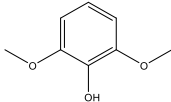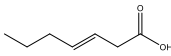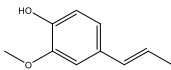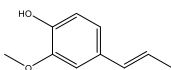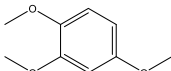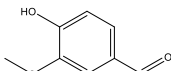
15.19	1,2-cyclopentanedione	$C_5H_6O_2$	98		98.04 (100.0 %), 99.04 (5.4 %)	Xylan
15.99	2-cyclohexen-1-ol	$C_6H_{10}O$	98		98.07 (100.0 %), 99.08 (6.5 %)	p-Hydroxyphenyl lignin
16.72	3-methyl-2-cyclopenten-1-one	C_6H_8O	96		96.06(100.0 %), 97.06 (6.5 %)	Holocellulose
17.70	2(5H)-furanone	$C_4H_4O_2$	84		84.02 (100.0 %), 85.02 (4.3 %)	Holocellulose
18.29	5-methyl-2(5H)-furanone	$C_5H_6O_2$	98		98.04 (100.0 %), 99.04 (5.4 %)	Holocellulose
18.96	3,4-dihydro-2-methoxy-2H-pyran	$C_6H_{10}O_2$	114		114.07 (100.0 %), 115.07 (6.5 %)	Holocellulose
19.75	2,3-dimethyl-2-cyclopenten-1-one	$C_7H_{10}O$	110		110.07 (100.0 %), 111.08 (7.6 %)	Holocellulose
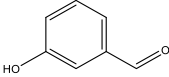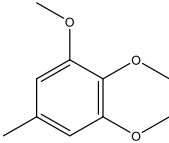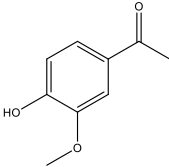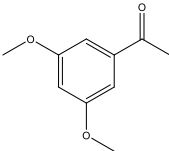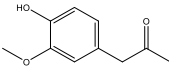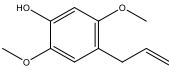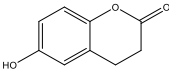
20.51	2-hydroxy-3-methyl-2-cyclopenten-1-one	$C_6H_8O_2$	112		112.05 (100.0 %), 113.06 (6.5 %)	Holocellulose
21.14	2,4-dimethyl-1,3-cyclopentanedione	$C_7H_{10}O_2$	126		126.07 (100.0 %), 127.07 (7.6 %)	Holocellulose
22.70	2-methoxyphenol (guaiacol)	$C_7H_8O_2$	124		124.05 (100.0 %), 125.06 (7.6 %)	Guaiacol lignin
24.21	methyl 2-furoate	$C_6H_6O_3$	126		126.03 (100.0 %), 127.04 (6.5 %)	Holocellulose
25.07	3-ethyl-2-hydroxy-2-cyclopenten-1-one	$C_7H_{10}O_2$	126		126.07 (100.0 %), 127.07 (7.6 %)	Holocellulose
25.30	2-methylphenol (o-Cresol)	C_7H_8O	108		108.06 (100.0 %), 109.06 (7.6 %)	p-Hydroxyphenyl lignin
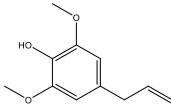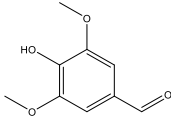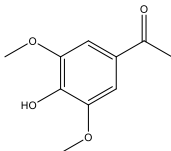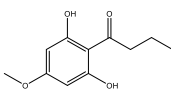
26.08	3-methyl-1,2-cyclopentanediol	$C_6H_{12}O_2$	116		116.08 (100.0 %), 117.09 (6.5 %)	Holocellulose
27.51	5-oxotetrahydrofuran-2-carboxylic acid	$C_5H_6O_4$	130		130.03 (100.0 %), 131.03 (5.4 %)	Holocellulose
27.90	6-butyltetrahydrofuran	$C_8H_{16}O$	128		128.12 (100.0 %), 129.12 (8.7 %)	Holocellulose
28.43	2-methoxy-4-methylphenol (Creosol)	$C_8H_{10}O_2$	138		138.07 (100.0 %), 139.07 (8.7 %)	Guaiacol lignin
28.63	3,4-heptadione	$C_7H_{12}O_2$	128		128.08 (100.0 %), 129.09 (7.6 %)	Holocellulose
28.84	propanoic anhydride	$C_6H_{10}O_3$	130		130.06 (100.0 %), 131.07 (6.5 %)	Holocellulose
32.10	5-acetyldihydro-2(3H)-furanone	$C_6H_8O_3$	128		128.05 (100.0 %), 129.05 (6.5 %)	Holocellulose
32.90	4-ethyl-2-methoxyphenol	$C_9H_{12}O_2$	152		152.08 (100.0 %), 153.09 (9.7 %)	Guaiacol lignin

33.60	dihydro-6-methyl-2H-pyran-3(4H)-one	$C_6H_{10}O_2$	144		144.07 (100.0 %), 115.07 (6.5 %)	Holocellulose
33.82	2,3-anhydro-D-mannosan	$C_6H_8O_4$	144		144.04 (100.0 %), 145.05 (6.5 %)	Hemicellulose
33.91	1-(2,5-dihydroxyphenyl)-ethanone	$C_8H_8O_3$	152		152.05 (100.0 %), 153.05 (8.7 %)	p-Hydroxyphenyl lignin
35.02	1,4:3,6-dianhydro-α-D-glucopyranose	$C_6H_8O_4$	144		144.04 (100.0 %), 145.05 (6.5 %)	Cellulose
36.09	4-hydroxy-2-methylacetophenone	$C_9H_{10}O_2$	150		150.07 (100.0 %), 151.07 (9.7 %)	p-Hydroxyphenyl lignin
36.64	2,3-dihydrobenzofuran	C_8H_8O	120		120.06 (100.0 %), 121.06 (8.7 %)	Lignin

37.18	2-methoxy-4-(2-propenyl)phenol (eugenol)	$C_{10}H_{12}O_2$	164		164.08 (100.0 %), 165.09 (10.8 %)	Guaiacol lignin
38.89	2,6-dimethoxyphenol (syringol)	$C_8H_{10}O_3$	154		154.06 (100.0%), 155.07 (8.7 %)	Syringol lignin
39.46	3-heptenoic acid	$C_7H_{12}O_2$	128		128.08 (100.0 %), 129.09 (7.6 %)	Holocellulose
40.00	2-methoxy-4-propenylphenol (isoeugenol)	$C_{10}H_{12}O_2$	164		164.08 (100.0 %), 165.09 (10.8 %)	Guaiacol lignin
42.64	(E)-2-methoxy-4-(1-propenyl)phenol (trans-isoeugenol)	$C_{10}H_{12}O_2$	164		164.08 (100.0 %), 165.09 (10.8 %)	Guaiacol lignin
43.45	1,2,4-trimethoxybenzene	$C_9H_{12}O_3$	168		168.08 (100.0 %), 169.08 (9.7 %)	Syringol lignin
43.63	4-hydroxy-3-methoxybenzaldehyde (vanillin)	$C_8H_8O_3$	152		152.05 (100.0 %), 153.05 (8.7 %)	Guaiacol lignin

45.38	3-hydroxybenzaldehyde	C₇H₆O₂	122		122.04 (100.0 %), 123.04 (7.6 %)	p-Hydroxyphenyl lignin
46.97	1,2,3-trimethoxy-5-methylbenzene	C₁₀H₁₄O₃	182		182.09 (100.0 %), 183.10 (10.8 %)	Lignin
47.54	1-(4-hydroxy-3-methoxyphenyl)-ethanone (apocynin)	C₉H₁₀O₃	166		166.06 (100.0 %), 167.07 (9.7 %)	Guaiacol lignin
49.73	3,5-dimethoxyacetophenone	C₁₀H₁₂O₃	180		180.08 (100.0 %), 181.08 (10.8 %)	Lignin
49.97	1-(4-hydroxy-3-methoxyphenyl)-2-propanone	C₁₀H₁₂O₃	180		180.08 (100.0 %), 181.08 (10.8 %)	Guaiacol lignin
50.54	2,5-dimethoxy-4(2-propenyl)-phenol	C₁₁H₁₄O₃	194		194.09 (100.0 %), 195.10 (11.9 %)	Guaiacol lignin
50.68	3,4-dihydro-6-hydroxy-2H-1-benzopyran-2-one	C₉H₈O₃	164		164.05 (100.0 %), 165.05 (9.7 %)	p-Hydroxyphenyl lignin

45.38	3-hydroxybenzaldehyde	$C_7H_6O_2$	122		122.04 (100.0 %), 123.04 (7.6 %)	p-Hydroxyphenyl lignin
46.97	1,2,3-trimethoxy-5-methylbenzene	$C_{10}H_{14}O_3$	182		182.09 (100.0 %), 183.10 (10.8 %)	Lignin
47.54	1-(4-hydroxy-3-methoxyphenyl)-ethanone (apocynin)	$C_9H_{10}O_3$	166		166.06 (100.0 %), 167.07 (9.7 %)	Guaiacol lignin
49.73	3,5-dimethoxyacetophenone	$C_{10}H_{12}O_3$	180		180.08 (100.0 %), 181.08 (10.8 %)	Lignin
49.97	1-(4-hydroxy-3-methoxyphenyl)-2-propanone	$C_{10}H_{12}O_3$	180		180.08 (100.0 %), 181.08 (10.8 %)	Guaiacol lignin
50.54	2,5-dimethoxy-4(2-propenyl)-phenol	$C_{11}H_{14}O_3$	194		194.09 (100.0 %), 195.10 (11.9 %)	Guaiacol lignin
50.68	3,4-dihydro-6-hydroxy-2H-1-benzopyran-2-one	$C_9H_8O_3$	164		164.05 (100.0 %), 165.05 (9.7 %)	p-Hydroxyphenyl lignin

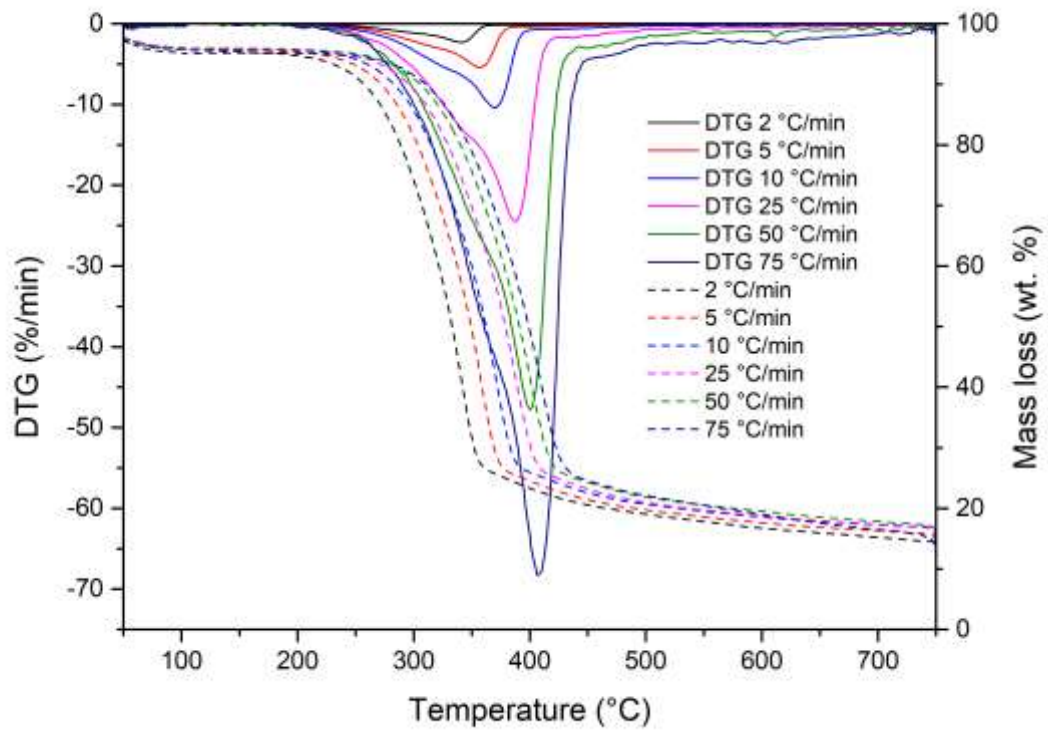|						
55.52	2,6-dimethoxy-4-(2-propenyl)-phenol	$C_{11}H_{14}O_3$	194		194.09 (100.0 %), 195.10 (11.9 %)	Syringol lignin
56.76	4-hydroxy-3,5-dimethoxybenzaldehdye	$C_9H_{10}O_4$	182		182.06 (100.0 %), 183.06 (9.7 %)	Syringol lignin
59.64	1-(4-hydroxy-3,5-dimethoxyphenyl)-ethanone	$C_{10}H_{12}O_4$	196		196.07 (100.0 %), 197.08 (10.8 %)	Syringol lignin
61.48	desaspidinol	$C_{11}H_{14}O_4$	210		210.09 (100.0 %), 211.09 (11.9 %)	Guaiacol lignin

Appendix B

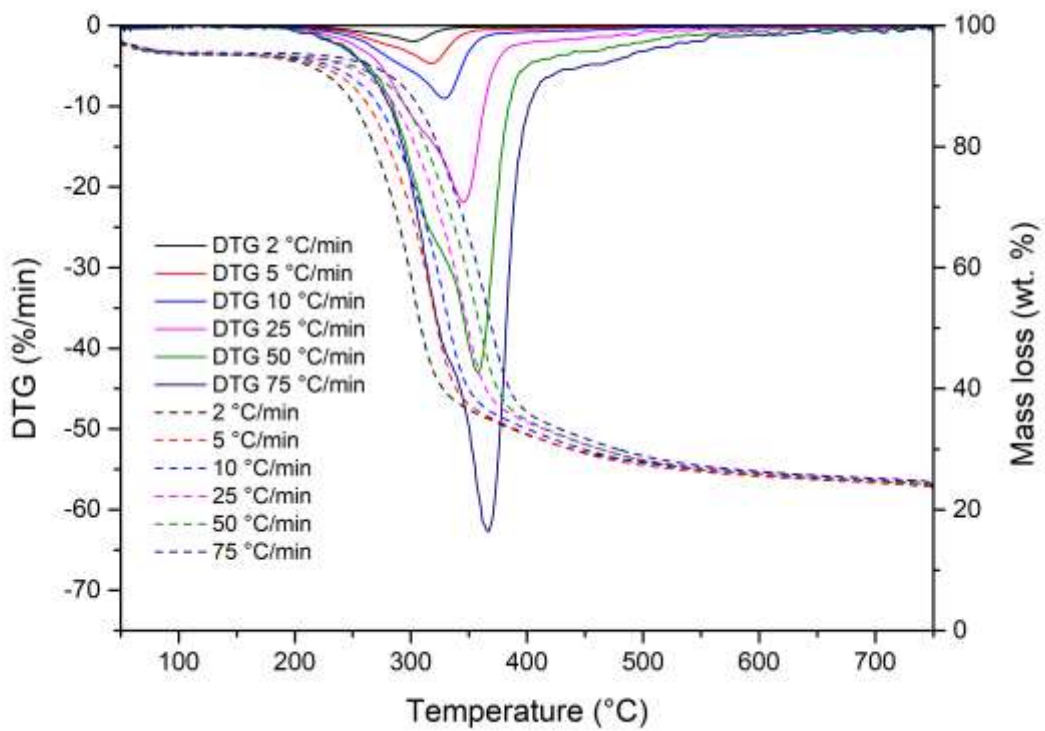**Figure B.1 DTG and mass loss of pine wood**
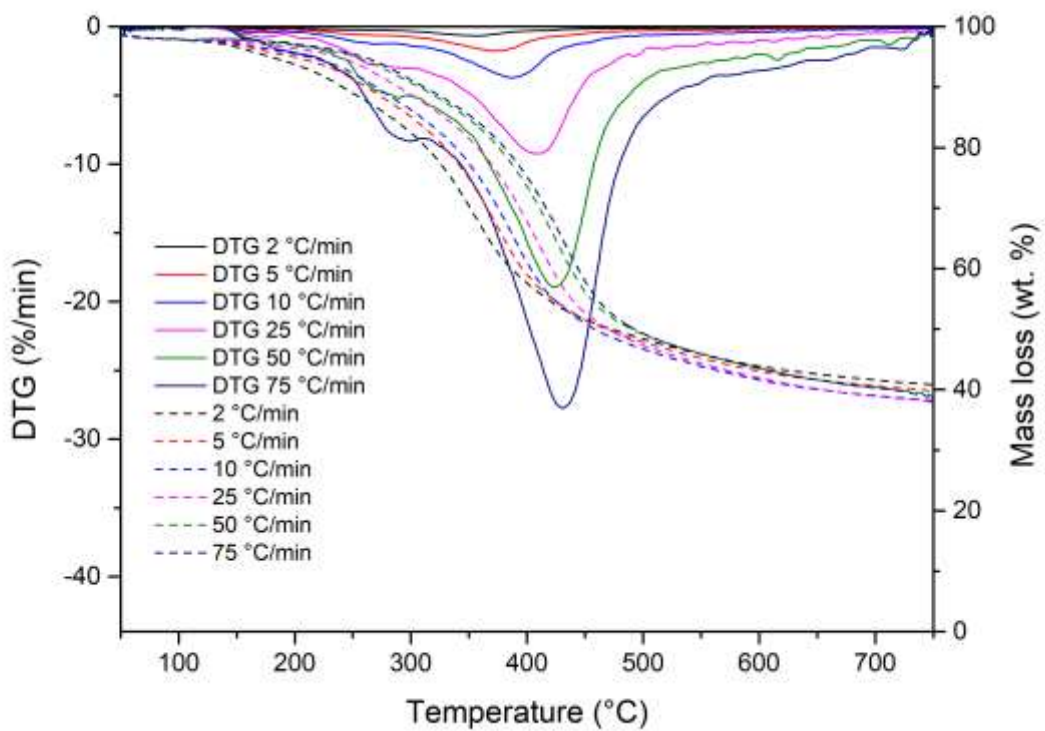
Figure B.2 DTG and mass loss wheat straw

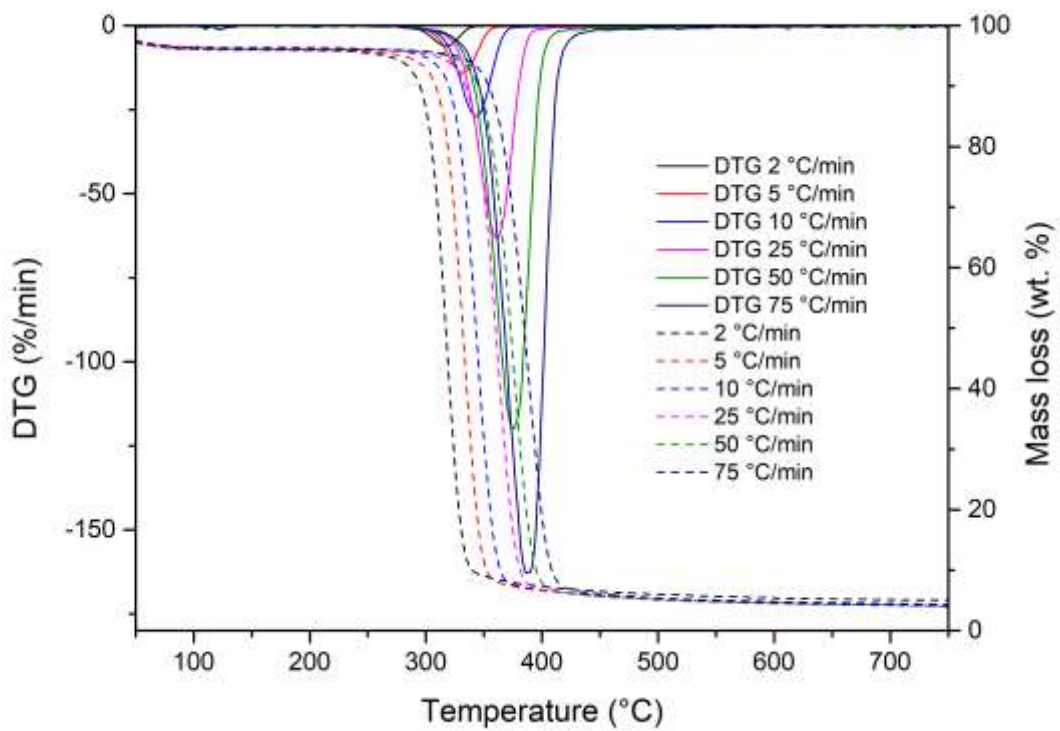**Figure B.3 DTG and mass loss LignoBoost lignin**

Figure B.4 DTG and mass loss of cellulose

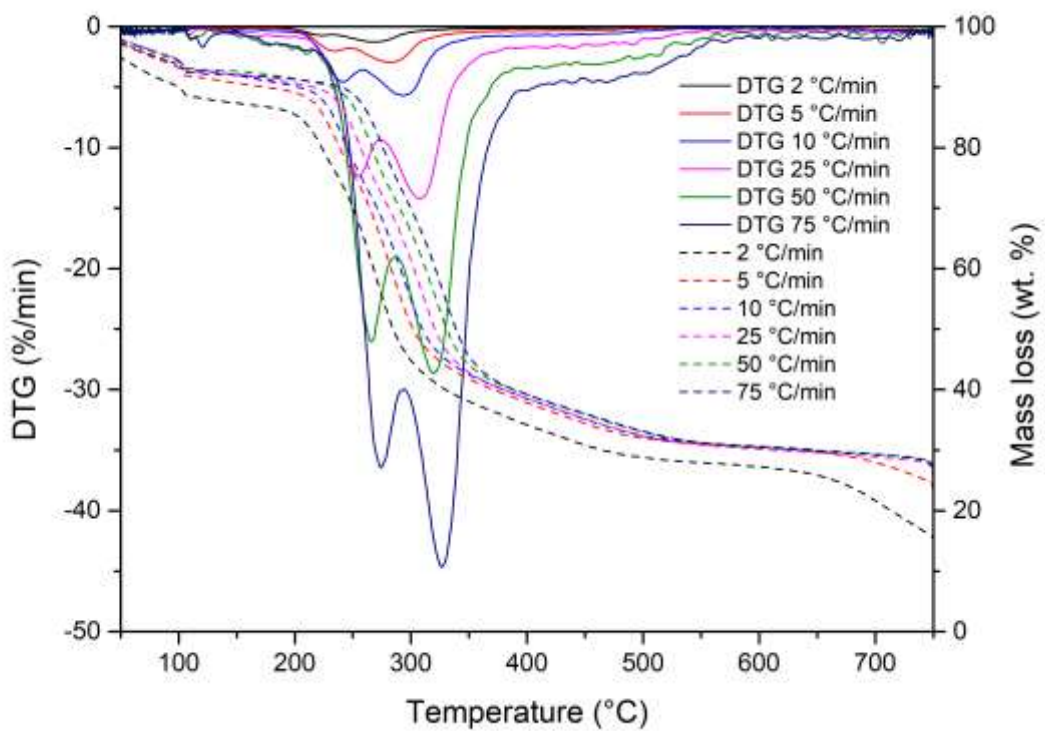**Figure B.5 DTG and mass loss of xylan**

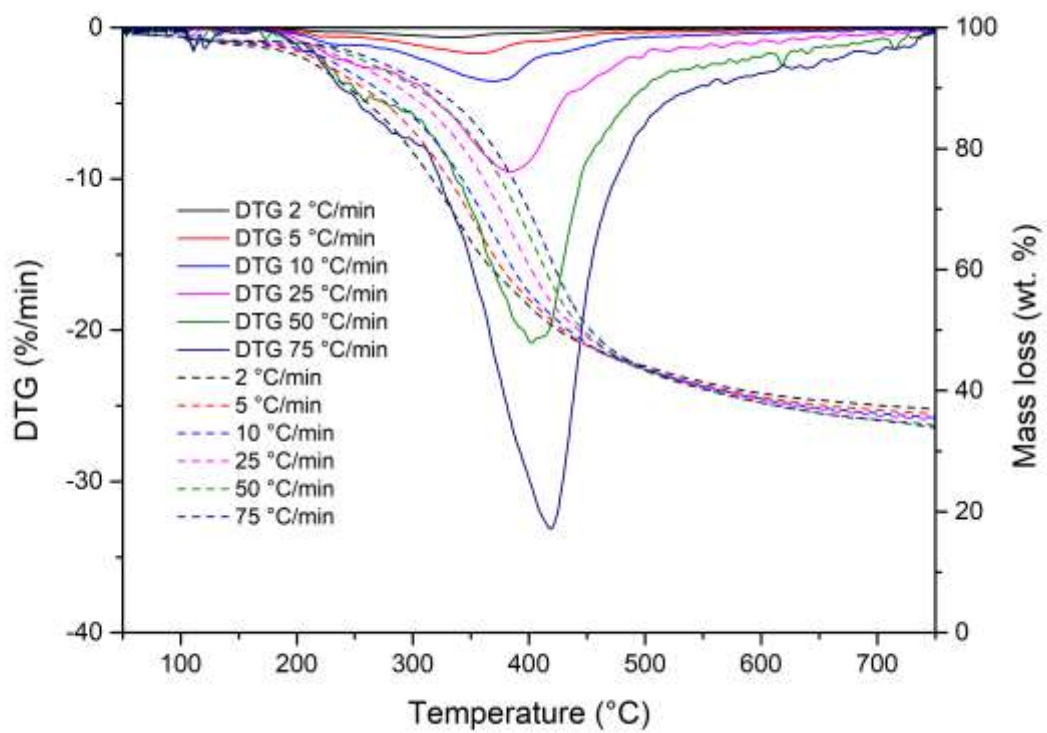**Figure B.6 DTG and mass loss of Organosolv lignin**

Appendix C

Degrees of Freedom	Confidence level (%)						
	50	90	95	98	99	99.5	99.9
1	1.00	6.31	12.71	31.82	63.66	127.32	636.58
2	0.82	2.92	4.30	6.97	9.93	14.09	31.60
3	0.77	2.35	3.18	4.54	5.84	7.45	12.92
4	0.74	2.13	**2.78**	3.75	4.60	5.60	8.61
5	0.73	2.02	2.57	3.37	4.03	4.77	6.87
6	0.72	1.94	2.45	3.14	3.71	4.32	5.96
7	0.71	1.90	2.37	3.00	3.50	4.03	5.41
8	0.71	1.86	2.31	2.90	3.36	3.83	5.04
9	0.70	1.83	2.26	2.82	3.25	3.69	4.78
10	0.70	1.81	2.23	2.76	3.17	3.58	4.59
15	0.69	1.75	2.13	2.60	2.95	3.25	4.07
20	0.69	1.73	2.09	2.53	2.85	3.15	3.85
25	0.68	1.71	2.06	2.49	2.79	3.08	3.73
30	0.68	1.70	2.04	2.46	2.75	3.03	3.65
40	0.68	1.68	2.02	2.42	2.70	2.97	3.55
60	0.68	1.67	2.00	2.39	2.66	2.92	3.46
120	0.68	1.66	1.98	2.36	2.62	2.86	3.37
∞	0.67	1.65	1.96	2.33	2.58	2.81	3.29

Table C.1. Values of student's t factor [278].

Appendix D

Table C.1 Gas products from different temperatures from LignoBoost lignin and pine wood

Gases (%)	LignoBoost lignin			Pine wood		
	275 °C	300 °C	325 °C	275 °C	300 °C	325 °C
Methane	0.01	0.05	0.07	0.01	0.02	0.05
Ethene	0.01	0.01	0.01	0.00	0.01	0.01
Ethane	0.00	0.01	0.01	0.00	0.00	0.01
Propene	0.00	0.01	0.01	0.01	0.03	0.04
Butane	0.00	0.00	0.01	0.03	0.01	0.01
Hydrogen	0.00	0.00	0.00	0.00	0.00	0.01
Carbon monoxide	0.05	0.09	0.09	0.00	0.00	0.10
Carbon dioxide*	99.92	99.85	99.81	99.94	99.95	99.80